Research Frontiers 2016

SPring-8
SACLA

ISSN 1349-0087
SPring-8 Document D2017-008

SPring-8/SACLA Research Frontiers 2016

CONTENTS

Physical Science

Chemical Science

Earth & Planetary Science

Industrial Applications

Note: The principal publication(s) concerning each article is indicated with all author's names in italics in the list of references.

Preface

Today, the SPring-8 campus operates two world-leading accelerator-based light source facilities and offers a unique environment where the two can be used synergistically.

SPring-8 (Super Photon ring 8 GeV), one of the world's largest synchrotron facilities, welcomed its 200,000th user in April 2016, just eighteen and a half years after it was opened to users in October 1997. SPring-8 has helped users from various scientific and industrial disciplines to realize numerous outstanding achievements. Currently, SPring-8 users are publishing over 1,000 research papers per year, and the ratio of papers in the top 1% of the citation index was as high as 2.5% for the papers published in 2014.

SACLA (SPring-8 Angstrom Compact free electron LAser) is the second operating hard X-ray Free Electron laser (XFEL) in the world and the first compact XFEL, which was opened to users in March 2012. SACLA produces femtosecond X-ray pulses with nearly full spatial coherence and offers research opportunities to users from various fields, including structural biology, nonlinear X-ray optics, ultrafast physics and chemistry, and high-energy-density science. In 2016, SACLA users published over 60 research papers, and the ratio of papers in the top 1% of the citation index was as high as 7.0% for all papers published by users.

A number of SPring-8 and SACLA users were awarded prizes in 2016 and 2017 for their achievements in science and technology. Prof. Yoshihiro Kawamura (Kumamoto University) was awarded the Medal with Purple Ribbon in 2017 for the research and development of amorphous metal alloys. In 2017, eight active users from academia and industry were awarded Prizes for Science and Technology by the Minister of Education, Culture, Sports, Science and Technology, and nine young users were awarded Young Scientists Prizes by the Minister.

In this volume, two comprehensive reviews are reported by Prof. Toshiyuki Shimizu (The University of Tokyo) and Prof. Akira Sekiyama (Osaka University). Active users of SPring-8 have also contributed the essence of their results as review articles in this volume. In addition, eight excellent articles are provided by active users of SACLA.

I am very grateful to the many authors and experts who contributed their papers to this volume. Special thanks are due to Dr. Naoto Yagi and the members of the editorial board for their continuous efforts.

土肥 義治

Yoshiharu Doi
President
Japan Synchrotron Radiation Research Institute (JASRI)

Editor's Note

Here is the 2016 issue of SPring-8/SACLA Research Frontiers that covers outstanding scientific outcomes of SPring-8 and SACLA in 2015 and 2016. The number of reports on experiments made at SACLA has been increasing since it started operation in 2011. In this issue, there are eight excellent articles (six last year) in Life Science, Physical Science and Chemical Science, proving that SACLA is becoming a common experimental tool for leading-edge sciences.

Reviews in this issue were contributed by Prof. Shimizu of University of Tokyo and Prof. Sekiyama of Osaka University. The former is on the crystal structure analysis of TLR proteins which are the key players in the innate immune system. This basic immune system is a relatively new discovery in biology (a subject of Nobel prize in 2011) and still a hot topic in the field. It is a great honor for us that structure of such topical proteins has been determined using SPring-8. The latter review is on the development and applications of HAXPES (HArd X-ray PhotoEmission Spectroscopy) which is an experimental technique developed mainly at SPring-8. As it requires a brilliant X-ray beam from an undulator, it is one of the techniques that make best use of SPring-8. It is well-known for its bulk-sensitive nature, but Prof. Sekiyama emphasizes there is a lot more to it.

Please note that SPring-8/SACLA Research Frontiers is made of two parts. The first is the scientific results (Scientific Frontiers) and the second is additional information on hard and soft infrastructures that support scientific research. Although some important numbers such as the operation time and the number of users are given in the second part, more complete statistical information on the operation of SPring-8 and SACLA is available on the website (http://www.spring8.or.jp/en/about_us/spring8data/).

This year, we are trying to update our distribution list because copies have been sent to the same addresses, with minute updates, over the years. We have realized that some people have already retired and may not need a copy. Thus, we are asking those who receive the copies to send us an email (to **frontiers@spring8.or.jp**) so that we can continue to send another issue next year. Please note that the full text of SPring-8/SACLA Research Frontiers is also available on the SPring-8 website (http://www.spring8.or.jp/en/news_publications/publications/research_frontiers/). For the list of publications produced by SPring-8 users and staff, please visit the publication database at http://www.spring8.or.jp/en/science/publication_database/.

On behalf of all the editors, I would like to thank those who helped us by recommending excellent research results suitable for publication in this issue, and the users and staff of SPring-8 who contributed their reports to this issue.

Naoto Yagi
- Editor in Chief -
Japan Synchrotron Radiation Research Institute (JASRI)

Editorial Board

SCIENTIFIC FRONTIERS

Review Article

Structural Characterization of Nucleic Acid-sensing Toll-like Receptors

The innate immune system senses pathogen-associated or cell damage-associated structurally conserved molecules through various pattern recognition receptors (PPRs) [1]. Nucleic acids that are released from viruses, bacteria or dead cells during infection or tissue damage are principal ligands to PPRs. PRR involved in nucleic acid recognition can be divided into two groups on the basis of cellular localization: several members of membrane-bound Toll-like receptors (TLRs) and cytoplasmic PPRs such as Nod-like receptors (NLRs), RIG-I like receptors (RLRs), and the DNA recognition receptor cyclic GMP-AMP synthase (cGAS).

TLRs, evolutionarily conserved membrane-spanning receptors homologous to the *Drosophila* Toll protein, are mostly expressed in macrophages and dendritic cells. The recognition of pathogen-associated molecular patterns (PAMPs) or damage-associated molecular patterns (DAMPs) by TLRs is critical for the activation of the transcription factor NF-κB or IRFs, leading to the production of pro-inflammatory cytokines or type I interferons (Fig. 1). TLRs are glycosylated type I integral membrane receptors with N-terminal extracellular leucine-rich repeats (LRRs), a transmembrane domain, and a C-terminal cytoplasmic domain (Fig. 2(a)). The LRR domain contains binding sites for PAMPs or DAMPs, while the cytoplasmic domain, known as the Toll/IL-1 receptor (TIR) region, activates downstream signaling cascades by interacting with adaptor proteins such as MyD88 and TRIF [2]. Biochemical and structural studies on TLR extracellular domains suggest the following mechanism of TLR activation. Inactive TLRs exist as monomers, and ligand binding induces dimerization of the extracellular TLR domain, producing a typical "m"-shaped structure, where the intracellular C-terminal regions of the two TLR protomers are positioned in close proximity. Subsequent dimerization of the intracellular TIR domain is followed by the recruitment of adaptor proteins that execute signal transduction.

Viral/bacterial nucleic acids are potent stimulators of innate immunity. In humans, nearly half the TLRs recognize nucleic acid ligands. TLR3 responds to double-stranded (ds) RNA, while TLR7 and TLR8, which are closely related, recognize single-stranded (ss)RNA, and TLR9 senses DNA with unmethylated cytosine phosphate-guanosine (CpG) motifs (Fig. 2(b)). In addition, mouse TLR13 detects bacterial 23S ribosomal RNA. In contrast to other TLRs, TLR3 and TLRs 7–9 are expressed on endosomal membranes, limiting the recognition of self-derived ligands that are released from dying cells (Fig. 1). In addition, the members of the TLR7 subfamily comprising TLRs 7, 8, and 9 contain a characteristic long inserted loop region (known as the Z-loop) composed of approximately 30 amino acid residues, and localized in the region between LRR14 and LRR15 (Fig. 2(a,b)). Z-loop processing is required for the activation of these TLRs.

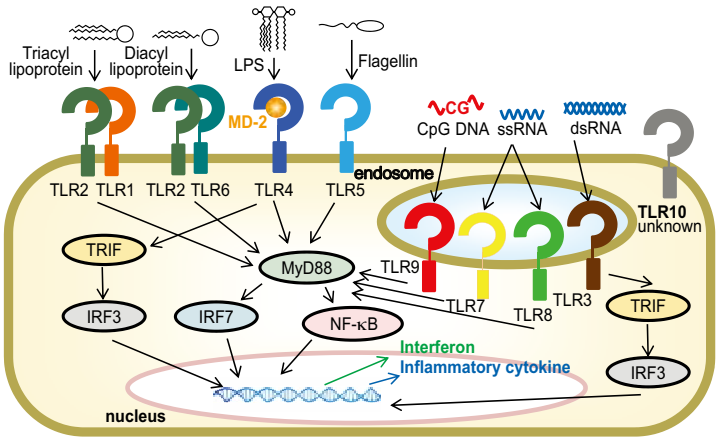

Fig. 1. **Schematic illustration of human TLR signaling**
TLR signaling is initiated by ligand-induced dimerization of receptors, followed by the engagement of TIR-domain-containing adaptor proteins, such as MyD88 and TRIF, which activate downstream signaling cascades. A major consequence of TLR signaling is the induction of proinflammatory cytokines and type I interferons. TLR5 and heterodimers of TLR2 and TLR1 or TLR6 are expressed at the cell surface, whereas TLR3 and TLR7–9 localize to the endosome, where they sense microbial and host-derived nucleic acids. TLR4 localizes to both the plasma membrane and the endosome.

Although TLR7 and TLR8 have been considered to primarily recognize ssRNA, they are also activated by small synthetic ligands such as imidazoquinolines and nucleoside analogs, raising a question concerning the molecular basis of the recognition of these structurally and chemically distinct ligands. Furthermore, expression patterns of TLR7 and TLR8 are different, but it remained to be determined whether or not the biochemical features and recognition mechanisms of TLR7 and TLR8 are different. Moreover, the mechanism of the recognition of a pathogenic DNA sequence by TLR9 has not been clarified in detail.

We used brilliant synchrotron X-rays at SPring8 BL41XU and KEK to determine the crystal structures of the LRR domains of TLR7 [3], TLR8 [4,5] and TLR9 [6]. First, the structures of unliganded and small synthetic ligand-bound TLR8 were determined (Fig. 3(a)) [4]. Chemical ligands bind to TLR8 at two equivalent positions on a symmetrical 2:2 complex, triggering the rearrangement of the dimeric configuration. Then, TLR8 C-termini are brought into closer proximity, thus generating a more compact structure than that of the m-shaped dimer. The ligand is positioned at the TLR8 dimer interface between the N-terminal half of one protomer and the C-terminal half of the other protomer, stabilizing the activated form of TLR8. Prior to structural studies of TLRs, it was not known whether the N-terminal fragment in the TLR7 family was required for ligand recognition following Z-loop processing. However, structural observations clearly demonstrated that both N- and C-terminal fragments of TLR8 are necessary for ligand recognition. Three key interactions are important in ligand recognition: (i) stacking interactions between the benzene ring of ligands and Phe405 of TLR8; (ii) hydrogen bonds between the amidine group of ligands and Asp543 of TLR8; and (iii) snug fitting of two substituents of a ligand to the small hydrophobic pocket formed between the two protomers (Fig. 3(b)).

Next, the crystal structure of TLR8 complexed with 20-mer ssRNA was determined [5]. Unexpectedly, the crystal structure revealed that rather than binding directly to the full-length ssRNA, TLR8 binds to RNA degradation products at two distinct sites (Fig. 3(a)). The first site, which accommodates the ssRNA degradation product uridine, is identical to a previously reported binding site for small synthetic ligands [4]. The second binding site located at the interior of the TLR8 ring structure is sandwiched between the concave surface and the Z-loop and holds ssRNA molecules longer than 2 nucleotides. Most recently, the structure of the activated TLR7-guanosine-ssRNA complex has been determined [3] (Fig. 3(a)). Analogous to the TLR8 structure, which recognizes uridine and ssRNA at distinct sites, TLR7 interacts with guanosine and polyU at two different sites. The first site is identical to that of TLR8, and accommodates small agonists; however, it preferentially binds guanosine, while TLR8 accommodates uridine. The second site presents an ssRNA-binding region distinct from that of TLR8 in its spatial position and ligand-recognition mode. As non-terminal uridine was specifically recognized whereas other uridines were loosely recognized, diverse oligonucleotides can be accomodated at the second site as long as they contain uridine. Taken all together, TLR7 is a dual sensor for guanosine and uridine-containing ssRNA, while TLR8 acts as a uridine sensor recognizing diverse nucleotide compositions of ssRNA. These findings indicate that although TLR7 and TLR8 are closely related receptors and demonstrate similar activation mechanisms, they have significant differences in ligand recognition patterns. Biochemical analysis provided further insights into the ligand specificity of TLR7 by showing that not only guanosine but also its modified derivatives (e.g., 7-methylguanosine and 8-hydroxyguanosine) may serve as TLR7 endogenous ligands [7].

Moreover, the research group clarified the crystal structure of three forms of TLR9, namely, unliganded TLR9, TLR9 bound to a CpG-containing DNA, and TLR9 bound to an inhibitory DNA (iDNA) [6]. CpG-containing DNA binds to TLR9 at a stoichiometric ratio of 2:2 in an extended conformation. CpG-

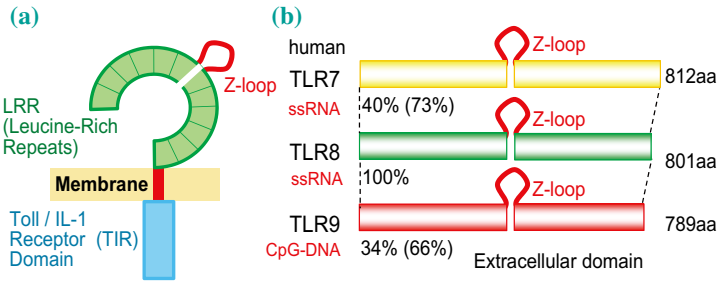

Fig. 2. **Schematic representation of nucleic acid-sensing TLRs** (**a**) Schematic representation of the domain organization in nucleic acid-sensing TLRs. TLRs consist of an extracellular LRR domain, a transmembrane domain, and a cytoplasmic TIR domain. The characteristic Z-loop is shown in red. (**b**) Schematic representation of the extracellular domains of nucleic acid-sensing TLRs. Sequence homology to TLR8 is shown, and numbers in parentheses are the values of sequence identity. The cognate ligands are also shown.

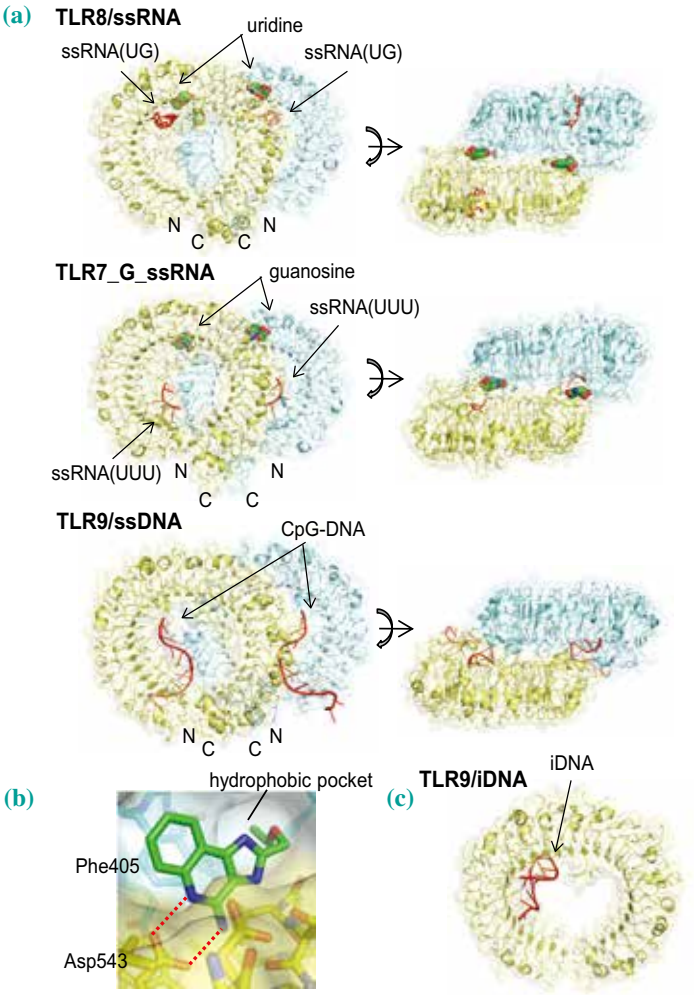

Fig. 3. **Structures of nucleic acid-sensing TLRs**
(**a**) Signaling complexes of nucleic acid-sensing TLRs. Front (left panels) ant top (right panels) views of the signaling complexes: TLR8/ssRNA (PDB: 4R07), TLR7_G_ssRNA (PDB: 5GMF), and TLR9/CpG DNA (PDB: 3WPC). (**b**) Ligand recognition by TLR8. The hydrogen bond is depicted as a red dotted line. (**c**) Structure of TLR9 in complex with iDNA.

containing DNA was recognized by its binding to the groove in the N-terminus of TLR9 of one protomer, while the C-terminal domain of the other protomer mainly binds to the DNA backbone. Thus, CpG-containing DNA acts as the molecular glue bridging two TLR9 monomers. In addition, not only the CpG motif but also its flanking regions are recognized by TLR9. It is generally accepted that TLR9 distinguishes pathogenic DNA partially on the basis of methylation status. Our works demonstrated that CpG methylation weakens the affinity of CpG to TLR9 and its ability to cause receptor dimerization, probably because of the disruption of water clusters that mediate interactions between CpG and TLR9. In the TLR9-iDNA complex, iDNA, which has a stem-loop conformation stabilized by intramolecular base-pairing, demonstrates a close fit to the concave surface of TLR9 (Fig. 2(c)). Binding interfaces of CpG-DNA and iDNA are partially overlapped. As iDNA exhibits a stronger binding affinity for TLR9 than do CpG-containing agonists, the overlap would account for the antagonistic effect of iDNA.

Synergistic activation by two ligands, revealed by the structural works in TLR7 and TLR8, is a new concept of the activation mechanism [3,5]. Although TLR7 and TLR8 exhibited the preference for guanosine and uridine, respectively, over other mononucleosides or mononucleotides at the first binding site, the binding affinity to these ligands is still lower than that to synthetic molecules (e.g., TLR8 has K_d values of 55 μM and 0.2 μM for uridine and R848, respectively). The lower affinity for mononucleosides can be attributed to the lack of the alkyl group harbored by the synthetic ligand, protruding into the hydrophobic pocket of the receptor generated by the agonistic form. However, the affinity of TLR7 and TLR8 to mononucleosides could be greatly increased by the binding of ssRNA with a shift in TLR8 K_d from 55 μM to 1 μM. This observation was confirmed in a cell-based immune response–activation assay showing that uridine stimulated substantial NF-κB activity only in the presence of a UG-rich ssRNA. The synergistic activation is also observed for guanosine derivatives and chemical ligands (e.g., loxoribine) in the presence of oligonucleotides in TLR7 [3,7]. Likewise, a synergistic activity between uridine analogs and ssRNA is demonstrated in TLR8 [7]. These findings suggest that an oligonucleotide binding at the second site increases receptor affinity to mononucleosides or chemical ligands at the first site, possibly via allosteric regulation.

Accumulating evidence suggests that proteolytic processing in endolysosomes is required for generating functional, mature TLRs. This requirement as well as localization within endosomal compartments reinforced the prevention of the activation of

TLRs by self-derived nucleic acid. In addition, proteolytic digestion of nucleic acid-sensing TLRs may restrain inappropriate activation in response to host DNA/RNA. The processing at the Z-loop of human TLR8 mediated by furin-like proprotein convertase and cathepsins produces functional TLR8 capable of ligand binding and signaling in endolysosomes. In addition, the cleaved form of TLR8 has been found to be predominant in immune cells. However, after proteolytic cleavage, the extracellular and intracellular domains must remain associated to provide the functional activity of the receptor [8,9]. This notion is supported by structural studies demonstrating that the N- and C-terminal domains of TLR7, TLR8, and TLR9 are connected and involved in ligand binding after Z-loop cleavage [3,4,6]. Biochemical and biophysical studies have revealed that the uncleaved Z-loop prevents the formation of the TLR8 dimer, which is essential for its activation [10]. Crystallographic analysis demonstrated that the uncleaved Z-loop located on the ascending lateral face prevents the approach of the dimerization partner by steric hindrance. Similarly to TLR8, TLR7 and TLR9 also contain the Z-loop, and thus, these proteins might also have this autoinhibition mechanism. This notion is supported by the observation that TLR9 with the uncleaved Z-loop was unable to dimerize irrespective of CpG-DNA presence [6].

Structural information on the nucleic acid-sensing TLRs adds to and provides new insights into the areas of the regulation of nucleic acid-sensing TLRs, proteolytic processing of TLR, synergistic activation mechanism through multiple ligand-binding sites, and nucleic acid degradation. In particular, the requirement of DNA and RNA processing for the activation of immune responses is a potentially paradigm-shifting discovery, emphasizing the importance of specific enzymes, such as RNases, DNases, and phosphatases (Fig. 4). Indeed, a recent study shows that DNA digestion by DNase II is required for TLR9 activation [11]. These newly obtained mechanistic insights may be a crucial step towards developing therapeutic drugs (agonists and antagonists) that target TLRs for the modulation of host response to pathogens.

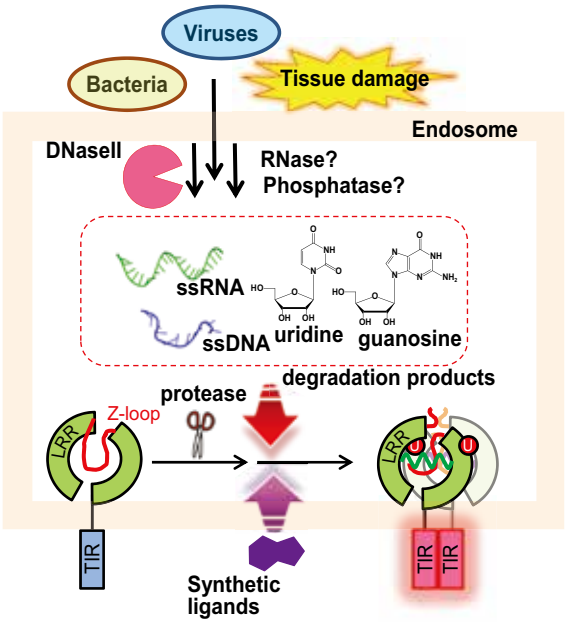

Fig. 4. **Proposed regulation mechanism of nucleic acid-sensing TLRs** Pathogen- and self-derived nucleic acids can be taken up to endolysosomes where they are digested by appropriate enzymes (DNase II, RNase, and/or phosphatase) to generate nucleosides and degradation products that are recognized by TLRs. TLRs 7–9 with the uncleaved Z-loop are monomers. Following Z-loop cleavage, TLRs 7–9 transforms into the activated dimer upon binding to processed nucleic acid agonists. In one example, TLR8 activated by uridine and ssRNA is shown. Synthetic ligands can directly activate TLR7/8.

Toshiyuki Shimizu

Graduate School of Pharmaceutical Sciences, The University of Tokyo

Email: shimizu@mol.f.u-tokyo.ac.jp

References

[1] C.A. Janeway *et al.*: Annu. Rev. Immunol. **20** (2002)197.
[2] T. Kawai *et al.*: Nat. Immunol. **11** (2010) 373.
[3] Z. Zhang *et al.*: Immunity **45** (2016) 737.
[4] H. Tanji *et al.*: Science **339** (2013) 1426.
[5] H. Tanji *et al.*: Nat. Struct. Mol. Biol. **22** (2015) 109.
[6] U. Ohto *et al.*: Nature **520** (2015) 702.
[7] T. Shibata *et al.*: Int. Immunol. **28** (2015) 211.
[8] M.M. Hipp *et al.*: J. Immunol. **194** (2015) 5417.
[9] M. Onji *et al.*: Nat. Commun. **4** (2013) 1949.
[10] H. Tanji *et al.*: Proc. Natl. Acad. Sci USA **113** (2016) 3012.
[11] M.P. Chan *et al.*: Nat. Commun. **6** (2015) 5853.

Review Article

Progress of Hard X-ray Photoemission Spectroscopy in a Decade; Its Bulk Sensitivity, Recoil Effects, and Polarization Dependence

Photoemission spectroscopy in the hard X-ray region has been one of the most improved experimental techniques since the development of insertion devices in the third-generation high-brilliance synchrotron radiation facilities, and has overcome the drawbacks of conventional photoemission for probing bulk electronic states such as surface sensitivity in the case of low-energy excitation (<~1 keV), as schematically shown in Fig. 1, and insufficiently low throughput in the case of high-energy excitation. Practical hard X-ray photoemission, known as HAXPES, has been established at undulator beamlines since 2000 [1,2], especially at SPring-8. As originally expected, HAXPES is employed for investigating the bulk and/or varied interface electronic structures of functional materials. On the other hand, a few intrinsic features of HAXPES have been revealed for this decade in addition to its bulk sensitivity. Here several HAXPES studies using these features are reviewed.

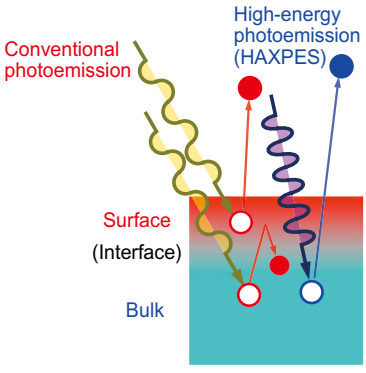

Fig. 1. Schematic diagram showing bulk sensitivity of HAXPES compared with that of conventional photoemission spectroscopy.

1. Instrumentation of HAXPES at BL19LXU

There are several setups for utilizing HAXPES at SPring-8. The setup of the beamline optics for HAXPES at BL19LXU is displayed in Fig. 2. The relative energy resolution of the beams supplied by the standard double-crystal Si(111) monochromator of typical hard X-ray beamlines in SPring-8, $\Delta E/E \sim 10^{-4}$, is insufficient for HAXPES at photon energies of several keV. Thus, a post-monochromator called a channel-cut crystal is usually employed. A Si(111) channel-cut crystal is often used in several beamlines in SPring-8 to obtain high energy resolution since the discrete photon energies can be selected from $h\nu \cong 6$, 8, and 10 keV using the (333), (444), and (555) reflections, where $\Delta E \sim 60$, 40, and 20 meV are available at $h\nu \cong 6$, 8, and 10 keV, respectively, without changing the beam path. To obtain higher photon flux, another Si channel-cut crystal with lower indices such as (311), (331), and (620) is used. The Si(620) reflection gives $\Delta E \sim 50$ meV at $h\nu = 7.9$ keV in BL19LXU. An overall experimental resolution of ~65 meV has so far been achieved [3]. Typical overall resolutions are set to 250–500 meV, which are sufficient for core-level photoemission in most cases since the lifetime broadening is similar to or larger than the above values.

The beam originally supplied from the undulator is horizontally linearly polarized. In the hard X-ray region with $h\nu = 5$–16 keV, a single-crystalline diamond is used as a phase retarder to switch the polarization, but the use of double single-crystalline diamonds, which compensate for the phase-shift inhomogeneity due to the angular divergence of the incoming X-ray beam, gives better polarization with a degree of linear polarization P_L close to ±1. As shown in Fig. 2, (100) diamonds are employed in BL19LXU, giving the (220) Bragg reflection with Laue geometry at $h\nu$ ~8 keV [4]. The horizontally polarized photons from the undulator are transformed into circular polarization by the first diamond plate, and a vertically polarized

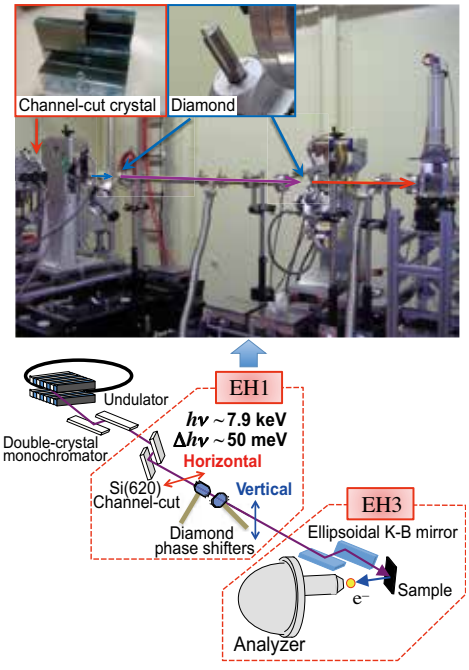

Fig. 2. Beamline optics for (polarized) HAXPES, Si channel-cut crystal, and single-crystalline diamond phase retarder.

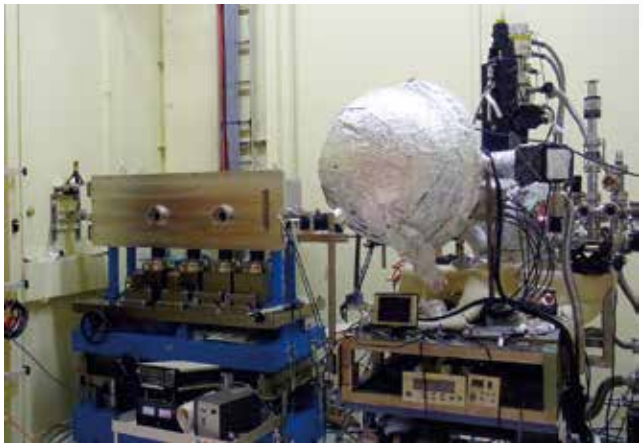

Fig. 3. Photograph of the hemispherical photoelectron spectrometer and focusing mirror for HAXPES.

X-ray is obtained by setting the optimized offset angle for the second plate. Vertical polarization with P_L better than –0.9 has been achieved at BL19LXU, which corresponds to over 95% of the components being vertically polarized. The thickness of each diamond is 0.25 mm and the transmittance of the X-ray beam after the double-crystal phase shifter is ~50%. Subsequently, the X-ray beam is focused onto the sample in the spectrometer chamber using an ellipsoidal Kirkpatrick-Baez mirror as shown in Fig. 3, where a focused spot size of ~25 μm × ~25 μm is feasible for HAXPES. In our HAXPES measurements, a lens mode with a magnification of 12, which is larger than that (= 5) for conventional angle-integrated soft X-ray and VUV photoemission, is employed.

2. Bulk electronic structures probed by HAXPES

In strongly correlated electron systems in which the on-site Coulomb repulsion U is not negligible, the electronic structure is often determined as a function of U/W, where W denotes the width of the bare band formed by the strongly correlated orbitals. Since W is reduced at the surface, the electronic states are often substantially different between the bulk and surface. When conventional photoemission with $h\nu < 1.5$ keV is applied to the core-level photoemission of strongly correlated electron systems, the contributions of the surface to the spectra prevent the clarifying of the bulk electronic states. Figure 4 shows a comparison between the Yb^{2+} $4f$ photoemission spectra near E_F at $h\nu = 700$ and 8180 eV for the Kondo semiconductor YbB_{12} [3,5]. There is a peak structure due to the Yb^{2+} $4f_{7/2}$ state in the vicinity of the Fermi level (E_F) in both spectra. In addition, one can observe the $4f$ contributions of the surface Yb^{2+} at the binding energy of ~0.9 eV in the spectrum at $h\nu$ = 700 eV with an energy resolution of ~100 meV, while such a surface contribution is negligible in the spectrum at $h\nu$ = 8180 eV with an energy resolution of ~65 meV.

Another example of HAXPES for strongly correlated materials is shown in Fig. 5, which shows valence-band photoemission spectra of the paradigmatic Mott transition system V_2O_3 [6]. As displayed in the figure, there is a prominent quasi-particle peak just below E_F and a small bump structure around –1.3 eV ascribed to the so-called lower Hubbard band (LHB) in the paramagnetic metallic (PM) phase. The relative weight of the quasi-particle peak is greater at $h\nu = 8180$ eV than at $h\nu = 700$ eV, which reflects the enhancement of the bulk contribution at $h\nu$ = 8180 eV due to the longer probing depth. The "bulk" photoemission spectrum extracted from the low-energy excitation data is in excellent agreement with the HAXPES spectrum, which indicates that HAXPES with $h\nu$ ~8 keV is truly bulk sensitive. On the other hand, the spectral weight is negligible in the antiferromagnetic insulating (AFI) phase, showing a gap opening. In addition, two spectral components are observed between E_F and –3 eV in the HAXPES spectrum in the AFI phase. One is a peak centered at –0.5 eV and the other is a shoulder at –1.3 eV close to the energy of the LHB in the PM phase. The spectral shape has $h\nu$ dependence, where the intensity of the former peak relatively increases with $h\nu$. The bulk spectrum extracted from the spectra at $h\nu = 700$ and 220 eV well reproduces the HAXPES spectrum, as seen in the PM phase. The shoulder centered at –1.3 eV has been concluded as LHB, which suggests that U is unchanged across the transitions and that the so-called orbital-selective Mott transition scenario is the most plausible for V_2O_3.

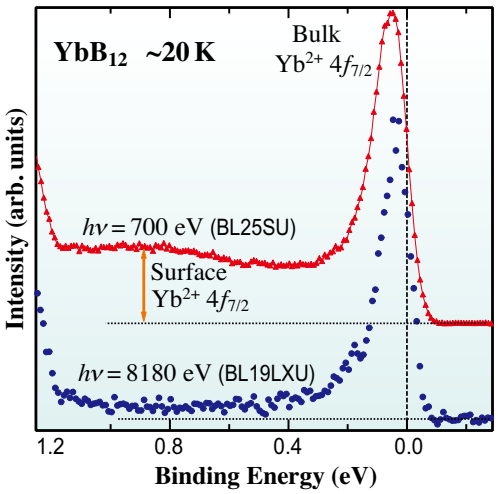

Fig. 4. Comparison of the HAXPES spectrum of YbB_{12} near E_F at $h\nu$ = 8180 eV with the soft X-ray photoemission spectrum at $h\nu$ = 700 eV. The spectrum at 700 eV was obtained at BL25SU.

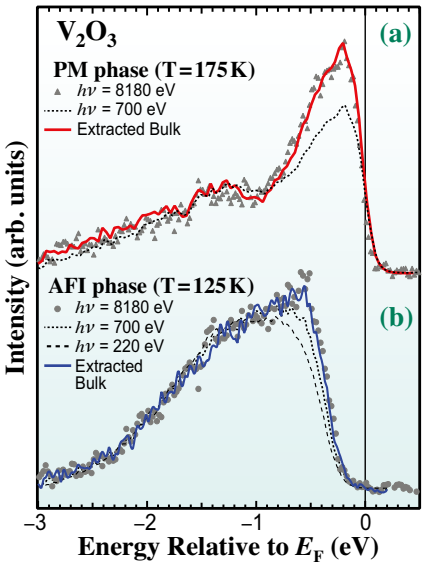

Fig. 5. Photon energy dependence of the valence-band photoemission spectra of V_2O_3 near E_F in the metallic and insulating phases as well as the "extracted" bulk spectra obtained from low-energy photoemission.

3. Recoil effects

For photoemission in solids, the basic formula $E_B = h\nu - E_K\phi$ applies, where E_B, E_K, and ϕ denote the electron binding energy, photoelectron kinetic energy, and the work function of the solid, respectively. In the photoemission from a single free atom with mass M, however, the recoil energy $E_R \cong (m/M)E_K$ is given to the photoionized atom, where m is the electron mass. The resulting E_K is thus slightly decreased by the amount E_R. While this recoil effect has been observed in the photoemission spectra of core levels in gases [7], it has been verified in solids [8,9] by the combination of HAXPES and soft X-ray photoemission with a lower $h\nu$ than that for HAXPES. A characteristic of the recoil effects is that E_R is larger for light elements. Figure 6 shows the hard and soft X-ray B 1*s* and Yb 4*d* core-level spectra of $Yb_{7/8}Lu_{1/8}B_{12}$ [9]. Although the shift of the peak binding energy with the change in the excitation energy is negligible for the Yb 4*d* spectra, it is noticeable and as large as ~300 meV for the B 1*s* spectra, which is comparable to E_R of ~400 meV. This difference between the light and heavy elements undoubtedly reflects the recoil effects in solids. Rather surprisingly, the recoil effects are not restricted to core-level excitations and are also seen in valence-band excitations, which has been verified by the $h\nu$ dependence of the valence-band photoemission for metallic Al, where the Fermi cutoff is shifted towards a higher E_B [10,11] as if an energy gap were opened in the HAXPES spectra. These phenomena suggest that the photoemission process takes place in the vicinity of the nucleus even for nearly free electrons in solids. On the other hand, the recoil effects are absent in the spectra near E_F for bulk VO_2 [12], which are correlated to the Debye temperature of materials.

4. Polarization dependence

In addition to bulk sensitivity, HAXPES at $h\nu$ = 5–10 keV has the unique characteristics of having photoionization cross sections for the *s* and *p* states comparable to those for the *d* and *f* states as well as strong orbital dependence of the photoelectron angular distribution with respect to the light polarization. As an overall tendency, the photoelectron intensity for the *s* state is strongly suppressed in the *s*-polarization configuration (*s*-pol., see the inset of Fig. 7) compared with the *p*-polarization configuration (*p*-pol.), while the *d* and *f* spectral weights are not significantly suppressed even in *s*-pol. Therefore, the extraction of the *s* contributions as well as the *d* and *f* contributions in the bulk valence band of solids becomes feasible by linear-polarization-dependent HAXPES. Figure 7 shows the polarization dependence of the valence-band HAXPES spectrum for polycrystalline silver. It can be seen that the spectral weight from E_F to 3 eV is relatively reduced in *s*-pol. This behavior indicates that the 4*d* bands are located far below E_F and are well separated from the conduction 5*sp* band crossing E_F for silver. In contrast, it has been

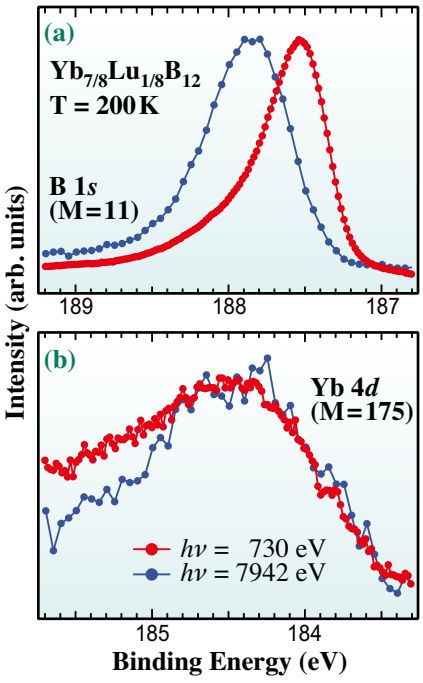

Fig. 6. Photon energy dependence of the B 1*s* and Yb 4*d* core-level photoemission spectra of $Yb_{7/8}Lu_{1/8}B_{12}$ demonstrating the recoil effects in the photoemission process of crystalline solids. M indicates mass of the atoms.

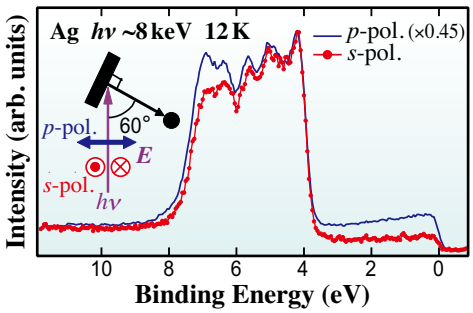

Fig. 7. Linear-polarization-dependent valence-band HAXPES spectra of polycrystalline silver. The inset shows the experimental geometry of the HAXPES measurements.

found that the 5*d* contributions to the conduction electrons are prominent in gold by polarization-dependent HAXPES [13].

Polarization dependence (linear dichroism (LD) in other words) is also seen in the *angle-resolved* core-level photoemission spectra (in other words, angular distributions of photoelectrons excited from core levels determined by the selection rules) of a partially filled subshell with a so-called multiplet structure for single-crystalline materials. (Note that an acceptance angle of ±several degrees is sufficient in this angle-resolved measurements.) Since the LD in the multiplet structure reflects the anisotropy in the Coulomb and exchange interactions between the electrons in a single site, the anisotropic charge distributions of a strongly correlated orbital with localized character can be revealed by LD in angle-resolved core-level HAXPES. The LD in angle-resolved Yb^{3+} $3d_{5/2}$ core-level HAXPES spectra was first observed for tetragonal $YbCu_2Si_2$ and $YbRh_2Si_2$, reflecting the 4*f*-orbital symmetry in the ground and excited states [14]. Here it should be emphasized that the LD was also seen even in a rather highly symmetric cubic crystal structure. Indeed, the Γ_8 ground-state symmetry for cubic YbB_{12} has been verified by the LD in the Yb^{3+} $3d_{5/2}$ core-level photoemission along the [100] and [111] directions, where the LD is mutually flipped at the same E_B [15]. These phenomena are not restricted to the Yb compounds and are widely seen in many rare-earth elements as shown in Fig. 8, which displays the polarization dependence of the Sm^{3+} $3d_{5/2}$ core-level HAXPES spectrum [16]. There is a main peak at a binding energy of 1081 eV and a shoulder structure at 1083 eV in the spectra, which correspond to the Sm^{3+} $3d^9 4f^5$ multiplet structure. The LD in the Sm^{3+} $3d_{5/2}$ spectra was clearly observed, where the peak at 1081 eV is stronger in *p*-pol. than in *s*-pol. but the spectral weight of the shoulder at 1083 eV is stronger in *s*-pol., which reflects the deviation of the anisotropic Sm^{3+} 4*f* distribution from the spherical symmetry.

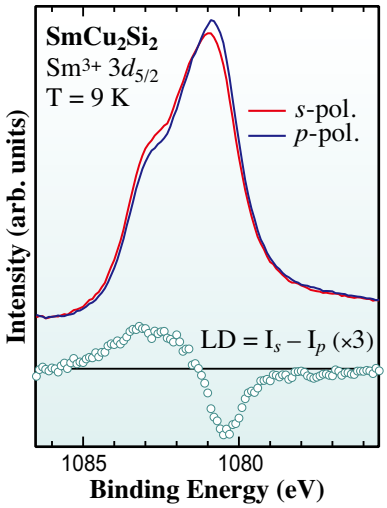

Fig. 8. Polarization dependence of the *angle-resolved* Sm^{3+} $3d_{5/2}$ core-level HAXPES spectrum along the [001] direction and the linear dichroism for $SmCu_2Si_2$.

5. Summary

Several HAXPES studies utilizing the characteristic features of HAXPES were reviewed. Although HAXPES studies such as those with momentum resolution and/or standing wave [17] and depth analysis [18] were not introduced here, the unique potential of HAXPES for investigating strongly correlated systems, functional materials, and buried interfaces will lead to many valuable clarifications of electronic structures.

Akira Sekiyama[a,b]

[a] Division of Materials Physics, Osaka University
[b] RIKEN SPring-8 Center

Email: sekiyama@mp.es.osaka-u.ac.jp

References

[1] K. Kobayashi *et al.*: Appl. Phys. Lett. **83** (2003) 1005.
[2] S. Thiess *et al.*: Solid State Commun. **132** (2004) 589.
[3] A. Sekiyama: J. Electron Spectrosc. Relat. Phenom. **208** (2016) 100.
[4] H. Fujiwara *et al.*: J. Synchrotron Rad. **23** (2016) 735.
[5] J. Yamaguchi *et al.*: Phys. Rev. B **79** (2009) 125121.
[6] H. Fujiwara *et al.*: Phys. Rev. B **84** (2011) 075117.
[7] L. Åsbrink: Chem. Phys. Lett. **7** (1970) 549.
[8] Y. Takata *et al.*: Phys. Rev. B **75** (2007) 233404.
[9] S. Suga and A. Sekiyama: Eur. Phys. J. Spec. Topic **169** (2009) 227.
[10] Y. Takata *et al.*: Phys. Rev. Lett. **101** (2008) 137601.
[11] S. Suga and A. Sekiyama: J. Electron Spectrosc. Relat. Phenom. **181** (2010) 48.
[12] S. Suga *et al.*: New J. Phys. **11** (2009) 073025.
[13] A. Sekiyama *et al.*: New J. Phys. **12** (2010) 043045.
[14] T. Mori *et al.*: J. Phys. Soc. Jpn. **83** (2014) 123702.
[15] Y. Kanai *et al.*: J. Phys. Soc. Jpn. **84** (2015) 073705.
[16] Y. Kanai *et al.*: J. Electron Spectrosc. Relat. Phenom. (2017) - in press.
[17] C.S. Fadely: J. Electron Spectrosc. Relat. Phenom. **190** (2013) 165.
[18] E. Ikenaga *et al.*: J. Electron Spectrosc. Relat. Phenom. **190** (2013) 180.

Crystal structures of CRISPR RNA-guided Cas9 and Cpf1 nucleases

Bacteria and Archaea utilize the CRISPR-Cas adaptive immune system for defense against invading genetic elements such as phages and plasmids. The CRISPR arrays in the microbial genome comprise direct repeats separated by variable spacer sequences derived from foreign genetic elements. The CRISPR arrays are transcribed and then processed into small CRISPR RNAs (crRNAs), which bind to Cas endonucleases to form effector ribonucleoprotein complexes. The Cas effector complexes cleave the foreign nucleic acids complementary to the crRNA guide. Based on the architecture of the effector module, the CRISPR-Cas systems can be divided into two classes. Class 1 systems use effector complexes comprising multiple Cas proteins, whereas class 2 systems employ a single effector nuclease, such as Cas9 (type II) or Cpf1 (type V). Cas9 uses dual RNA guides (a crRNA and a *trans*-activating crRNA) or a chimeric single-guide RNA (sgRNA), and cleaves a double-stranded DNA target complementary to the crRNA guide (Fig. 1(a)). In contrast, Cpf1 is guided by a single crRNA and cleaves a double-stranded DNA target (Fig. 1(b)). In addition to the RNA-DNA complementarity, Cas9 and Cpf1 require a short nucleotide sequence adjacent to the target site, called a protospacer adjacent motif (PAM). Cas9 and Cpf1 have been harnessed for a variety of new technologies, exemplified by genome editing in various cell types and organisms. Previous structural studies of Cas9 from *Streptococcus pyogenes* (SpCas9) and *Staphylococcus aureus* (SaCas9) provided mechanistic insights into RNA-guided DNA cleavage by Cas9 and enhanced molecular engineering of Cas9 variants with improved functionality [1,2]. Furthermore, a structural comparison between the two Cas9 orthologs revealed both divergent and convergent structural features among orthologous CRISPR-Cas9 systems.

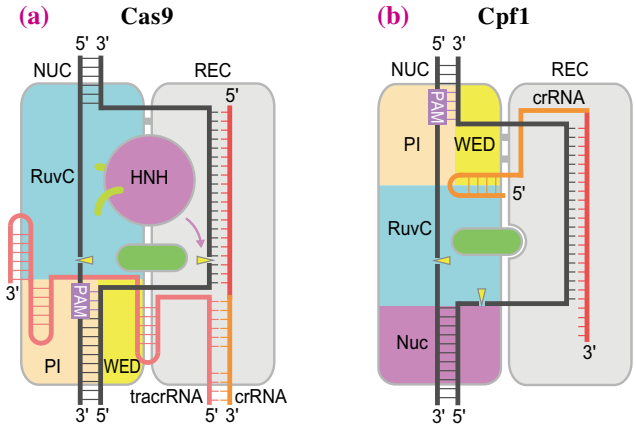

Fig. 1. RNA-guided DNA cleavage by Cas9 **(a)** and Cpf1 **(b)**.

Cas9 orthologs have diverse amino-acid sequences and recognize distinct guide RNA and PAM sequences. Cas9 from *Francisella novicida* (FnCas9), one of the largest Cas9 orthologs, consists of 1629 residues and is significantly larger than SpCas9 (1368 residues) and SaCas9 (1053 residues). To elucidate the RNA-guided DNA cleavage mechanism of FnCas9, we crystallized FnCas9 in a complex with the sgRNA and its DNA targets containing either TGG or TGA as the PAM, collected X-ray diffraction data at SPring-8 **BL41XU**, and determined the structures at 1.7 Å resolution [3] (Fig. 2(a)). The structures revealed that FnCas9 recognizes the guide RNA-target DNA heteroduplex within the central channel between the REC and RuvC domains. The HNH and RuvC endonuclease domains are located at positions suitable for cleaving the target and non-target DNA strands, respectively. The PAM DNA duplex is bound to the groove between the WED and PI domains, and the TGR PAM is recognized by Arg1556 and Arg1585 in the PI domain. A structural comparison of FnCas9 with SpCas9 and SaCas9 revealed striking conserved and divergent features among the orthologous CRISPR-Cas9 systems. Furthermore, we used the structural information to engineer a variant that can recognize the altered YG PAM. The FnCas9 variant modified endogenous target sites with the YG PAM in mouse zygotes, thereby expanding the target space in Cas9-mediated genome editing.

Using molecular evolution, SpCas9 has been engineered to exhibit altered PAM specificities. Whereas wild-type SpCas9 recognizes the NGG PAM, the engineered VQR (D1135V/R1335Q/T1337R), EQR (D1135E/R1335Q/T1337R), and VRER (D1135V/G1218R/R1335E/T1337R) variants recognize the NGA, NGAG, and NGCG PAMs, respectively. These SpCas9 variants thus contribute to expanding the target space in Cas9-mediated genome editing applications. To elucidate the altered PAM recognition mechanisms of the SpCas9 variants, we crystallized the three SpCas9 variants in complexes with the sgRNA and its PAM-containing DNA targets, collected X-ray diffraction data at BL41XU, and determined their structures at 2.0–2.2 Å resolutions [4] (Fig. 2(b)). Whereas the third G in the PAM is recognized by Arg1335 in wild-type SpCas9, the third A in the PAM is recognized by R1335A in the VQR and EQR variants. The third C in the PAM is recognized by R1335E in the VRER

variant. A structural comparison of the three SpCas9 variants with wild-type SpCas9 revealed that the multiple mutations induce an unexpected structural displacement in the sugar-phosphate backbone of the PAM duplex, thereby enabling direct base-specific hydrogen-bonding interactions between the PAM-interacting residue and the altered PAM nucleotides. Our findings explain the altered PAM specificities of the SpCas9 variants and establish a framework for the further engineering of CRISPR-Cas9.

Since, except for the RuvC domain, Cpf1 shares no sequence similarity with other proteins, the crRNA-guided DNA cleavage mechanism of Cpf1 remains unknown. We crystallized *Acidaminococcus sp.* Cpf1 (AsCpf1) in a complex with the crRNA and its target DNA, collected X-ray diffraction data at BL41XU, and determined the structure at 2.8 Å resolution [5] (Fig. 2(c)). The structure revealed that AsCpf1 adopts a bilobed architecture consisting of the REC and NUC lobes. The REC lobe can be divided into the REC1 and REC2 domains, whereas the NUC lobe comprises the RuvC, WED, PI, and Nuc domains. Except for the RuvC domain, the five domains have new protein folds. The crRNA 5' handle adopts an unexpected pseudoknot and is recognized by the WED and RuvC domains. In contrast, the crRNA guide segment and the target DNA strand form the RNA-DNA heteroduplex, which is accommodated within the central channel between the REC and NUC lobes. The PAM DNA duplex adopts a distorted double-stranded conformation and is recognized by the WED-REC1-PI domains in base- and shape-dependent manners, consistent with the recognition of TTTV PAM by AsCpf1. The RuvC domain is located at a position suitable for cleaving the non-target DNA strands. Notably, the Nuc domain is located adjacent to the RuvC domain, and mutational analysis revealed the involvement of the Nuc domain in the cleavage of the target DNA strand. These findings indicated that the RuvC and Nuc domains jointly participate in generating DNA double-strand breaks. A structural comparison of AsCpf1 with Cas9 reveals both striking similarity and major differences, thereby explaining their distinct functionalities. Although except for the RuvC domain, Cpf1 and Cas9 share no sequence similarity, they use similar bilobed architectures to recognize the RNA-DNA heteroduplex. In contrast, Cpf1 and Cas9 recognize their PAM sequence and cleave the DNA target in distinct manners. These structural findings revealed an intriguing functional convergence between the two class 2 CRISPR-Cas nucleases.

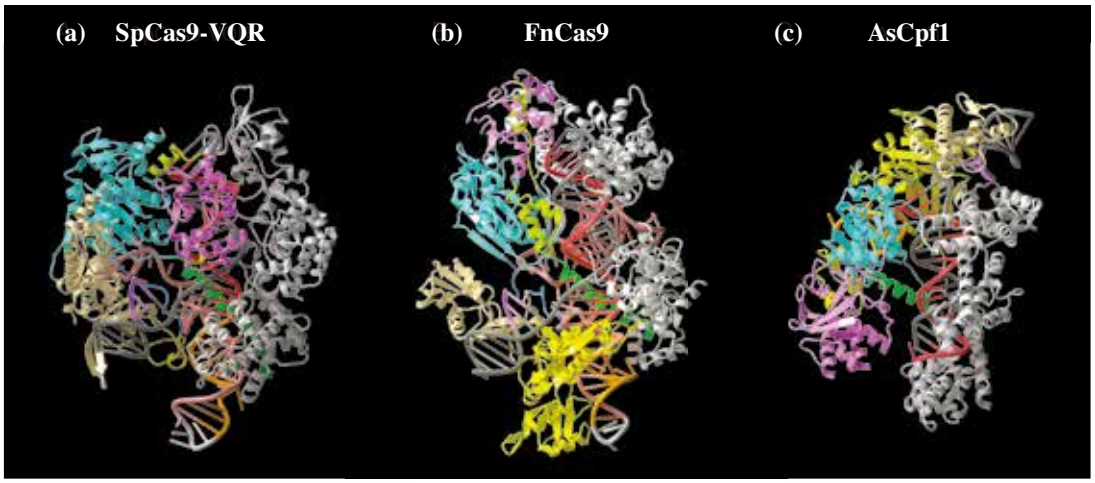

Fig. 2. **(a–c)** Crystal structures of FnCas9-sgRNA-DNA (a), SpCas9 VQR-sgRNA-DNA (b), and AsCpf1-crRNA-DNA (c). Structural images were prepared using CueMol (http://www.cuemol.org).

Hiroshi Nishimasu[a,b,*] and Osamu Nureki[a]

[a] Department of Biological Sciences, The University of Tokyo
[b] PRESTO / JST

*Email: nisimasu@bs.s.u-tokyo.ac.jp

References

[1] H. Nishimasu *et al.*: Cell **156** (2014) 935.
[2] H. Nishimasu *et al.*: Cell **162** (2015) 1113.
[3] *H. Hirano, J.S. Gootenberg, T. Horii, O.O. Abudayyeh, M. Kimura, P.D. Hsu, T. Nakane, R. Ishitani, I. Hatada, F. Zhang, H. Nishimasu and O. Nureki: Cell* ***164*** *(2016) 950.*
[4] *S. Hirano, H. Nishimasu, R. Ishitani, O. Nureki: Mol. Cell* ***61*** *(2016) 886.*
[5] *T. Yamano, H. Nishimasu, B. Zetsche, H. Hirano, I.M. Slaymaker, Y. Li, I. Fedorova, T. Nakane, K.S. Makarova, E.V. Koonin, R. Ishitani F. Zhang and O. Nureki: Cell* ***165*** *(2016) 949.*

Crystal structures of endothelin ET_B receptors revealed the activation mechanism by endothelin-1

Endothelin-1 (ET-1) is the most potent and long-lasting vasoconstrictor ever discovered, which is a 21-amino-acid-long peptide hormone isolated from the supernatant of porcine endothelial cells [1]. ET-1 and its related isopeptides ET-2 and ET-3 participate in various physiological processes, such as neural development, cell proliferation, sodium homeostasis and vascular regulation, by activating cytoplasmic G-protein signals through two subtype receptors, ET_A and ET_B, both of which belong to the class A G-protein-coupled receptors (GPCRs) [2].

ET_A and ET_B share 60% sequence similarity and both receptors bind to ET-1 in a quasi-irreversible manner with sub-nanomolar affinities and extremely low dissociation rates (on the order of days). However, the physiological roles of the two receptors are quite distinct. For example, in vasoregulation, ET_A induces primary vasoconstriction, whereas ET_B mainly induces vasorelaxation via NO-mediated signaling (Fig. 1). The endothelin system, including the three isopeptides and the opposing and balanced actions of the two receptors, is related to the progression of various diseases such as arterial hypertension, atherosclerosis, heart failure and cancer [3]. Therefore, non-selective and subtype-selective antagonists for the endothelin receptors (bosentan, macitentan and ambrisentan) have been developed and indeed clinically used for the treatment for pulmonary arterial hypertension (PAH). Despite such importance, little has been understood about how these receptors perceive endothelin peptides and activate cytoplasmic G-protein signals.

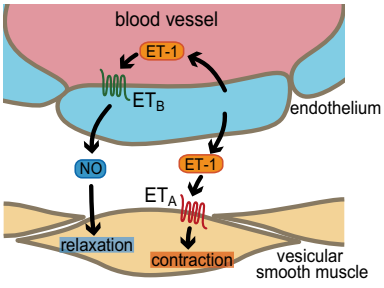

Fig. 1. Schematic diagram of the vascular tone regulation by endothelin. ET-1 is produced in the endothelial cells by multistep processing, and the mature peptides are secreted into extracellular spaces. While the secreted ET-1 can act on distant organs through the blood flow, most of the secreted ET-1 act in autocrine and paracrine manners. The ET_A receptor is predominantly expressed in the vesicular smooth muscle cells and mediates vasoconstriction, whereas the ET_B receptor in the endothelium cells mediates the NO release and thus induces vasodilation.

Recent advances in crystallographic techniques, such as lipidic cubic phase (LCP) crystallization and the use of the fusion-protein strategy to promote crystallization, have led to an increasing number of high-resolution GPCR structures [4]. Together with protein dynamics studies, these structures have allowed better understanding of the molecular mechanism of the GPCRs, such as agonist or antagonist binding, agonist-induced conformational changes and consequent G-protein activation. However, only a limited number of peptide-activated GPCR structures have been reported so far. Therefore, how peptide molecules, especially those with high molecular weights, bind and activate their receptors still remains poorly understood.

The intrinsic flexible nature of GPCRs generally hampers their crystallization. To overcome this problem, a thermostabilized ET_B receptor was established by mutagenesis screening [5]. Five point mutations were introduced to increase the stability of the receptor in the ligand-unbound state as compared with the wild-type receptor. This construct still retained the ability of agonist binding and G-protein activation and thus appeared suitable for visualizing multiple conformations of the receptor. T4 lysozyme (T4L) or modified T4 lysozyme (mT4L) was fused into the third intracellular loop (ICL3) to promote crystallization. The LCP crystals of these constructs were obtained in the absence or presence of the endogenous agonist ET-1, and the diffraction datasets were collected at the micro-focused beamline **BL32XU**, SPring-8. Finally, the structures of the ET_B receptor in the complex with ET-1 (Fig. 2(a)) and in the ligand-free form were determined at 2.5 Å and 2.8 Å resolutions, respectively [6] (Fig. 2(b)).

The ET_B receptor adopts the canonical GPCR fold with seven transmembrane (TM) helices and a short amphipathic helix 8 that runs parallel to the membrane. The ET-1 peptide penetrates into the receptor core, with its flexible C-terminal tail inserted in the depths of the binding pocket and specifically recognized by the receptor. This manner of binding is consistent with the essential role of the C-terminal tail of ET-1 for receptor binding and activation. The interacting surface area between ET-1 and the ET_B receptor is the largest ever reported for the GPCR structures. In addition, ECL2 and the N-terminal tail of the receptor together form a lidlike architecture that covers the orthosteric ligand binding pocket, thereby preventing ET-1 dissociation. These structural features well explain the irreversible binding of ET-1. The amino acid residues involved in the receptor interaction are highly conserved in the

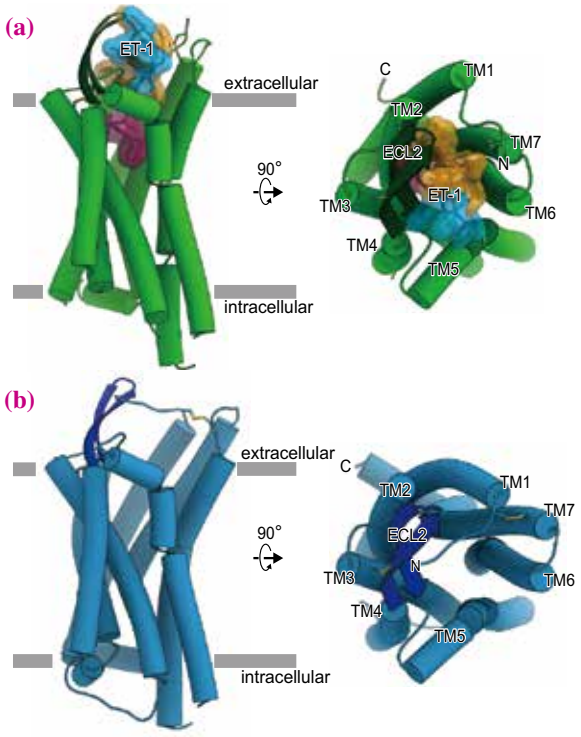

Fig. 2. Overall structures of the ET_B receptor in different conformations. The crystal structures of the ET-1-bound **(a)** and ligand-unbound **(b)** receptors are shown as cylinder models, viewed from within the membrane plane (left panels) and from the extracellular side (right panels). The bound ET-1 peptide is shown as a surface representation with the same colors as those in the original paper; cyan: N-terminal region, yellow: α-helical region, red: C-terminal region. Transmembrane helices, ECL2 and the N- and C-termini are indicated by the labels.

three isopeptides (ET-1 to ET-3). However, mutation analysis suggested that these three isopeptides have slightly different binding properties, probably caused by the indirect effects of the amino acid residues of their N-terminal regions that are not involved in the receptor binding. These results provided insights into the different selectivity between the two receptor subtypes.

The structural comparison of the ET-1-bound and ligand-free structures of the ET_B receptor revealed agonist-induced dynamic conformational changes in the extracellular orthosteric pocket. These structures, together with the previous biochemical studies, suggested that the inward movement of the extracellular portions of TM6 and TM7 is the critical event for receptor activation. The ET-1-induced conformational changes propagate to the receptor core and also to the cytoplasmic side of the receptor, which involves the collapse of the allosteric Na^+ binding site that is conserved among class A GPCRs. These structural features suggested that ET-1 binding induces the flexibility in the cytoplasmic side of the receptor, especially in the cytoplasmic segment of TM6, thus promoting subsequent G-protein binding at the cytoplasmic interface (Fig. 3). The activation mechanism proposed in this study is similar to those of other GPCRs, including the M2 acetylcholine receptor, the μ-opioid receptor and the β-2 adrenergic receptor, therefore suggesting a conserved mechanism for the G-protein activation in class A GPCRs.

In summary, the current study reported the first crystal structures of the ET_B receptor in the ligand-unbound inactive and ET-1-bound partially active conformations, which revealed the molecular basis for the irreversible binding of ET-1 and the ET-1-dependent activation process of the receptor. These mechanisms are likely conserved in the ET_A receptor. These notions provided a critical view for understanding the mechanism of the endothelin receptors and other peptide GPCRs. The current structures of the ET_B receptor also provided important information for the development of drugs targeting endothelin receptors, thus paving the way for the more effective treatment of PAH and other diseases associated with the endothelin system in the future.

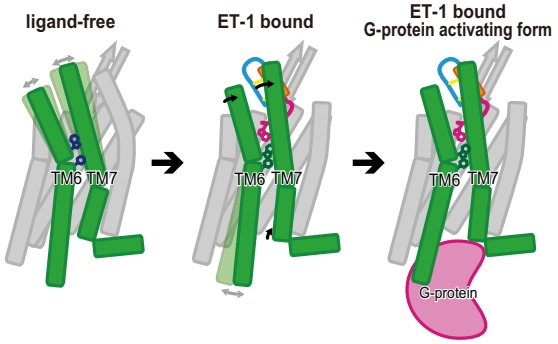

Fig. 3. Schematic diagrams of the receptor activation by ET-1. The extracellular portions are flexible when the receptor is in the apo state (left). ET-1 binding induces a major rearrangement in the orthosteric pocket, which involves the inward shift of the extracellular portions of TM6 and TM7 (middle). These conformational changes propagate to the receptor core and cytoplasmic side, which induces the cytoplasmic segment of the receptor to adopt a flexible conformation in the ET-1 bound state and thus promotes G-protein binding (right).

Tomohiro Nishizawa*, Wataru Shihoya and Osamu Nureki

Department of Biophysics and Biochemistry,
The University of Tokyo

*Email: t-2438@bs.s.u-tokyo.ac.jp

References

[1] M. Yanagisawa *et al.*: Nature **332** (1988) 411.
[2] M. Barton *et al.*: Can. J. Physiol. Pharmacol. **86** (2008) 485.
[3] J. Xiang *et al.*: Curr. Opin. Pharmacol. **37** (2016) 1055.
[4] R.M. Kedzierski *et al.*: Annu. Rev. Pharmacol. Toxicol. **41** (2001) 851.
[5] A. Okuta *et al.*: J. Mol. Biol. **428** (2016) 2265.
[6] *W. Shihoya, T. Nishizawa, A. Okuta, K. Tani, N. Dohmae, Y. Fujiyoshi, O. Nureki and T. Doi: Nature **537** (2016) 363.*

Mechanistic insights from conformational ensembles of the mammalian fructose transporter GLUT5

Simple carbohydrates, such as glucose and fructose, are a major source of energy for the body. Incorporation of these molecules into mammalian cells is mediated mainly by GLUT and SGLT transporters. Humans and mammals have 14 subtypes of GLUT facilitative transporters, each of which shows a distinct pattern of substrate preference and tissue distribution [1]. Of these, GLUT5 is a fructose-specific facilitative transporter, expressed mainly on the apical surface of the enterocytes and responsible for the absorption of dietary fructose in the small intestine (Fig. 1). The current excessive consumption of fructose in the Western diet is associated with an increased incidence of metabolic disorders such as obesity and non-alcoholic steatohepatitis [2]. Growing interest has therefore been focused on the structure and mechanism of GLUT5. In this study, we used brilliant synchrotron X-rays at SPring-8 **BL41XU**, Diamond Light Source, and European Synchrotron Radiation Facility to analyze GLUT5 conformational ensembles by crystallography to provide mechanistic insights into the structural dynamics of this facilitative transporter during the transport process [3].

It is still challenging to determine the crystal structure of a human or mammalian membrane protein. This is reflected in the difficulties encountered with the production, stability, and crystallization of a membrane protein. An antibody-aided crystallographic approach was taken to determine the structure of rat GLUT5 in the outward-facing conformation (Figs. 2(a) and 2(c)). We generated an Fv antibody fragment that specifically bound to a conformational epitope on the intracellular hydrophilic surface of rat GLUT5 and acted as a “crystallization chaperone”. The GLUT5 structure consists of two symmetrical six transmembrane (TM) helix bundles, plus five additional helices on the intracellular side. A central cavity between the two TM bundles allows the passage of substrate molecules. In this crystal structure, the central cavity is open to the extracellular side. A different approach was taken to shift the conformation equilibrium into an inward-facing state. A previous study has shown that C-terminal truncated mammalian GLUT1 is locked to an inward-facing form and does not have transport activity [4]. On the basis of this knowledge, we produced a 28-residue C-terminal truncation mutant of bovine GLUT5 to successfully determine the crystal structure (Figs. 2(b) and 2(d)). The C-terminal-deleted GLUT5 adopts an inward-facing conformation, in which the central cavity is open to the cytoplasmic side. Combining these structural data with biochemical studies, we identified the essential amino acid residues for substrate binding located in the central cavity. Most essential residues are located on the TM7, TM10, and TM11 in the C-terminal half, suggesting that GLUT5 has an asymmetrical substrate-binding mode. Furthermore, we have shown that a single point mutation in the substrate-binding site (Gln166 → Glu) is sufficient to switch the substrate-binding preference of GLUT5 from fructose to glucose.

A comparison between the outward-facing and inward-facing structures shows that the two major TM bundles undergo a rigid-body-like rotation of approximately 15°. The key characteristic of the global rotation is the formation and breakage of salt bridges between the two TM bundles on the cytoplasmic side. The two TM bundles are linked by a couple of salt bridges in the outward-facing state, whereas these salt bridges are broken in the inward-facing state.

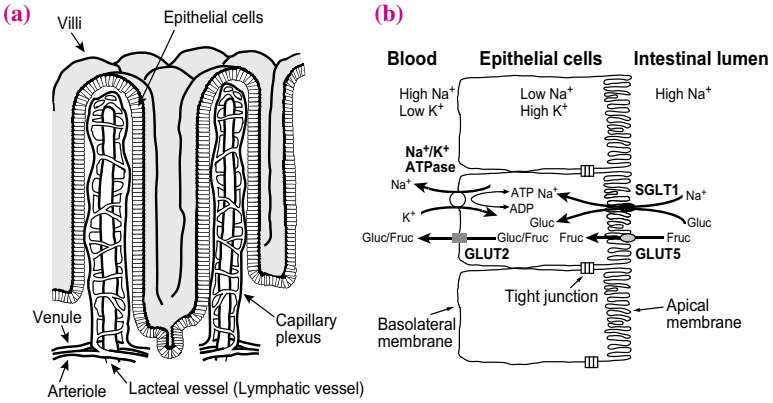

Fig. 1. Transepithelial hexose absorption in the human small intestine. **(a)** Villi of the small intestine. **(b)** Transport of monosaccharides across the epithelial cell layers. Glu: glucose, Fruc: fructose.

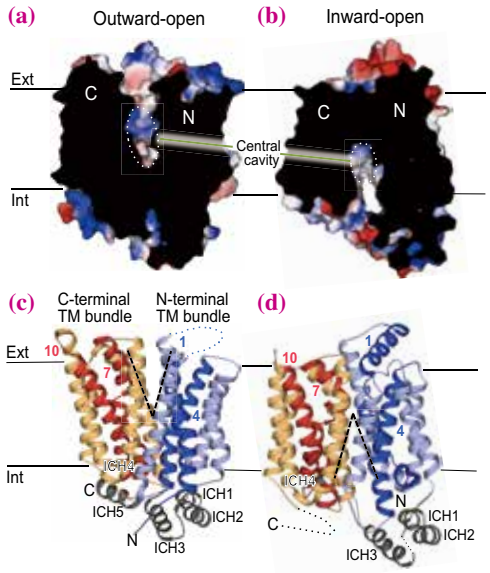

Fig. 2. Overall structure of GLUT5. Cross section through the surface electrostatic potential of the outward-facing rat GLUT5 **(a)** and inward-facing bovine GLUT5 **(b)** structures, as viewed within the plane of the membrane. The central cavity is shown as a dotted ellipse. Ribbon representations of outward-facing **(c)** and inward-facing **(d)** structures.

Interestingly, mutagenesis experiments confirmed that substrate binding is coupled with salt bridge formation in the outward-facing state. A more detailed superposition of the structures in the two different conformations revealed how the central cavity closes via a conformational change. On the extracellular side, TM1 and TM7 move to close the central cavity. In contrast, on the intracellular side, TM4 and TM10 contribute to the closing of the cavity. The movement of TM7 and TM10 is beyond the rigid-body rotation. They undergo a local conformational change to occlude the substrate-binding site. During the transition from the outward-facing state to the inward-facing state, the upper half of TM7 is markedly distorted to form an extracellular gate. On the other hand, the lower half of TM10 moves a large distance to open the intracellular gate.

There are two canonical models for transporters. In the rocker-switch mechanism, the transporter simply undergoes a rigid-body rotation of the two major TM bundles. In the gated-pore mechanism, the transporter forms an extracellular gate and an intracellular gate to control the substrate transport, but it does not undergo a rigid-body rotation of the two domains. For GLUT5, the transport mechanism is a fusion of the two canonical models. Therefore, we proposed a new model, in which the transport occurs by a combination of a global "rocker-switch"-like movement of the TM bundles and a local asymmetric "gated-pore"-like rearrangement. This scenario is depicted in Fig. 3. Initially, the transporter is waiting for the substrate in the outward-facing state (Fig. 3(a)). The substrate molecule enters the substrate-binding site in the central cavity. TM7 moves towards TM1 and forms the extracellular gate. The substrate binding is the driving force to break the inter-domain salt bridges (Fig. 3(b)). The transporter undergoes rigid-body rotation. The TM10 moves away from the TM4 and opens the intracellular gate before the substrate molecule is released into the cytoplasm (Fig. 3(c)). The transporter undergoes a transition from the inward-facing state (Fig. 3(d)) to the outward-facing state (Fig. 3(a)), again by forming inter-domain salt bridges.

Further effort will be required to find the missing link and understand the transport cycle completely, for example, a structural determination of the GLUT5-substrate analog complexes in the occluded state as well as molecular dynamics simulations. A deeper understanding of the GLUT5 structure and mechanism, as described here, should facilitate the structure-based design of novel inhibitors with therapeutic potential.

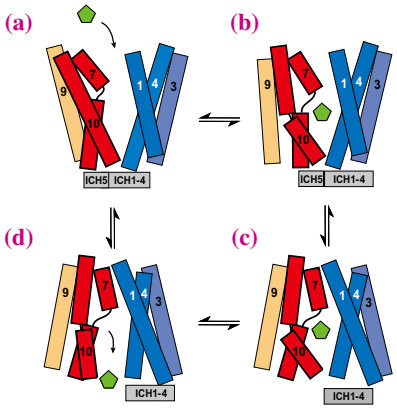

Fig. 3. Alternating-access transport mechanism in GLUT5. Green pentagons indicate fructose molecules.

Norimichi Nomura[a,*], So Iwata[a] and David Drew[b]

[a] Graduate School of Medicine, Kyoto University
[b] Dept. of Biochemistry & Biophysics, Stockholm University

*Email: nnomura@mfour.med.kyoto-u.ac.jp

References

[1] M. Mueckler, B. Thorens: Mol. Aspects Med. **34** (2013) 121.
[2] P.J. Havel: Nutr. Rev. **63** (2005) 133.
[3] *N. Nomura, G. Verdon, H.J. Kang, T. Shimamura, Y. Nomura, Y. Sonoda, S.A. Hussien, A.A. Qureshi, M. Coincon, Y. Sato, H. Abe, Y. Nakada-Nakura, T. Hino, T. Arakawa, O. Kusano-Arai, H. Iwanari, T. Murata, T. Kobayashi, T. Hamakubo, M. Kasahara, S. Iwata and D. Drew: Nature* ***526*** *(2015) 397.*
[4] Y. Oka *et al.*: Nature **345** (1990) 550.

Crystal structure of eukaryotic translation initiation factor 2B

The eukaryotic translation initiation factor 2B (eIF2B) is the guanine nucleotide exchange factor for eIF2. eIF2 carries the methionylated initiator tRNA (Met-tRNA$_i$) to the ribosome in a GTP-dependent manner and is released from the ribosome as the GDP-bound form after the recognition of an initiation codon. To participate in the next round of translation initiation events, eIF2 must be converted into the GTP-bound form by eIF2B (Fig. 1) [1]. However, this nucleotide exchange activity of eIF2B is inhibited by the phosphorylation of eIF2. The phosphorylation of eIF2 is known to be rapidly induced by eIF2 kinases under various stress conditions such as viral infection and amino acid deprivation, and the phosphorylated eIF2 forms a tight inactive complex with eIF2B. As a result of this inhibition, the cellular level of the active GTP-bound eIF2 is lowered and the supply of Met-tRNA$_i$ to the ribosomes is limited. Thus, protein synthesis under stress is globally restricted and stress response genes that contain some special elements on their mRNAs are selectively translated.

eIF2B is a heterodecameric protein composed of two sets of five non-identical subunits (α-ε), while eIF2 is a heterotrimer composed of three subunits (α-γ). Yeast eIF2B is known to be divided into two types of subcomplexes [2]. The α, β and δ subunits of eIF2B form a regulatory subcomplex that is responsible for the recognition of stress-induced phosphorylation on the α subunit of eIF2 (eIF2α) and a formation of the tight inactive eIF2-eIF2B complex. On the other hand, the γ and ε subunits of eIF2B form the catalytic subcomplex that is responsible for the exchange of GDP on the γ subunit of eIF2 (eIF2γ). In the last few decades, genetic and biochemical studies have identified residues in the eIF2B subunits that are essential for these regulatory and catalytic interactions with eIF2. However, the molecular mechanisms of these interactions have hardly been described since the tertiary structure of the eIF2B decamer was unknown.

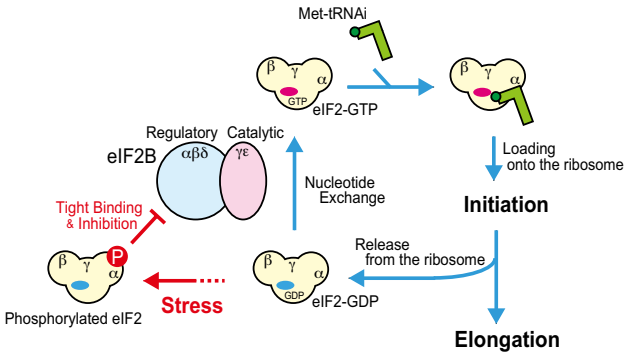

Fig. 1. Schematic representation of eIF2B-mediated translational control.

Toward structural analysis, our group established a bacterial expression system for the large-scale production of *Schizosaccharomyces pombe* eIF2B, which then was successfully crystallized [3]. X-ray diffraction data of the eIF2B crystals were collected at SPring-8 **BL32XU** and **BL41XU** and at Photon Factory beamlines. The initial phases were determined from the selenomethionine-derivative data set by the single-wavelength anomalous dispersion method [4]. The crystal structure of eIF2B was finally refined to a resolution of 3.0 Å, revealing its decameric architecture. A hexameric regulatory subcomplex composed of the α-α homodimer and two β-δ heterodimers occupies the central part of the structure and two catalytic subcomplexes composed of the γ-ε heterodimer are attached to the regulatory subcomplex on its β-δ heterodimer faces (Fig. 2). Both the HEAT domain and the NF motif in the ε subunit, the key elements required for an efficient nucleotide exchange reaction, reside in the "distal" side of the catalytic subcomplex.

Furthermore, we identified the interfaces for eIF2α and eIF2γ on the molecular surface of eIF2B by the site-directed incorporation of *p*-benzoyl-L-phenylalanine (*p*Bpa), a photoreactive synthetic amino acid, and photo-cross-linking with eIF2. Photo-cross-links with eIF2α were detected when *p*Bpa was incorporated in the cavity region at the center of the regulatory subcomplex, while those with eIF2γ were detected on the distal face of the catalytic subcomplex, adjacent to the NF motif (Fig. 3(a)). These results show that the phosphorylation status of eIF2α is recognized at the central cavity, while the catalysis of nucleotide exchange on eIF2γ is performed on the distal face. Intriguingly, our docking model of eIF2 and eIF2B revealed that it is difficult for a single molecule of eIF2 to interact simultaneously with these two interfaces. Therefore, we proposed that these two types of eIF2-eIF2B interactions are mutually exclusive and that two or more distinct states are present in the eIF2-eIF2B complex. When eIF2γ binds on the distal face of the catalytic subcomplex, the complex is in the "productive" state, where nucleotide exchange is catalyzed by the HEAT domain and the NF motif. On the other hand, when eIF2α is captured at the central cavity in the regulatory subcomplex, the

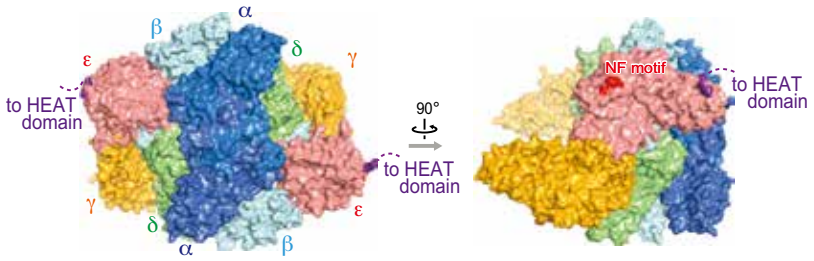

Fig. 2. Overall structure of *S. pombe* eIF2B. The α, β, γ, δ and ε subunits are colored blue, cyan, orange, green and salmon pink, respectively. The NF motifs in the ε subunits are shown in red. The HEAT domains at the C-terminus of the ε subunits were not observed in our structure and the observed C-terminal residues of the ε subunits are colored purple.

complex is in the "non-productive" state, where nucleotide exchange is not performed. Since the stress-induced phosphorylation of eIF2α tightens the interaction with the regulatory subunits of eIF2B and stabilizes the non-productive state of the eIF2-eIF2B complex, nucleotide exchange reactions are restricted (Fig. 3(b)).

Our study first revealed the decameric architecture of eIF2B and paves the way for the mechanistic understanding of stress-induced, eIF2B-mediated translational control. Future structural studies are expected to unveil the molecular mechanisms of nucleotide exchange and the recognition of eIF2α phosphorylation.

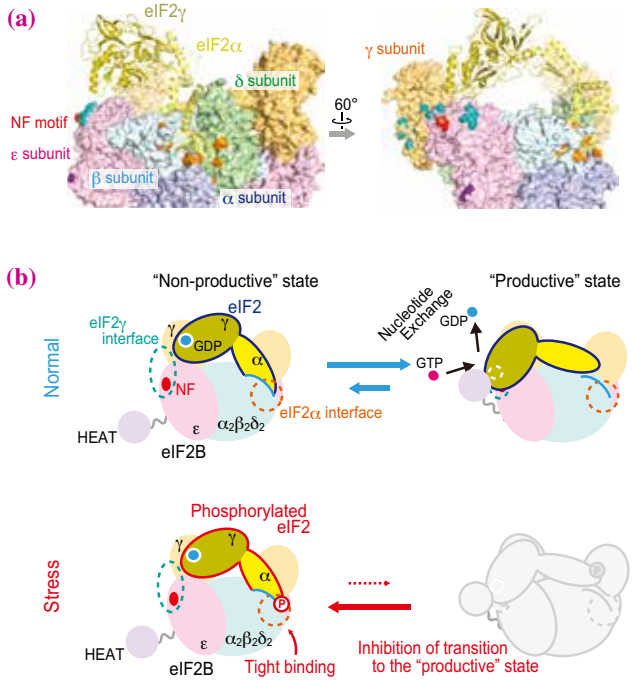

Fig. 3. **(a)** Mapping of the photo-cross-linked eIF2B sites and the docking of eIF2 and eIF2B. The sites that cross-linked with eIF2α and eIF2γ are colored in orange and teal, respectively. In the docking, the structures of aIF2α and γ from PDB ID: 2QMU [5] were used instead of eIF2, and the N-terminal domain of a/eIF2α was positioned in the central cavity of eIF2B. **(b)** Schematic representations of the proposed mechanism of eIF2B inhibition by phosphorylated eIF2.

Kazuhiro Kashiwagi[a], Takuhiro Ito[a]
and Shigeyuki Yokoyama[b,*]

[a] RIKEN Center for Life Science Technologies/Yokohama
[b] RIKEN Structural Biology Laboratory/Yokohama

*Email: yokoyama@riken.jp

References

[1] R.J. Jackson *et al.*: Nat. Rev. Mol. Cell Biol. **11** (2010) 113.
[2] G.D. Pavitt: Biochem. Soc. Trans. **33** (2005) 1487.
[3] K. Kashiwagi *et al.*: J. Struct. Funct. Genomics **17** (2016) 33.
[4] *K. Kashiwagi, M. Takahashi, M. Nishimoto, T.B. Hiyama, T. Higo, T. Umehara, K. Sakamoto, T. Ito and S. Yokoyama: Nature **531** (2016) 122.*
[5] L. Yatime *et al.*: Proc. Natl. Acad. Sci. USA **104** (2007) 18445.

Ultra-high resolution crystal structure and charge density analysis of HiPIP in bacterial photosynthesis

More than 110,000 protein structures determined by X-ray crystallography are now available in the Protein Data Bank (PDB). Most of these deposited structures fall in the range of conventional resolution of between 1.5 Å and 3.0 Å. In this resolution range, structures provide information on the folding of protein molecules and the architecture of their active sites but are insufficient in their precision and quantity to elucidate the molecular mechanism of protein functions directly from structural information. However, the recent technological development of synchrotron radiation has enabled us to obtain high-quality X-ray diffraction data at ultra-high resolutions to extract more detailed structural information such as the hydrogen position and charge density distribution in protein crystal structures. We have determined the crystal structure of a high-potential iron-sulfur protein (HiPIP) from a thermophilic bacterium at 0.48 Å resolution and performed charge-density analyses, where the distributions of valence electrons in metalloproteins were clearly visualized for the first time [1]. HiPIP is an electron-transfer protein involved in the primary process of bacterial photosynthesis, where sunlight energy is converted to chemical energy (Fig. 1(a)). This protein carries electrons from the cytochrome bc_1 complex to the photosynthetic reaction center to reduce the photo-oxidized bacteriochlorophyll dimer (special pair) in the reaction center [2].

Diffraction data from crystals of HiPIP were collected at SPring-8 **BL41XU** with high-energy X-rays (λ = 0.45 Å, E = 27.6 keV) (Fig. 1(b)). The structure was successfully refined at 0.48 Å resolution which is, to date, one of the highest resolutions among all the protein structures deposited in PDB. The structure was initially refined with the conventional independent spherical atom model (ISAM) parameters, where residual electron densities were observed around each atom. Further refinement was performed using the multipolar atomic model (MAM) [3] in order to obtain charge-density information. The final R factor is 7.16% (R_{free} = 7.80%) for 301,119 reflections (PDB ID: 5D8V).

The Fe_4S_4 cluster is coordinated by four cysteine residues and is further surrounded by aromatic residues (Fig. 1(a)). Several distorted peptide bonds largely deviated from the planar configuration are observed mostly in the proximal region of the Fe_4S_4 cluster. Valence electrons of the polypeptide portion are visualized for the side and main chains of the polypeptide portion in the residual maps refined by the ISAM and in the deformation maps refined by the MAM.

The charge-density analysis also indicates a nonspherical distribution of the electron density around the Fe_4S_4 cluster (Fig. 2(a)). The Fe 3d-orbital electron densities are observed around the Fe atoms, whereas the bridging S and Cys-S_γ atoms are surrounded by diffused S 3p-orbital electrons. The Fe_4S_4 cluster consists of two subclusters: subcluster 1 composed of FE1, FE2, S3, S4, Cys43-S_γ and Cys46-S_γ and subcluster 2 composed of FE3, FE4, S1, S2, Cys61-S_γ and Cys75-S_γ. The Fe-S bonds within the subclusters

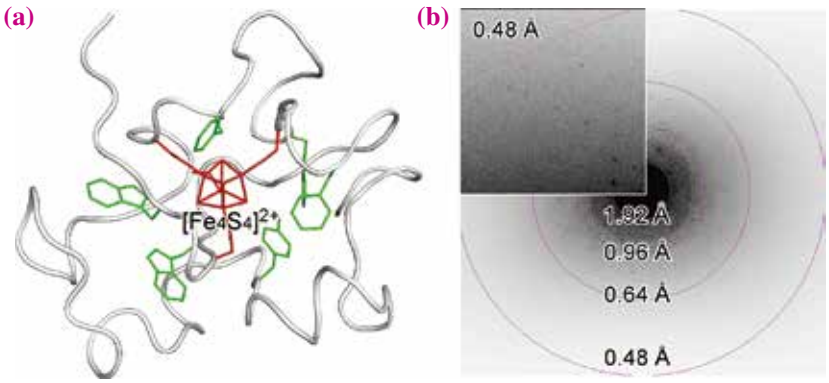

Fig. 1. Structure of high-potential iron-sulfur protein (HiPIP) and an ultra-high resolution diffraction image from its crystals. **(a)** Overall view shown as a tube model, where the iron-sulfur cluster and aromatic residues are represented as red and green sticks, respectively. HiPIP from *Thermochromatium tepidum* is composed of 83 amino acid residues and has an Fe_4S_4 cluster. **(b)** Diffraction image obtained at BL41XU, in which diffraction spots are observed at 0.48 Å resolution.

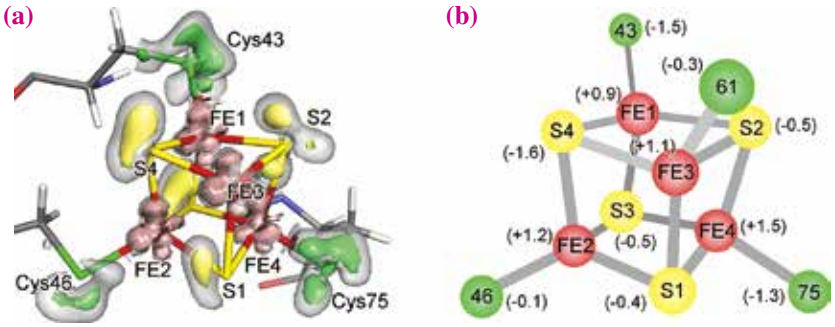

Fig. 2. Structure of the Fe_4S_4 cluster in HiPIP. **(a)** Deformation map of the Fe_4S_4 cluster represented as gray isosurfaces (+0.1 e/Å^3), with red, yellow and green (+0.3 e/Å^3) isosurfaces representing iron, cluster-sulfur and cysteine-sulfur atoms, respectively. **(b)** Schematic representation of the cluster in which atomic charges are indicated in parentheses near the corresponding atoms.

are long, whereas those bridging two subclusters are short in the Fe_4S_4 cluster. The overlaps between the Fe 3*d* and S 3*p* orbitals are generally smaller for shorter Fe-S bonds and larger for longer bonds. The atomic charges for the $Fe_4S_4(Cys\text{-}S_\gamma)_4$ moiety were derived by using the atoms in molecules (AIM) theory [4] (Fig. 2(b)). The atomic charge of FE1 is lower than those of other iron atoms and that of S4 is also lower than those of other bridging S atoms. The atomic charges of Cys43-S_γ and Cys75-S_γ are lower than those of Cys46-S_γ and Cys61-S_γ. The total atomic charges for subclusters 1 and 2 are –1.62 and +0.15, respectively, indicating that subcluster 1 is important for storing electronic charges.

It was found that the valence electrons of S atoms of $Fe_4S_4(Cys\text{-}S_\gamma)_4$ interact with H atoms in the charge-density map (Fig. 3). The atomic charges of S atoms correlate with the interaction between valence electrons and H atoms. Among the four bridging S atoms, S4, whose atomic charge is the largest, has no such interactions but the other three S atoms with smaller charges must have significant interactions. These findings imply that charge transfer from S to H atoms is involved in the reduction of the negative charges of S through the interactions.

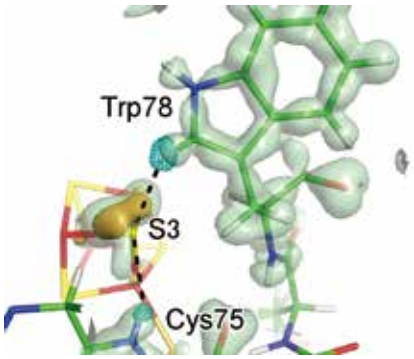

Fig. 3. Interactions between the Fe_4S_4 cluster and the protein environment. Deformation electron densities around S3 of the Fe_4S_4 cluster are presented as light green and pale yellow isosurfaces at contour levels of +0.1 and +0.3 e/Å^3, respectively. Cyan meshes show omit-map densities of the amide H of Cys75 and a H atom of Trp78 at a contour level of 3σ.

Kazuki Takeda[a], Yu Hirano[b] and Kunio Miki[a,*]

[a] Dept. of Chemistry, Graduate School of Science, Kyoto University
[b] Tokai Quantum Beam Science Center, National Institutes for Quantum & Radiological Science and Technology (QST)

*Email: miki@kuchem.kyoto-u.ac.jp

References

[1] *Y. Hirano, K. Takeda and K. Miki: Nature* ***534*** *(2016) 281.*
[2] C.W. Carter Jr.: in Handbook of Metalloproteins, Wiley, New York (2001) p. 602.
[3] B. Zarychta *et al.*: Acta Crystallogr. A **63** (2007) 108.
[4] R.F.W. Bader: Atoms in Molecules: A Quantum Theory, Oxford Univ. Press, Oxford (1990).

Redox-coupled proton transfer mechanism in nitrite reductase revealed by SPring-8 and SACLA

Since the invention of the Haber–Bosch process, the amount of fixed nitrogen in soil and water has been increasing, and this trend has a significant influence on the global environment. Fixed nitrogen is oxidized to nitrite (NO_2^-) by nitrification and then converted to gaseous dinitrogen (N_2) by microbial denitrification, which closes the nitrogen cycle. The reduction of NO_2^- to toxic nitric oxide ($NO_2^- + 2H^+ + e^- \rightarrow NO + H_2O$) is referred to as the key step in denitrification and is catalyzed by copper nitrite reductase (CuNiR).

CuNiR is a homotrimeric protein comprised of two distinct Cu sites per monomer (Fig. 1). Type 1 Cu (T1Cu) with a Cys–Met–His_2 ligand set is an electron acceptor, whereas type 2 Cu (T2Cu) with a His_3 ligand set is a catalytic center. Spaced ~12.5 Å apart, the two Cu sites are linked by an electron pathway, a Cys–His bridge. Two conserved residues, Asp98 and His255 (*Alcaligenes faecalis* numbering), are located at the T2Cu site and are bridged by a water molecule called bridging water. They are essential to the CuNiR activity because they assist proton-coupled electron transfer (PCET) to the substrate NO_2^-. However, the catalytic mechanism of CuNiR is controversial.

Analyses of the nitrite reduction mechanism in CuNiR using conventional synchrotron radiation crystallography (SRX) have encountered difficulties because X-ray photoreduction changes the native structures of metal centers and the enzyme–substrate complex. In recent years, serial femtosecond crystallography (SFX) using ultrabright femtosecond pulses from X-ray free electron lasers (XFELs) has opened a new age of structural biology. Using the high photon density in the focused XFEL beam, which achieves single-pulse diffraction within femtosecond exposure time, SFX enables protein structure determination from micrometer- to submicrometer-size crystals at ambient temperature. The femtosecond pulse duration allows the "diffraction-before-destruction" approach by circumventing radiation damage (photoreduction) of the sample because the diffraction process can be terminated in a timescale shorter than that of the damage process.

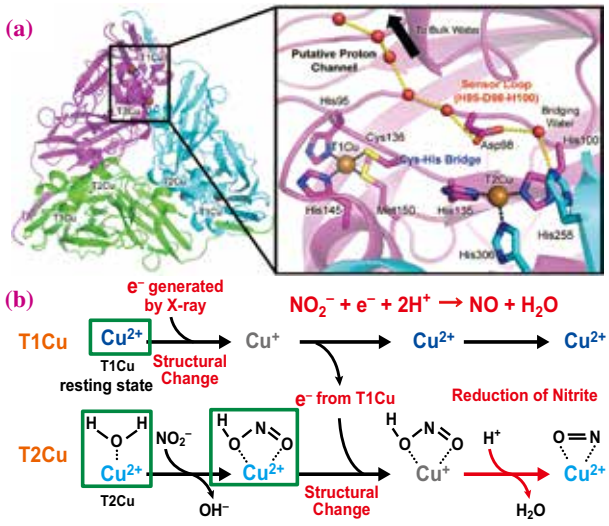

Fig. 1. **(a)** Overall structure (left) and catalytic site (right) of CuNiR (PDB ID: 1AS7 [3]) drawn as ribbon models. The yellow dashed lines and black dashed lines represent hydrogen bonds and coordination bonds, respectively. **(b)** Catalytic scheme of CuNiR. The structures surrounded by green rectangles are in oxidized states, which are susceptible to photoreduction by X-rays.

In this study, we utilized photoreduction in SRX at SPring-8 **BL26B1** and **BL26B2** to initiate a catalytic reaction of CuNiR from *Alcaligenes faecalis* (*Af*NiR) and to trap enzymatically produced intermediary structures [1]. Furthermore, to visualize intact CuNiR structures, we applied SFX at SACLA **BL3**, which enables damage-free structural determination and evaluation of the native conformational population at room temperature. By comparing SRX and SFX data, we obtained new insights into PCET and nitrite reduction in CuNiR.

The $N^{\delta 1}$ atom of catalytically important His255 can form a hydrogen bond (H-bond) with the carbonyl O atom of Glu279 and/or the hydroxyl O atom of Thr280, and this Glu–Thr pair is conserved in CuNiRs. Compared with the imidazole ring of His255 in the intact SFX resting-state structure refined at 2.03 Å resolution, the imidazole ring in the photoreduced SRX resting-state structure at 1.20 Å resolution is rotated by about 20° (Fig. 2(a)). Hence, by the reduction of the copper center, the H-bond partner of His255 was changed from Glu279 to Thr280. Moreover, we recently showed that the imidazole ring of His244 in CuNiR from *Geobacillus thermodenitrificans* (*Gt*NiR), which corresponds to His255 in *Af*NiR, rotates as a result of photoreduction [2]. These results indicate that the rotation of His is a universal phenomenon during CuNiR catalysis.

Using mutated *Af*NiR, we further proved that the rotated state of His255 is a transient conformation important for the CuNiR activity. The activities of the T280V and T280S mutants were, respectively, 20% and 29% of the WT activity. Because the T280V

mutant lacks the hydroxyl O atom that can form an H-bond with His255, the rotation of His255 is inhibited in this mutant. Although the T280S mutant maintains a hydroxyl group in the side chain, it rotates more flexibly than that of Thr, which means that His255 is not always able to form an H-bond with Ser280. Therefore, the T280S mutant showed lower activity than that of WT but higher activity than that of T280V.

We propose that His255 is a redox-coupled switch for proton transfer (Fig. 2(b)). Because the hydroxyl O atom of Thr280 is less negatively charged than the carbonyl O atom of Gln279, the $N^{\delta 1}$ atom of His255 forms a longer and weaker H-bond with Thr280. As a result, the H atom is more attracted to the $N^{\delta 1}$ atom, and a proton on the $N^{\varepsilon 2}$ atom moves to the bridging water. It is considered that a proton is supplied to NO_2^- via the bridging water (or even Asp98). It is an interesting fact that the proton transfer from His255 via the bridging water has also been supported by recent computational studies.

The vertical binding mode is known to occur in many biomimetic model complexes of Cu(II)–NO_2^- and supported by computational chemistry. However, the SRX CuNiR structures reported previously have shown the near face-on modes. In this study, an SFX NO_2^- complex structure was solved at 1.60 Å resolution by the single-wavelength anomalous diffraction (SAD) method using Cu as a phasing element. This is the first example of phase determination with natural heavy atom binding sites using the data obtained with SFX. Then, two SRX NO_2^- complex structures at a cryogenic temperature (Cryo) and room temperature (RT) were determined at 1.30 and 1.54 Å resolutions, respectively.

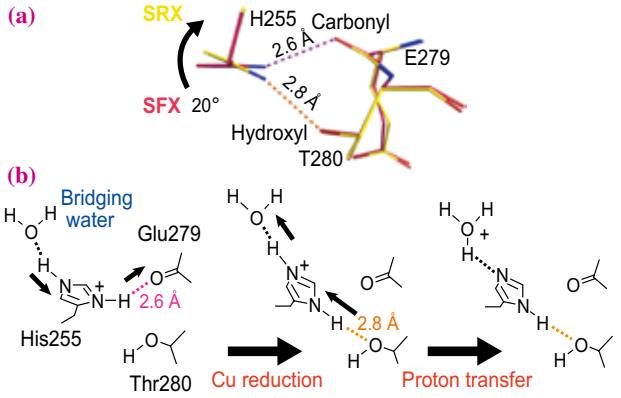

Fig. 2. **(a)** Switching of H-bond partners. The SFX and SRX resting-state structures are shown in pink and yellow, respectively. Dashed lines represent H-bonds. **(b)** Proposed mechanism of efficient proton transfer driven by the rotation of His255. Dashed lines represent H-bonds. Thin black arrows illustrate the directions in which H atoms are attracted.

The NO_2^- binding mode in the SFX structure was vertical, whereas that in the Cryo SRX or RT SRX structure was near face-on (Fig. 3). It is most probable that the conformational change of NO_2^- from vertical to near face-on is induced by photoreduction. Furthermore, the N atom of NO_2^- becomes closer to His255 when NO_2^- changes its conformation from vertical to near face-on, meaning that owing to steric hindrance (<3.5 Å), near face-on NO_2^- might inhibit the reverse rotation of His255 and hence reverse proton transfer.

Our study has demonstrated that combining SRX and SFX technology is extremely effective as a powerful tool for studying the catalytic process of redox enzymes.

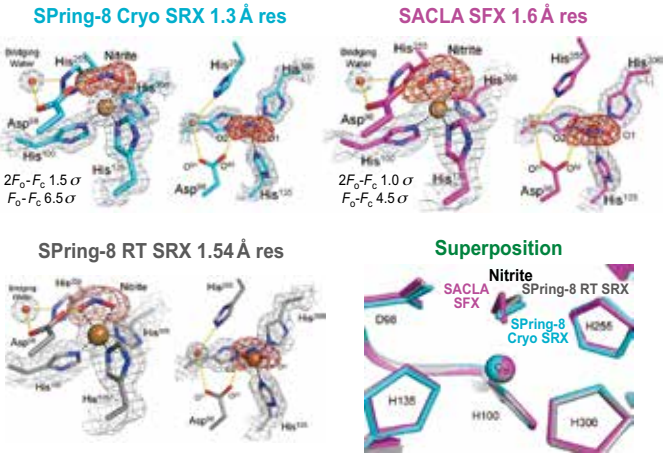

Fig. 3. NO_2^- complex structures of CuNiR determined by SFX (magenta), Cryo SRX (cyan), and RT SRX (gray). Superposition of the structures indicates that the binding modes of NO_2^- on T2Cu are different among the structures.

Eiichi Mizohata[a,*], Yohta Fukuda[a] and Tsuyoshi Inoue[a]

[a] Department of Applied Chemistry, Osaka University

*Email: mizohata@chem.eng.osaka-u.ac.jp

References

[1] *Y. Fukuda, K.M. Tse, T. Nakane, T. Nakatsu, M. Suzuki, M. Sugahara, S. Inoue, T. Masuda, F. Yumoto, N. Matsugaki, E. Nango, K. Tono, Y. Joti, T. Kameshima, C. Song, T. Hatsui, M. Yabashi, O. Nureki, M.E.P. Murphy, T. Inoue, S. Iwata, E. Mizohata: Proc. Natl. Acad. Sci. USA* ***113*** *(2016) 2928.*
[2] Y. Fukuda *et al.*: J. Biochem. **159** (2016) 527.
[3] E.I. Tocheva *et al.*: Science **304** (2004) 867.

Single-wavelength anomalous dispersion (SAD) phasing with native anomalous scatterers using serial femtosecond crystallography

Calculation of the electron density requires complex structure factors. While the absolute values of structure factors are experimentally measurable, their phases are not. This is known as *the phase problem* of crystallography. When the structures of homologous proteins for molecular replacement are unavailable, we have to rely on experimental phasing, where phases are derived from isomorphous difference signals between native and derivative crystals, or anomalous dispersion effects of anomalous scatterers. Sulfur is the lightest element that provides useful anomalous differences at wavelengths commonly used for protein crystallography. Since almost all proteins contain sulfurs from methionines and cysteines, experimental phasing with sulfur does not require protein derivatization, which can be tedious and tricky. However, the signals from sulfurs are much weaker than those from heavier atoms and great care must be taken to accurately measure them.

In serial femtosecond crystallography (SFX), independent diffraction patterns from tens of thousands of microcrystals are combined to yield a dataset. This is because pulses from an X-ray free electron laser (XFEL) are so powerful that a single shot completely destroys a crystal. As each crystal provides only one diffraction image, indexing and orientation determination are more challenging than by using the traditional rotation method. Moreover, every observation is partial since crystals are virtually stationary during the femtosecond X-ray exposure. Scaling and outlier rejection are also problematic because of inhomogeneities in the crystal size and quality, and fluctuations of the beam intensity and spectrum. These issues could potentially limit the quality of SFX datasets.

Since single wavelength anomalous dispersion phasing with sulfur atoms (S-SAD) requires highly accurate data, it provides a unique opportunity to test the quality of SFX datasets. In addition, SAD phasing shares some similarities with time-resolved studies in that both depend on the accurate measurement of tiny differences between Friedel pairs or between excited and reference datasets, respectively. Thus, the study of the data quality and how to optimize it will benefit not only experimental phasing but also other SFX experiments.

In this study, we solved the structure of lysozyme by S-SAD (Fig. 1) [1]. Although lysozyme is a model protein, it is no easier to solve by S-SAD; lysozyme contains eight cysteines and two methionines in 129 residues (Fig. 1), giving rise to the expected anomalous signal, or a Bijvoet ratio $<|\Delta F|>/<|F|>$ of only 1.6%. Before this study, the gadolinium SAD phasing of lysozyme [2] carried out at LCLS, an XFEL facility at Stanford, was reported. In this case, the Bijvoet ratio was larger than 10%.

Lysozyme microcrystals (7–10 μm) were suspended in a grease medium [3]. The experiments were performed at SACLA **BL3** on the Diverse Application Platform for Hard X-ray Diffraction in SACLA (DAPHNIS) [4]. The X-ray wavelength was 1.77 Å (7 keV) and each X-ray pulse delivered ~7×10^{10} photons within a 10 fs duration (FWHM) to the grease matrix. The X-ray beam was focused to 1.5×1.5 μm^2. The crystals in the grease matrix were serially loaded using a high-viscosity micro-extrusion injector system installed in a helium chamber. Diffraction images were collected using a 4 M pixel detector built with eight panels of multi-port charge-coupled device (MPCCD).

Diffraction images were filtered by a data processing pipeline developed for SACLA [5] based on *Cheetah*. Out of about 700,000 images collected, about 450,000 images with more than 20 spots were retained as hits and processed by *CrystFEL*. About 180,000 images were indexed by *DirAx*. Integrated intensities were scaled by per-image scale factors (but not B factors) before merging. No sigma cutoff or partiality correction was applied.

Because the data quality improves with the multiplicity, we attempted to phase the dataset from varying numbers of indexed images. As shown in Fig. 2, the data quality indicators improved with the number of merged images. It turned out that at least 150,000 indexed images were necessary to solve this structure. Interestingly, the data precision (CC_{ano}) remained low even when the accuracy (peak height in the anomalous difference map) was sufficiently high to solve the structure.

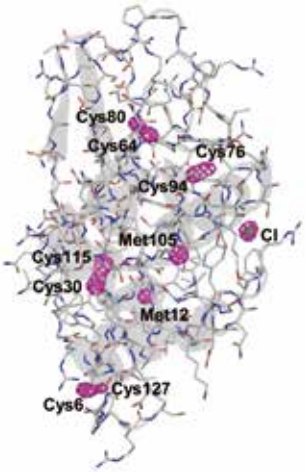

Fig. 1. Anomalous difference Fourier map (contoured at 6.0σ) calculated by *ANODE*, showing sulfur and chlorine atoms. [1]

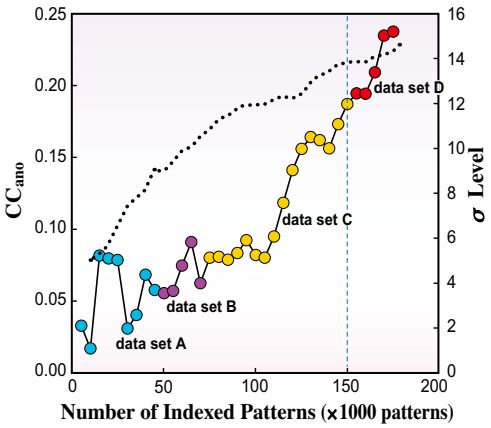

Fig. 2. Data quality statistics with varying number of merged images. The solid line indicates CC_{ano}. See the original paper [1] for the details of the four datasets. The peak height of the Met105 sulfur atom in the anomalous difference map is shown as the dotted black line. 150,000 images (blue dashed line) had to be merged for successful phasing.

Experimental phasing was performed with the *SHELX* suite. Systematic trials of parameter combinations were essential for the success. First, up to 500,000 trials of *SHELXD* were executed at various high-resolution limits between 2.0 and 3.0 Å to locate anomalous scatterers. When only 150,000 indexed images were used, reflections to 2.2 Å had to be used and the best solution only appeared after 320,000 trials. In contrast, solutions could be found more easily at a lower resolution with fewer trials when more images were merged. Next, the experimentally phased map was calculated and improved by iterative autotracing and density modification in *SHELXE*. Here, the number of sites, the high-resolution cutoff and the solvent content were systematically varied. Although the initial map was noisy and fragmented, the iterations improved the phase and *SHELXE* eventually traced 90 out of 129 residues (Fig. 3). *Buccaneer* automatically completed the model in the experimental map from *SHELXE*.

After the publication of this research, we also reported the Cu-SAD phasing of a metalloenzyme with a Bijvoet ratio of 1.7% [6]. Other groups reported the S-SAD phasing of thaumatin [7] and A2a G-protein-coupled receptor [8], with Bijvoet ratios of 2.1% and 1.9%, respectively. Although these results collectively establish that data from SFX are sufficiently accurate to detect small differences, it is noteworthy that all of these studies required more than 100,000 indexed images. To reduce the number of necessary images, and thus sample consumption and beam time, further improvements in data processing algorithms are under way.

The raw data (diffraction images) have been deposited in CXIDB (ID #33; http://cxidb.org/id-33.html). Readers are encouraged to reprocess our data to learn SFX and try their new ideas.

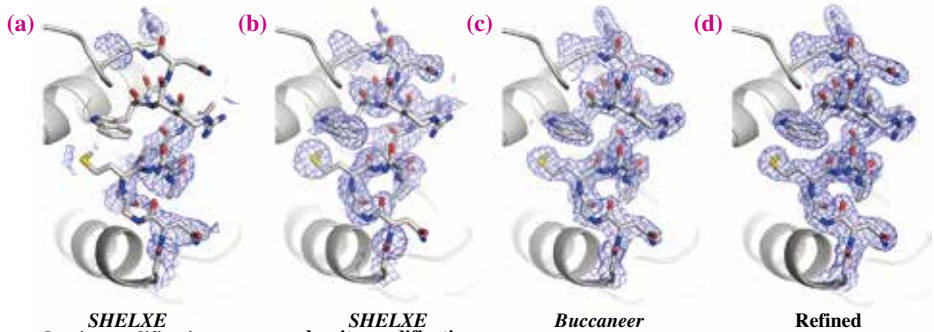

Fig. 3. $2F_o - F_c$ electron density maps contoured at the 1.0σ level from the various steps of the phasing process. SAD phasing was performed by (**a**) *SHELXE* with density modification, followed by (**b**) autotracing of the main chain in *SHELXE* and (**c**) automatic modeling of side chains and remodeling of the main chain by *Buccaneer*. (**d**) shows the final refined map. [1].

Takanori Nakane[a], So Iwata[b,c] and Michihiro Sugahara[b,*]

[a] Graduate School of Science, The University of Tokyo
[b] RIKEN SPring-8 Center
[c] Graduate School of Medicine, Kyoto University

*Email: msuga@spring8.or.jp

References

[1] *T. Nakane, C. Song, M. Suzuki, E. Nango, J. Kobayashi, T. Masuda, S. Inoue, E. Mizohata, T. Nakatsu, T. Tanaka, R. Tanaka, T. Shimamura, K. Tono, Y. Joti, T. Kameshima, T. Hatsui, M. Yabashi, O. Nureki, S. Iwata and M. Sugahara: Acta Crystallogr. D Biol. Crystallogr.* ***71*** *(2015) 2519.*
[2] T. Barends *et al.*: Nature **505** (7482) (2014): 244-247.
[3] M. Sugahara *et al.*: Nat. Methods **12** (2015) 61.
[4] K. Tono *et al.*: J. Synchrotron Rad. **22** (2015) 532.
[5] T. Nakane *et al.*: J. Appl. Crystallogr. **49** (2016) 1035.
[6] Y. Fukuda *et al.*: Proc. Natl. Acad. Sci. USA **113** (2016) 2928.
[7] K. Nass *et al.*: IUCrJ **3** (2016) 180.
[8] A. Batyuk *et al.*: Sci. Adv. **2** (2016) e1600292.

Single-pulse enhanced coherent diffraction imaging of bacteria with an X-ray free-electron laser

Coherent diffraction imaging (CDI) is a very promising way for high-resolution imaging of non-periodic objects. This technique is based on the principle that the oversampled coherent diffraction patterns obtained from samples are recorded in the far field and then directly reconstructed real-space images using phase retrieval algorithms [1]. The achievable spatial resolution for CDI is principally limited by the wavelength of the incident X-rays. Recently, X-ray Free Electron Lasers (XFEL) with femtosecond and ultra-bright X-ray pulses combined with CDI overcome radiation damage limits and facilitate to achieve images by single-shot imaging based on a diffraction-before-destruction scheme [2]. However, presently, even with the ultra-bright XFEL, the achievable resolution of biomaterials is less than the required to study the cells and their internal structures because of the low scattering intensities. Hence, how to improve the low scattering ability of biomaterials is very important to the investigation of high-resolution single-shot imaging and its applications.

Theoretically, the scattering intensity at diffraction angle θ is proportional to the incident X-ray intensity and the form factors of the samples. Therefore, brighter X-ray source and increasing the form factors are two possible parameters. For single-shot CDI, the incident single pulse contains around 10^{12} photons at SACLA. Here, we demonstrated the promising single-shot CDI method [3] to enhance the scattering intensity and spatial resolution by labeling the low scattering biomaterials with heavy atoms. The bacterium *staphylococcus aureus* (*S. aureus*) was chosen as a model system and gold nanoclusters was selected as the labeling materials to investigate the scattering intensity and resolution enhancement. In order to compare the enhancement, two kinds of *S. aureus* samples were prepared: one, labeling of gold nanoclusters with a mean diameter of 9.8 nm; second, control samples with same culture conditions without gold labeling.

The experiment was performed at SACLA **BL3** [4]. Sketch of the experimental setup is shown in Fig. 1. To demonstrate the enhancement of signal and resolution by CDI, the labeled and control *S. aureus* were deposited onto 50-nm-thick Si_3N_4 membranes separately. By scanning the fixed membranes with focused XFEL single pulses, a multi-port charge-coupled device (MPCCD) detector was used to record the diffraction signals.

The diffraction patterns of the control and labeled *S. aureus* are shown in Figs. 2(a) and 2(b) respectively. Intuitively, the diffraction pattern of the labeled samples extended to the edge of the detectors, whereas the diffraction signals from the control sample are weak and mainly concentrated in the center of the detector. In order to quantitatively compare the signals intensity, the power spectrum density (PSD) of the two diffraction patterns were calculated and shown in Fig. 2(c) (blue curve for labeled and black curve for control). The highest spatial frequency of the labeled *S. aureus* is 81 μm^{-1} corresponding to a theoretical resolution of 12 nm, while the control sample is only about 45 μm^{-1} corresponding to a resolution of 22 nm. The spatial frequency of the labeled diffraction patterns is about twice of the control one. We also performed more diffraction patterns and the PSD curves showed the similar results. Since these diffraction patterns were recorded under the same experimental conditions, it confirms that diffraction signals has been significantly increased by labeling with gold nanoclusters.

Though the gold labeling increases scattering intensity, the achievable resolution depends on multiple factors, including the signal intensity, signal to noise ratio, missing low spatial frequency data and so on. To analyze the resolution enhancement, both the control and the labeled *S. aureus* patterns were reconstructed with HIO retrieval algorithm. Figures 3(a) and 3(b) show the reconstructed images from the diffraction patterns shown in Fig. 2. As there is few cellular structures could be identified with the achievable resolution, it is difficult to compare the image resolutions of the control and labeled *S. aureus* directly. To quantitatively estimate the resolution, the phase retrieval transfer function (PRTF) of reconstructed images were calculated. As shown in Fig. 3(c), the PRTF curves indicate that the achievable resolution is about 143.5 nm for control

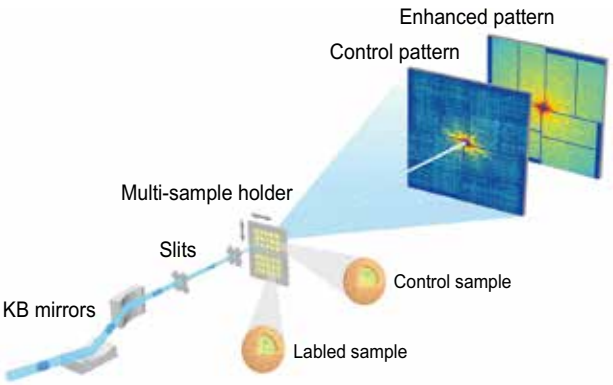

Fig. 1. Schematic layout of the enhanced single-pulse coherent diffraction imaging experiment.

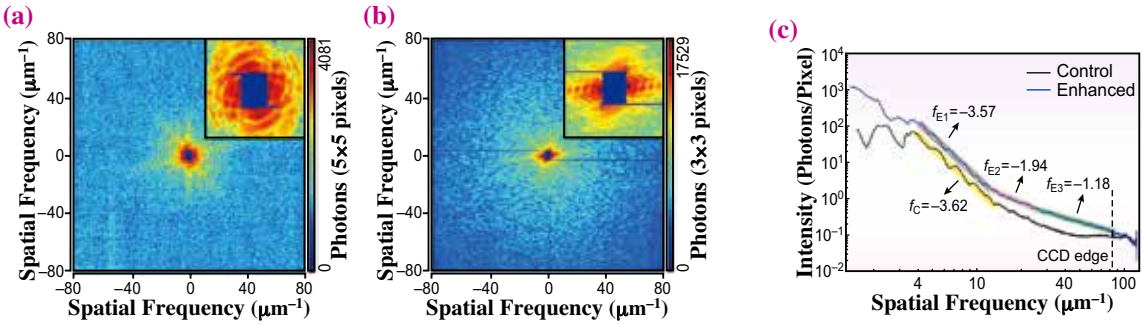

Fig. 2. **(a)** and **(b)** Representative diffraction patterns of control and labeled *S. aureus*. **(c)** Comparison of PSD curves of control and labeled diffraction patterns.

S. aureus (black curve) and 54 nm for labeled sample (blue curve) which is increased by a factor of 2.6.

During our experiment, it was found that by labeling with gold nanoclusters, both the diffraction signals and achievable resolution could be increased obviously. We analyzed and discussed the intrinsic causes for signal and resolution enhancement according to reference enhancement model. By introducing labeling, the recorded diffraction intensity includes three parts as presented in equation 1:

$$I_{sc} = I_{cell} + I_{Au} + 2\sqrt{I_{cell} I_{Au}} \cos(\phi_{cell} - \phi_{Au}) \qquad (1)$$

At high spatial frequency of the diffraction patterns, the signal mainly comes from the labeled gold nanoclusters and the interference between the cell and gold nanoclusters. Furthermore, the interference signal facilitates the phase retrieval and reconstruction. Since more such useful signals were used for reconstruction, the achievable resolution could be improved. Therefore, labeling biomaterials with appropriate heavy materials provides a promising way to enhance the scattering intensity and resolution using single-shot CDI without radiation damage.

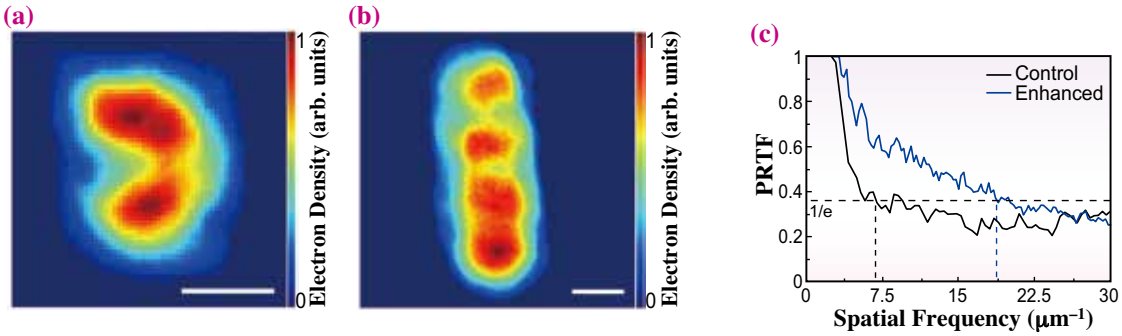

Fig. 3. **(a)** and **(b)** Reconstructed images of the control and labeled *S. aureus* from Figs. 2(a) and 2(b). **(c)** Phase retrieval transfer function curves calculated from the reconstruction results.

Jiadong Fan[a], Tetsuya Ishikawa[b] and Huaidong Jiang[a,*]

[a] School of Physical Science and Technology, ShanghaiTech University, China
[b] RIKEN SPring-8 Center

*Email: jianghd@shanghaitech.edu.cn

References

[1] J. Miao *et al.*: Science **348** (2015) 530.
[2] R. Neutze *et al.*: Nature **406** (2000) 752.
[3] *J. Fan, Z. Sun, Y. Wang, J. Park, S. Kim, M. Gallagher-Jones, Y. Kim, C. Song, S. Yao, J. Zhang, J. Zhang, X. Duan, K. Tono, M. Yabashi, T. Ishikawa, C. Fan, Y. Zhao, Z. Chai, X. Gao, T. Earnest and H. Jiang: Sci. Rep.* ***6*** *(2016) 34008.*
[4] T. Ishikawa *et al.*: Nat. Photonics **6** (2012) 540.

X-ray fiber diffraction: a tool for understanding the structural dynamics of tubulin dimers in native microtubules

When we are going to know structural details of biological molecules, there would be two possibilities; electron microscopy and X-ray crystallography. Owing to remarkable improvements in cryo-electron microscopy techniques using direct electron detectors, impressive progresses showing high-resolution (~0.3 nm) images of various biological molecules in action are now appearing regularly in leading journals. Since details of protein architectures at the atomic scale have been obtained by X-ray crystallography, we can now combine them with electron micrographs to gain more direct insights into the functions of biomolecules than we expected by conventional tools used over a decade ago. This would also be the case for X-ray fiber diffraction/X-ray solution scattering analysis, which we expect will become the third major method used for structural biology.

One of the main advantageous points to use X-ray diffraction is that it enables us to acquire information on native biological molecules functioning in aqueous solutions at moderate temperatures. Here, two main drawbacks should be briefly mentioned, that is, we cannot completely prevent damage induced by focused high energy X-ray beams, and we can only collect indirect information on molecular structures such as structural repeats, mean size and shape. However, owing to the following five improvements achieved for our fiber diffraction technique, X-ray fiber diffraction is now one of the most powerful tools for investigating tubulin molecule dynamics in microtubules [1-3].

First, in our technique of X-ray fiber diffraction, we have successfully revived a flow-aligning technique to collect data from live axonemes of sea-urchin spermatozoa [1,2]. The technique of shear-flow alignment, first theoretically described by Jeffery [4,5], seems to be old-fashioned as it was applied to TMV [6,7] and actin fibers [8] in the 1960s. However, we found that including methylcellulose or other harmless polymers that induce high viscosity of the buffer medium enabled us to accomplish the homogeneous orientation of biological filaments [1]. This polymer technique could be applied to other types of biological filaments, e.g., axonemes [1,2], microtubules [1,3], collagen and TMV [1]. Second, damage to biological materials can be neglected or minimized even under irradiation with high-flux beam of 1×10^{15} photons/s (BL40XU) with 100×0.25 s exposures, because a specimen under the shear flow is continuously renewed at the millisecond time scale (see below). Thus, every time we are looking at diffractions from a fresh specimen with little beam damage. Third, as the use of shearing flows to align fibers are also stirring up the specimen continuously in solution, we can change the medium conditions at a fast time scale (<100 ms). This is quite convenient for investigating the effects of chemicals on biological filaments, e.g., stabilizer or destabilizer of microtubules. Fourth, a rheometer-type shear-flow apparatus composed of two flat disks (round microscope cover slips) was placed separately in parallel (Fig. 1), where small air bubbles contaminating the viscous solution are immediately excluded from the X-ray beam path by circumferential flows occurring in the apparatus chamber. Finally, the most dramatic improvement to be stressed is the time course of fiber alignment. In the case of microtubules, a homogeneous orientation can be accomplished in a few seconds and structural information can be acquired after about a second (exposure time of 0.2–0.3 s). This is highly advantageous when we are going to analyze the structure of labile filaments such as microtubules.

We estimated the total amount of microtubule specimen required for our experiments performed at two SPring-8 beamlines, **BL45XU** (2×10^{11} photons/s) for SAXS and high-flux **BL40XU** (1×10^{15} photons/s). The volume of the sample placed in the X-ray beam path (0.1×0.2 mm^2) was approximately 7 nL. As the total volume of the specimen placed between the two round cover slips was 80 μL (between a/b and c/d in Fig. 1), only 0.009% of total specimen in the shear-

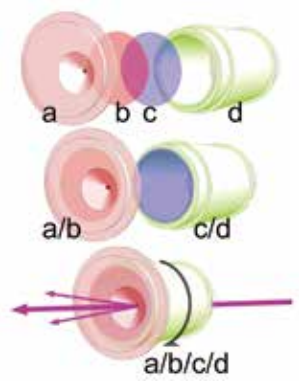

Fig. 1. Schematic drawing of the apparatus for the shear-flow alignment of microtubules showing a copper plate **(a)** holding a round cover slip **(b)**. Another round slip **(c)** was glued on a long tube made of machinable ceramic **(d)**. A medium containing porcine brain microtubules was placed in the narrow gap (0.35 mm) between the two cover slips (between a/b and c/d). After starting to spin (black arrow) the long tube (c/d), the X-ray beam (magenta) was incident to the specimen at a site 7.5 mm away from the center of rotation. Diffraction signals were acquired on the left side of the apparatus.

flow chamber was irradiated. This small portion of the sample solution containing around 1×10^7 microtubules with an average length of 10 μm provide us enough intensity of diffraction signals with 0.25 and 30 s exposure by BL40XU and BL45XU, respectively. In particular, from the strong fourth-order reflections, approximately 1 nm, we could precisely determine the changes in the axial tubulin repeat (Fig. 2). Under the present experimental conditions, where the round cover slip is spinning at 10 – 20 rps to induce a shear flow (shear rate, 1300 – 2600 s^{-1}), each microtubule within the specimen medium remains the beam path of the X-ray for only 0.2 – 0.4 ms on average. Thus, damage of the microtubules caused by the X-ray beam would be negligible, if any.

Figure 3 shows an example of the dynamic changes in an axial tubulin repeat. In this case, a downward shift (lower angle) of the fourth-order reflections was clearly observed after applying paclitaxel, which indicates that the mean axial tubulin repeat became longer within 30 s after the addition of a microtubule stabilizer. Microtubules are composed of self-assembled tubulin heterodimers stacked in a cylindrical wall having a two-dimensional unit arrangement. Our observation revealed that the microtubule structure has some flexibility and that each tubulin dimer inside microtubules can change its molecular configuration immediately after binding to paclitaxel. In the present study, the structural change was finished within 30 s. Our recent preliminary observations with higher time resolution (<0.25 s) indicated that the actual structural shift was completed faster (<1 s).

The examples shown here are the dynamic changes in an axial tubulin repeat, but we also observed structural dynamics in the diffraction of equatorial signals [3] corresponding to a change in the microtubule diameter or spacing between protofilaments, the longitudinal arrays of tubulin units. Along with other detailed information of the static structure of tubulin dimer molecules obtained by crystallography [9] and cryo-electron microscopy [10,11], we expect to obtain more insight into the dynamics of tubulin structure, i.e., how the molecular configuration of tubulin dimers is flexible and adaptive depending on their chemical and physical states, and how it is correlated to the microtubule functions and the control of eukaryotic cell shapes and motility.

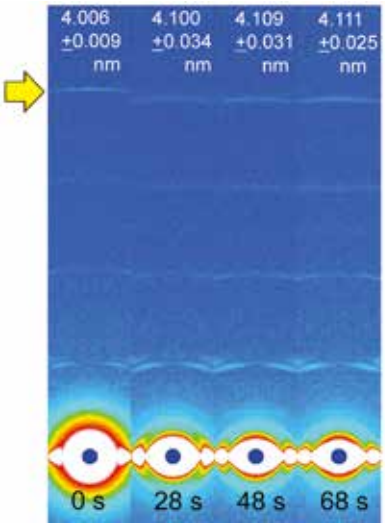

Fig. 3. Structural changes of microtubules after mixing with paclitaxel. Patterns of meridional diffraction signals obtained by 20 s exposure are shown. From the fourth-layer-line (yellow arrow), tubulin axial repeat was determined.

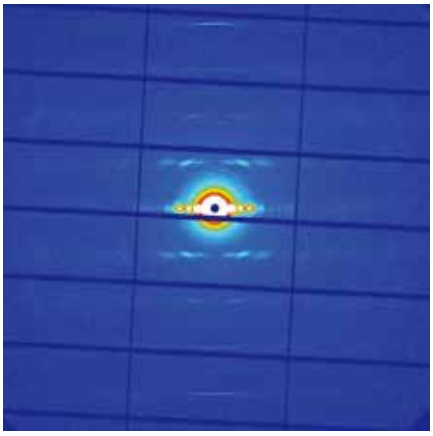

Fig. 2. Example of X-ray fiber diffraction of microtubules. The image was acquired by PILATUS 3X 2M at BL45XU using microtubules assembled with GTP at 37.0°C. Yellow arrow indicates the fourth-order reflection (~1 nm) of axial tubulin repeat (~4 nm).

Shinji Kamimura

Department of Biological Sciences, Chuo University

Email: skam@bio.chuo-u.ac.jp

References

[1] T. Sugiyama *et al.*: Biophys. J. **97** (2009) 3132.
[2] S. Toba *et al.*: Biophys. J. **108** (2015) 2843.
[3] *S. Kamimura, Y. Fujita, Y. Wada, T. Yagi and H. Iwamoto: Cytoskeleton **73** (2016) 131.*
[4] G.B. Jeffery: Proc. R. Soc. Lond. A **102** (1922) 161.
[5] R.G. Larson: The Structure and Rheology of Complex Fluids (1999) Oxford Univ. Press.
[6] E.W. Taylor & W. Cramer: Biophys. J. **3** (1963) 143.
[7] J.D. Bernal & I. Fankuchen: J. Gen. Physiol. **25** (1941) 111.
[8] K. Maruyama: J. Biochem. **55** (1964) 277.
[9] B. Gigant *et al.*: Cell **102** (2000) 809.
[10] H. Li *et al.*: Structure **10** (2002) 1317.
[11] G.M. Alushin *et al.*: Cell **157** (2014) 1117.

Secondary structure analysis of Lewy bodies in the brain of Parkinson's disease patients

Parkinson's disease (PD) is a progressive neurodegenerative disorder of the central nervous system that mainly affects the motor system. Four motor symptoms are associated with PD: tremor, rigidity, slowness of movement, and postural instability. PD is the most common neurodegenerative disorder after Alzheimer's disease, and there is no basic treatment to control the development of the disease. It had been known for quite some time that Lewy bodies (LBs), abnormal protein aggregates, are formed in the brain of Parkinson's disease patients, and it is thought that LBs play an important role in the onset of the disease. LBs mainly consist of α-synuclein (α-syn), which is a 140-amino acid protein abundant in presynaptic terminals of nerve cells in the brain. α-syn is highly expressed in the central nervous system and erythrocytes, yet its function remains obscure. Although α-syn exists *in vitro* as an intrinsically disordered monomeric protein [1], it transforms into fibrils after agitation at 120 to 1000 rpm for a few days. Because these fibrils have a β-sheet-rich structure and a cross-β conformation, as can be seen by Fourier transform infrared spectroscopy (FTIR) and X-ray diffraction, these fibrils are often regarded as 'amyloid fibrils,' which are defined biophysically as fibrillar polypeptide aggregates with a cross-β conformation. Although elucidating the fibrillization process of α-syn is difficult, several studies have indicated that misfolded monomers undergo self-assembly into metastable oligomeric intermediates and finally, into amyloid-like fibrils. Recent epoch-making studies showed that the fibril seeds formed *in vitro* as described above can be propagated in the mouse brain [2]. The hypothesis stating that α-syn fibrils are involved in the pathogenesis of PD is under investigation *in vivo* as well as *in vitro.* On the other hand, the secondary structure of proteins in LBs in the human brain has not been clarified. Several electron microscopy (EM) studies demonstrated that LBs contain a filamentous amyloid-like structure, which is morphologically similar to wild-type α-syn fibrils *in vitro* [3]. In addition, they showed that typical LBs have granular components in the core and radially arranged fibrils in the halo. These results indicate that 'amyloid fibrils' which are pathologically characterized as depositions of protein fibrils with a specific appearance in EM, are part of LBs. However, EM cannot provide information on the secondary structure of a protein, and thus, whether LBs have a β-sheet conformation is unclear. Although Congo red, Thioflavin-T, and Thiazin red can be used for amyloid detection, their staining provides little information on the structure. The secondary structural information on proteins is important for developing treatment drugs. Because LBs cannot be induced *in vivo* or *in vitro*, to confirm that LBs contain amyloid fibrils, it is necessary to verify the abundance of the β-sheet.

Fourier transform infrared microspectroscopy (FTIR) is an established structural analysis method and is sensitive to the secondary structure of proteins. The absorption maxima for α-helix (~1655 cm^{-1}), β-sheet (~1630 cm^{-1}), and random coil (~1645 cm^{-1}) structures are included in the frequency range of the amide I band. FTIR also provides information on the amount of lipids in the beam. Because FTIR produces the spectrum derived from a chemical bond, it provides detailed structural information that cannot be obtained by staining and EM. However, the FTIR measurement of LBs is not easy for several reasons. The main difficulty is that LBs are too small to be irradiated with an infrared beam, and their density is too low to obtain a significant signal. To overcome this, a strong and small infrared beam is required. For this reason, we used the synchrotron radiation SPring-8 **BL43IR**.

Brain tissue samples from three patients (83-year-old female, 76-year-old male, and 74-year-old female) with neuropathologically confirmed PD were studied. The samples were fixed in 4% buffered formaldehyde and embedded in paraffin according to routine tissue processing for pathological examination. For each sample, 10-μm-thick sections were cut and deposited on CaF_2. Tissue sections were immunostained by anti-human phosphorylated α-syn (Ser129) monoclonal antibody. These samples were allowed to dry at room temperature. The brilliance of infrared synchrotron radiation (IR-SR) at BL43IR is more than two orders

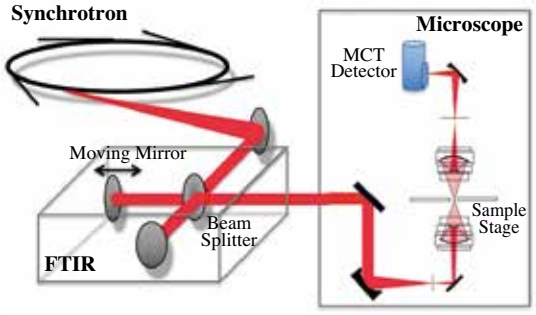

Fig. 1. Optical layout of the microspectroscopic station at BL43IR. The infrared synchrotron light is injected into the FTIR (Bruker VERTEX70) interferometer, and the light then goes to the microscope (Bruker HYPERION2000). Infrared light transmitted through a sample is detected by an MCT (HgCdTe) detector.

of magnitude higher than that of the laboratory source in the fingerprint region of 2000–1000 cm^{-1}. A Fourier transform infrared (FTIR: Bruker VERTEX 70) spectrometer was used with IR-SR as the infrared source (Fig. 1). A tissue sample on an adjustable motorized x–y mapping stage was observed with an optical microscope (Bruker HYPERION 2000). A rectangular region of 100 μm × 100 μm including amyloid deposits or LBs was mapped with an aperture size of 7 μm × 7 μm and 3–5 μm steps in the horizontal and vertical directions. Interferograms were acquired with 400 scans, and signals were averaged and Fourier transformed to generate a spectrum with a nominal resolution of 3 cm^{-1}.

The total protein distribution was evaluated by calculating the sum of the absorbances at 1540 cm^{-1} and 1640 cm^{-1}. The proportion of β-sheet structures was analyzed by curve fitting to the FTIR spectra ranging from 1700 cm^{-1} to 1600 cm^{-1}. Spectrum data were fitted using four Gaussian species centered at 1628 cm^{-1} and 1680 cm^{-1} (β-sheets), and 1648 cm^{-1} and 1661 cm^{-1} (random coils, α-helices, and others) as in previous reports. During the fitting procedure, the peak height was free, whereas the width at half height was maintained at < 25 cm^{-1}. A reasonable fit was obtained as shown in Fig. 2. The lipid distribution was based on the area of the symmetric CH_2 band at 2850 cm^{-1} (2858–2848 cm^{-1}, baseline 3000–2750 cm^{-1}). Our results showed a shift in the infrared spectrum, which indicates the abundance of a β-sheet-rich structure in LBs. Also, 2D infrared mapping of LBs revealed that the content of the β-sheet structure is higher in the halo than in the core, and the core contains a large amount of proteins and lipids (Fig. 3) [4].

Here, we present, to our knowledge, the first data on the secondary structure of LBs obtained using synchrotron FTIR microscopy (FTIRM). Furthermore, β-sheet mapping was performed to elucidate the process of generation of LBs. Our FTIRM approach has the potential for elucidating the pathology of many amyloid-related diseases. However, since the laboratory FTIR instruments do not have sufficient brightness, FTIRM measurement of brain tissues requires synchrotron radiation. This has been limiting the use of this technique, particularly for medical researchers. However, since many synchrotron radiation facilities have recently been constructed worldwide, more researchers now have better access to FTIRM for biological samples.

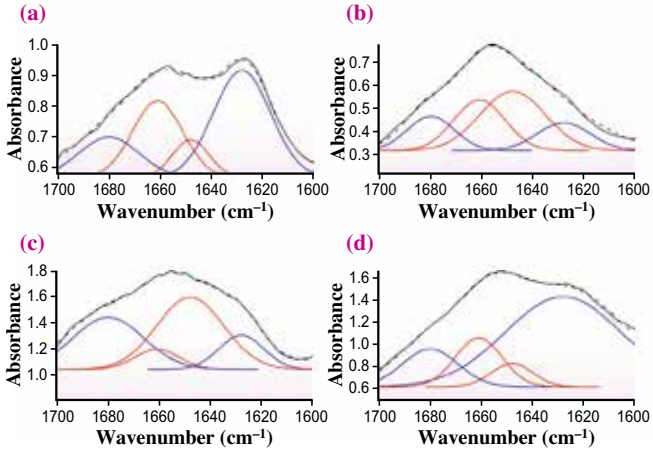

Fig. 2. FTIRM spectra (amide I region) obtained from **(a)** fibrils of α-syn expressed in *E. coli*, **(b)** normal brain tissue from the brain of a patient with PD, **(c)** the core of an LB, and **(d)** the halo of an LB (solid black lines). Blue and red lines represent the contributions of β-sheet structures and non-β-sheet structures (random coils, α-helices, and others), respectively. The dashed lines represent the fitted curves. Data were fitted using a Gaussian species model centered at 1628 cm^{-1}, 1680 cm^{-1} (β-sheets, blue line), 1648 cm^{-1}, and 1661 cm^{-1} (random coils, α-helices, and others, red lines.

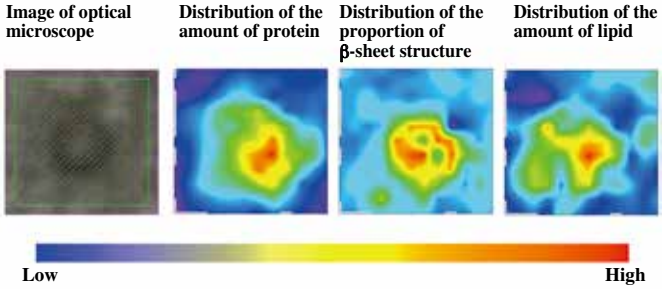

Fig. 3. Visible and FTIR images of typical LBs in the *substantia nigra* of the midbrain derived from the 83-year-old female PD patient. Shown from left to right are a microscope image, the amount of total proteins, the proportion of β-sheet structures, and the amount of lipids. The color bar indicates low (blue) to high (red) contents. The area shaded with green was scanned with 4 μm steps, 12 × 11 pixels = 48 × 44 $μm^2$.

Katsuya Araki[a,*], Naoto Yagi[b] and Hideki Mochizuki[a]

[a] Department of Neurology, Osaka University Graduate School of Medicine
[b] Japan Synchrotron Radiation Research Institute (JASRI)

*Email: araki@neurol.med.osaka-u.ac.jp

References

[1] K. Araki *et al.*: Sci. Rep. **6** (2016) 30473.
[2] K. C. Luk *et al.*: Science **338** (2012) 949.
[3] T. Iwatsubo *et al.*: Am. J. Pathol. **148** (1996) 1517.
[4] *K. Araki, N. Yagi, Y. Ikemoto, H. Yagi, C. Choong, H. Hayakawa, G. Beck, H. Sumi, H. Fujimura, T. Moriwaki, Y. Nagai, Y. Goto and H. Mochizuki: Sci. Rep.* ***5*** *(2015) 17625.*

Discovery of new bone calcium dissolution phenomenon: images of calcium exuding from bone captured for the first time using a high-sensitivity 3D X-ray microscope at SPring-8

Osteocytes extend the canaliculi in all directions and interconnect with each other. Osteocytes and bone canaliculi networks fill the inside of bones [1]. The bone remodeling process is thought to occur as follows. When a fracture occurs in a bone, osteocytes detect the fracture using canaliculi and then transmit signals to osteoblasts on the bone surface via the bone canaliculi to promote the differentiation of osteoclasts, which resorb bone and break down the damaged section. Osteoblasts are then formed to repair the bone resorption lacunae. It was previously thought that the main purpose of bone canaliculi networks was to transmit signals concerning bone repair and to supply nutrients.

The serum calcium concentration is maintained at a constant level (serum calcium homeostasis). Too much or too little serum calcium can pose vital risks. When a requirement for calcium arises in the body because of pregnancy or disease, the bone surface is broken down by osteoclasts that resorb bone and dissolve calcium. Only osteoclasts were previously thought to maintain the serum calcium concentration through bone resorption. However, the fact that an artificially created mouse model without any osteoclasts was able to survive suggests an alternative mechanism for homeostatic calcium maintenance. The process of supplying bone calcium through osteoclast activation has the disadvantage of weakening bone through repeated bone resorption because resorption takes a week but bone remodeling takes several months. Therefore, we investigated whether the serum calcium concentration can be maintained using osteocytes.

The tibial cortical bone of 4–14-week-old female mice was observed using a newly conceived Talbot-defocus multiscan X-ray microscope [2], which was constructed at the undulator beamline **BL20XU**, SPring-8. Because the beam radiated from SPring-8 is a strong parallel X-ray, it is possible to create a monochrome X-ray microscope. We assembled a 6 m microscope in order to achieve ×20 magnification with a pixel size of 0.2 μm. The specimen was rotated while the images were taken, and three-dimensional (3D) computed tomography (CT) revealed hundreds of osteocytes and bone canaliculi networks. The same site was observed using two different methods, and two types of highly sensitive, high-resolution 3D images over a wide field of view were produced (Fig. 1). Using Talbot phase contrast imaging [3], it was possible to differentiate the brightness of two points 1 μm apart. Using defocus phase contrast imaging [4], it was possible to produce clear 3D images of bone canaliculi of 0.2 μm diameter emerging from the osteocytes. It was also possible to differentiate the calcium concentration in the area surrounding the osteocytes and bone canaliculi networks by observing the same spot using the two different methods.

(1–1) We captured an image showing a phenomenon wherein bone calcium was depleted in a concentric manner over an area of approximately 4 μm width that surrounded the bone canaliculi extending from the osteocytes (Fig. 1(b) and Fig. 2). An image showing the phase parallel to the bone canaliculi revealed decreased calcium concentration in accordance with the canaliculi path (Fig. 1(b,d)).

(1–2) The area of bone was divided into an osteocyte/bone canaliculi zone with a decrease in calcium concentration surrounding the canaliculi (Fig. 1(a) zone L)), a zone with no change in calcium concentration (Fig. 1(a)-H)), and a zone midway between the two (Fig. 1(a)-M)).

(1–3) A cross-sectional image of the bone canaliculi showed a greater extent of bone loss near the center in almost all of the canaliculi, (red spots in Fig. 2).

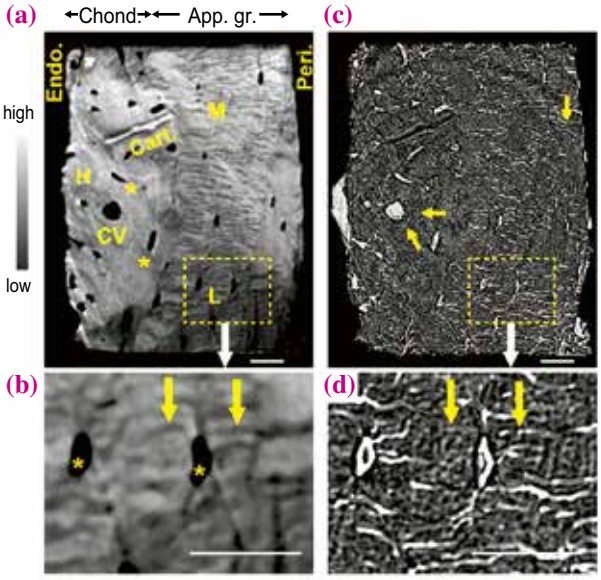

Fig. 1. Synchrotron X-ray tomographic images of tibial cortex in 4-week-old mice. **(a)** Degree of mineralization obtained by Talbot phase-contrast imaging. CV, capillary vessel. Asterisks, osteocytes. **(c)** Osteocytic lacunae and canaliculi observed by defocus phase-contrast imaging. Arrows, osteocyte canaliculi.**(b)** and **(d)** Enlargements of the rectangular areas in (a) and (c), respectively. Scale bars, 20 μm

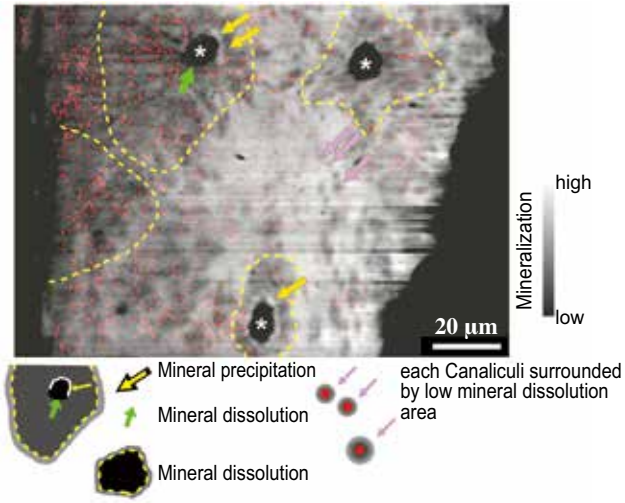

Fig. 2. Coronal section perpendicular to canaliculi. An overlaid image of the degree of mineralization, visualized by Talbot phase-contrast imaging (grayscale), and the canaliculi position, visualized by defocus phase-contrast imaging (red). Yellow dotted lines, low mineralization zone around osteocytes. Asterisks, osteocytes. Yellow arrows, perilacunar hypermineralization.

Osteocytes surrounded by a narrow area of calcium dissolution have high perilacunar mineralization at the edge (yellow arrows in Fig. 2). In contrast, osteocytes on the side with a decreased calcium concentration exhibited low perilacunar mineralization at the edge (green arrow in Fig. 2). It is thought that the H, M, and L zones in Fig. 1 reflect the progress of calcium dissolution.

Bone canaliculi were closely connected to capillary vessels and the bone surface (yellow arrows in Fig. 1(c)). It appears that serum calcium is supplied and deposited into bones via the bone canaliculi and that calcium is constantly being accumulated in bones by this mechanism. This suggests that the L zone was created as a result of bone dissolution by osteocytes after which calcium is replenished in the bone over a long period of time and that the accumulation and recovery of lost calcium occur. Therefore, it is conceivable that the high perilacunar mineralization in the H zone occurs when the calcium concentration increases (Fig. 3).

A study of different mouse bone specimens under different conditions demonstrated the following characteristics with regard to the bone calcium dissolution phenomenon next to the bone canaliculi [5]:
1 - The phenomenon was observed regardless of the age of the mice.
2 - The phenomenon was observed with Fos KO mice without osteoclasts. Osteocytes appear to dissolve calcium around bone canaliculi independent of osteoclasts.
3 - Calcium dissolution even occurred in many lactating mouse specimens.

On the basis of the above findings, it is conceivable that osteocytes and bone canaliculi networks are involved in bone mineral dissolution and storage and that this action is not accompanied by structural changes in bone tissue. Many drugs used in the treatment of osteopenia suppress bone resorption by osteoclasts, causing old bone to be left over, and the bones become frail. It is hoped that new methods of treatment without side effects can be developed by controlling bone dissolution, the formation of new bone, and the action of osteocytes without bone dissolution.

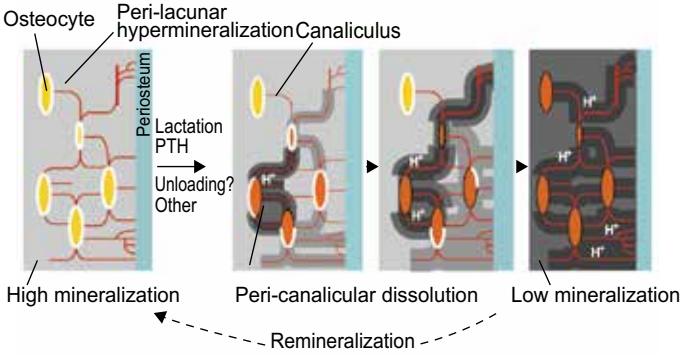

Fig. 3. Model of pericanalicular demineralization. Pericanalicular dissolution starts with a subset of osteocytes in high mineralization zones. Perilacunar hypermineralization is partially or totally lost as pericanalicular demineralization progresses, giving rise to larger zones of intermediate to low mineralization. Yellow ovals: osteocytes that do not direct demineralization. Red ovals: osteocytes directing pericanalicular demineralization. High mineralization zones are likely restored by remineralization.

Nobuhito Nango[a] and Atsushi Momose[b]

[a] Ratoc System Engineering Co., Ltd.
[b] Institute of Multidisciplinary Research for Advanced Materials, Tohoku University

*Email: nango@ratoc.co.jp

References

[1] L.F. Bonewald: J. Bone Miner. Res. **26** (2011) 229.
[2] N. Nango *et al.*: Biomed. Opt. Express **4** (2013) 917.
[3] Y. Takeda *et al.*: Appl. Phys. Express **1** (2008) 117002.
[4] A. Snigirev *et al.*: Rev. Sci. Instrum. **66** (1995) 5486.
[5] *N. Nango, S. Kubota, T. Hasegawa, W. Yashiro, A. Momose and K. Matsuo: Bone **84** (2016) 279.*

Imaging the increase in pulmonary blood flow at birth

Lung aeration at birth stimulates a significant increase in pulmonary blood flow (PBF). This process is essential for taking over the role of gas-exchange from the placenta, as well as restoring the left ventricle preload to maintain cardiac output that is lost following umbilical cord occlusion [1]. The pulmonary transition into neonatal life is influenced by a number of stimuli, with the entry of air and clearance of liquid from the airways acting as the primary trigger for this process [2]. This is mediated through a range of vasoactive and mechanical factors to decrease pulmonary vascular resistance (PVR) and rapidly increase PBF [3]. Although much research has focused on understanding this process, the suggested mechanisms have been based on the assumption that, at birth, air entry stimulates a local increase in PBF to promote ventilation/perfusion matching. This assumption was based on the well-established relationship between regional ventilation and perfusion in the adult lung, largely because until recently we have not had the technology to investigate this relationship at birth.

Examining the regional distribution of pulmonary dynamics non-invasively during this transition period can only be achieved by imaging. However, real-time imaging of regional pulmonary ventilation has been difficult due to the low density of lung tissue. Development of phase-contrast (PC) X-ray imaging not only allows imaging of the lungs with high temporal and spatial resolution, down to the smallest air sacs, but can be combined with simultaneous microangiography. Utilizing such techniques with the high brilliance and collimation of monochromatic synchrotron radiation as an X-ray source, provides a unique insight into changes with aeration and perfusion in the lungs at birth with exceptional detail. The regional relationships between lung aeration and the increase in PBF are not well known and indeed, our previous studies have shown that perfusion is not spatially related to lung aeration, as partial lung aeration triggers a global increase in PBF [4]. The vasoactive and mechanical factors that normally contribute to an increase in PBF were not expected to be active in unaerated lung regions, yet PBF appeared to increase regardless of local aeration. In this study, we sought to isolate the effect of local oxygenation in this process and further investigate the mechanisms regulating the increase in PBF at birth.

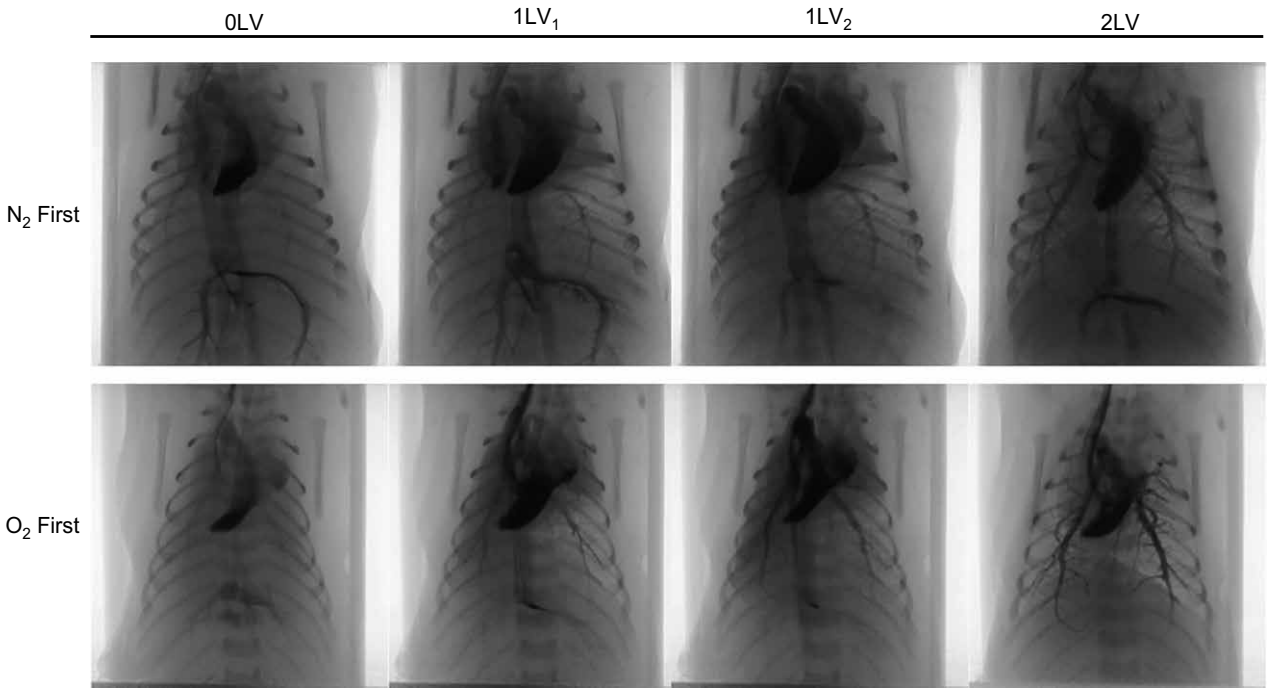

Fig. 1. Representative X-ray image sequences of newborn rabbits imaged prior to ventilation (0LV), following unilateral ventilation of the right lung ($1LV_1$) with either 100% N_2 or 100% O_2, subsequent ventilation with air (21% O2) in both kittens ($1LV_2$), and later ventilation of both lungs with air (2LV). Images were obtained 1–3 s following iodine bolus injection.

Simultaneous PC X-ray imaging and angiography was performed at SPring-8 **BL20B2** to compare aeration and perfusion in newborn rabbit kittens as previously described [4,5]. We imaged kittens first while the lungs remained unaerated and liquid filled, then with a single lung ventilated with either 100% N_2 (0% O_2), air (21% O_2) or 100% O_2. Kittens were further imaged with the ventilated gas switched to air, then with both lungs ventilated. We were able to demonstrate changes in PBF before and after ventilation of a single lung (Fig. 1). We consistently found that, in all parameters measured, the greatest change occurred between the pre-ventilation and the initial unilateral ventilation periods, with relatively minor changes occurring thereafter. This confirmed that partial lung aeration induces a widespread increase in PBF, which is mediated by a potent mechanism that is unrelated to oxygenation levels, as these changes occurred even following partial ventilation with 100% N_2. Perfusion of vessels rapidly increased and pulmonary transit time rapidly decreased in both lungs following aeration of a single lung (Fig. 2). These changes are indicative of downstream vasodilatation, vessel recruitment and an associated fall in PVR. Additionally, high oxygen concentration appeared to have an additive effect on pulmonary vasodilatation and PBF, which was localized to aerated lung regions. This suggests that there are a number of factors that work independently to increase PBF at birth.

In summary, PC imaging and microangiography can be utilized to demonstrate that partial lung aeration triggers a global increase in PBF, leading to a potential mismatch between pulmonary ventilation and perfusion. Furthermore, we show that a highly potent stimulus unrelated to oxygenation or local aeration can initiate these changes but is not fully explainable with our current knowledge of this process. We conclude that regionalized inhomogeneous aeration of the lung, as is common in preterm newborn infants during the onset of air breathing, may result in these widespread changes in PBF and occur regardless of inspired oxygen. The underlying mechanisms remain to be investigated, but could relate to a neural reflex as indicated by the rapid and global nature of PBF changes caused by air entry into the lungs.

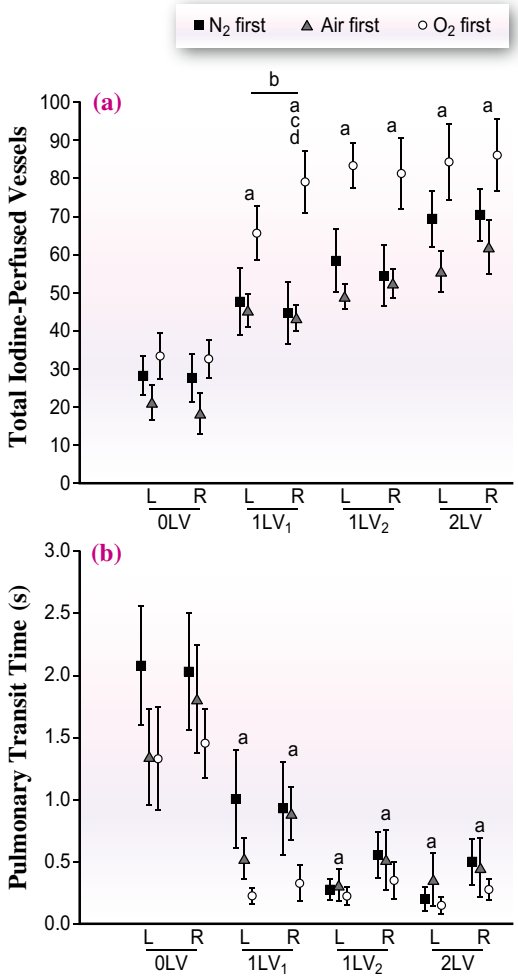

Fig. 2. **(a)** Mean iodine-perfused vessel number (±SEM) in the left and right lungs. **(b)** mean arterial transit time (s ± SEM) in the left and right lungs. Data shown are at each ventilation period (0LV, $1LV_1$, $1LV_2$ and 2LV) in N_2 first (solid squares), air first (crosses) and O_2 first (open circles) groups. [a]$P<0.05$ compared to baseline (0LV) in the same lung in the same group; [b]$P < 0.05$ left lung *vs.* right lung in O_2 first; [c]$P<0.05$ air first *vs.* O_2 first; [d]$P < 0.05$ N_2 first *vs.* O_2 first.

J. A. R. Lang[a], J. T. Pearson[b,c,d], M. J. Kitchen[e], and S. B. Hooper[a,*]

[a] The Ritchie Centre, Monash University, Australia
[b] Monash Biomedical Imaging Facility and Department of Physiology, Monash University, Australia
[c] Australian Synchrotron, Australia
[d] Department of Cardiac Physiology, National Cerebral and Cardiovascular Center Research Institute, Japan
[e] School of Physics and Astronomy, Monash University, Australia

*Email: stuart.hooper@monash.edu

References

[1] S. Bhatt *et al.*: J. Physiol. **591** (2013) 2113.
[2] Y. Gao and J. Raj: Physiol. Rev. **90** (2010) 1291.
[3] A. te Pas *et al.*: J. Pediatr. **152** (2008) 607.
[4] J. Lang *et al.*: J. Appl. Physiol. **117** (2014) 535.
[5] *J.A. Lang, J.T. Pearson, C. Binder-Heschl, M.J. Wallace, M.L. Siew, M.J. Kitchen, A.B. te Pas, A. Fouras, R.A. Lewis, G.R. Polglase, M. Shirai, S.B. Hooper: J. Physiol.* ***594*** *(2016) 1389.*

Formation process of superconducting phase of sulfur hydride with T_c ~203 K

At the end of 2014, a joint theoretical and experimental investigation broke the record for the superconducting critical temperature T_c by more than 30 K, reaching 203 K for hydrogen sulfide under a high pressure of above 100 GPa,which was the first increase in 20 years [1]. This material has two superconducting phases. One phase, called the "low-T_c phase", is obtained by compressing over 100 GPa at a low temperature of around 200 K, and exhibits T_c ~150 K at 200 GPa. The second phase, called the "high-T_c phase", exhibiting T_c ~203 K, appears upon annealing the low-T_c phase at room temperature. The material shows "conventional" superconductivity, which can be explained by Bardeen-Cooper-Schrieffer (BCS) theory, because of its strong isotope effect in the superconductivity of H_2S and D_2S. On the basis of this theory, Ashcroft proposed that metallic hydrogen and hydrogen-rich compounds will become high-T_c superconductors because hydrogen is the lightest element and thus has the highest phonon frequency ω_{ph} for a given value of T_c among the elements in the periodic table [2]. For metallization, an extremely high pressure will be required (a pressure above 400 GPa was predicted for pure hydrogen in recent theoretical work). However, hydrogen-rich compounds are expected to require a lower pressure. On the basis of this proposal, some hydride superconductors have been searched theoretically, but only silane (SiH_4) with T_c ~17 K has been observed experimentally so far.

H_2S has been theoretically predicted to have a relatively high T_c of ~80 K above 100 GPa compared with other hydrides [3]. This value is consistent with the experimentally observed superconductivity in the low T_c phase. However, T_c of ~200 K does not follow from this prediction. Around the same time as Ref. 1, a theoretical work proposed that high-pressure-synthesized H_3S will show superconductivity in its hexagonal and cubic structures under pressure [4]. In particular, the cubic structure was predicted to yield a high T_c of ~200 K by contribution from metallic hydrogen realized in this phase. Other stoichiometries of H_xS_y were further studied theoretically by different groups in numerous works. Most of the results supported the hypothesis that the high T_c is related not to H_2S but to H_3S in the cubic structure; H_2S is unstable at high pressures and should decompose to sulfur and higher hydrides, probably to H_3S ($3H_2S \rightarrow 2H_3S+S$). Thus, it was suggested that molecular H_2S decomposes to sulfur hydride with a higher content of hydrogen upon compression and annealing.

In order to elucidate the mechanism of the superconductivity and search for synthesize materials having a higher T_c towards achieving a room-temperature superconductor, the crystal structure of the superconducting phase and its phase diagram of sulfur hydride must be revealed. To investigate the formation process of the superconducting phases, we performed *in situ* X-ray diffraction (XRD), at the high-pressure beamline **BL10XU**, SPring-8 (Fig. 1) using a diamond anvil cell (DAC). At this beamline, simultaneous XRD, electrical resistance and Raman spectroscopy measurements can be performed at low temperatures in the upstream experimental hutch. For the generation of an extremely high pressure of over 100 GPa, a small sample chamber with a diameter of less than 50 μm is needed. For such a small chamber, a focused X-ray beam with a diameter of about 2 μm can be used in the downstream hutch. The DAC was used for the generation of high pressures. Hydrogen sulfide loaded in a small hole in a rhenium gasket was set on a pressure cell with electrodes (vapor-deposited gold or platinum on a diamond surface) for electrical resistance measurement. Pressurization, XRD, resistivity and Raman scattering measurements with the DAC can be performed at the same time in a Gifford-McMahon type refrigerator in the beamline. The first-order Raman spectra of the diamond anvil was measured using the on-line Raman spectroscopy system in the beamline for pressure determination.

H_2S is a gas under ambient conditions and is liquefied by cooling to around 200 K. After loading liquid H_2S into the sample chamber of the DAC, we pressurized H_2S to over 100 GPa in the cryostat while maintaining a low temperature of ~200 K, and then the cell temperature was increased to room temperature. From the *in situ* XRD measurements, we observed that the intensity of the diffraction peaks from the sample suddenly decreases upon cooling to 200 K and the peaks disappeared at pressures of around 20 GPa at 200 K. This also occurred

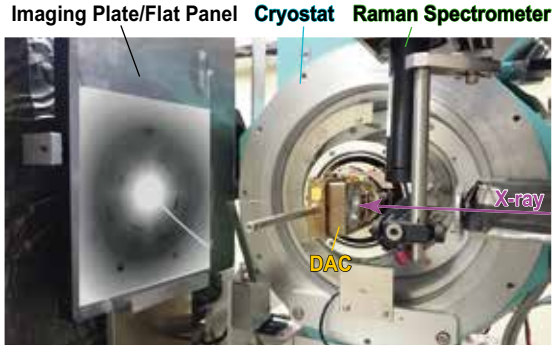

Fig. 1. Measurement system in the upstream-side chamber of BL10XU. X-ray diffraction, electrical resistance and Raman scattering measurements at low temperatures were performed at the same time.

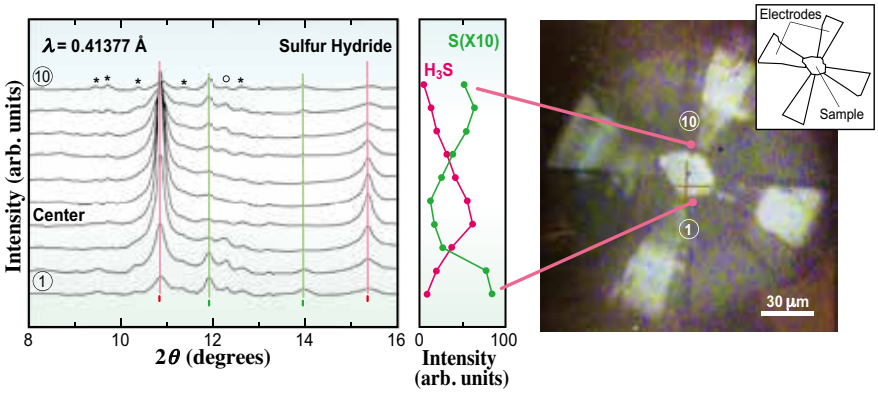

Fig. 2. XRD profiles of the sulfur hydride and pure sulfur along the line indicated in the image (150 GPa). The scanning was performed using an X-ray beam with a diameter of 2 μm from No. 1 to No. 10 shown in the photograph of the sample chamber. The red and green lines in the plots on the left indicate the reflections from cubic H_3S and β-Po sulfur, respectively. Open circles indicate the reflection possibly from the high-pressure phase IV of elemental sulfur. The reflections indicated by the asterisks (*) do not belong to the sample. The center graph indicates the position dependence of the intensity of the main peaks of H_3S and β-Po sulfur.

during compression to 150 GPa at 200 K and during heating to 256 K at around 150 GPa. A diffraction peak corresponding to the body-centered cubic (bcc) structure appeared from 260 K and its intensity was enhanced with increasing temperature up to room temperature. By using the X-ray scanning method with a focused synchrotron X-ray beam, the peaks of the obtained XRD profile of the high T_c phase were separated into the theoretically predicted cubic H_3S and the β-Po sulfur phase, which is the high-pressure phase of pure sulfur (Fig. 2). Raman scattering measurements elucidated that there were no hydrogen molecules in the sample chamber. Therefore, it is considered that H_2S lost its long-range periodic order as a result of low-temperature compression and dissociated into H_3S and elemental sulfur. It was also confirmed that the cubic H_3S is the high T_c phase from the electrical resistance measurements. However, the XRD measurements were only able to determine the positions of sulfur atoms because of the relatively weak scattering of X-rays by hydrogen atoms. As shown in Fig. 3, the theoretically predicted structures of the high T_c phase have the same bcc symmetry of the positions of sulfur atoms in both structures and the only difference is in the positions of the hydrogen atoms. However, electrical resistance measurements might allow us to distinguish these phases from the change in the pressure dependence of T_c around 150 GPa as shown by the dashed line in Fig. 3 [5].

In this article, the recent progress in the crystal structural investigation of the sulfur hydride system has been reported. The discovery of this high-T_c superconductor has accelerated technical advances and both experimental and theoretical research on superconductivity at pressure of over 100 GPa. It is expected that the novel experimental process (compression at low temperatures) for obtaining the high-T_c phase of sulfur hydride clarified in recent experiments will enable the high-pressure synthesis and further investigation of not only other hydrides but also new materials.

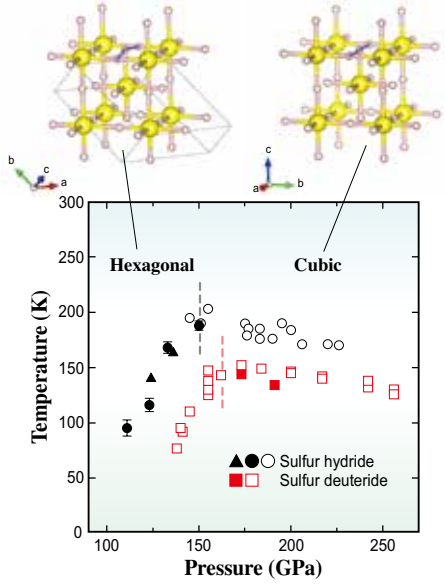

Fig. 3. Pressure dependence of T_c for high-T_c phases. Open circles and squares are from Ref. 1, and closed circles and squares are from Ref. 5. The dashed line indicates the phase boundary between the hexagonal and cubic structures shown at the top of this figure.

Mari Einaga

KYOKUGEN, Osaka University

Email: einaga@hpr.stec.es.osaka-u.ac.jp

References

[1] A.P. Drozdov *et al.*: Nature **525** (2015) 73.
[2] Y. Li *et al.*: J. Chem. Phys. **140** (2014) 174712.
[3] N.W. Ashcroft: Phys. Rev. Lett. **21** (1968)1748; Phys. Rev. Lett. **92** (2004) 187002.
[4] D. Duan *et al.*: Sci. Rep. **4** (2014) 6968.
[5] *M. Einaga, M. Sakata, T. Ishikawa, K. Shimizu, M.I. Eremets, A.P. Drozdov, Ivan A. Troyan, N. Hirao and Y. Ohishi: Nat. Phys.* ***12*** *(2016) 835.*

Atomic visualization of cleaved bimetal-intercalated graphite superconductor by photoelectron holography

Graphite intercalation compounds (GICs are old and new superconducting materials. The highest transition temperature (T_c) value for the GIC superconductors at ambient pressure is currently 11.5 K for CaC_6 [1]. Other than the confirmation of T_c at 65 mK for BaC_6 in 2015, the members of the GIC superconductor family have remained unchanged for many years. Recently, a new series of bimetal-intercalated graphite superconductors, $Ca_xK_{1-x}C_y$, has been successfully fabricated by a group at Okayama University [2]. As K and Ca atoms intercalated, a graphite flake became a golden superconducting compound (Fig. 1). The T_c of KC_8 was only 136 mK, but the introduction of a very small amount of Ca drastically increased this value. T_c for $Ca_xK_{1-x}C_y$ continuously increased to 11.5 K ($x = 1$; CaC_6) as x increased [2].

The direct visualization of three-dimensional (3D) atomic arrangements around intercalant atoms is essential to clarify the superconducting mechanism. X-ray diffraction is a standard method of determining bulk crystal structures, but it is not suitable for the local structure analysis of nonperiodic alloy compounds. Moreover, the cleaved surface of GICs is readily degraded by moisture and oxygen in the atmosphere. The local structure around the intercalant atoms of bimetal GIC superconductors has remained unclear.

Optical holograms are widely used in our daily lives as security devices on credit cards, for example. 3D structure information can be recorded in an optical hologram based on the wavelike nature of light. Similarly, the 3D atomic arrangement can be recorded using an electron wave [3]. A photoelectron wave emitted from an atom by X-ray excitation is partially scattered by the surrounding atoms. As a result, an interference pattern between direct and e waves, a *photoelectron hologram*, is formed. Photoelectron holography (PEH) is a powerful method for studying surface and subsurface atomic structures in 3D owing to the short probing depth of photoelectrons. Recently, we have developed a new holography algorithm, the scattering pattern-extraction algorithm (SPEA)-maximum entropy method (MEM) for reconstructing atomic arrangements [4]. In this method, the 3D images of atomic arrangements around a photoelectron emitter atom are directly obtained from element-specific holograms.

Photoelectron spectrum and hologram measurements were carried out [5] using a two-dimensional display-type analyzer installed at the circularly polarized soft X-ray beamline **BL25SU**, SPring-8. A superconducting $Ca_{0.11}K_{0.89}C_{7.1}$ sample ($T_c = 9.9$ K) has recently been prepared by Kubozono's group. We made a vacuum sample transfer system for transfer between Okayama and SPring-8 in order to prevent the degradation of the samples cleaved at the laboratory in inert Ar gas. The photoelectron spectra of this cleaved surface showed only C 1*s* and K 2*p* peaks, and the Ca 2*p* peak intensity was less than a few hundredths of that of the K 2*p* peak. The observation of the K dominant structure at the cleaved surface implies that Ca atoms are dispersed in the bulk and likely form high T_c domains.

Figures 2(a) and 2(b) show full-hemisphere C 1*s* and K 2*p* photoelectron holograms obtained at a kinetic energy of 600 eV. The incidence direction of the soft X-ray was aligned along the surface normal. From these holograms, we directly reconstructed atomic images from the few-layer region of the cleaved surface. Atomic images of the graphene were collected

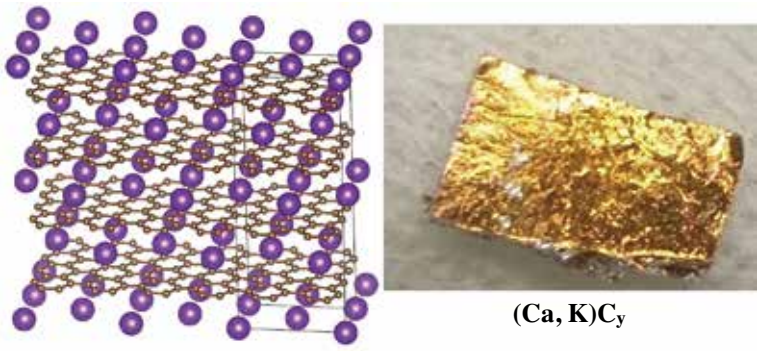

Fig. 1. **(a)** KC_8 crystal structure. **(b)** Photograph of $(Ca,K)C_y$ sample.

in the in-plane cross sections of the layers 3.3 Å and 5.7 Å above the photoelectron emitter C atom and the stacking structures were determined as *AB*- and *AA*-type, respectively. An intercalant metal atom layer was found between two *AA*-stacked graphenes. The K atomic image revealing 2 × 2 periodicity, occupying every second center site of C hexagonal columns, was reconstructed as shown in Figs. 2(c) and 2(d).

These observations revealed that the cleavage preferentially occurs at the K atom intercalated layers containing no Ca atoms, which are likely the most fragile part of the crystal sample. The most important result of the present study is that the cleaved surface does not always represent the average bulk structure. The structure and composition of the surface and the bulk can be substantially different, especially in a layered system. Special attention must therefore be paid when using surface-sensitive methods, such as photoelectron spectroscopy and scanning probe microscopy.

A surface phonon is often softened by bulk truncation, structure modification, and interaction with adsorbates. Recently, the superconductivity of In and Pb monoatomic layers and GIC and FeSe ultrathin films on surfaces has been discovered and has attracted substantial fundamental interest. The crystal sizes of newly developed functional materials are often very small and the densities of impurity atoms playing important roles are low. As mentioned above, PEH is one of the most effective methods for studying surface and subsurface atomic structures in 3D. Our technique for directly visualizing atomic arrangements by element-selective PEH is expected to be a powerful tool for developing new superconducting materials.

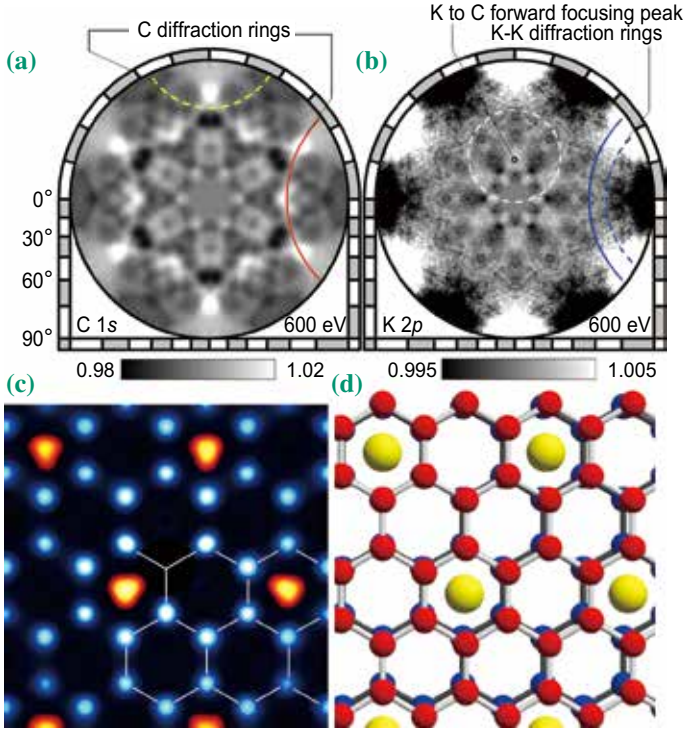

Fig. 2. **(a)** C 1*s* and **(b)** K 2*p* photoelectron intensity angular distributions (holograms) obtained from $(Ca,K)C_y$. Diffraction contrasts are indicated by gray scale. **(c)** Images showing atomic arrangements of C (blue) and K (orange) layers. **(d)** Structure model of the cleaved surface region of $(Ca,K)C_y$.

Fumihiko Matsui[a,*], Yoshihiro Kubozono[b] and Tomohiro Matsushita[c]

[a] Graduate School of Materials Science, Nara Institute of Science and Technology
[b] Research Laboratory for Surface Science, Okayama University
[c] Japan Synchrotron Radiation Research Institute (JASRI)

*Email: matui@ms.naist.jp

References

[1] N. Emery *et al.*: Phys. Rev. Lett. **95** (2005) 087003.
[2] H.L.T. Nguyen *et al.*: Carbon **100** (2016) 641.
[3] J.J. Barton: Phys. Rev. Lett. **61** (1988) 1356.
[4] T. Matsushita *et al.*: J. Electron Spectrosc. Relat. Phenom. **195** (2014) 365.
[5] *F. Matsui, R. Eguchi, S. Nishiyama, M. Izumi, E. Uesugi, H. Goto, T. Matsushita, K. Sugita, H. Daimon, Y. Hamamoto, I. Hamada, Y. Morikawa, Y. Kubozono: Sci. Rep.* ***6*** *(2016) 36258.*

Kagome lattice of oxygen in N_2-O_2 system

The purpose of our research is to study for new magnetic orders of the oxygen molecule O_2. O_2 is a molecular magnet with a magnetic moment of $2\mu_B$ perpendicular to the molecular axis. In the pressure-temperature (*P*-*T*) phase diagram of oxygen, rich polymorphism with a unique magnetic order arises from the magnetic interaction between O_2 molecules. We previously found a new solid phase in the pressure-composition phase diagram of the N_2-O_2 binary system [1]. This phase has a hexagonal structure and does not occur in pure O_2 or pure N_2. By Rietveld refinement (Fig. 1), we determined the structure of this phase to be a hexagonal lattice (*P*6/*mmm*) with seven molecules in the unit cell. In this structure (Fig. 2), the molecules occupy three different sites. Three molecules in the 6(*i*) site form a kagome lattice and their molecular axes are almost parallel to the *c* axis because of orientational ordering. Supporting evidence for the formation of the kagome lattice in O_2 has been obtained from other experimental results [1].

The spin kagome lattice is a fascinating system among the frustrated spin systems and its magnetic property has attracted much attention from many condensed-matter physicists. Therefore, our interest is focused on the hexagonal phase of the N_2-O_2 binary system because this phase is a promising candidate for the $S = 1$ kagome lattice system. In order to investigate the stability and magnetic property of the hexagonal phase, X-ray diffraction experiments and magnetic measurements were performed under high-pressure and low-temperature conditions. In the present work, the sample composition of N_2-48 mol% O_2 was adopted because for this composition the hexagonal phase is stable in a wide pressure range [1]. Powder X-ray diffraction experiments were conducted using an angle-dispersive method with a DAC at SPring-8 **BL10XU**. Magnetization measurements were performed using the MPMS and a pencil-type DAC.

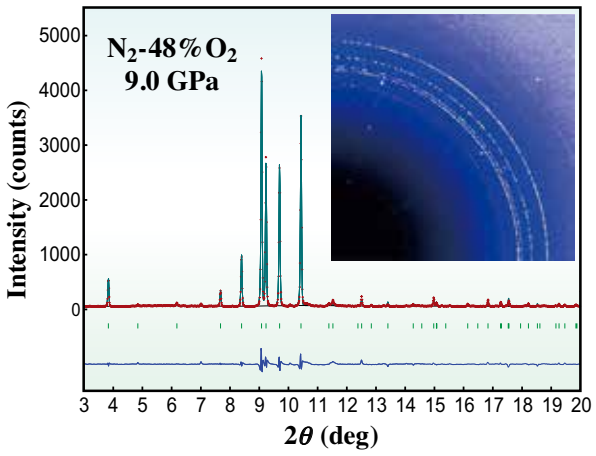

Fig. 1. Diffraction pattern and image of the hexagonal phase of 48%O_2 sample at 9.0 GPa. By Rietveld analysis, the pattern was well explained as a structure model of S.G.: *P*6/*mmm*.

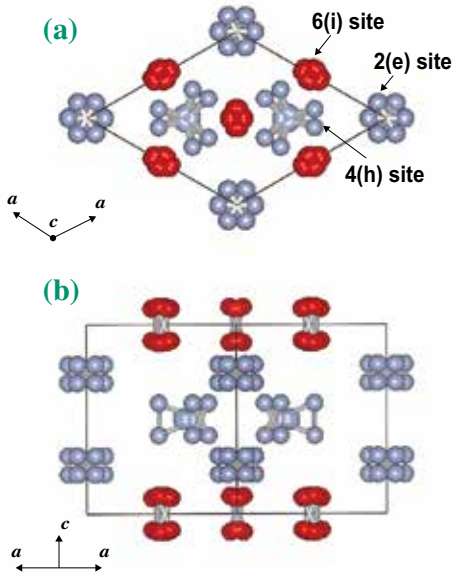

Fig. 2. Structural model of the hexagonal (*P*6/*mmm*) phase, showing views from the *c* axis **(a)** and the [110] direction **(b)**. The rotational disorder of molecules was simulated by placing 1/8 or 1/12 atom into the 24(*r*) site for each molecule. Molecules in the 6(*i*) site (colored in red) form a kagome lattice in the *c* plane, and their molecular axes are almost parallel to the *c* axis because of the orientational order, while molecules in the other sites (colored in gray) are freely rotating.

From the X-ray diffraction experiments, we obtained the phase diagram shown in Fig. 3(a) [2]. Upon cooling to 90 K at a low pressure of 1 GPa, the fluid phase transformed to the hexagonal phase via the well-known hcp phase of β-N_2 and the cubic (*Pm*3*n*) phase of γ-O_2 or δ-N_2. Upon further cooling, the hexagonal phase transformed to a monoclinic phase at 60 K. At 3 GPa, each transition temperature was increased. Above 4 GPa, the hexagonal phase (*P*6/*mmm*) transformed to an orthorhombic phase prior to its transformation to the monoclinic phase. The hexagonal-to-orthorhombic phase transition was second-order-like and was indicated by the broadening of the diffraction lines.

The phase diagram suggests that the hexagonal phase with the kagome lattice is stable in a relatively wide temperature and/or pressure range. The β phase ($R\bar{3}m$) of pure oxygen, which consists of a spin triangular lattice, also transforms into a monoclinic or orthorhombic phase at a low temperature to eliminate the geometrical frustration.

Structure analyses were conducted for patterns of the orthorhombic and monoclinic phases [2]. The unit cell of the orthorhombic phase is derived from an orthorhombic deformation of the hexagonal phase and is equivalent to a twofold hexagonal phase unit cell. From classical molecular dynamics (MD) simulations and Rietveld refinement, the phase was explained as the *Cmmm* space, the molecular axis of O_2 was almost parallel to the *c* axis, and the N_2 molecules were in a state of rotational disorder. These facts suggest that the transition to the orthorhombic phase is not driven by the ordering of the rotational motion of molecules. The structure of the monoclinic phase was also analyzed by the same process. An MD simulation at 10 K indicated orientational ordering for not only O_2 but also N_2 molecules. The $P2_1/a$ space group accounted for the results of the simulation. The results of the Rietveld refinement suggest that the diffraction pattern is due to the monoclinic $P2_1/a$ phase. The transition to the monoclinic phase may result from the ordering of the rotational motion of N_2 molecules. The transition from the hexagonal phase to the monoclinic phase was accompanied by a distortion of the kagome lattice.

Figure 3(b) shows the representative temperature changes of the magnetic susceptibility χ of the sample [2]. At a low temperature, χ shows a sudden drop. The onset temperature T_A of the drop is 38 K at 0 GPa and increases with increasing pressure. The estimated reduction of χ, $\Delta\chi$, is 58.1×10^{-6} emu/g and decreases with increasing pressure. The behavior of χ suggests a change in the magnetic property of the sample such as a transition to an antiferromagnetic state. It was found that the magnetic anomaly at 1 GPa corresponds well to the cubic-hexagonal phase transition. Therefore, the anomaly should be due to the structure phase transition. The results suggest that the hexagonal phase has a specific magnetic ordered state, arising from the molecular magnetic moment of O_2. These results provide evidence for the formation of the kagome lattice in O_2 in the hexagonal phase.

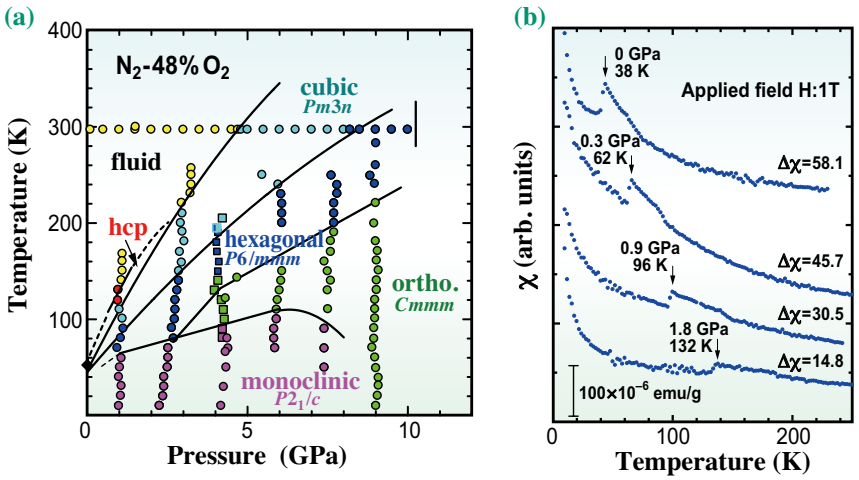

Fig. 3. **(a)** Pressure-temperature phase diagram of N_2-48 mol% O_2 sample. Circles and squares correspond to cooling and heating cycles, respectively. **(b)** Representative temperature changes in the sample magnetic susceptibility χ.

Yuichi Akahama[a,*] and Hiroshi Fujihisa[b]

[a] Graduate School of Material Science, University of Hyogo
[b] National Institute of Advanced Industrial Science and Technology

*Email: akahama@sci.u-hyogo.ac.jp

References

[1] Y. Akahama *et al.*: J. Phys. Conf. Series **500** (2014) 182001.

[2] *Y. Akahama, D. Ishihara, H. Yamashita, H. Fujihisa, N. Hirao, Y. Ohishi: Phys. Rev. B* ***94*** *(2016) 064104.*

Visualization of magnetic domain formation in neodymium magnet via scanning hard X-ray nanoprobe

Many kinds of magnets support modern life. Among them, neodymium magnet ($Nd_2Fe_{14}B$; abbreviated to Nd-Fe-B) is one of the most useful because it is the strongest permanent magnet currently available. This material has been applied to various products including high-efficiency electric motors for low-emission hybrid/electric vehicles, energy-saving air conditioners, and electric power generators. This powerful magnet is regarded as vital for achieving a green society. To further improve the energy-saving performance of high-power motors, an alternative permanent magnet that can maintain superior performances even at high temperatures is still desired. In other words, it is necessary to develop a new magnetic material that has an increased maximum energy product, $(BH)_{max}$, or an enhanced coercive field. Understanding the mechanism of the magnetization reversal process of permanent magnets will be a key to achieving this because the coercivity value is related to the reversal mechanism. A Nd-Fe-B magnet is produced by sintering fine grains with diameters of a few micrometers. As a result, the material has an inhomogeneous microstructure, which is likely the origin of the high coercivity of Nd-Fe-B sintered magnet. To clarify the relation between the microstructure and the magnetic properties, microscopic observation of the chemical and magnetic states is essential.

A scanning hard X-ray nanoprobe is one of the most promising techniques for the microscopic observation of sintered magnets. The technique at SPring-8 **BL39XU** [1,2] enables magnetic and chemical imaging with a spatial resolution of 100 nm under high magnetic fields of up to 22 kOe. Additionally, this X-ray nanoprobe allows the observation of uneven surfaces, such as the fractured surface of the bulk of a sintered magnet. This feature is a major advantage over other magnetic microscopy techniques such as Kerr microscopy, Lorentz transmission electron microscopy, and scanning transmission soft X-ray microscopy, which are only applicable to optically flat or polished surfaces or very thin specimens.

In this study, we used the scanning hard X-ray nanoprobe to visualize the formation process of magnetic domains at the fractured surface of a Nd-Fe-B sintered magnet during the demagnetization cycle [2]. In addition to the magnetic imaging, we performed X-ray fluorescence (XRF) microscopy measurement of the sample to discuss the correlation between the elemental distribution and the magnetic properties. Figure 1(a) shows a scanning electron microscopy (SEM) image of the fractured surface of a $Nd_{14.0}Fe_{79.7}Cu_{0.1}B_{6.2}$ magnet. Approximately 20 grains with diameters of ~5 μm can be seen at the fractured surface, where the microstructures are almost conserved as the bulk state. Figures 1(b–d) show XRF images of the same area as the SEM image in Fig. 1(a). The scan step was 250 nm for all images. The SEM and XRF images were obtained with no magnetic field. In the XRF images, elemental distributions of (a) Fe, (b) Nd, and (c) Cu are reproduced. The $Nd_2Fe_{14}B$ main-phases with a high Fe concentration and Nd-rich phases adjacent to the $Nd_2Fe_{14}B$ main-phase grains are clearly resolved. Cu is distributed non-uniformly at the boundaries of the $Nd_2Fe_{14}B$ main-phase grains. Areas of high Cu concentration are found adjacent to the Nd-rich regions at the triple junctions. By local X-ray absorption spectroscopy (XAS) analysis at the Cu *K* edge, the chemical state of the segregated Cu was determined to be an alloy with Nd [2].

Figures 2(a–g) show scanning XMCD images of magnetic domain structures whose magnetization directions are parallel to the crystallographic *c*-axis (perpendicular to the surface). A nanofocused and circularly polarized X-ray beam was scanned over a 15×15 μm² area corresponding to the middle parts of

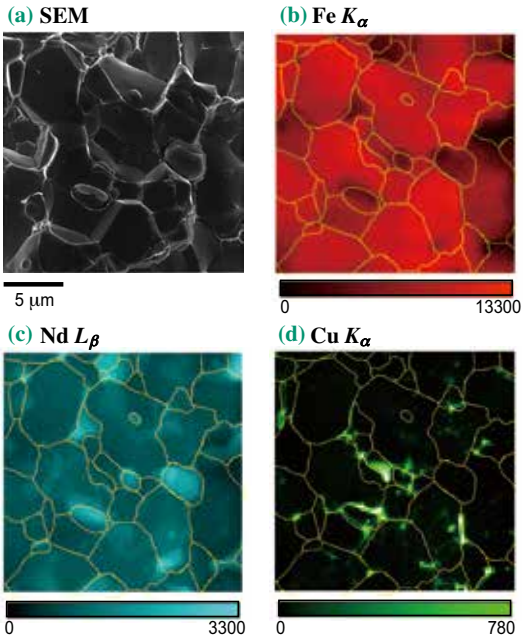

Fig. 1. **(a)** Scanning electron microscopy (SEM) image and scanning X-ray fluorescence images of **(b)** Fe, **(c)** Nd, and **(d)** Cu obtained at the fractured surface of a $Nd_{14.0}Fe_{79.7}Cu_{0.1}B_{6.2}$ sintered magnet. Horizontal color scales indicate the X-ray fluorescence intensity counted per 0.1 s.

the XRF images shown in Figs. 1(b–d), and the XMCD signals at the Nd L_2 edge (6.725 keV) were recorded by the fluorescence mode using a four-element silicon drift detector. The scan step was 300 nm and the acquisition time was 0.8 s per pixel (0.4 s each for left- and right-circular polarization). The resulting magnetic images clearly demonstrate the creation of the initial magnetic domains followed by the expansion of domain structures in a grain-to-grain manner with increasing demagnetization field.

The evolution of magnetic domains in the magnetization reversal process was found to proceed in the following steps: i) nucleation of initial multiple domains in particular grains; ii) expansion of reversed magnetic domains inside the grains by domain wall motion; and iii) propagation of reversal domains to the neighboring grains across the grain boundaries by intergranular exchange coupling. Furthermore, we confirmed that the formation of the magnetic domain structures is reproducible. In another demagnetization cycle, the domain evolution process was similar to the previous one. The initial reversed domains were created in the same grains with almost identical patterns. The subsequent domain extension process occurred in a similar manner. This result suggests the presence of particular nucleation sites that trigger the reversal of magnetization in the Nd-Fe-B sintered magnet.

By comparing the magnetic domain images in Figs. 2(a–g) and the XRF image of Cu in Fig. 1(d) and by performing statistical analyses, the magnetization reversal in $Nd_2Fe_{14}B$ grains adjacent to the segregated Cu tends to occur earlier than that of the other grains apart from the Cu grains. This suggests that the microstructures in the region around the Nd-rich phase with segregated Cu play a key role in determining the magnetic nucleation sites. Please refer to Ref. 2 for a detailed discussion.

In summary, magnetic imaging by a scanning hard X-ray nanoprobe is a novel technique for studying the correlation between the chemical microstructure and the magnetic domain structures of permanent magnets and their evolution processes. The element specificity provided by this technique will be useful for studying other varieties of magnet that have microstructures with characteristic elemental distributions. Another scanning soft X-ray nanoprobe has recently been developed at SPring-8 **BL25SU** [3,4], which will provide opportunities for magnetic microscopy with higher magnetic image contrast for 3*d* transition metals, such as Fe, with a superior spatial resolution, as well as novel sample environments with strong magnetic fields as high as 80 kOe.

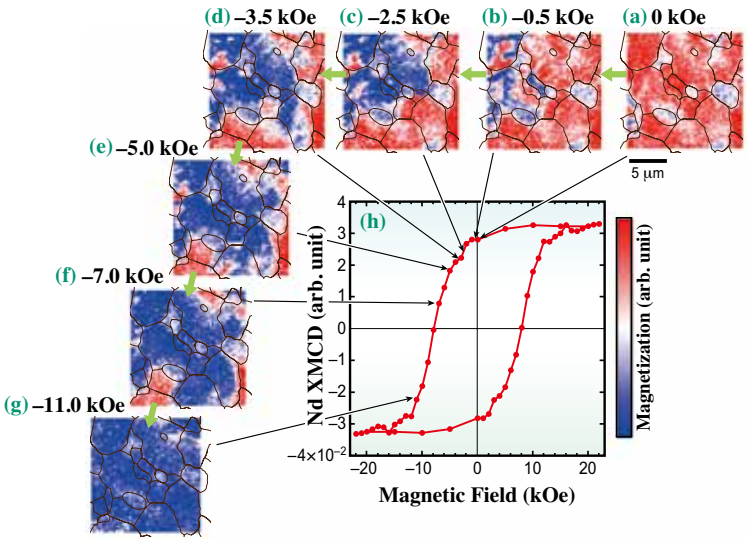

Fig. 2. **(a)–(g)** Magnetic domain structures at the fractured surface of a $Nd_{14.0}Fe_{79.7}Cu_{0.1}B_{6.2}$ sintered magnet as a function of external magnetic field. The magnetic images were obtained in a demagnetization cycle at various field points indicated on the magnetic hysteresis loop in **(h)**.

Motohiro Suzuki

Japan Synchrotron Radiation Research Institute (JASRI)

Email: m-suzuki@spring8.or.jp

References

[1] M. Suzuki *et al.*: J. Phys. Conf. Ser. **430** (2013) 012017.
[2] *M. Suzuki, A. Yasui, Y. Kotani, N. Tsuji, T. Nakamura and S. Hirosawa: Acta Mater.* ***106*** *(2016) 155.*
[3] D. Billington *et al.*: TMS 2017 Annual Meeting and Exhibition, Feb. 26 - Mar. 2, 2017, San Diego USA.
[4] Y. Shiratsuchi *et al.*: AIMS Materials Sci. **2** (2015) 484.

What is the nature of the magnetic state in a photo-doped Mott insulator?

A central aim of condensed matter physics is to tune materials' properties in order to achieve new functionalities or to optimize existing functionality. Historically this has typically been accomplished using chemical substitution. Laser excitation now offers an exciting alternative method, with the advantage that the resulting states are tunable and reversible [1]. There are even reports of transient control of high temperature superconductivity in complex oxide materials [2]. So far, however, efforts to controllably access and refine the properties of new transient states with lasers have been held back by difficulties in probing the momentum and energy dependence of the electronic and magnetic correlations characterizing these states.

We recently made the first implementation of time-resolved resonant inelastic X-ray scattering (tr-RIXS) exploiting the ultrafast and highly brilliant X-ray pulses available at the SPring-8 Angstrom Compact free electron LAser (SACLA) and the Linear Coherent Light Source (LCLS) [3]. This technique was used to measure the nature of the magnetic state in the layered antiferromagnetic Mott insulator Sr_2IrO_4 after we "photo-doped" the material with a laser pulse designed to excite carriers across the insulating gap. We found that the non-equilibrium magnetic state, 2 ps after the excitation, exhibits strongly suppressed long-range magnetic order, but hosts photo- carriers that induces strong, non-thermal magnetic correlations. These two-dimensional (2D) antiferromagnetic correlations recover within a few picoseconds, whereas the three-dimensional (3D) long-range magnetic order restores on a fluence-dependent timescale of a few hundred picoseconds. These dramatically different timescales suggest that measuring the dimensionality of magnetic correlations will be vital for our efforts to understand ultra-fast magnetic processes and that tr-RIXS represents a very powerful new tool for this endeavor.

Figure 1 outlines our approach. Photo-excitation is achieved by visible 620 meV (2 μm) infrared photons incident on the sample. X-ray pulses with an energy of 11.215 keV then come in and are scattered from the Sr_2IrO_4 sample. This particular X-ray energy corresponds to a resonance in which an Ir 2*p* core electron is promoted into the Ir 5*d* valance band before an electron in a different valence state fills the core hole and an X-ray photon is re-emitted. Due to the properties of the core hole, this process is sensitive to the magnetic correlations [4] of the Ir spins. Elastic measurements of the scattered X-ray photons access the magnetic Bragg peak, which is primarily sensitive to the presence or absence of 3D antiferromagnetic order. We also implemented a spectrometer in order to energy-resolve the scattered photons and access the magnetic excitations that, due to the very weak interlayer magnetic coupling, provide information about the 2D magnetic correlations.

Our magnetic Bragg peak measurements at SACLA **BL3** are plotted in Figs. 2(a) and 2(b). Upon photo-excitation magnetic order is suppressed faster than 300 fs (the time resolution of our experiment). For fluences above 6 mJ/cm^2, 3D magnetic order is destroyed almost entirely. The magnetic recovery then occurs on two time-scales: partial recovery starts in a few ps; but complete recovery takes somewhere between 100 to several thousand ps [3].

We then used tr-RIXS to investigate the nature of the 2D correlations in the transient state, choosing a pump fluence of 6 mJ/cm^2 in order to destroy the 3D magnetic order. Figure 2(c) plots the RIXS spectra at a momentum transfer of Q = (π, 0), which is sensitive to nearest-neighbor correlations along the Ir-O-Ir bond direction. We find essentially the same spectra before and after photo-excitation proving for the first time that 2D magnetic correlations exist in the transient state, despite the suppression of 3D magnetic order. We then examined Q = (π, π) (Fig. 2(d) and 2(e)), which is sensitive to small 2D fluctuations of the antiferromagnetic order. These 2D magnetic correlations recover on a ps timescale. With this in mind, we reexamined the magnetic Bragg peak measurements and found that all the data could be fit

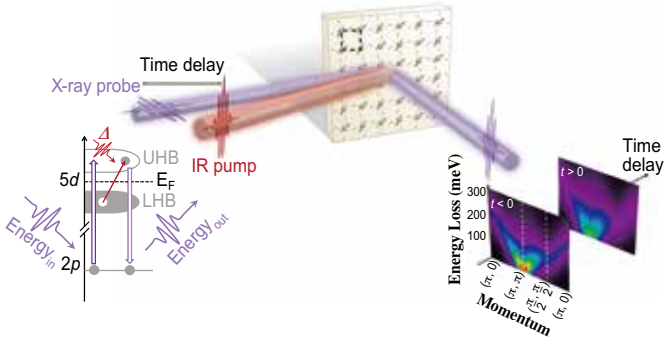

Fig. 1. An illustration of the experimental setup. Photo-excitation, depicted in red, drives electrons across the Mott gap of Sr_2IrO_4. X-rays, shown in purple, are sensitive to magnetism via the Ir *L*-edge resonant scattering cross-section. By measuring the scattered X-rays as a function of energy loss, momentum-transfer and time delay, we can infer the time-dependent magnetic correlations in the transient state. The RIXS planes plot simple spin-wave calculations based on an increased thermal population of magnons after the pulse.

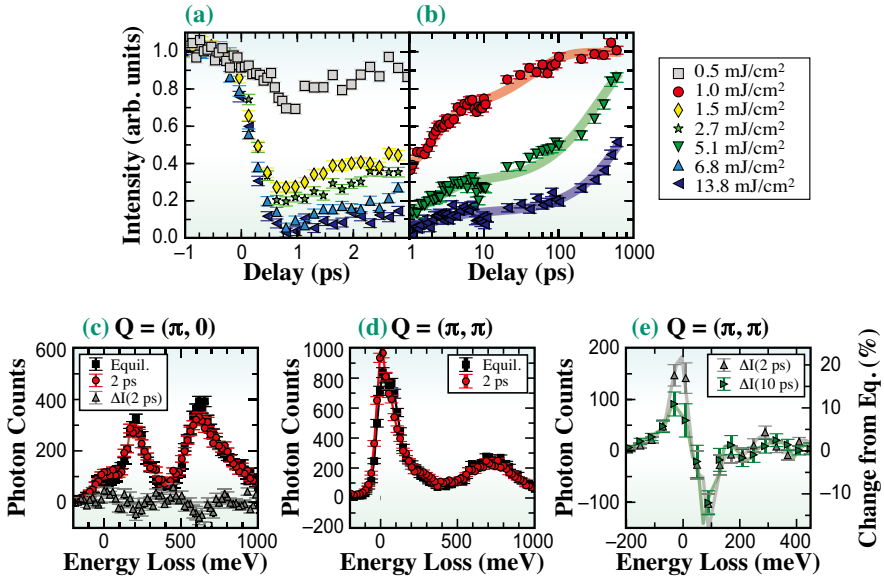

Fig. 2. **(a, b)** Measurements of the magnetic Bragg peak intensity, which is sensitive to the 3D antiferromagnetic order, as a function of time delay after photo-doping at different fluences. A fast suppression is followed by a two-stage recovery. **(c)-(e)** RIXS spectra at different Q points before and after photo-doping at 6 mJ/cm^2. (c) The spectrum at (π, 0) indicating that 2D nearest neighbor magnetic interactions recover faster than 2 ps after photo-doping. Data at (π, π) are shown as total spectra (d) and difference spectra (e).

with a two-timescale recovery function (colored lines in Fig. 2(a) and 2(b)) with one fast (ps) timescale and one slow timescale from 100–1000 ps that we associate with 2D and 3D correlations respectively.

Figure 3 plots the dependence of the correlation time scales on the pump fluence. 2D correlations depend weakly on the fluence, changing from 1.5 ps at 0.5 mJ/cm^2 to 2 ps at 13.8 mJ/cm^2. Meanwhile 3D correlations are much slower with a timescale that varies roughly linearly with fluence up to 1,130 ps at 13.5 mJ/cm^2. After magnetic order is destroyed the 2D correlations recover over a few ps. As the 2D magnetic recovery is weakly dependent on the fluence, this process is likely controlled by the strength of intrinsic interactions (such as the magnetic exchange constant of 60 meV). The correlated Ir-O planes then develop inter-plane 3D correlations over hundreds of ps. Since this timescale is linear in fluence, we assume that this process is governed by the timescale over which spins can dump their excess energy into the lattice in order to evolve back towards the ground state.

A full understanding of magnetism in transient states requires studying both 2D and 3D correlation. Tr-RIXS is a uniquely powerful way to access these states on ultra-fast timescales and is therefore likely to play an important role in understanding and manipulating the properties of complex oxides with light.

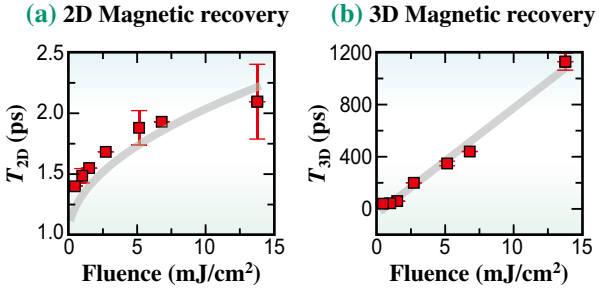

Fig. 3. **(a)** Fluence-dependent magnetic recovery timescales for the 2D correlations and **(b)** the 3D correlations.

M. P. M. Dean[a,*], Y. Cao[a], X. Liu[b] and J. P. Hill[c]

[a] Department of Condensed Matter Physics and Materials Science, Brookhaven National Laboratory, USA
[b] Beijing National Lab. for Condensed Matter Physics and Institute of Physics, Chinese Academy of Sciences, China
[c] National Synchrotron Light Source II (NSLS-II), Brookhaven National Laboratory, USA

*Email: mdean@bnl.gov

References

[1] J. Zhang & R.Averitt: Annu. Rev. Mater. Res. **44** (2014) 19.
[2] D. Fausti *et al.*: Science **331** (2011) 189.
[3] *M.P.M. Dean, Y. Cao, X. Liu, S. Wall, D. Zhu, R. Mankowsky, V. Thampy, X.M. Chen, J.G. Vale, D. Casa, J. Kim, A.H. Said, P. Juhas, R. Alonso-Mori, J.M. Glownia, A. Robert, J. Robinson, M. Sikorski, S. Song, M. Kozina, H. Lemke, L. Patthey, S. Owada, T. Katayama, M. Yabashi, Y. Tanaka, T. Togashi, J. Liu, C.R. Serrao, B.J. Kim, L. Huber, C.-L. Chang, D.F. McMorrow, M. Först and J.P. Hill: Nat. Mater.* ***15*** *(2016) 601.*
[4] L.J.P. Ament *et al.*: Rev. Mod. Phys. **83** (2011) 705.
[5] J. Kim *et al.*: Phys. Rev. Lett. **108** (2012) 177003.

Nanoscale structural rearrangement in the doped polar semiconductor $Ge_{1-x}Mn_xTe$

GeTe is an intriguing semiconductor exhibiting a huge variety of properties. The system solidifies around 730°C in a cubic structure. Upon cooling through approximately 430°C the unit cell distorts and a rhombohedral polar structure is realized, making GeTe one of the simplest ferroelectric compounds. A sketch of both unit cells superimposed in the pseudocubic setting of GeTe is shown in Fig. 1.

In spite of its classification as a semiconductor, it has a metallic resistivity with charge-carrier concentrations of the order of 10^{21} cm^{-3} thanks to unintentionally self-doped holes due to Ge vacancies. GeTe features a multivalley band structure which is responsible for the emergence of superconductivity and its role in thermoelectric devices. GeTe-related materials are also known for their phase-change memory functionality as it is utilized, e.g., in digital versatile disks (DVD). In the latter, light- / heat-pulses are used to switch the structure of the device locally between amorphous and crystalline back and forth. Here we report a magnetic analogue of this effect: Upon Mn doping GeTe becomes ferromagnetic [1] and we successfully demonstrated that as long as the system remains rhombohedral, there are two different magnetic phases as shown in the phase diagram in Fig. 2 [2]. Therein the ferromagnetic transition temperature T_c is plotted against the Mn concentration x (see Ref. 2 for details). Which magnetic phase is realized depends on the heat treatment: Slow controlled cooling ("cc") from the melt establishes a ferromagnetic phase with high ferromagnetic transition temperatures T_c up to ~180 K, while quenching ("q") from 620°C, i.e., from the cubic phase, yields T_c values which are a factor of five to six smaller around the maximum of the dome-like high-T_c phase line in Fig. 2. Upon further increasing the Mn concentration, the polar distortion of the unit cell is more and more suppressed. The heat-treatment effect disappears when the Mn doping concentration becomes sufficiently large to realize cubic crystalline symmetry even at low temperatures. As it will be discussed below, this is not a sharp structural phase transition but rather a crossover. This structural transition range is indicated in gray in Fig. 2.

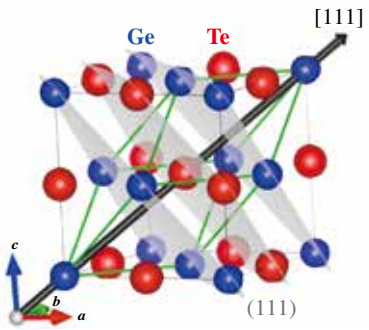

Fig. 1. Sketch of the structure of $Ge_{1-x}Mn_xTe$: The high-temperature cubic (rock-salt type) and the low-temperature rhombohedrally-distorted structures of GeTe are superimposed in its pseudo-cubic setting. The Ge and Te atoms are shown in blue and red, respectively. The gray layers are the crystallographic (111) planes and the black arrow indicates the direction of polar distortion, i.e., the cubic [111] direction.

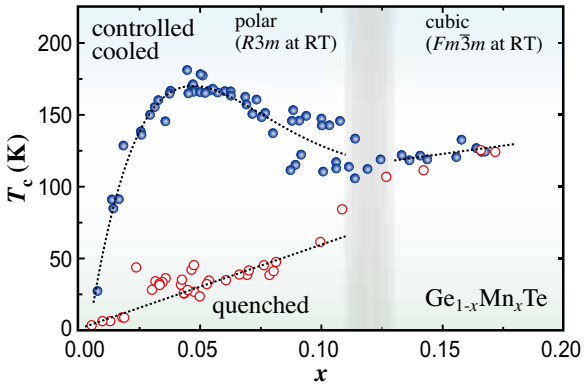

Fig. 2. Magnetic phase diagram of $Ge_{1-x}Mn_xTe$: The ferromagnetic transition temperature T_c is plotted vs the Mn concentration x. The filled blue symbols give the ferromagnetic T_c of controlled-cooled, the open red symbols of quenched samples. The gray shaded area indicates the structural crossover x range where the structure changes doping-induced from rhombohedral to cubic even at low temperatures. Dotted lines are guides to the eyes.

Apparently the rhombohedral distortion is essential for the observation of these two distinct ferromagnetic phases. To gain insight how the two different heat-treatment recipes affect the structure of $Ge_{1-x}Mn_xTe$, we measured various samples throughout the phase diagram at SPring-8 **BL44B2**. An analysis of the high-resolution synchrotron XRD patterns in combination with EDX measurements revealed (see Ref. 2), that quenched low-T_c samples exhibit a comparably homogeneous Mn distribution throughout a sample while controlled-cooled high-T_c samples are characterized by strong Mn inhomogeneity and the formation of Mn-rich regions. Exemplarily, XRD data on a magnified view of the cubic 220_c reflection around $2\theta \approx 13.5°$ are shown for four selected samples in Figs. 3(a) and 3(b): (a) x = 0.050, T_c = 24 K, "q" (red data) and x = 0.047, T_c = 171 K, "cc" (blue data); (b) x = 0.166, T_c = 125 K, "q" (red) and x = 0.164, T_c = 127 K, "cc" (blue). The big difference between quenched and controlled-cooled rhombohedral samples is that quenched samples exhibit rather sharp

reflections as seen in Fig. 3(a). The two peaks in the red data are identified as the 104_h and 110_h reflections (in hexagonal setting) as expected for rhombohedral GeTe. In contrast, the 104_h reflection of the similarly doped controlled-cooled sample shown in blue in Fig. 3(a) has split into two peaks of lower intensity. There is also a shoulder visible around $2\theta \approx 13.5°$ and the 110_h peak has broadened as compared to the data of the quenched sample. The 104_h reflection contains information about the degree of the rhombohedral distortion, i.e., a broadening or even splitting of this reflection indicates that the degree of the rhombohedral distortion changes throughout the sample. We interpret this as an indication of the formation of different domains in controlled-cooled samples which obey the same global rhombohedral symmetry but exhibit varying distortion angles. For simplicity we assume here only two differently distorted domains labeled "*R*1" and "*R*2" in Fig. 3(a). The domain *R*1 is assumed to be strongly distorted and hence the corresponding XRD reflection is seen at a lower angle. This domain does not contain much Mn dopants and is similar to pristine GeTe. On the other hand, *R*2 is only weakly distorted and consists of the aforementioned Mn-rich regions.

As for the data of the quenched and controlled-cooled samples with larger Mn concentrations shown in Fig. 3(b), there is only one sharp peak visible for each of them (again red data was taken on a quenched, blue data on a controlled-cooled sample). Both samples are cubic and the respective 220_c reflections are comparable, i.e., there is no clear difference in the XRD patterns any more between controlled-cooled and quenched samples.

The underlying mechanism here is a spinodal decomposition. When cooling a sample which is rhombohedral at room temperature in a controlled and slow manner from its cubic high-temperature phase, the Mn ions agglomerate and form the weakly distorted phase fractions *R*2. The latter are several 10 nm in diameter and as discussed in more detail in Ref. 2, *R*2 is responsible for the emergence of the high-T_c phase. The clustering leads to a very inhomogeneous situation with Mn-rich regions embedded in a Mn-poor almost pristine GeTe matrix. Upon further Mn doping, the Mn concentration becomes locally so large that some *R*2 domains switch into cubic structure. This probably starts to happen around the maximum of the dome-like high-T_c phase line in Fig. 2, i.e., as soon as cubic phase fractions in controlled-cooled samples appear, the ferromagnetic T_c is suppressed. On the other hand, in quenched samples there is no time to allow for a relocation of Mn ions and hence a much more homogeneous situation is established. In this sense the homogeneous Mn distribution in the cubic high-temperature phase is "frozen" although the crystal nevertheless distorts rhombohedrally upon quenching. We identify this more homogeneous situation with a large single matrix of *R*1 phase fraction. The ferromagnetism in this low-T_c phase is understood in a Rudermann-Kittel-Kasuya-Yoshida (RKKY) framework. When a sample is sufficiently doped so that the structural transition to cubic has completed, there is no difference in the ferromagnetism any more between samples grown by either cooling recipe, i.e., both heat treatments yield a homogeneous arrangement of the Mn dopants.

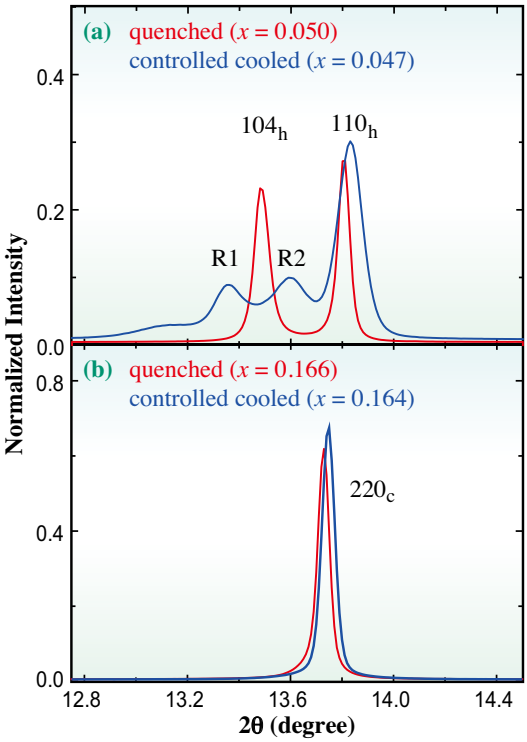

Fig. 3. XRD data taken at SPring-8 of **(a)** a quenched (red, $x = 0.050$) and a controlled-cooled rhombohedral sample (blue, $x = 0.047$) around the (104) and (110) reflections (hexagonal setting) and **(b)** a quenched (red, $x = 0.166$) and controlled-cooled cubic sample (blue, $x = 0.164$) around the corresponding single cubic (220) peak. The labels *R*1 and *R*2 mark an additional peak splitting due to differently distorted rhombohedral phase fractions, see text.

Markus Kriener[a,*], Taro Nakajima[a] and Kenichi Kato[b]

[a] RIKEN Center for Emergent Matter Science (CEMS)/ Wako
[b] RIKEN SPring-8 Center

*Email: markus.kriener@riken.jp

References

[1] R.W. Cochrane *et al.*: Phys. Rev. B **9** (1974) 3013.
[2] *M. Kriener, T. Nakajima, Y. Kaneko, A. Kikkawa, X.Z. Yu, N. Endo, K. Kato, M. Takata, T. Arima, Y. Tokura and Y. Taguchi: Sci. Rep.* ***6*** *(2016) 25748.*

Pressure-induced suppression of charge disproportionation in $CaCu_3Fe_4O_{12}$

Perovskites containing quadrivalent iron exhibit unique characteristics. Compared with perovskite Fe^{2+} or Fe^{3+} oxides, the lower number of 3*d* electrons and the weaker screening of the nuclear charge result in deepening of the 3*d* orbitals and a strong tendency for them to hybridize with the O 2*p* orbitals. These hybridized electronic states are responsible not only for the good conductivity of the materials but also for their various interesting physical properties.

Typical simple perovskites containing quadrivalent iron are $CaFeO_3$, $SrFeO_3$, and $BaFeO_3$. These perovskites share certain characteristics such as a large negative charge transfer energy and electrical and magnetic properties that are governed by the O 2*p*-hole character. The hole dynamics lead to a variety of electronic states, such as a metal (orthorhombic) to semiconductor ($T<290$ K, monoclinic) transition coupled to the breathing phonon mode of CFO, where the instability due to orbital degeneracy is lifted through the charge disproportionation (CD: $2Fe^{4+} \rightarrow Fe^{3+} + Fe^{5+}$) and the metallic antiferromagnetism with a helical spin structure of cubic $SrFeO_3$, and the magnetic-field-induced ferromagnetism of cubic $BaFeO_3$.

A-site-ordered perovskite iron oxides $AA'_3B_4O_{12}$ have been synthesized by advanced high-pressure methods. The A'-sites and B-sites are primarily occupied by Cu^{2+} ions and by Fe^{4+} or $Fe^{3.75+}$ ions, respectively. These oxides undergo two characteristic transitions depending on the size of the ions in the A-site. One is intersite charge transfer (CT), which takes place for comparatively large alkaline-earth metals (e.g., Sr) and rare-earth metal ions (La, Pr, Nd, Sm, Eu, Gd, and Tb) [1-3]. The other is CD, which takes place for comparatively small alkaline-earth metals (Ca) and rare-earth metal ions (Dy, Ho, Er, Tm, Yb, and Lu) [3,4]. These generation mechanisms remove the structural instability caused by metal-oxygen bond strains in the case of the former and by orbital instability in the Fe^{4+} (d^4) state in the case of the latter. The most notable characteristic of the A-site-ordered perovskite oxide $CaCu_3Fe_4O_{12}$ (CCFO) is that CD at 210 K is accompanied by ferrimagnetic and metal-semiconductor transitions. The resulting charge-disproportionated $CaCu_3^{2-}$ $(Fe^{3+}\ 2Fe^{5+}2)O_{12}$ is a B-site Fe^{3+}–O–Fe^{5+} ferromagnetically coupled compound [4].

We carried out X-ray diffraction, X-ray absorption spectroscopy (XAS), and ^{57}Fe Mössbauer spectroscopy to investigate the effect of pressure on the CD, CT, spin transitions, and crystal structure of CCFO. From our results, we constructed a CCFO *P*–*T* magnetic phase diagram [5].

Typical Mössbauer spectra are shown in Figs. 1(a-j). At ambient pressure, a paramagnetic singlet was observed above 210 K (Fig. 1(a)), while the low-temperature spectra at 8 K consisted of two magnetically split components with hyperfine fields of 41.6 T (Fe^{3+}) and 22.5 T (Fe^{5+}) in the high-spin state (Fig. 1(b)). Essentially the same behavior was observed up to ~12 GPa. First, various transitions occur in the pressure range of 13–15 GPa. The transition temperature peaks at approximately 350 K at 15 GPa before entering a perceptible decline. The spectra taken at 15 GPa and 298 and 8 K (Figs. 1(f) and 1(g)) already contained two magnetically split sextets. The shape of the spectra at 15 GPa supports the asymmetry of the intensity and the line width as a cause of the charge-disproportionated state. We concluded that these split components were a new charge-ordering state, which we named a slightly charge-disproportionated state ($Fe^{(4-\delta)+}$, $Fe^{(4+\delta)+}$, where δ denotes less than one). As we measured the electrical resistance under pressure, the pressure-induced semiconductor-metal transition appeared around the critical pressure of the first suppression of the CD ($Fe^{3+} + Fe^{5+} \rightarrow Fe^{(4-\delta)+} + Fe^{(4+\delta)+}$) at ~15 GPa. It is contemplated that the delocalization of e_g electrons proceeded upon applying pressure. Therefore, the electron hopping becomes faster and the number

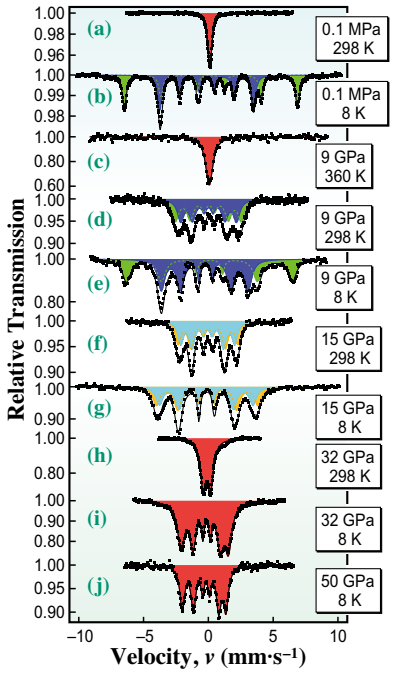

Fig. 1. Typical high-pressure ^{57}Fe Mössbauer spectra.

of electrons that contribute to the magnetic moment decreases. As a result, the valence, which is obtained from the isomer shift, is close to the mean valence (Fe^{4+}) and the hyperfine field decreases; thus, it can be concluded that the slightly charge-disproportionated state was stabilized.

Secondly, various marked changes occurred in the pressure range of 20–32 GPa. At 32 GPa, the 298 K spectrum was fitted to a non-magnetic doublet component (Fig. 1(h)). At 8 K, however, the spectrum changed into a magnetic sextet component with a small hyperfine field of 10.8 T and a quadrupole splitting of −0.14 mm/s (Fig. 1(i)). These spectra indicated a number of changes in the electronic state. The first was a complete suppression of the CD ($Fe^{(4-\delta)+} + Fe^{(4+\delta)+} \rightarrow 2Fe^{4+}$), the second was a low-spin transition, and the third was a rapid decrease in the magnetic ordering temperature to ~135 K. The cause of the decrease in the magnetic ordering temperature is thought to be that the superexchange interaction is weak owing to an absence of electrons in the e_g orbital. Similar Mössbauer spectra were maintained up to 50 GPa (Fig. 1(j)). High-spin and low-spin components coexisted in the pressure range of 25–30 GPa. The low-spin transition is complete at ~30 GPa.

Figure 2(a) shows XAS spectra around the Cu *K* edge under various pressures, which we observed at SPring-8 **BL39XU**. The energy of the absorption edge is around $E = 8.987$ keV. The absorption energies exhibit a very small shift below 0.5 eV with increasing pressure. This result indicated that the valence of the Cu ions in CCFO is almost constant. The energy shift is about 2 eV when the valence of Cu ion changes from divalent to trivalent. As a result of the ^{57}Fe Mössbauer spectroscopy and XAS, no CT between Cu and Fe was detected.

X-ray powder diffraction measurements were carried out at pressures of up to 51 GPa at SPring-8 **BL10XU**. All the peaks of the diffraction pattern at each pressure could be assigned to a cubic perovskite structure and no additional reflections were detected within the resolution of the measurements. The pressure dependence of the volume could be fitted well by the Birch-Murnaghan equation of the state (Fig. 2(b)), yielding a bulk modulus of K_0 = 242 GPa below ~22 GPa. However, on the application of higher pressure, the volume did not follow this compression curve, which may have been due to the low-spin transition. After the low-spin transition was completed, the compression curve showed a gradual decline.

The high-pressure measurements of CCFO were conducted to investigate changes in its charge, spin configuration, and electrical conduction. The results revealed CD suppression, a high-spin to low-spin transition, and a semiconductor-metal transition. In particular, we found a novel pressure-induced two-step CD suppression ($Fe^{3+} + Fe^{5+} \rightarrow Fe^{(4-\delta)+} + Fe^{(4+\delta)+} \rightarrow 2Fe^{4+}$). Finally, the phase diagram is presented in Fig. 3.

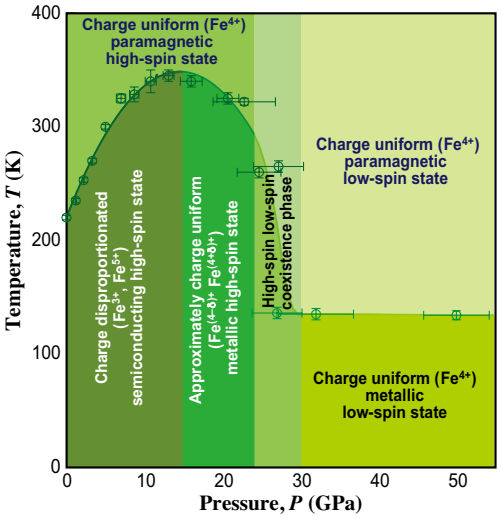

Fig. 3. *P*–*T* magnetic phase diagram.

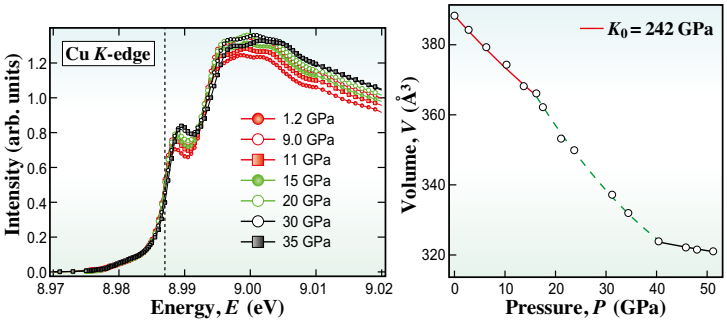

Fig. 2. **(a)** XAS spectra around the Cu *K* edge measured under various pressures at $T = 300$ K. **(b)** Compression curves at $T = 298$ K.

Takateru Kawakami

Dept. of Physics, College of Humanities and Sciences, Nihon University

Email: ta-kawakami@phys.chs.nihon-u.ac.jp

References

[1] Y. W. Long *et al.*: Nature **458** (2009) 60.
[2] I. Yamada *et al.*: Angew. Chem., Int. Ed. **50** (2011) 6579.
[3] I. Yamada *et al.*: Inorg. Chem. **52** (2013) 13751.
[4] I. Yamada *et al.*: Angew. Chem., Int. Ed. **47** (2008) 7032.
[5] *T. Kawakami, Y. Sekiya, A. Mimura, K. Kobayashi, K. Tokumichi,I. Yamada, M. Mizumaki, N. Kawamura, Y. Shimakawa, Y. Ohishi, N. Hirao, N. Ishimatsu, N. Hayashi and M. Takano*: J. Phys. Soc. Jpn. **85** (2016) 034716.

Development of H^- conductive oxyhydrides

Efficiency of the hydrogen transport in solids is a key to determining the performance of electrochemical devices such as fuel cells and batteries. Indeed, active studies on proton (H^+) conduction in oxides and other systems have been carried out. In contrast, hydrogen can also accept one electron to form a hydride ion (H^-). Hydride ions are also attractive for use as charge carriers because they are similar in size to oxide and fluoride ions, which are suitable for fast ionic conduction, while they also exhibit strong reducing properties owing to their standard H^-/H_2 redox potential (–2.3 V), which is comparable to that of Mg/Mg^{2+} (–2.4 V). Hydride ion conductors may therefore be applied in energy storage/conversion devices with high energy densities. However, pure H^- conduction has been verified only for a few hydrides of alkaline earth metals such as BaH_2 [1]. Unfortunately, utilization of the hydrides is difficult because of their structural inflexibility, which makes it difficult to control the lattice structure to create smooth transport pathways as well as the conducting hydride ion content. We have considered oxyhydrides, where hydride ions and oxide ions share anion sublattices, as candidate hydride conductors equipped with flexible anion sublattices.

A further complication in achieving pure H^- conduction in an oxide framework structure is the difficulty in inhibiting electron conduction. It is well known that hydride ions act as electron donors in oxides, transferring electrons from hydride ions to the lattice. This causes the conduction of electrons accompanied by a characteristic change in the hydrogen charge from H^- to H^+. Indeed, the perovskite and mayenite-type oxyhydrides are dominated by electron conduction caused by the dissociation of hydride ions into electrons and protons [2,3]. In the present study, we attempted to synthesize a series of K_2NiF_4-type oxyhydrides, $La_{2-x-y}Sr_{x+y}LiH_{1-x+y}O_{3-y}$ ($0 \le x \le 1$, $0 \le y \le 2$, $0 \le x+y \le 2$), which are equipped with cation sublattices featuring cations more electron-donating than H^- and anion sublattices that exhibit flexibility in the storage of H^-, O^{2-}, and vacancies [4].

The oxyhydrides $La_{2-x-y}Sr_{x+y}LiH_{1-x+y}O_{3-y}$ were synthesized by a solid-state reaction under high pressure and temperature using a cubic anvil cell. Synchrotron X-ray diffraction (SXRD) measurements in this study were performed at SPring-8 **BL02B2**. A Debye-Scherrer diffraction camera was used for measurements at 298 K. The SXRD pattern of La_2LiHO_3 ($x=y=0$) was assigned to the K_2NiF_4-type structure with an orthorhombic *Immm* symmetry. Figure 1 shows SXRD patterns of solid solutions between La_2LiHO_3 and Sr_2LiH_3O, represented as $La_{2-y}Sr_yLiH_{1+y}O_{3-y}$ ($x=0$, $0 \le y \le 2$). Here, the H:O ratio changes accordingly as La is substituted with Sr, maintaining the simple A_2BX_4 composition (*A*:La, Sr; *B*:Li; *X*:O, H). In $La_{2-x}Sr_xLiH_{1-x}O_3$ ($0 \le x \le 1$, $y = 0$) and

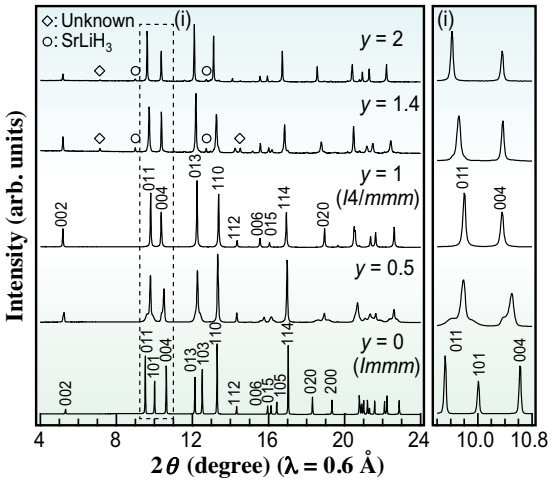

Fig. 1. Comparison of the synchrotron X-ray diffraction patterns for $La_{2-x-y}Sr_{x+y}LiH_{1-x+y}O_{3-y}$ ($x = 0$, $0 \le y \le 2$).

$La_{1-x}Sr_{1+x}LiH_{2-x}O_2$ ($0 \le x \le 1$, $y = 1$), Regarding the Sr-substituted series of $La_{2-y}Sr_yLiH_{1+y}O_{3-y}$, the diffraction peaks continuously shifted to lower angles with increasing *y* and the lattice symmetry changed from *Immm* ($y < 1$) to *I*4/*mmm* ($y \ge 1$).

The compositions and structures of $La_{2-y}Sr_yLiH_{1+y}O_{3-y}$ ($y = 0, 1, 2$) were determined by X-ray and neutron Rietveld analyses. Figure 2 shows the determined crystal structures of $La_{2-y}Sr_yLiH_{1+y}O_{3-y}$. In La_2LiHO_3, the two apical sites of the LiX_6 octahedra are occupied only by O^{2-}, while the four in-plane apexes are orderly occupied by O^{2-} and H^- in an orderly manner. These results indicate that the highly charged cations, i.e., La^{3+} and Sr^{2+}, require highly charged anions around them. $LaSrLiH_2O_2$ is composed of tetragonal $(LiH_2)^-$ and $(LaSrO_2)^+$ layers alternately stacked along the *c* axis. A further increase in the hydride content up to Sr_2LiH_3O results in the formation of $(Sr_2HO)^+$ layers. A Rietveld analysis for the anion deficient series, $La_{1-x}Sr_{1+x}LiH_{2-x}O_2$ ($x > 0$, $y = 1$), was also carried out. As a result, it was clarified that vacancies were introduced at the LiH_4 plane with increasing *x*.

The ionic conductivities of $La_{2-x-y}Sr_{x+y}LiH_{1-x+y}O_{3-y}$ were examined by impedance measurement. For the vacancy-free composition $La_{2-y}Sr_yLiH_{1+y}O_{3-y}$ ($x = 0$), the conductivity increases with increasing H^- content, with the highest conductivity of 3.2×10^{-5} S cm^{-1} at 573 K being observed for Sr_2LiH_3O ($y = 2$). The introduction of hydride ions into the anion sites of the K_2NiF_4 structure improved the ionic conductivity, suggesting that the primary charge carriers are these hydride ions. The conduction is further facilitated by the introduction of vacancies, as can be seen for both $La_{2-x}Sr_xLiH_{1-x}O_3$ ($y = 0$) and $La_{1-x}Sr_{1+x}LiH_{2-x}O_2$ ($y = 1$), reaching 2.1×10^{-4} S cm^{-1} for $La_{0.6}Sr_{1.4}LiH_{1.6}O_2$ at 590 K.

To further identify the nature of charge carriers, an all-

solid-state Ti/La_2LiHO_3/TiH_2 cell was constructed using La_2LiHO_3 as the solid electrolyte, and the galvanostatic discharge reaction was examined. Figure 3(a) shows the discharge curve of the cell, displaying a constant discharge current of 0.5 μA at 573 K. The cell showed an initial open circuit voltage of 0.28 V, which is consistent with the theoretical value calculated from the standard Gibbs energy of formation of TiH_2. During the electrochemical reaction, the cell voltage dropped rapidly from 0.28 V to 0.06 V, and then decreased gradually to 0.0 V. This steep drop-off in the first reaction step corresponds to an increase in the hydride ion content at the anode in accordance with the constant current discharge reaction

$$Ti + xH^- \rightarrow TiH_x + xe^- ,$$

where the reaction at the cathode is as follows:

$$TiH_2 + xe^- \rightarrow TiH_{2-x} + xH^- .$$

These discharge reactions were confirmed by observation of the phases that appeared following the reaction. Figure 3(b) shows the synchrotron X-ray diffraction patterns for the cathode, electrolyte, and anode, both before and after the reaction. The absence of any variation in the diffraction patterns of the electrolyte indicates that the La_2LiHO_3 electrolyte is stable when in contact with the Ti and TiH_2 electrodes during the reaction. The phase changes detected for the cathode and anode materials are consistent with those expected from the Ti-H phase diagram [5], where the δ-TiH_2 phase releases hydrogen and is transformed into α-Ti through a two-phase (α-TiH_b + δ-TiH_{2-a}) coexistence region. In the case of the cathode, additional diffraction peaks corresponding to the α-Ti phase were detected. In addition, the signals corresponded to a shift of TiH_2 to a higher angle, thus indicating that lattice shrinkage takes place with the release of hydrogen from TiH_2. In the case of the anode, peaks corresponding to the δ-TiH_2 phase were detected. These results indicate that during the electrochemical reaction, hydride ions are released from the TiH_2 cathode and diffuse into the Ti anode through the La_2LiHO_3.

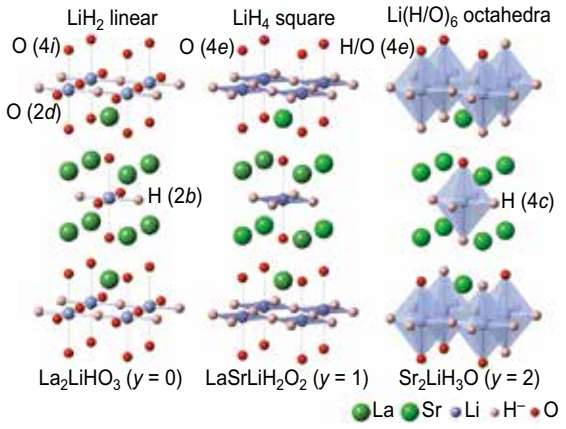

Fig. 2. Crystal structures of $La_{2-x-y}Sr_{x+y}LiH_{1-x+y}O_{3-y}$ ($x = 0$, $y = 0, 1, 2$).

In conclusion, pure H^- conduction was realized in the $La_{2-x-y}Sr_{x+y}LiH_{1-x+y}O_{3-y}$ system. The present successful construction of an all-solid-state electrochemical cell exhibiting H^- diffusion confirms not only the capability of the oxyhydride to act as H^- solid electrolyte but also the possibility of developing electrochemical solid devices based on H^- conduction.

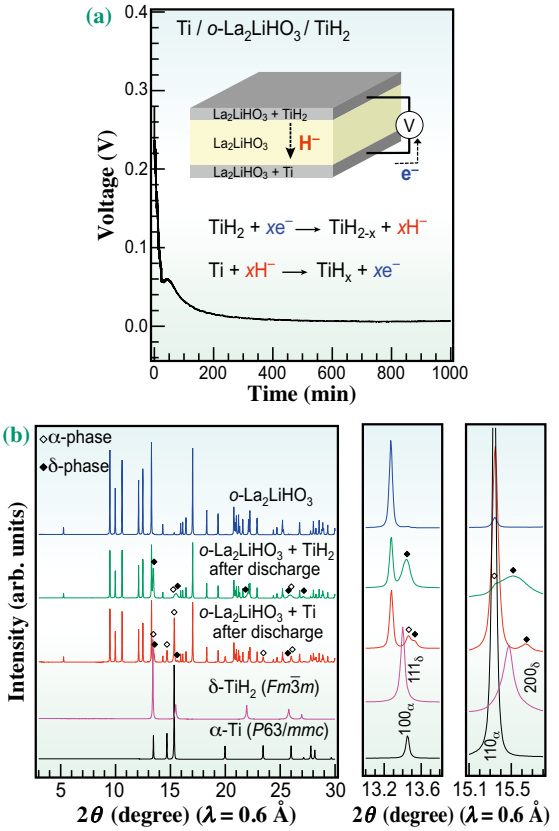

Fig. 3. All-solid-state hydride cell. **(a)** Discharge curve for a solid-state battery with the Ti/La_2LiHO_3/TiH_2 structure. The inset shows an illustration of the cell and the proposed electrochemical reaction. **(b)** X-ray diffraction patterns for the electrolyte (La_2LiHO_3), cathode (TiH_2 + La_2LiHO_3), and anode (Ti + La_2LiHO_3) materials after the reaction.

Genki Kobayashi[a,*] and Ryoji Kanno[b]

[a] Research Center of Integrative Molecular Science, Institute for Molecular Science
[b] School of Materials and Chemical Technology, Tokyo Institute of Technology

*Email: gkobayashi@ims.ac.jp

References

[1] M.C. Verbraeken *et al.*: Nat. Mater. **14** (2015) 95.
[2] K. Hayashi *et al.*: Nature **419** (2003) 462.
[3] Y Kobayashi *et al.*: Nat. Mater. **11** (2012) 507.
[4] *G. Kobayashi, Y. Hinuma, S. Matsuoka, A. Watanabe, M. Iqbal, M. Hirayama, M. Yonemura, T. Kamiyama, I. Tanaka R. Kanno: Science **351** (2016) 1314.*
[5] A. San-Martin, F.D. Manchester: Bulletin of Alloy Phase Diagrams **8** (1987) 30.

Transient structure determination of resonantly vibrating quartz by short-pulse X-ray diffraction under alternating electric field

Quartz is the most common mineral on earth and is widely used as an oscillator to generate a stable clock signal for watches and other electric circuits because of its piezoelectricity and stable mechanical vibration. The piezoelectricity of quartz (SiO_2) has typically been explained by ionic displacements of Si^{4+} and O^{2-} relative to each other under a mechanical stress and/or an electric field [1]. However, the ionic displacements of Si^{4+} and O^{2-} are strongly restricted by covalent Si–O bonds and are too small to be detected by usual X-ray diffraction experiments. The small atomic displacements induced by an electric field should be enhanced by applying an alternating electric field with the resonant frequency. In order to detect the small atomic displacements induced by an electric field, we determined the transient crystal structure of a resonantly vibrating quartz crystal under an alternating electric field by time-resolved X-ray diffraction at SPring-8 **BL02B1** [2].

A commercial AT-cut quartz oscillator with a resonant frequency of 30 MHz was used in the experiment. AT-cut crystals, which are most commonly used for oscillators because of their high frequency stability over a wide temperature range, show a thickness-shear vibration under an alternating electric field. Transient X-ray diffraction patterns during the resonant vibration were measured by using short-pulse X-rays with a pulse width of 50 ps radiated from SPring-8. The sample was repeatedly irradiated with short-pulse X-rays with a fixed frequency of 26.1 kHz by applying a high-speed X-ray pulse chopper. To synchronize the resonant vibration of the quartz oscillator with the repetitive short-pulse X-rays, a hybrid alternating electric field consisting of 1000 cycles of a sine wave with the resonant frequency (1000 cycles × 1/30 MHz = 33 μs) and repetitions at 26.1 kHz (38 μs/period) was used to drive the resonant thickness-shear vibration. Momentary X-ray diffraction patterns (X-ray wavelength: 0.41 Å) diffracted within 50 ps in a period around the 995th cycle of the alternating electric field were repeatedly stored on a cylindrical image plate camera to improve the counting statistics during the exposure time. The transient crystal structure was investigated over one period by tuning the delay time Δt of the alternating electric field to the reference clock signal of SPring-8.

Figure 1 shows the time dependence of the lattice constant γ under the alternating electric field with an amplitude of 0.18 kV/mm, which was determined by the least-squares refinement of ~400 Bragg peak positions (d-spacing > 0.40 Å) recorded on one oscillation photograph. The γ angle substantially changes sinusoidally with a period of 33 ns = 1/30 MHz. The change in γ, $|\Delta\gamma| = |\gamma - 90°|$, reaches a maximum of 0.15° at Δt = 9 and 25 ns. $|\Delta\gamma|$ under a static electric field of 0.18 kV/mm is estimated to be ~10^{-5}° from the piezoelectric constant d_{11} = –2.31 pm/V [3]. Therefore, the lattice strain is amplified by ~10^4 times by the resonant effect.

The momentary crystal structures of the resonantly

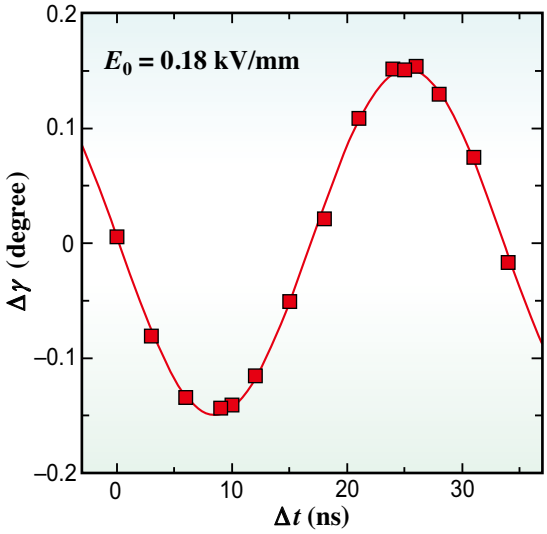

Fig. 1. Time dependence of the lattice constant γ of resonantly vibrating quartz.

vibrating quartz at Δt = 9 and 25 ns were determined by the least-squares refinement of over 3700 Bragg intensities (d-spacing > 0.35 Å). The strained quartz consisted of three crystallographically independent SiO_4 tetrahedra. The Si–O distances (~1.61 Å), O–Si–O angles, (~109°) and Si–O–Si angles (~143°) at the times Δt = 9 and 25 ns were investigated. No changes in the Si–O distances and O–Si–O angles were observed within the standard deviations (~0.2 pm and ~0.1°, respectively) during the resonant vibration. This indicates that the rigid SiO_4 tetrahedra were hardly distorted against the substantial lattice strain. However, specific Si–O–Si angles bridging the rigid SiO_4 tetrahedra changed under the lattice strain as shown in Table 1. The stained triclinic unit cell contains six independent oxygen atoms (O(1)–O(6)). The changes in the four independent Si–O–Si angles at O(1), O(4), O(5) and O(6) are comparable with the standard deviations (~0.1°). In contrast, the Si–O–Si angles at O(2) and O(3) appear to decrease and increase, respectively, from Δt = 9 to 25 ns.

The substantial deformation of the Si–O–Si angles at O(2) and O(3) can be explained by oxygen displacements induced by the electric field and the orientation relations between the Si–O–Si planes and the electric field. The shifts of electron charge from the neutral atoms, which were estimated from the electron charge densities obtained by the maximum entropy method, were +2.8(1)e (e: elementary charge) for a silicon atom and −1.4(1)e for an oxygen atom. These values are comparable with those obtained from the theoretical ionic formula [4]. When the anionic oxygen atoms are displaced by the electric field, the Si–O–Si angles are deformed. However, the oxygen is hardly displaced if the Si–O–Si plane is parallel to the electric field due to the rigid Si–O bonds. The angles between the electric field and vectors normal to the Si–O–Si planes, ϕ, at O(2) and O(3) are closer to 90° than those at other oxygen atoms as shown in Table 1 and Fig. 2.

Table 1. Si–O–Si angles at the times Δt = 9 and 25 ns, and angles between the electric field and vectors normal to the Si–O–Si planes ϕ

	Si–O–Si angle (deg.)		ϕ (deg.)
	Δt = 9 (ns)	Δt = 25 (ns)	
Si(1)–O(1)–Si(3)	143.97(11)	143.81(12)	60
Si(1)–O(2)–Si(3)	144.19(11)	143.41(12)	83
Si(2)–O(3)–Si(1)	143.37(10)	144.02(11)	83
Si(2)–O(4)–Si(1)	143.50(11)	143.82(12)	59
Si(3)–O(5)–Si(2)	143.73(16)	143.27(17)	26
Si(3)–O(6)–Si(2)	143.42(15)	143.61(17)	26

Therefore, the Si–O–Si angles at O(2) and O(3) are substantially deformed during the resonant vibration.

The easy displacements of specific anionic oxygen atoms (O(2) and O(3)) and the collateral resilient deformation of Si–O–Si angles resulted in the resonant vibration under substantial lattice strain. The resilient bending vibration of Si–O–Si angles in the AT-cut quartz oscillator revealed in this study is essential for the generation of a stable clock signal for watches and other electric circuits.

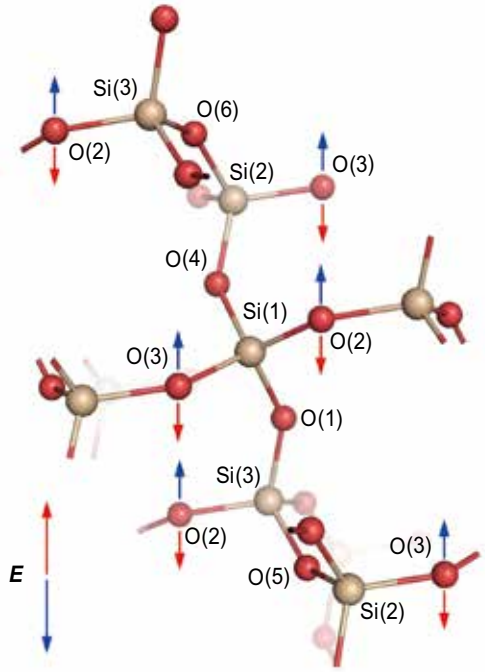

Fig. 2. Crystal structure of quartz and oxygen displacements of O(2) and O(3) induced by the electric field E.

Shinobu Aoyagi

Department of Information and Basic Science,
Nagoya City University

Email: aoyagi@nsc.nagoya-cu.ac.jp

References

[1] A. Meissner: Z. Tech. Phys. **8** (1927) 74.
[2] *S. Aoyagi, H. Osawa, K. Sugimoto, A. Fujiwara, S. Takeda, C. Moriyoshi and Y. Kuroiwa: Appl. Phys. Lett.* ***107*** *(2015) 201905.*
[3] R. Bechmann: Phys. Rev. **110** (1958) 1060.
[4] Y.-N. Xu and W.Y. Ching: Phys. Rev. B **51** (1995) 17379.

Atomic-scale disproportionation in amorphous silicon monoxide

Silicon monoxide (SiO) was first reported by Charles Mabery in 1887 [1] and has been widely used as surface coatings, insulating layers in integrated circuits, dielectric material in capacitors, and anode materials for Li-ion batteries. However, the atomic structure of SiO has been debated for nearly a century despite numerous experimental and theoretical efforts devoted to this problem. Although a random bonding Si-($Si_{4-x}O_x$) tetrahedral configuration can satisfy the stoichiometry of SiO, experiments and theoretical calculations have suggested that it is inherently unstable and undergoes an unusual disproportionation by forming amorphous Si- and SiO_2-like clusters [2]. However, it has been long known that the heat of combustion of amorphous SiO is significantly higher than that of an equilibrium mixture of amorphous Si and SiO_2 and, importantly, the X-ray diffraction (XRD) patterns of amorphous SiO cannot be interpreted by the summation of amorphous Si and SiO_2 spectra. The unique and well-defined local atomic configurations of SiO have not been directly realized by experiments mainly because of the limitation in spatial resolution of conventional diffraction methods. In this study [3] we employ our recently developed angstrom beam electron diffraction (ABED) method to investigate the local structure of amorphous SiO, which is supplemented by synchrotron high-energy XRD (HEXRD) and computational simulations based on molecular dynamics (MD) and reverse Monte Carlo (RMC) calculations.

Figure 1 shows the X-ray structure factor $S(Q)$ of amorphous SiO measured at SPring-8 **BL04B2**, together with those of amorphous Si and SiO_2 reported in the literatures [4,5]. The $S(Q)$ of amorphous SiO appears to be intermediate between those of amorphous Si and SiO_2. However, the summation curve of amorphous Si and SiO_2 is not fully consistent with that of SiO, agreeing with previous observations. In particular, the first sharp diffraction peak of the summation data splits into two sub-peaks, which cannot reproduce the first peak at $Q \sim 1.8$ Å^{-1} of amorphous SiO. The good agreement between the summation curve and SiO at the high Q portion indicates that the short-range structure of amorphous SiO could be similar to those of Si-4Si and Si-4O tetrahedra in amorphous Si and SiO_2.

The local atomic structure of amorphous SiO was investigated by ABED as illustrated in Fig. 2(a). Figure 2(c)-(e) show three typical ABED patterns obtained from dark, bright and interface regions in a high-angle annular dark-field scanning transmission electron microscope (HAADF-STEM) image of Fig. 2(b). The diffraction patterns in Figs. 2(c) and 2(e) are akin to those of amorphous Si and SiO_2 with the smallest Q values ($Q \sim 2.0$ and 1.5 Å^{-1}) in HEXRD. Meanwhile, the simulated ABED patterns based on suboxide-type tetrahedra match well with the experimental one (Fig. 2(d)). The simulated ABED patterns of amorphous Si, SiO_2 and SiO_x clusters are shown in Fig. 2(c')-(e'), together with the corresponding atomic models (Fig. 2(c")-(e")).

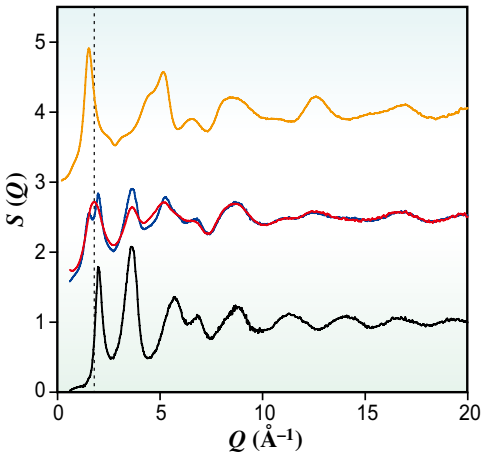

Fig. 1. X-ray total structure factors $S(Q)$ of amorphous SiO, Si and SiO_2. The X-ray $S(Q)$ of amorphous SiO obtained from HEXRD (red) is shown together with the $S(Q)$ data of amorphous Si (black) and SiO_2 (orange) reported in the references [4] and [5], respectively. The $S(Q)$ profile for the summation of amorphous Si and SiO_2 is shown as a blue curve. [3]

On the basis of the ABED and HEXRD results, we constructed an atomic model of amorphous SiO by the combination of MD simulations and RMC modeling. The final structure model is shown in Fig. 3(a), in which the coordinates of Si-4Si and Si-4O tetrahedral from the amorphous Si and SiO_2 regions are still visible. The $S(Q)$ profile of the model is well consistent with that of HEXRD (Fig. 3(b)). Additionally, the suboxide-type tetrahedral coordinates (Si-(3Si, O), Si-(2Si, 2O) and Si-(Si, 3O)) revealed by ABED are formed at the Si/SiO_2 interface regions during the structure relaxation. The density functional theory calculations confirm the presence of the suboxide-type tetrahedra in the interface regions. These suboxide-type tetrahedra keep the random networks in amorphous Si and SiO_2 continuously across the interface regions. The number fractions of the five typical atomic coordinates are

shown in Fig. 3(c). There are considerable amounts of suboxide-type tetrahedra of Si-(3Si, O), Si-(2Si, 2O) and Si-(Si, 3O) from interface regions. These suboxide-type tetrahedra as the transition layers bridge amorphous Si and amorphous SiO_2 by preserving the continuity of the random networks of Si and SiO_2.

In summary, we systematically investigated the atomic structure of amorphous SiO by utilizing the ABED, complemented with synchrotron HEXRD and MD-RMC simulations. The ABED experiment provides direct evidence on the atomic-scale disproportionation in amorphous SiO, predicted by theoretical calculations. The distinctive interfacial structure between amorphous Si and SiO_2 clusters, revealed by the sub-nanoscale electron diffraction, uncovers the structural origins of amorphous SiO different from the simple mixture of Si and SiO_2.

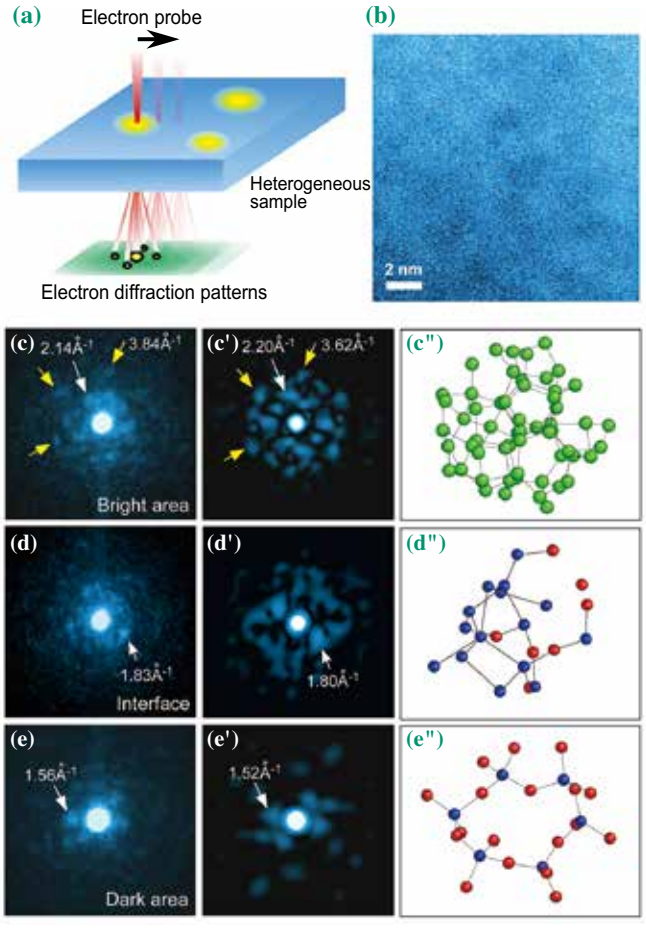

Fig. 2. **(a)** The schematic diagram of the ABED measurements of amorphous SiO with nanoscale structural heterogeneity. **(b)** HAADF-STEM image of the amorphous SiO. **(c)-(e)**, Typical ABED patterns taken from bright, interface and dark regions in the HAADF-STEM image shown in (b). **(c')-(e')** Simulated ABED patterns based on the atomic models of amorphous Si, interfacial suboxide-type tetrahedra and amorphous SiO_2 in **(c")-(e")**. [3]

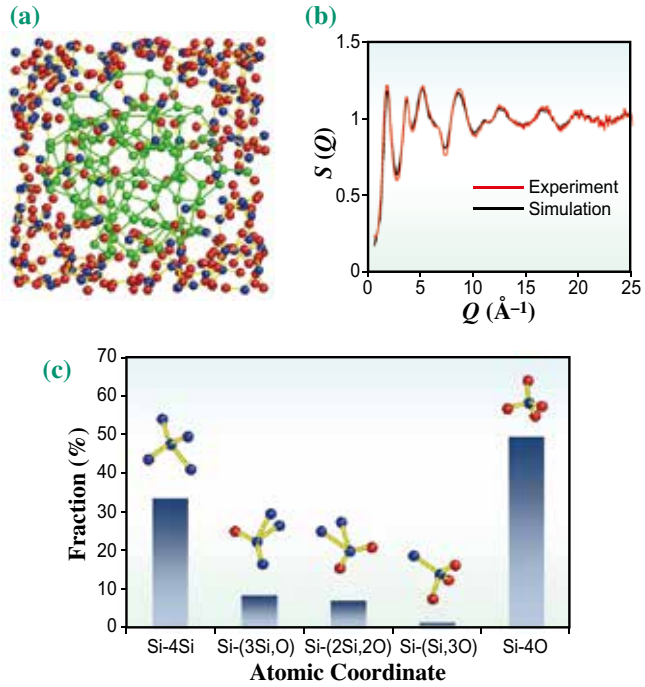

Fig. 3. **(a)** Reconstructed heterostructure model of amorphous SiO. The inner part corresponds to an amorphous Si cluster and the outer part is amorphous SiO_2 matrix. The blue, red and green circles denote Si and O in amorphous SiO_2 and Si in the Si cluster, respectively. **(b)** Experimental and simulated X-ray total structure factor $S(Q)$ curves. **(c)** Fractions of the five atomic coordinates found in amorphous SiO. Si-4Si and Si-4O are from the Si cluster and SiO_2 matrix while Si-(3Si, O) Si-(2Si, 2O) and Si-(Si, 3O) appear at the interfacial regions between the Si cluster and amorphous SiO_2 matrix. [3]

Akihiko Hirata[a,*], Hideto Imai[b] and Mingwei Chen[a,c]

[a] WPI Advanced Institute for Materials Research, Tohoku University
[b] NISSAN ARC Ltd.
[c] State Key Laboratory of Metal Matrix Composites and School of Materials Science and Engineering, Shanghai Jiao Tong University, China

*Email: hirata@wpi-aimr.tohoku.ac.jp

References

[1] C.F. Mabery: Amer. Chem. J. **9** (1887) 11.
[2] A. Hohl *et al.*: J. Non-Cryst. Solids **320** (2003) 255.
[3] *A. Hirata, S. Kohara, T. Asada, M. Arao, C. Yogi, H. Imai, Y. W. Tan, T. Fujita and M. W. Chen: Nat. Commun. 7 (2016) 11591.*
[4] K. Laaziri *et al.*: Phys. Rev. Lett. **82** (1999) 3460.
[5] S. Kohara and K. Suzuya: J. Phys.: Condens. Matter **17** (2005) S77.

Structure of Li_2S-P_2S_5 sulfide glasses

Sulfide glasses are materials of interest for solid electrolytes in lithium ion batteries (LIBs) [1], because the realization of an all-solid-state battery will enable the miniaturization of battery packages and reduce safety issues compared with those of LIBs with an organic electrolyte. Significant progress has been made so far with the discovery of numerous sulfide compounds with high ionic conductivities such as $Li_7P_3S_{11}$ [2], $Li_{10}GeP_2S_{12}$ [3], $Li_{10}SnP_2S_{12}$ [4], and $Li_7P_2S_8I$ [5]. All these materials are derived from Li_2S-P_2S_5 sulfide glasses. Therefore, the nature of Li_2S-P_2S_5 glasses must be clarified in detail to continue the development of advanced Li ionic conductors targeted at the realization of all-solid-state batteries.

To clarify the origin of the ionic conduction, we present a comparative fundamental study of the structures of the $67Li_2S$-$33P_2S_5$ ($67Li_2S$), $70Li_2S$-$30P_2S_5$ ($70Li_2S$), and $75Li_2S$-$25P_2S_5$ ($75Li_2S$) glasses. The lithium ionic conductivities of $67Li_2S$, $70Li_2S$, and $75Li_2S$ were found to be 5.6×10^{-5} S/cm, 1.4×10^{-4} S/cm, and 3.0×10^{-4} S/cm, respectively. We performed high energy X-ray diffraction measurements at SPring-8 **BL04B2**, and analyzed the environment of the Li^+ ions by structural analyses combining X-ray and neutron diffraction measurements with the aid of density functional theory (DFT), reverse Monte Carlo (RMC) simulation, and Raman spectroscopy to reveal the relationship between structural properties and Li ionic conduction. Binary Li_2S-P_2S_5 glasses, which consist of PS_x polyhedral anions, are well-known superionic conductors. To quantitatively evaluate the fraction of PS_x polyhedral anions, the Raman spectra of the $67Li_2S$, $70Li_2S$, and $75Li_2S$ glasses were obtained, as shown in Fig. 1(a). It is known that bands in the frequency range of 330–480 cm^{-1} are sensitive to the S-P-S bond angle. We assigned the three bands at approximately 425 cm^{-1}, 410 cm^{-1}, and 390 cm^{-1} to the stretching vibration of the P-S bonds in the PS_4^{3-} (*ortho*-thiophosphate) ion, $P_2S_7^{4-}$ (*pyro*-thiophosphate) ion, and $P_2S_6^{4-}$ (an ethanelike structure with a P-P bond) ion, respectively. The ratios of the PS_4^{3-}, $P_2S_7^{4-}$, and $P_2S_6^{4-}$ ions were estimated using a Lorentzian function, shown as dotted lines in Fig. 1(b), and are summarized as open circles, open triangles, and open squares in Fig. 1(c), respectively. It is clear that the ratio of PS_4^{3-} ions increases with the Li_2S content, while the ratios of $P_2S_7^{4-}$ and $P_2S_6^{4-}$ ions decrease. Intriguingly, it was found that $P_2S_6^{4-}$ ions exist in these glasses with ratios of approximately 33.0%, 18.3%, and 4.4% in $67Li_2S$, $70Li_2S$, and $75Li_2S$, respectively, whereas they should not be contained in the stoichiometric compositions ($0PS_4$:$100P_2S_7$ in $67Li_2S$, $50PS_4$:$50P_2S_7$ in $70Li_2S$, and $100PS_4$:$0P_2S_7$ in $75Li_2S$). This means that there is a sulfur deficiency in these glasses.

Figure 2 shows experimental X-ray total structure factors, $S^X(Q)$, for the $67Li_2S$, $70Li_2S$, and $75Li_2S$ glasses. Oscillations in $S^X(Q)$ remain up to the high Q region, which is evidence for well-defined short-range order in the formation of P-S bonds. The difference between the three compositions is not significant in both sets of diffraction data. To uncover the relationship between the glassy structure and the high ionic conductivity for these glasses, we modeled the atomic structure of the Li_2S-P_2S_5 glasses by DFT/RMC simulation using X-ray and neutron diffraction data,

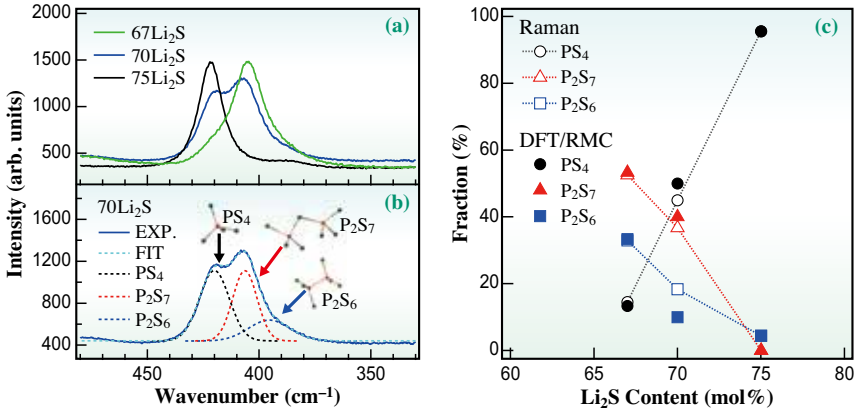

Fig. 1. **(a)** Raman spectra in the range of 330–480 cm^{-1} for Li_2S-P_2S5 glasses. Black, blue, and green lines represent $75Li_2S$, $70Li_2S$, and $67Li_2S$ glasses, respectively. **(b)** Spectral decomposition of Raman spectrum for $70Li_2S$ glass. Blue line, experimental data; dotted lines, fitting result for all PS polyhedral anions (light blue), PS_4 (black), P_2S_7 (red), and P_2S_6 (blue). **(c)** PS*x* polyhedral fractions for Li_2S-P_2S_5 glasses derived from Raman spectra (open marks) and DFT/RMC model (filled marks).

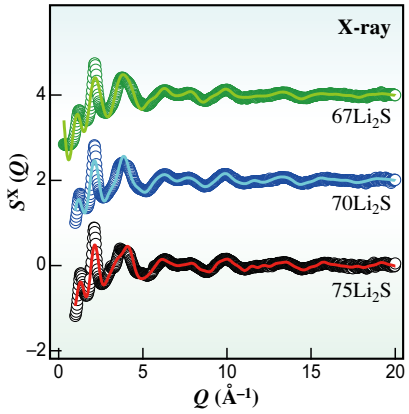

Fig. 2. Total structure factors $S(Q)$ at room temperature for Li_2S-P_2S_5 glasses derived from X-ray diffraction. Circles, experimental data; lines, DFT/RMC model.

fixing the ratios of the PS_4^{3-}, $P_2S_7^{4-}$, and $P_2S_6^{4-}$ ions on the basis of Raman spectroscopy measurements to reproduce the plausible glassy structures. The total structure factors $S^X(Q)$ of the Li_2S-P_2S_5 glasses derived from the DFT/RMC model are shown in Fig. 2 as lines. The DFT/RMC model is consistent with the experimental data.

The DFT/RMC structure is consistent with both the diffraction data and the Raman data, and we compared the electronic structure in terms of each PS_x polyhedral anion for the $70Li_2S$ glass. Figures 3(a) and 3(b) show the partial density of states (p-DOS) of the $70Li_2S$ glass for the S 3*p*-orbital and P 3*p*-orbital, respectively. It is apparent that the orbitals form a hybrid orbital between the phosphorus and sulfur; the highest occupied molecular orbital (HOMO) is located at –4.0 to –0.5 eV and the lowest unoccupied molecular orbital (LUMO) is located at 1.5 to 5.0 eV. The positive charge of the P ion is large owing to the hybrid orbital. However, the p-DOS plots of the P ion reveal that the P_2S_7 anion only differs from the PS_4 and P_2S_6 anions as follows (Fig. 3(b)). A shallow level appears near the bottom of the LUMO at approximately 2.0 eV in the P_2S_7 anion, which is related to a covalent bond between the P ion and the bridging sulfur (BS) ion in the P_2S_7 anion. This electron transfer is expected to weaken the positive charge of the P ions, which attract Li^+ ions to the P_2S_7 anions more strongly than the other PS_x polyhedral anions. Furthermore, it is easy for the attracted Li^+ ions to remain around the P_2S_7 anions, which may suppress the lithium ionic conduction in solid electrolytes.

In this study, we found that $P_2S_6^{4-}$ ions as well as PS_4^{3-} and $P_2S_7^{4-}$ ions are present in $67Li_2S$, $70Li_2S$, and $75Li_2S$ glasses on the basis of Raman spectroscopy measurement. Density functional theory and reverse Monte Carlo simulations (DFT/RMC) quantitatively reproduced the results of high-energy X-ray diffraction, neutron diffraction, and Raman spectroscopy, fixing the ratios of PS_4^{3-}, $P_2S_7^{4-}$, and $P_2S_6^{4-}$ ions. The electronic structure of the DFT/RMC model suggests that the existence of the P_2S_7 anion may suppress lithium ionic conduction. Thus, the control of the edge sharing between PS_x anions and Li ions without electron transfer between the P ion and the BS ion is expected to facilitate lithium ionic conduction in a solid electrolyte, which should contribute to the development of all-solid batteries.

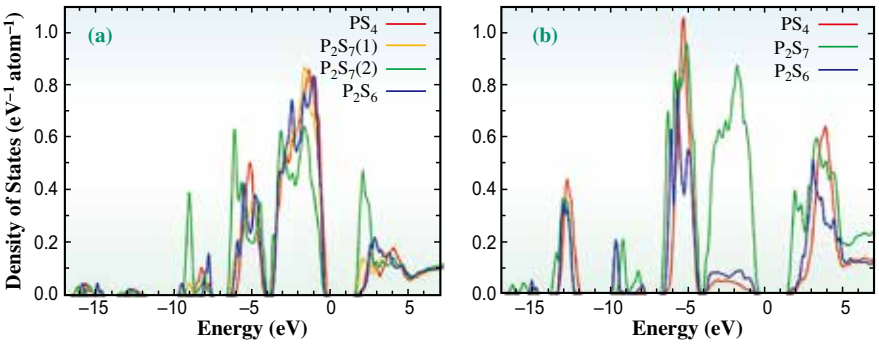

Fig. 3. Partial DOS for **(a)** S 3*p*-orbital and **(b)** P 3*p*-orbital of $70Li_2S$ glass.

K. Ohara[a,b,*], A. Mitsui[a,c], Y. Uchimoto[a] and Z. Ogumi[a]

[a] Kyoto University
[b] Japan Synchrotron Radiation Research Institute (JASRI)
[c] Toyota Motor Corporation

*Email: ohara@spring8.or.jp

References

[1] Y. Kato *et al.*: Nature Energy **1** (2016) 16030.
[2] Y. Seino *et al.*: Energ. Environ. Sci. **7** (2014) 627.
[3] N. Kamaya *et al.*: Nat. Mater. **10** (2011) 682.
[4] P. Bron *et al.*: J. Am. Chem. Soc. **135** (2013) 15694.
[5] E. Rangasamy *et al.*: J. Am. Chem. Soc. **137** (2015) 1384.
[6] *K. Ohara, A. Mitsui, M. Mori, Y. Onodera, S. Shiotani, Y. Koyama, Y. Orikasa, M. Murakami, K. Shimoda, K. Mori, T. Fukunaga, H. Arai, Y. Uchimoto, and Z. Ogumi: Sci. Rep.* ***6*** *(2016) 21302.*

Mapping 3D crystallographic orientation and strain fields in deformed polycrystalline aluminum alloy by diffraction-amalgamated grain boundary tracking

A comprehensive description of the structure of polycrystalline materials is the basis for understanding their physical and mechanical characteristics. Conventional scientific principles concerning polycrystalline materials have, however, been developed on the basis of two-dimensional (2D) observations of surfaces or thin films. A series of surface microscopic observations provides a certain amount of information on the time evolution behaviors of deformation, damage, and fracture in polycrystalline materials. Such information, however, may be considered unrepresentative of the bulk of a given material in the sense that surface-specific phenomena are often observed. To investigate actual phenomena in the bulk of a polycrystalline material, a sectioned surface can be examined, for example, by electron backscattering diffraction technique. This, however, is a fundamentally destructive and nonsequential mode of observation, and any results should therefore be interpreted with caution due to the three-dimensional (3D) complexity of microstructural features in practical materials. It has been vital, therefore, for other procedures to be developed to obtain accurate 3D *in situ* representations of polycrystalline materials.

The 3D grain structure and orientation map of polycrystalline materials can be obtained by using 3D X-ray diffraction, diffraction contrast tomography, and differential-aperture X-ray microscopy regardless of the material. All these techniques, however, require X-ray diffraction to map grain boundaries, and this means that, owing to the resulting occurrence of intensity reduction, spot blurring, and spot overlap during plastic deformation, the techniques are vulnerable to plastic deformation [1]. Spot overlap is mainly attributable to the orientation spread of individual grains.

In this study, we proposed a new technique, named diffraction-amalgamated grain boundary tracking (DAGT), which can be applied to large tensile deformation of a polycrystalline aluminum alloy. This technique is composed of an X-ray diffraction technique and a grain boundary tracking (GBT) technique, and proposed by the authors for imaging 3D polycrystalline structures and local strain distributions [2]. The GBT technique enables the accurate reconstruction of 3D grain morphologies during deformation, even close to fracture. Precise image registration is then performed for the X-ray microtomography images captured before and after gallium application to identify particles located along the gallium-enhanced grain boundaries the 3D marker-based registration is performed to calculate the necessary image shifts in all the translational and rotational directions. Each grain is then reconstructed as a polygonal mesh by connecting particles located along the grain boundaries as plane-triangle components. This triangulation of the surface of individual grains is repeated at each loading step by employing the microstructural tracking technique [3], enabling visualization of the deformation behavior of each polygonal grain by tracking all the grain boundary particles throughout deformation. A 'pencil-beam' X-ray diffraction technique is coupled with the GBT technique. Diffraction spots are obtained from all the grains during the DAGT experiment and then back-projected to a sample position to calculate the crystallographic orientation of all the grains visualized with the GBT technique [4].

Figure 1 is a schematic representation of the setup used in the pencil-beam XRD experiment, as part of the DAGT technique. Monochromatic radiation from a monochromator is collimated with a Fresnel zone plate or slit collimator to form an X-ray pencil beam to facilitate data analysis by limiting the number of diffraction spots obtained for each X-ray path. By rotating the sample through 180°, the pencil beam can scan in both the lateral and horizontal directions, thereby illuminating every location in the region of interest, from all possible directions with respect to the rotation axis of the sample, at a typical scanning step of 10 μm.

A DAGT experiment was performed using the X-ray imaging beamline **BL20XU** in SPring-8. Figure 2, in which the color of individual grains and plots is dependent on the crystallographic orientation, shows individual grains over the entire region of interest before and after plastic deformation of 27.0%. To examine

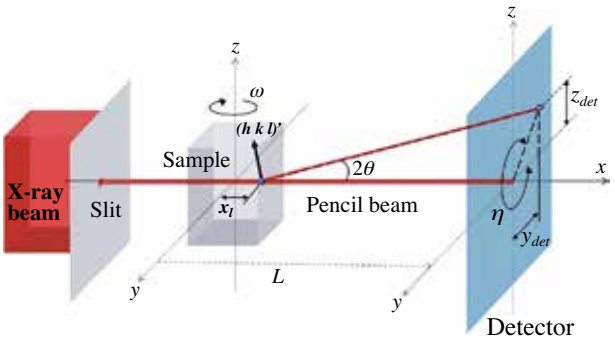

Fig. 1. Schematic diagram of the setup for the pencil-beam XRD experiments.

the texture evolution during tensile deformation, the average orientations of the grains before and after plastic deformation are represented in inverse pole figures for the loading directions in Figs. 2(c) and 2(d), respectively. Figures 2(b) and 2(d), which show the distribution of the crystallographic orientation after uniaxial tensile deformation, reveal that certain crystallographic axes are almost parallel to the tensile direction. The stereographic triangle in Fig. 2(d) clearly shows that the orientation space is subdivided into three regions, including grains with their tensile axes near the crystallographic <111> direction, along the hypotenuse, and outside these regions. The first and second groups correspond to the deformation texture characteristic to tensile deformation, which has preferential orientations of <111> and <112> in the case of aluminum alloys.

Figure 3, which illustrates such a spatially distributed orientation in a specific grain, was plotted from stacked 2D images of the orientation distribution, drawn on the corresponding *x*-*y* cross sections. Six grains are adjacent to the grain in this virtual cross section. Some of these grains share relatively wide grain-boundary areas with the grain. Some grains have average orientations close to <112>, while the others are on average close to <111>. It is interesting to note that the crystallographic orientation in the lower left side of the grain, which is adjacent to the grains having average orientations close to <112>, is different from that in the other regions; at the same time, this region exhibits intense shear strain, as shown in Fig. 3(b). The internal orientation gradient is observable in Fig. 3. The 3D observation, in which a more complex 3D grain shape is observable than in conventional 2D observation, has revealed the effects of inhomogeneous and strong interactions with selected surrounding grains.

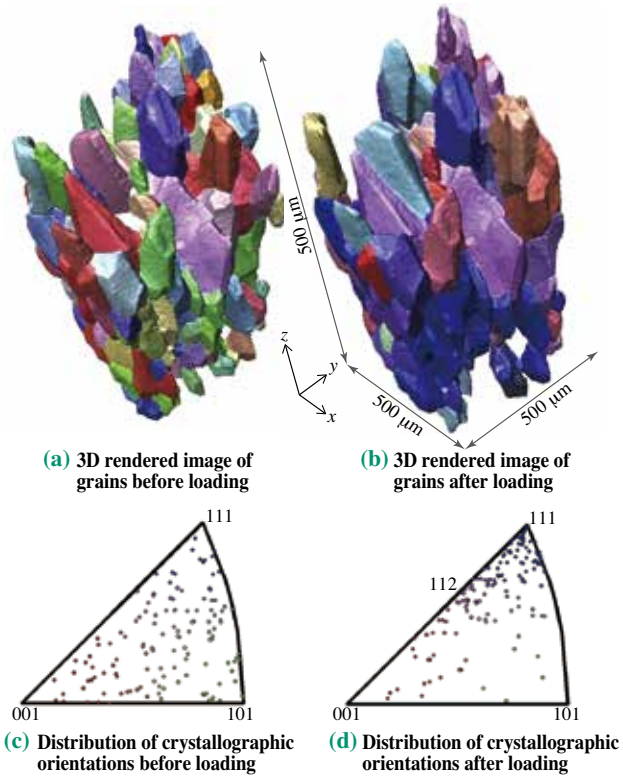

(a) 3D rendered image of grains before loading
(b) 3D rendered image of grains after loading
(c) Distribution of crystallographic orientations before loading
(d) Distribution of crystallographic orientations after loading

Fig. 2. Results of the DAGT analysis, showing the distributions of crystallographic orientations before and after loading with a plastic strain of 27.0%. The colors of the grains and inverse pole markings represent locations in the inverse pole figures: [001] oriented grains are red, [101] green, and [111] blue.

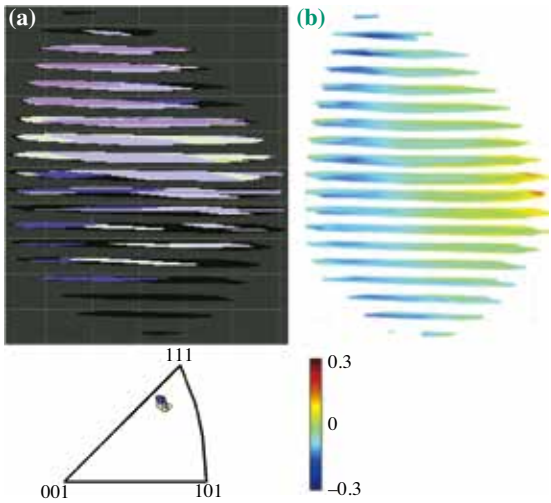

Fig. 3. Results of the DAGT analysis, showing the 3D distribution of crystallographic orientation in a grain **(a)**, and the corresponding 3D distribution of shear strain, γ_{xy} **(b)**. The colors in (a) represent the locations in the inverse pole figure.

Kyosuke Hirayama[a,*], Hiroyuki Toda[a] and Masakazu Kobayashi[b]

[a] Department of Mechanical Engineering, Kyushu University
[b] Department of Mechanical Engineering, Toyohashi University of Technology

*Email: hirayama@mech.kyushu-u.ac.jp

References

[1] L. Margulies *et al.*: Science **291** (2001) 2392.
[2] H. Toda *et al.*: Acta Mater. **61** (2013) 5535.
[3] M. Kobayashi *et al.*: Acta Mater. **56** (2008) 2167.
[4] *H. Toda, D.J. LeClere, T. Kamiko, Y. Suzuki, A. Takeuchi, K. Uesugi, M. Kobayashi: Acta Mater.* ***107*** *(2016) 310.*

Controlling photovoltage responses at $SrRuO_3/SrTiO_3$ heterostructures

Strontium titanate ($SrTiO_3$: STO) has been regarded as one of the key transition-metal oxides owing to its chemical stability, non-toxic nature, and exotic electron correlation effects. Furthermore, the perovskite structure of the STO crystal enables us to design a rich variety of layered metal oxide materials by the epitaxial growth of oxide films. Recently, the photoinduced response of STO has attracted broad interest owing to its wide range of applications including solar cells, photodiodes, photoelectrolysis, and photocatalysts. As a photovoltaic component, STO crystals have a major advantage of being transparent to visible light, enabling new uses and functionalities that are fundamentally impossible using silicon-based solar cells. Regarding the use of photoinduced phenomena in technology, the generation of the photovoltage is the most fundamental optical response, and therefore extensive studies have been carried out to clarify mechanisms in the surface photovoltage (SPV) effect. The SPV effect is induced by photoexcited carriers near a surface or an interface. Thus, the SPV effect is expected to be sensitive to surface/interface band bending (i.e., the surface/interface band alignment). However, effect of the surface/interface band alignment on the photovoltage responses, especially on technologically important oxide surfaces, has not been well studied. In this study [1], therefore, we study the band-alignment dependence of the SPV effect of STO by controlling the band alignment at the STO surface via the epitaxial growth of a $SrRuO_3$ (SRO) thin film.

We demonstrate that the photovoltage response in STO can be enhanced by more than two orders of magnitude by the epitaxial growth of a two monolayer (ML) SRO thin film (0.8 nm). Furthermore, we show that the photoresponse phenomenon can be understood from the band alignment. Since the perovskite structure has a major advantage for the fabrication of layered structures, the approach to controlling space-charge layers by the growth of an overlayer described in this study is fundamentally applicable for a variety of oxide heterojunctions, and can therefore be used to control and design optoelectronic devices such as high-efficiency photoelectrochemical devices and solar cells.

All photoemission spectroscopy (PES) experiments were conducted at SPring-8 **BL07LSU**, where synchrotron radiation (SR), the second-harmonic generation of a Ti:sapphire laser (3.05 eV), and a time-of-flight electron analyzer were synchronized. Thus, as shown in Fig. 1(a), the time-resolved measurements at a delay time (t) were performed by the pump (laser)-probe (SR) method [2]. Using a soft X-ray as a probe light, surface-sensitive experiments were performed. A two-ML thin film of SRO was epitaxially grown on a 0.05 wt% Nb-doped STO(001) substrate (Fig. 1(b)) by pulsed laser deposition (PLD). The film thicknesses were controlled by monitoring the intensity oscillations of a reflection high-energy electron diffraction spot. The STO and SRO/STO samples were cleaned by

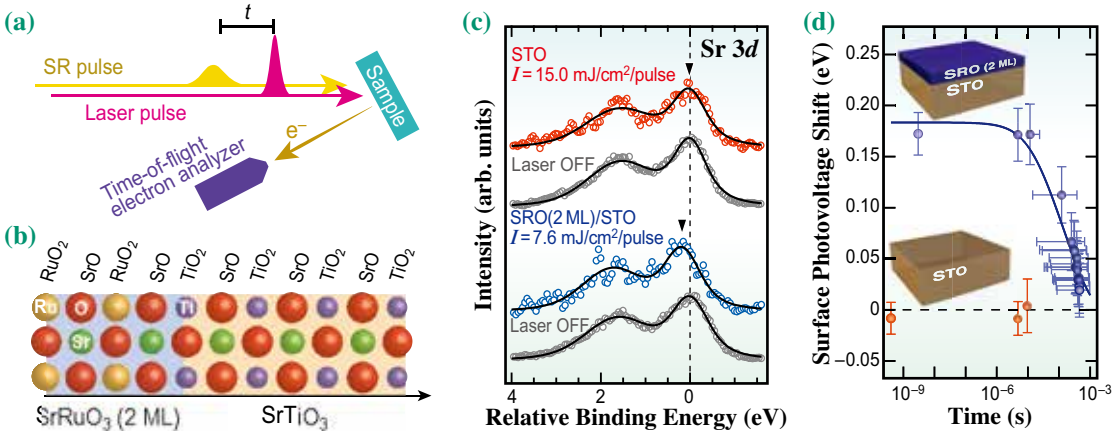

Fig. 1. **(a)** Schematic drawing of time-resolved PES measurements. **(b)** Schematic image of the atomic structure near the SRO(2 ML)/STO interface. **(c)** Energy shifts of Sr 3d peaks obtained at the STO surface and the SRO/STO interface, as monitored by time-resolved core-level spectra taken before and after pumping at a delay time of t = 9.6 μs. Here, pumping intensities of 15.0 mJ/cm^2/pulse and 7.6 mJ/cm^2/pulse were used for the STO surface and SRO/STO interface, respectively. The spectra are plotted with respect to the Sr $3d_{5/2}$ peak before optical excitation (Laser OFF). The spectra were fitted by Voigt functions with backgrounds (solid lines) and the peak positions after the excitation are indicated by triangles. **(d)** Time dependence of the SPV shifts traced by time-resolved Sr 3d core-level PES measurements at STO (orange circles) and SRO/STO (blue circles). The solid curve shows the fitting result for the SRO/STO interface using the thermionic relaxation model [3].

annealing at 650°C under an oxygen pressure of 1×10^{-3} Pa for 60 min after introducing the samples into an ultrahigh vacuum (UHV) chamber.

Figure 1(c) shows Sr 3*d* PES spectra of the surfaces of STO and SRO/STO taken at t = 9.6 μs. Compared with the laser off position, the spectra show a clear shift of the peak position at the SRO/STO surface but not at the STO surface. This energy shift indicates the generation of SPV only at the SRO/STO surface. The relaxation of the SPV shifts is plotted in Fig. 1(d), where a relaxation time constant of 0.77 ms is obtained for the SRO/STO surface using a thermionic relaxation model [3].

Since the photoinduced phenomena result from the dynamics of the photoexcited carriers, which are governed by the electronic potential induced by the interface electronic structure, the drastic difference in the photoresponse between the SRO/STO interface and STO surface can originate from the band-bending structure near the surface/interface. Thus, in order to determine the band alignments, valence band (Fig. 2(a)) and Ti 2*p* (Fig. 2(b)) PES spectra were measured. The downward band-bending structure at the STO surface was determined from the energy position of the valence band maximum (VBM), indicating the formation of an accumulation layer at the STO surface as shown in Fig. 2(c). On the other hand, the upward band-bending structure at the SRO/STO interface was determined from the energy difference of the Ti 2*p* peak positions between the STO surface and SRO/STO interface, indicating the formation of a depletion layer at the interface (Fig. 2(d)) owing to the formation of Schottky barriers. From the experimentally obtained conduction band minimum (CBM) positions, depth profiles of the carrier electron density in the STO substrates were simulated by self-consistently solving the Poisson-Schrödinger equations [4]. The calculated results reveal significant differences in the relaxation width of the band-bending structures. The potential variation on the bare STO surface indicates the strongly localized nature of the accumulated electrons near the surface (<3 nm). On the other hand, the depletion layer in the SRO/STO heterostructure was found to have a much longer relaxation length (>40 nm). The calculated results also show that the mean density of carrier electrons is about 200 times larger at the accumulation layer of the STO surface than at the depletion layer of the SRO/STO interface. The large mean density of the carrier electrons at the STO surface prevents the generation of SPV due to the pinning effect. Therefore, a higher laser intensity by more than two orders of magnitude is required for the STO surface to induce the same amount of the SPV shift as that induced for the SRO/STO interface when the number of photoexcited carriers is proportional to the laser intensity.

In summary, we have demonstrated that the interface electrostatic potential and the photovoltage responses in a metal oxide heterostructure can be controlled by atomic-scale design of the layered heterostructure. In the SRO/STO system, the character of the STO space-charge layer can be changed from an accumulation type to a depletion type by the growth of the SRO film. The resulting optical responses of STO are enhanced by more than two orders of magnitude.

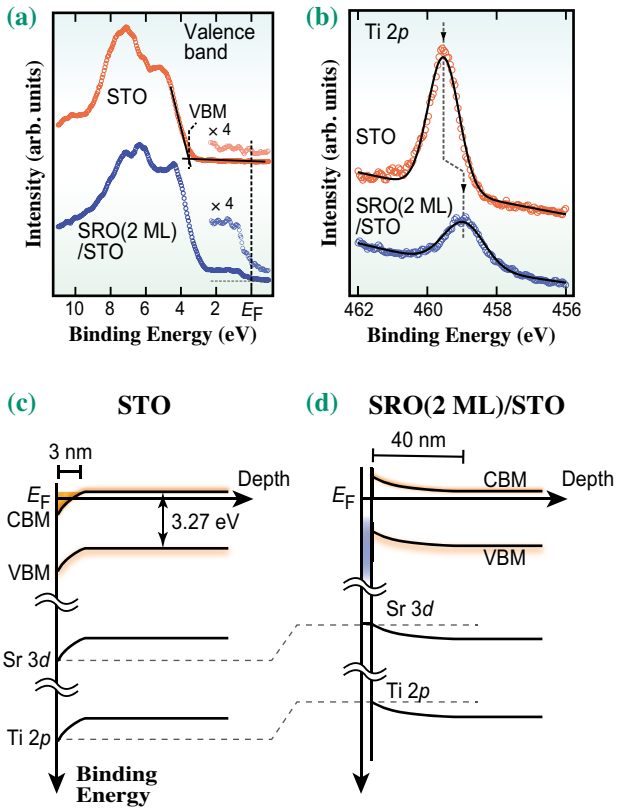

Fig. 2. **(a, b)** Valence band (a) and Ti 2*p* (b) photoelectron spectra of the STO surface and SRO(2 ML)/STO interface. **(c, d)** Band diagrams of the STO surface (c) and SRO(2 ML)/STO (d).

Ryu Yukawa*,†, Susumu Yamamoto and Iwao Matsuda

Institute for Solid State Physics, The University of Tokyo

*Email: ryukawa@post.kek.jp

† Present address: Institute of Materials Structure Science, KEK

References

[1] *R. Yukawa, S. Yamamoto, K. Akikubo, K. Takeuchi, K. Ozawa, H. Kumigashira, and I. Matsuda: Adv. Mater. Interfaces* **3** *(2016) 1600527.*
[2] M. Ogawa *et al.*: Rev. Sci. Instrum. **83** (2012) 023109.
[3] D. Bröcker *et al.*: Chem. Phys. **299** (2004) 247.
[4] R. Yukawa *et al.*: Surf. Sci. **641** (2015) 224.

Sub-nanometer resolution of atomic motion during electronic excitation in phase-change materials

Optical recording materials such as those used for DVD-RAM are semiconducting chalcogen compounds largely composed of Te and the class of such compounds is often referred to as phase-change materials (PCMs). To date, the typical time for phase change between the amorphous and crystalline states has been thought to be on the order of a nanosecond. In recent years, however, first-principles calculations have predicted that by use of electronic excitation, such transitions can be made to occur on picosecond time scales. If these predictions are realized, both low power operation and high data throughput of phase-change memory will be possible.

By intentionally creating an excited state in a solid, it is possible to induce displacements in atomic positions allowing manipulation of the crystal structure of the solid [1]. The displacements of atomic positions in an excited state, however, occur typically on sub-nanometer length scales making it impossible to detect such small changes using visible laser light with a wavelength of several hundred nanometers. In order to measure such small changes in atomic position on picosecond time scales, it is necessary to use sub-nanometer wavelength light from an X-ray laser in a measurement such as time-resolved X-ray diffraction (XRD). We have used the free-electron X-ray laser facility, SACLA **BL3**, to carry out time-resolved XRD measurements of the atomic motion in an optically excited phase-change material [2].

In the experiment, epitaxial $Ge_2Sb_2Te_5$ films (thickness 35 nm) grown on a silicon substrate were excited with ultrashort laser light (30 fs, 800 nm). In order to capture the resulting atomic motion after excitation, XFEL pulses (10 fs, 10 keV) were used to stroboscopically observe changes in the sample structure using a multiple port readout CCD (MPCCD) detector to record time-resolved XRD images (Fig. 1). The (222) diffraction plane was chosen for observation in the time-resolved diffraction experiments and changes in both the location and intensity of the XRD peaks were observed with sub-picosecond time resolution (Fig. 2). In addition, as the (222) diffraction vector probed atomic displacements normal to the surface, the symmetry of the diffraction geometry was optimal for observing the atomic displacements induced by the pump laser. In this way, the changes in the positions of the atoms constituting the $Ge_2Sb_2Te_5$ single crystal could be followed on an ultrafast sub-picosecond time scale.

The displacement of atoms was found to reach a maximum at about 20 ps (Fig. 2(b)) after the laser pump pulse resulting in a maximum diffraction peak shift (0.05 $Å^{-1}$) with a corresponding atomic displacement of about 2 picometers. Subsequently after a few ns, the atom positions were found to revert to their original positions. Shifts to lower angles of the XRD peaks reflect an increase in the lattice spacing of the crystal, while reductions in the intensity of the peaks reflect an increase in the magnitude of mean square vibrations of the atoms around their average positions (Debye-Waller Effect). The changes are schematically indicated in the bottom of Fig. 1, which visualizes the initial lattice softening resulting from bond breaking (frame I) and the following local atomic rearrangements induced by the electronic excitation (frame II). Subsequent to this, electron-phonon interactions induce a rapid rise in the lattice temperature leading to an expansion of the lattice plane spacing (frame III).

As shown in Fig. 3(a) the diffraction peak intensity does not fully recover even 1.8 ns after excitation due to residual thermal effects, which completely disappear after 3~5 ns depending on the excitation fluence. The return of the diffraction peak to its initial intensity level demonstrates that the $Ge_2Sb_2Te_5$ film is not amorphized by the laser pump pulse and that the pump-probe process is fully reversible. For finer

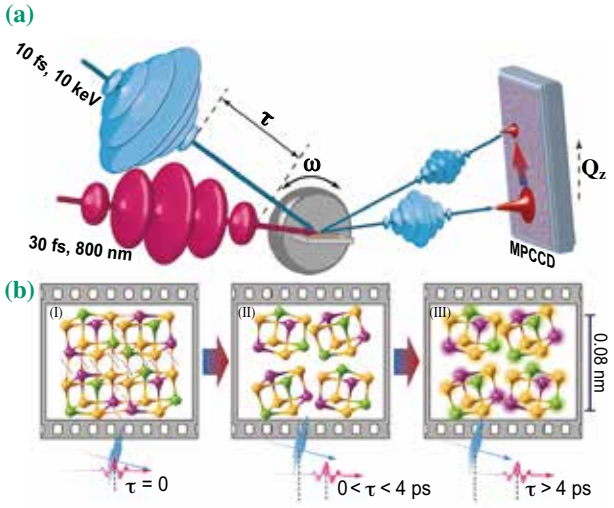

Fig. 1. **(a)** A schematic representation of the pump-probe time-resolved XRD technique. ω represents the rotation of the sample and Q_z represents the scattering vector. **(b)** Frames (I) to (III) show schematic changes in the $Ge_2Sb_2Te_5$ single crystal induced by the femtosecond excitation pulse. Ge atoms are shown in green, Te atoms – in yellow, and Sb atoms are shown in purple.

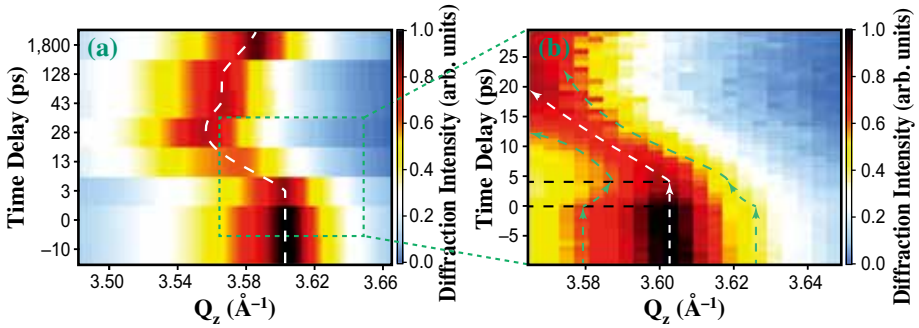

Fig. 2. Time-resolved changes in (222) plane XRD signal. White dashed line indicates the peak position of the signal and green dashed lines show the change of whole diffraction spot. **(a)** Changes in the XRD peak from –10 ~ +1800 ps (1.8 ns) are shown. The horizontal axis is the scattering vector. **(b)** Changes in the XRD peak from –10 ~ +30 ps are shown in magnified form.

delay time steps for times up to 10 ps (Fig. 3(b)), we found different dynamics between the diffraction peak intensity and the corresponding peak position shift after excitation that is clearly indicated by an inflection point in the time-dependent diffraction intensity curve and the absence of a diffraction peak position change until 4 ps. These observations indicate the lack of thermal effects immediately after laser exposure.

The current research results suggest that the phase change process in both rewritable optical recording films and nonvolatile memory phase-change materials can occur on picosecond time scales. Also recently it was found that similar sub-picosecond processes occur in thin film GeTe/Sb_2Te_3 superlattices [3]. The application of the current techniques to phase change in superlattices may lead to future generations of phase-change material based devices that switch at sub-terahertz rates while offering lower power operation than the current generation of $Ge_2Sb_2Te_5$ polycrystalline films.

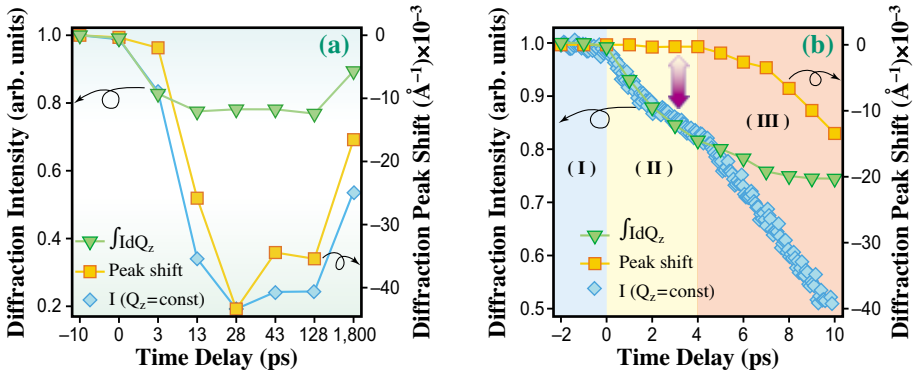

Fig. 3. **(a)** Normalized integrated diffraction intensity (inverted triangles) and corresponding peak position shift along Q_z (squares), together with normalized integrated diffraction intensity (diamonds) for a fixed X-ray beam angle of incidence as a function of time up to 1800 ps. **(b)** The same as (a) but for a finer time delay step up to 10 ps. The both-side arrow indicates the different dynamics between the diffraction integrated intensity and the peak position. The three stages labeled (I), (II), and (III) correspond to the atomic configuration process in Fig. 1.

Kirill V. Mitrofanov[a], Paul Fons[a] and Muneaki Hase[a,b,*]

[a] Nanoelectronics Research Institute, National Institute of Advanced Industrial Science and Technology
[b] Division of Applied Physics, Faculty of Pure and Applied Sciences, University of Tsukuba

*Email: mhase@bk.tsukuba.ac.jp

References

[1] A.V. Kolobov *et al.*: Nat. Chem. **3** (2011) 311.
[2] *K. V. Mitrofanov, P. Fons, K. Makino, R. Terashima, T. Shimada, A. V. Kolobov, J. Tominaga, V. Bragaglia, A. Giussani, R. Calarco, H. Riechert, T. Sato, T. Katayama, K. Ogawa, T. Togashi, M. Yabashi, S. Wall, D. Brewe and M. Hase: Sci. Rep.* ***6*** *(2016) 20633.*
[3] M. Hase *et al.*: Nat. Commun. **6** (2015) 8367.

Observation of femtosecond X-ray damage processes via X-ray pump–X-ray probe scheme

Since the discovery of X-rays in the 19th century, scientists have continuously endeavored to develop brighter X-ray sources. One of the most remarkable breakthroughs is the emergence of synchrotron light sources, which generate brilliant X-ray beams with intensity many orders of magnitude higher than those of X-rays generated previously. Such brilliant X-rays have provided a pathway to the measurement of high-quality X-ray scattering data, which has enabled the structure determination of complex systems including giant proteins, functional units of living organisms, and viruses. However, the increase in brilliance is also accompanied by the severe problem of X-ray radiation damage to the samples. For precise structure determination, a sufficient scattering signal should be recorded before the samples are severely damaged. The problem of radiation damage was considered to be an intrinsic issue associated with X-ray scattering experiments, setting a fundamental limit on the resolution in X-ray structure determination.

X-ray Free Electron Lasers (XFELs), which generate femtosecond X-ray pulses, may completely avoid the problem of radiation damage. In the first several femtoseconds after the irradiation of an X-ray beam, it has been predicted that atoms do not change their positions owing to inertia [1]. Thus, the ultrashort pulse duration of XFEL light allows us to use intense X-ray radiation beyond the conventional X-ray dose limit. This innovative concept, known as '*diffraction before destruction*' has paved a clear way to the high-resolution structure determination of weak scattering objects, including nanometer-size protein crystals and non-crystalline biological particles. Moreover, structural determination of a single biomolecule with atomic resolution is expected as an ultimate application of XFELs.

Despite the potential impact of XFELs on structure determination, a detailed understanding of the femtosecond X-ray damage processes has been lacking. In particular, evaluation of the ignition time of the atomic displacement, which is crucial for realizing advanced XFEL applications, has not yet been investigated. Although improving our knowledge of the X-ray damage processes is essential for all aspects of XFEL science, experimental verifications have not been realized owing to the extreme difficulty of carrying out observations with ultrahigh space (ångstrom) and time (femtosecond) resolutions. As a new approach to investigating the femtosecond X-ray damage processes, we have developed an X-ray pump–X-ray probe scheme at SACLA **BL3** and investigated the femtosecond X-ray damage processes in diamond [2].

A schematic illustration of the experiment is shown in Fig. 1. We operated the XFEL source in a two-color twin-pulse mode [3]. Here, the eight upstream undulators were tuned to generate a 6.1 keV X-ray pulse to excite (i.e., pump) the sample. The remaining undulators generated a 5.9 keV X-ray pulse to probe the temporal changes in the crystalline structure of diamond through Bragg reflection. The time interval between the twin pulses was controlled by a magnetic chicane located downstream of the eighth undulator. The X-ray intensity was increased up to ~10^{19} W/cm^2 with a two-stage focusing system [4]. Note that this intensity is almost the highest value achievable at current XFEL facilities. We set a thin diamond film at the focal point and measured the Debye-Scherrer rings of the 111 and 220 reflections with two multiport

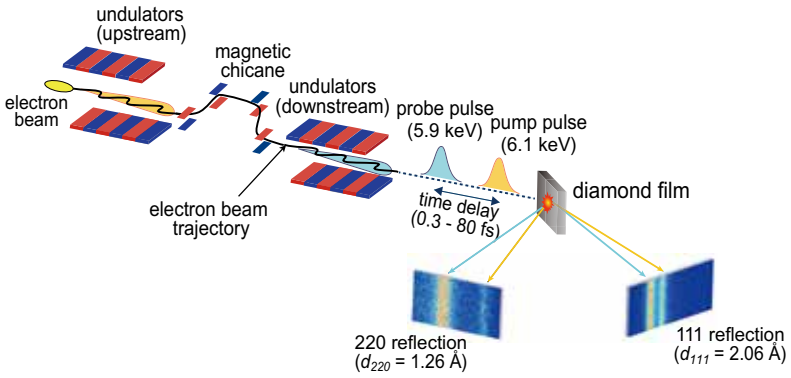

Fig. 1. Schematic illustration of X-ray pump–X-ray probe experiment at SACLA BL3. Twin XFEL pulses with tunable time separation were generated by the two-color twin pulse mode of SACLA. The XFEL pulses, which were focused with X-ray mirrors, irradiated a thin film of diamond powder crystals. Debye-Scherrer rings of 111 and 220 reflections in the horizontal direction were measured using two MPCCD detectors.

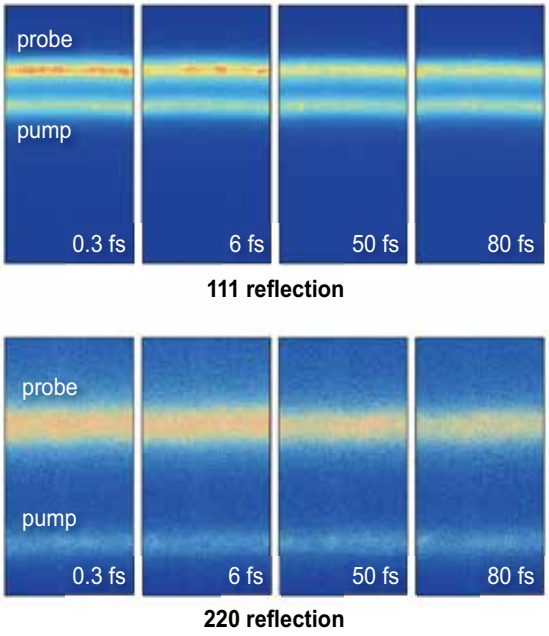

Fig. 2. MPCCD images of 111 and 220 Bragg reflection images at time intervals between pump and probe pulses of 0.3 fs, 0.6 fs, 50 fs, and 80 fs, which were averaged over multiple shots with specific fluences of the pump ($(3.1\pm0.2)\times10^4$ J·cm^{-2}) and probe ($(6.9\pm1.1)\times10^4$ J·cm^{-2}) pulses.

charge-coupled device (MPCCD) detectors.

Figure 2 shows MPCCD images of the 111 and 220 reflections, which were averaged over multiple shots with specific fluences of the pump and probe pulses. In the reflection patterns of both the 111 and 220 reflections, we can observe two well-separated diffraction peaks, reflecting the differences in the Bragg angles for the pump and probe pulses. For both the 111 and 220 reflections, the pump diffraction intensities were almost constant regardless of the time separation between the twin pulses, which indicates that little radiation damage occurred during the irradiation of the pump pulse. In contrast, the probe diffraction intensities gradually decreased as the time separation increased. We consider that these changes were indicative of X-ray-induced atomic displacement.

To quantitatively analyze the X-ray damage processes, we assumed that the displacements of the carbon atoms were independent and random with a mean of zero. Under this assumption, the diffraction intensity of Bragg reflection is reduced by a factor of $\exp(-q^2\sigma^2)$, where q is the scattering vector and σ is the root-mean-square displacement perpendicular to the Bragg plane. Using this representation of the diffraction intensities, we evaluated temporal changes in the atomic displacement perpendicular to the (111) and (220) planes (σ_{111}, σ_{220}). Figure 3 shows the temporal changes in σ_{111} and σ_{220} for three different pump pulse fluences. In all cases, σ_{111} and σ_{220} rapidly increased 20 fs after irradiation of the pump pulse, indicating that the critical time for the ignition of the X-ray-induced structural changes was 20 fs for the present fluences of the pump pulses. This result proves that sub-10-fs XFEL pulses enable damageless structural determinations and supports the validity of the theoretical predictions of ultraintense X-ray–matter interactions.

The X-ray pump–X-ray probe scheme demonstrated here is expected to be a highly effective way of exploring femtosecond X-ray–matter interactions due to its ultrahigh time and space resolution. This scheme should contribute to verifying and improving the theory of X-ray interactions with matter and stimulate advanced XFEL applications, as well as the investigation of exotic states of matter generated by intense X-ray irradiation.

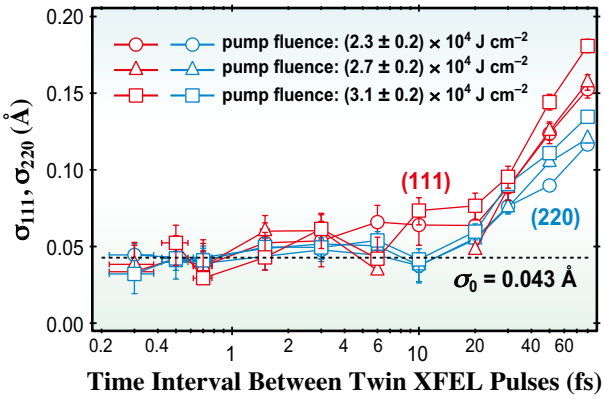

Fig. 3. Temporal changes in atomic displacement in diamond after irradiation of probe pulses for different fluences of pump pulses ($(2.3\pm0.2)\times10^4$ J cm^{-2}, $(2.7\pm0.2)\times10^4$ J cm^{-2}, and $(3.1\pm0.2)\times10^4$ J cm^{-2}). The atomic displacement of carbon atoms in diamond in the undamaged state ($\sigma=0.043$ Å) is also shown for comparison.

Ichiro Inoue[a,*] and Makina Yabashi[a,b]

[a] RIKEN SPring-8 Center
[b] Japan Synchrotron Radiation Research Institute (JASRI)

*Email: inoue@spring8.or.jp

References

[1] R. Neutze *et al.*: Nature **406** (2000) 752.
[2] T. Hara *et al.*: Nat. Commun. **4** (2013) 2919.
[3] *I. Inoue, Y. Inubushi, T. Sato, K. Tono, T. Katayama, T. Kameshima, K. Ogawa, T. Togashi, S. Owada, Y. Amemiya, T. Tanaka, T. Hara and M. Yabashi: Proc. Natl. Acad. Sci. USA* ***113*** *(2016) 1492.*
[4] H. Mimura *et al.*: Nat. Commun. **5** (2014) 3539.

Interference between ϕ and $\Lambda(1520)$ photoproduction channels

The ϕ-$\Lambda(1520)$ interference effect in the $\gamma p \rightarrow K^+K^-p$ reaction has been measured for the first time in the energy range from 1.673 to 2.173 GeV at SPring-8 **BL33LEP** [1]. The relative phases between ϕ and $\Lambda(1520)$ production amplitudes were obtained in the kinematic region where the two resonances overlap. The measurement results support the occurrence of strong constructive interference when K^+K^- pairs are observed at forward angles but destructive interference for proton emission at forward angles. This fact suggests possible exotic structures such a hidden-strangeness pentaquark state, a new Pomeron exchange or rescattering processes via other hyperon states.

ϕ-meson production has the unique feature within gluon dynamics of being a result of OZI suppression due to the dominant $s\bar{s}$ structure of the ϕ meson, which is predicted to proceed via a Pomeron trajectory with $J^{PC} = 0^{++}$. Cross sections for diffractive ϕ photoproduction are thus predicted to increase smoothly with photon energy, as shown in Fig. 1(a). However, a bump structure at $\sqrt{s} = 2.1$ GeV in forward differential cross sections was first reported by the LEPS collaboration [2]. Recent theoretical studies have related this to a coupling between the ϕp and $K^+\Lambda(1520)$ channels, because the bump structure was observed to be very close to the threshold of $\Lambda(1520)$ production. The ϕ-$\Lambda(1520)$ interference may also account for the bump structure, but it has not yet been measured in K^+K^-p photoproduction. Despite extensive experimental effort devoted to the photoproduction of ϕ mesons near the threshold, the nature of the bump structure has not yet been explained in detail.

The experiment was carried out using the LEPS detector at BL33LEP. Linearly polarized photons with energies from 1.5 to 2.4 GeV were incident on a 15 cm liquid-hydrogen target, in which K^+, K^- and p particles were produced and then passed through the LEPS spectrometer (Fig. 2).

The measured K^+K^- and K^-p mass spectra for the selected K^+K^-p events were fitted with lineshapes from processes simulating the ϕp, $\Lambda(1520)K^+$ and non-resonant K^+K^-p channels. The best-fit lineshapes for ϕ, $\Lambda(1520)$ and non-resonant K^+K^-p well reproduce the K^+K^- and K^-p mass spectra, as shown in Fig. 3.

The fits with Monte Carlo lineshapes were based on the events beyond the ϕ-$\Lambda(1520)$ interference region in which the two resonances appear. The fit results were then interpolated into the interference region, keeping the magnitudes of the Monte Carlo lineshapes determined from the fit. This simultaneous fit with Monte Carlo lineshapes is a self-consistent method of reproducing the measured K^+K^- and K^-p mass spectra.

Forward differential cross sections for the ϕ and $\Lambda(1520)$ production channels were measured using the best-fit results with Monte Carlo lineshapes in the ϕ and $\Lambda(1520)$ mass bands except for the interference region. We reconfirmed the existence of the bump structure around $E_\gamma = 2.0$ GeV. The differential cross sections for $\Lambda(1520)$ photoproduction in the forward

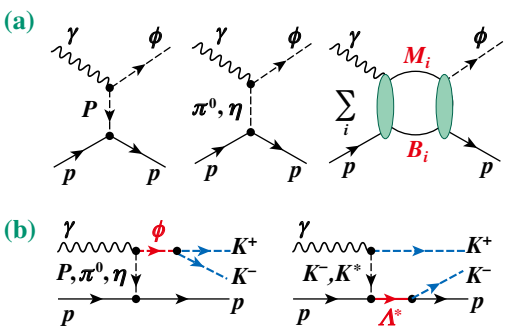

Fig. 1. **(a)** Diagrams showing the dominant photoproduction of ϕ meson from proton. **(b)** Photoproduction of K^+K^-p via ϕ and $\Lambda(1520)$ resonances produced by Pomeron and K/K^* exchanges, respectively.

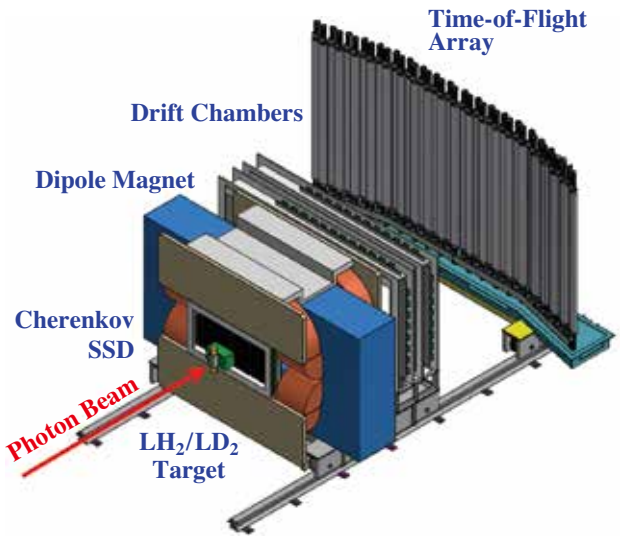

Fig. 2. Schematic view of the LEPS experimental setup for the photoproduction of hadrons at BL33LEP beamline.

angular regions are compared with the previous LEPS results [3]. Interestingly, the two cross-section results show the bump structure at the same E_γ, which may indicate a strong correlation between ϕ and $\Lambda(1520)$. However, the difference between the cross sections obtained with and without the interference region is not large enough to account for the bump structure. For forward K^+K^- events in the energy region of $1.973 < E_\gamma < 2.073$ GeV, the integrated event yield in the interference region approaches close to the maximum bound for the ϕ-Λ interference. Moreover, the relative phase flips its sign as a function of photon energy E_γ. For K^-p events, the relative phase in the energy region of $1.973 < E_\gamma < 2.073$ GeV clearly remains at a positive value, while in other energy regions it indicates destructive interference.

In summary, the photoproduction of the $\gamma p \rightarrow K^+K^-p$ reaction was measured using the LEPS detector at energies from 1.57 to 2.40 GeV. The ϕ-$\Lambda(1520)$ interference measurement is a good probe for studying the origin of enhanced production cross sections for ϕ and $\Lambda(1520)$ near $\sqrt{s} = 2.1$ GeV. We observed clear ϕ-$\Lambda(1520)$ interference effects in the energy range from 1.673 to 2.173 GeV. The data obtained in the present study provide the first-ever experimental evidence for the ϕ-$\Lambda(1520)$ interference effect in ϕ photoproduction. The relative phases suggest strong constructive interference for K^+K^- pairs observed at forward angles, while destructive interference results from the emission of protons at forward angles. The nature of the bump structure may originate from interesting exotic structures such as a hidden-strangeness pentaquark state, a new Pomeron exchange or rescattering processes via other hyperon states.

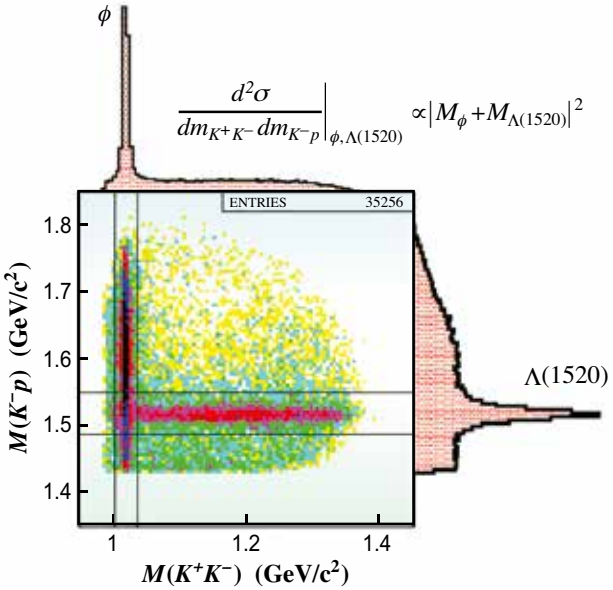

Fig. 3. Scatter plot of the invariant mass of the K^+K^- system *versus* that of the K^-p system with projections onto each invariant mass axis.

Sun Young Ryu for the LEPS Collaboration

Research Center for Nuclear Physics, Osaka University

Email: syryu@rcnp.osaka-u.ac.jp

References

[1] *S. Y. Ryu, J.K. Ahn, T. Nakano, D.S. Ahn, S. Ajimura, H. Akimune, Y. Asano, W.C. Chang, J.Y. Chen, S. Daté, H. Ejiri, H. Fujimura, M. Fujiwara, S. Fukui, S. Hasegawa, K. Hicks, K. Horie, T. Hotta, S.H. Hwang, K. Imai, T. Ishikawa, T. Iwata, Y. Kato, H. Kawai, K. Kino, H. Kohri, Y. Kon, N. Kumagai, P.J. Lin, Y. Maeda, S. Makino, T. Matsuda, N. Matsuoka, T. Mibe, M. Miyabe, M. Miyachi, Y. Morino, N. Muramatsu, R. Murayama, Y. Nakatsugawa, S. Nam, M. Niiyama, M. Nomachi, Y. Ohashi, H. Ohkuma, T. Ohta, T. Ooba, D.S. Oshuev, J.D. Parker, C. Rangacharyulu, A. Sakaguchi, T. Sawada, P.M. Shagin, Y. Shiino, H. Shimizu, E.A. Strokovsky, Y. Sugaya, M. Sumihama, A.O. Tokiyasu, Y. Toi, H. Toyokawa, T. Tsunemi, M. Uchida, M. Ungaro,28 A. Wakai, C.W. Wang, S.C. Wang, K. Yonehara, T. Yorita,1 M. Yoshimura, M. Yosoi and R.G.T. Zegers: Phys. Rev. Lett.* ***116*** *(2016) 232001.*
[2] T. Mibe *et al.*: Phys. Rev. Lett. **95** (2005) 182001.
[3] H. Kohri *et al.*: Phys. Rev. Lett. **104** (2010) 172001.

Synchrotron radiation Mössbauer spectroscopy for ^{61}Ni nanoparticles

Mössbauer spectroscopy is a well-established and effective method in physics, chemistry, biology and Earth science. It provides element-specific information on the electronic states of each constituent in complex materials, such as valence and magnetism. Most Mössbauer studies have been performed using ^{57}Fe and ^{119}Sn with γ-rays from radioactive isotope (RI) sources, although the Mössbauer effect has been observed in approximately 100 nuclides of nearly 50 elements (Fig. 1). One major difficulty in Mössbauer spectroscopy using nuclides other than ^{57}Fe and ^{119}Sn is the preparation of RI sources. With the exception of ^{57}Fe and ^{119}Sn (purchasable), we should synthesize the RI using a reactor or an accelerator, as is also the case with ^{61}Ni Mössbauer spectroscopy. This difficulty is avoided by using synchrotron radiation (SR); we can extract X-rays with an appropriate energy for Mössbauer spectroscopy from SR. Furthermore, the high brilliance of SR facilitates Mössbauer measurement for materials under extreme conditions, such as high pressures. SR-based Mössbauer absorption spectroscopy is one such method in the energy domain [1], and measurement using the many nuclides shown in Fig. 1 is promising. Recently, the measurement efficiency of this method was drastically improved [2]. Thus, although the natural abundance of ^{61}Ni is only 1.14%, it has become realistic to perform the SR-based Mössbauer absorption spectroscopy of Ni samples including nanoparticles without expensive isotope enrichment.

The hexagonal close-packed (hcp) structure is known to be the metastable state for Ni metal. Recently, hcp-Ni nanoparticles have been synthesized by many groups using chemical reduction methods because hcp-Ni nanoparticles are expected to show novel functionality different from that of typical face-centered cubic (fcc) Ni, such as catalytic action. However, it has been suspected that the nanoparticles formed nickel carbide (Ni_3C) in which the Ni arrangement is the same as that in hcp-Ni; hcp-Ni and Ni_3C can hardly be distinguished by X-ray diffraction (XRD). Furthermore, the magnetism of hcp-Ni is still debated. Theoretical calculations predicted the ferromagnetism of hcp-Ni with an atomic magnetic moment similar to that of fcc-Ni of approximately 0.6 μ_B (μ_B: Bohr magneton). In contrast, the experimentally observed magnetization of hcp-Ni nanoparticles is at most one-fifth of that of fcc-Ni. Since Ni_3C is non-magnetic, this discrepancy also casts doubts. Still, other possible factors should be considered: surface oxidization, magnetic impurities, and so forth. To study hcp-Ni nanoparticles in detail, we performed measurements using ^{61}Ni SR-based Mössbauer absorption spectra.

The experimental setup for ^{61}Ni SR-based Mössbauer absorption spectroscopy is shown in Fig. 2. The experiments were performed at SPring-8 **BL09XU** and **BL11XU**. The operating mode of the electron-storage ring was the "203 bunch" mode, where SR with the energy of ^{61}Ni nuclear resonance is transmitted by a sample in a cryostat. The samples were Ni metal (1 mm thickness at 20 K) or hcp-Ni nanoparticles (0.9 g (component Ni)/cm^2 at 4 K). The nanoparticles were synthesized by a chemical reduction method and coated with polyvinylpyrrolidone. Their crystallite size was around 40 nm as determined by XRD. Both samples were without ^{61}Ni enrichment. Then, the SR was scattered by $^{61}Ni_{0.86}V_{0.14}$ (enrichment: 86.2%) foil at typically 30 K in another vacuum cryostat. The nuclear resonance energy of the foil was scanned using the Doppler effect by controlling its velocity. An eight-element Si avalanche photodiode (APD) detector was built in the vacuum cryostat of the Ni-V foil, and

H		Elements including nuclides where Mössbauer effect has been observed															He
Li	Be												B	C	N	O	F	Ne
Na	Mg	Elements without nuclides where Mössbauer effect has been observed											Al	Si	P	S	Cl	Ar
K	Ca	Sc	Ti	V	Cr	Mn	Fe	Co	Ni	Cu	Zn	Ga	Ge	As	Se	Br	Kr	
Rb	Sr	Y	Zr	Nb	Mo	Tc	Ru	Rh	Pd	Ag	Cd	In	Sn	Sb	Te	I	Xe	
Cs	Ba	*	Hf	Ta	W	Re	Os	Ir	Pt	Au	Hg	Tl	Pb	Bi	Po	At	Rn	
Fr	Ra	**	104~															
*Lanthanide		La	Ce	Pr	Nd	Pm	Sm	Eu	Gd	Tb	Dy	Ho	Er	Tm	Yb	Lu		
**Actinide		Ac	Th	Pa	U	Np	Pu	Am	Cm		Cf	Es	Fm	Md	No	Lr		

Fig. 1. Table of elements exhibiting Mössbauer effect.

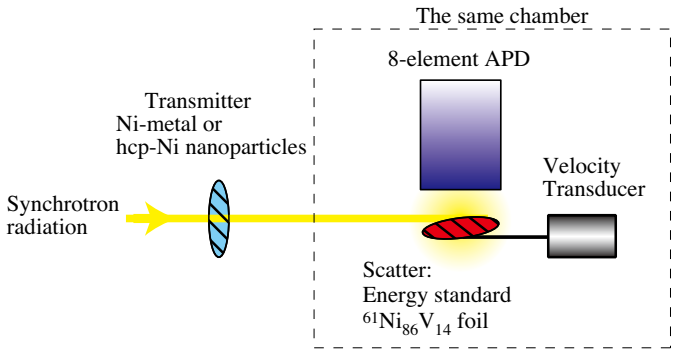

Fig. 2. Schematic drawing of the developed X-ray windowless system for ^{61}Ni SR-based Mössbauer absorption spectroscopy.

thus there was no X-ray window between the foil and detector, whereas such a window was used in the previous measurement system reported in Ref. 1. This X-ray windowless system [2] drastically improves the detection rate of signals, because both X-rays and electrons can be detected as the emission from the foil, and the distance between the foil and detector can be short, giving a large solid angle for the detector subtended at the foil. Since nuclear resonant scattering (NRS) by ^{61}Ni is emitted with a delay (half-life 5.34 ns), the NRS was separated from the strong immediate electronic scattering by setting a time window of 3 ns to 20 ns after the SR incidence. The detail of the measurement system is given in Ref. 3.

The ^{61}Ni Mössbauer spectra of bulk fcc-Ni metal and hcp-Ni nanoparticles are shown in Fig. 3. We successfully obtained the spectra within 20 h. The spectrum of the bulk shows a magnetic hyperfine field of 7.7±0.2 T, which agrees well with previous results. The spectrum of the hcp-Ni nanoparticles was reasonably analyzed by assuming one component with a magnetic hyperfine field of 3.4±0.9 T. It does not show a secondary component, such as a 7.7 T (fcc-Ni) or 10 T (nickel oxide NiO) component, and thus the contamination of fcc-Ni and NiO due to surface oxidization of the nanoparticles was below the statistical error of the spectrum. The 3.4 T field also disagrees with that of non-magnetic Ni_3C. One likely substance for this magnetic hyperfine field is the presence of nickel carbide with less carbon than Ni_3C. In fact, carbon might be supplied during the synthesis. Fang *et al.* [4] calculated the decrease in the atomic magnetic moment of Ni in NiC_x as x increases in the framework of ferromagnetic order. In the framework, the 3.4 T field corresponds to an atomic magnetic moment of 0.3 μ_B under a proportionality assumption similar to that for fcc-Ni, where 7.7 T corresponds to 0.6 μ_B. From the value of 0.3 μ_B, the chemical composition of the nanoparticles is $NiC_{0.1}$ using the calculation in Ref. 4.

In summary, we observed ^{61}Ni SR-based Mössbauer absorption spectra of hcp-Ni nanoparticles using an X-ray windowless system. Although the nanoparticles were not enriched, we successfully obtained the spectrum within 20 h. The Mössbauer spectrum of hcp-Ni revealed that the impurity levels of fcc-Ni and NiO were below the detectable limit, and the nanoparticles consisted of a single component. The spectrum shows the magnetic hyperfine field of 3.4±0.9 T at 4 K, corresponding to an atomic magnetic moment of 0.3 μ_B. This can be understood as corresponding to nickel carbide ($NiC_{0.1}$). Note that this method is also effective for the detailed study of many materials containing Ni. In fact, ^{61}Ni Mössbauer spectroscopy of the cathode material of a Li-ion battery and a Ni-substituted protein has already been measured using this system [5].

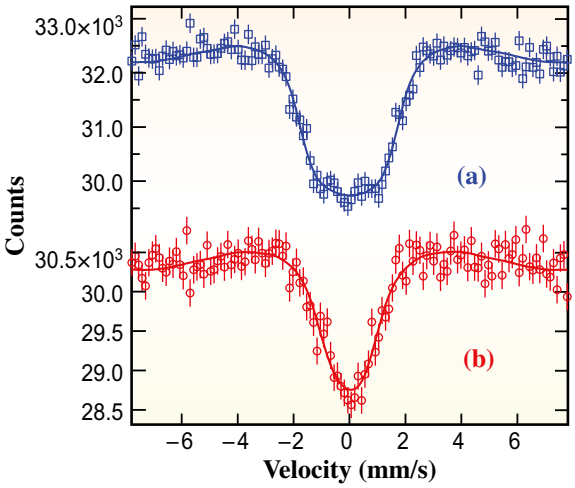

Fig. 3. ^{61}Ni SR-based Mössbauer absorption spectra of **(a)** Ni metal and **(b)** hcp-Ni nanoparticles. The open circles and squares are experimental data and the lines were fitted by the formulas discussed in Ref. 1.

Ryo Masuda and Makoto Seto*

Research Reactor Institute of Kyoto University

*Email: seto@rri.kyoto-u.ac.jp

References

[1] M. Seto *et al.*: Phys. Rev. Lett. **102** (2009) 217602.
[2] R. Masuda *et al.*: Appl. Phys. Lett. **104** (2014) 082411.
[3] *R. Masuda, Y. Kobayashi, S. Kitao, M. Kurokuzu, M. Saito, Y. Yoda, T. Mitsui, K. Hosoi, H. Kobayashi, H. Kitagawa and M. Seto: Sci. Rep.* ***6*** *(2016) 20861.*
[4] C.M. Fang *et al.*: Phys. Rev. B **86** (2012) 134114.
[5] T. Segi *et al.*: Hyperfine Interact. **237** (2016) 7; L.B. Gee *et al.*: Inorg. Chem. **55** (2016) 6866.

Structural stability originating from hierarchy of bond stiffness in thiolate-protected gold clusters

Metal nanoparticles (NPs) exhibit specific thermal properties and phase transition behaviors that are considerably different from the corresponding bulk metal [1]. For example, the melting point of a metal NP is significantly less than that of the bulk metal [2]. A crucial factor that governs thermal behaviors is the hierarchy of the bonding within NPs; metal–metal bonds on the surface are generally softer than those within the core. However, an atomic-level understanding of the effect of a variety of structural parameters on bond stiffnesses has not yet been attained because of the experimental difficulties in defining the atomic packing of a metal NP and the interfacial structure with the surrounding environment.

Recently, thiolate (RS)-protected gold clusters $Au_n(SR)_m$ with well-defined compositions have gained much attention as ideal platforms for studying the structure-property correlation and the size-dependent evolution of properties [3]. Among them, $Au_{25}(SR)_{18}$, $Au_{38}(SR)_{24}$, and $Au_{144}(SR)_{60}$ are representative systems that have been studied extensively. Single-crystal X-ray diffraction analysis and theoretical calculations showed that these clusters have an icosahedral-based gold core protected by $-SR-(Au-SR)_x-$ (x = 1 or 2) oligomers (Fig. 1). In addition, it has been identified that there are two classes of Au–Au bonds with different lengths (radial and lateral bonds) within the icosahedral cores (Fig. 1). The $Au_n(SR)_m$ clusters (n = 25, 38, 144) provide an ideal opportunity to study the hierarchy of the bond stiffness within Au clusters with well-defined atomic structures and surface modification.

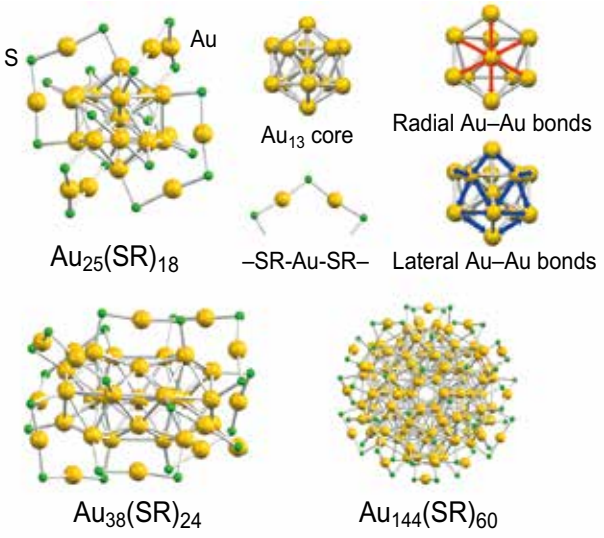

Fig. 1. Structures of $Au_{25}(SR)_{18}$, $Au_{38}(SR)_{24}$, and $Au_{144}(SR)_{60}$.

The stiffnesses of the Au–S and Au–Au bonds within $Au_{25}(PET)_{18}$, $Au_{38}(PET)_{24}$, and $Au_{144}(PET)_{60}$ (PET = PhC_2H_4S) were investigated by analyzing the temperature dependence of Au L_3-edge EXAFS (Extended X-ray Absorption Fine Structure) spectra recorded at SPring-8 **BL01B1** [4]. The temperature dependences of Debye-Waller (DW) factors for individual bonds were analyzed in the framework of the Einstein model, in which a metal cluster is treated as an ensemble of quantum harmonic oscillators. Figure 2(A) shows the Fourier-transformed (FT) EXAFS spectra of $Au_{25}(PET)_{18}$ measured at 300 and 8 K. The spectrum at 8 K exhibits a peak for the Au–Au bonds in the range of 2.1–3.0 Å together with a peak for Au–S bonds at 1.5–2.0 Å, whereas the peak for the Au–Au bonds is not discernible at 300 K. This temperature dependence suggests that the thermal fluctuation of the Au–Au bonds is larger that of the Au–S bonds. The curve fitting analysis of the FT-EXAFS spectrum at 8 K revealed that the Au–Au peak was composed of two components, corresponding to the radial and lateral Au–Au bonds in the icosahedral core. As shown in Fig. 2(A), the FT-EXAFS spectrum of $Au_{25}(PET)_{18}$ at 8 K was reproduced by a simulation using single crystal data.

Figure 2(B) shows the temperature dependence of the DW factor for each bond of $Au_{25}(PET)_{18}$. The DW values for both the radial and lateral Au–Au bonds increase monotonically with the temperature, whereas those of the Au–S bonds remain almost constant in the temperature range of 8–300 K. The Einstein temperature, θ_E, which is a measure of bond stiffness, was evaluated by fitting the temperature dependence of the DW factors (Fig. 2(B)). The θ_E values estimated for the Au–S and the radial and lateral Au–Au bonds were 429 ± 38, 137 ± 10, and 101 ± 4 K, respectively. This result indicates that the Au–S bond is the stiffest among them and that the radial Au–Au bonds are stiffer than the lateral ones in the gold core. Similar analysis was conducted for $Au_{38}(PET)_{24}$ and $Au_{144}(PET)_{60}$. The θ_E values of the Au–S and the radial and lateral Au–Au bonds were 416 ± 57, 153 ± 11, and 106 ± 15 K for $Au_{38}(PET)_{24}$, and 381 ± 45, 148 ± 11, and 128 ± 9 K for $Au_{144}(PET)_{60}$, respectively.

To the best of our knowledge, these results are the first experimental evidence of the hierarchy of the Au–Au bond stiffnesses in thiolate-protected Au clusters. The data indicate that thiolate-protected Au clusters can be viewed as “soft” icosahedral Au cores capped by “rigid” $-SR-(Au-S)_x-$ oligomers

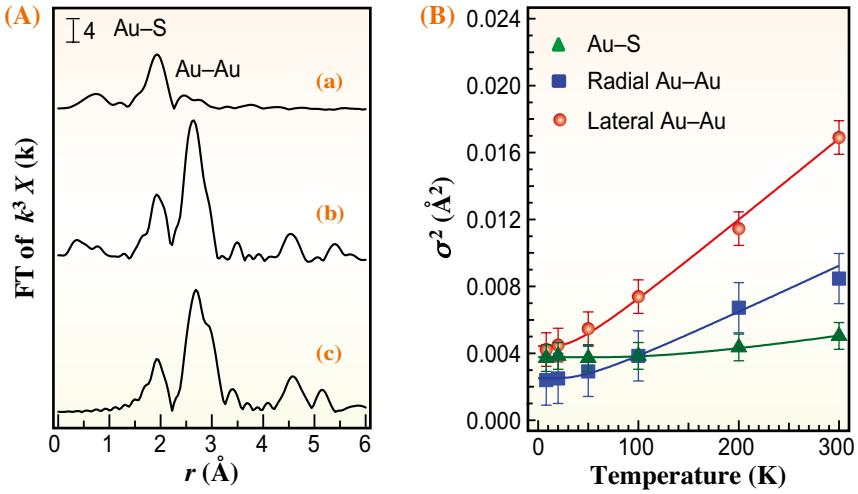

Fig. 2. **(A)** Au L_3-edge FT-EXAFS spectra of $Au_{25}(PET)_{18}$ measured at (a) 300 and (b) 8 K and (c) obtained by simulation. **(B)** Temperature dependences of the DW values for Au–S and radial and lateral Au–Au bonds of $Au_{25}(PET)_{18}$.

(Fig. 3(A)). Interestingly, the radial Au–Au bonds in the icosahedral core are stiffer than those of bulk gold (θ_E = 135 K) [5]. Similar inspection of the distribution of the stiff Au–Au bonds revealed that they are distributed not only in the center of the core but also on the surface of the core. The rigid ring structures are formed by bridging the stiff Au–Au bonds on the surface and the Au–S bonds (Fig. 3(B)). These rigid ring structures may act as frameworks to enhance the thermal stability of the thiolate-protected gold clusters.

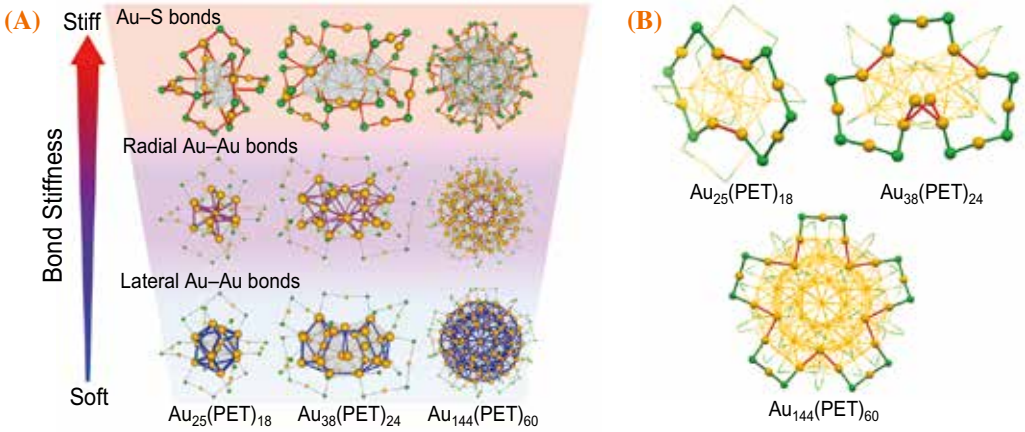

Fig. 3. **(A)** Hierarchy of bond stiffnesses and **(B)** rigid ring network structures in $Au_{25}(PET)_{18}$, $Au_{38}(PET)_{24}$, and $Au_{144}(PET)_{60}$.

Seiji Yamazoe[a,b,*] and Tatsuya Tsukuda[a,b]

[a] Department of Chemistry, The University of Tokyo
[b] Elements Strategy Initiative for Catalysts and Batteries (ESICB), Kyoto University

*Email: yamazoe@chem.s.u-tokyo.ac.jp

References

[1] C.L. Cleveland *et al.*: Phys. Rev. Lett. **81** (1998) 2036.
[2] P. Buffat, J.-P. Borel: Phys. Rev. A **13** (1976) 2287.
[3] T. Tsukuda and H. Häkkinen: Protected Metal Clusters: From Fundamental to Applications (Elsevier, 2015).
[4] *S. Yamazoe, S. Takano, W. Kurashige, T. Yokoyama, K. Nitta, Y. Negishi and T. Tsukuda: Nat. Comm. 7 (2016) 10414.*
[5] P. Kluth *et al.*: AIP Conf. Proc. **882** (2007) 731.

2D-XAFS imaging of Ce oxidation states in Pt/$Ce_2Zr_2O_x$ particles during oxygen storage and release processes

An assembly of non-uniform particles in a powder is a typical form of a heterogeneous solid catalyst. There are heterogeneous hierarchical structures (morphology, surface structures, domain boundaries, and so forth) in a solid catalyst. The reactivity of a solid catalyst is determined by such structural heterogeneity, but it is still difficult to visualize and understand the real active parts and heterogeneous reaction modes in a heterogeneous solid catalyst.

$Ce_2Zr_2O_x$ (CZ; $x = 7-8$) solid solution with an ordered arrangement of Ce and Zr atoms has been reported to exhibit excellent oxygen storage/release properties [1]. Almost 90% of the Ce atoms in CZ bulk can participate in the redox process for oxygen storage/release and the structure of CZ changes between oxidized $Ce_2Zr_2O_8$ (Ce^{4+}) and reduced $Ce_2Zr_2O_7$ (Ce^{3+}). We performed scanning nano-XAFS measurements at the Ce L_{III}-edge to visualize the distribution of Ce oxidation states in individual CZ particles and investigated the role of Pt in the oxygen storage/release processes. The nano-XAFS imaging showed the heterogeneous reaction modes and active parts in individual CZ particles for the first time [2].

Scanning nano-XRF and nano-XAFS measurements were conducted at SPring-8 **BL36XU** and **BL39XU**. Hard X-rays from an undulator were monochromatized by Si(111) crystals and focused by Kirkpatrick-Baez mirrors to a size of 409(h) × 154(v) nm^2 at 6 keV (Fig. 1). A sample enclosed in an XAFS cell with an inert He flow was mounted on an encoded-feedback translation stage (10 nm resolution) at the focal point of the X-ray beam and inclined at a tilt of 30° with respect to the optical path. Incident and fluorescent X-rays were detected by a He-filled ion chamber and a 21-element Ge detector (Canberra, EGPX 40 × 40 × 7-21PIX), respectively. Scanning nano-XRF mappings were measured every 150 nm at 122 energies at the L_{III}-edge (5.68 – 5.80 keV). The Ce valence was calculated by the linear combination fitting of the Ce L_{III}-edge nano-XANES spectra of $Ce_2Zr_2O_7$ (Ce^{3+}) and $Ce_2Zr_2O_8$ (Ce^{4+}) [3].

The CZ particles (0.2–2.0 μm) and commercial micron-size Pt particles (Alfa Aesar, 0.2–1.6 μm) were dispersed on a SiN membrane. The location and distribution of isolated CZ particles were evaluated by SEM analysis and three representative particles (Particle 1: a CZ particle with Pt attached to the side of the particle; Particle 2: a CZ particle with Pt attached to the edge of the particle; Particle 3: a CZ particle without Pt) were selected for nano-XAFS analysis. Oxygen storage and release were processed with a flow of O_2 or 10% H_2/N_2 at 1,000 mL·min^{-1} for 1 h.

Figure 2 shows the BEI-SEM images and the observed 2D mappings of the Ce valence states of Particles 1–3 after the oxygen storage and release

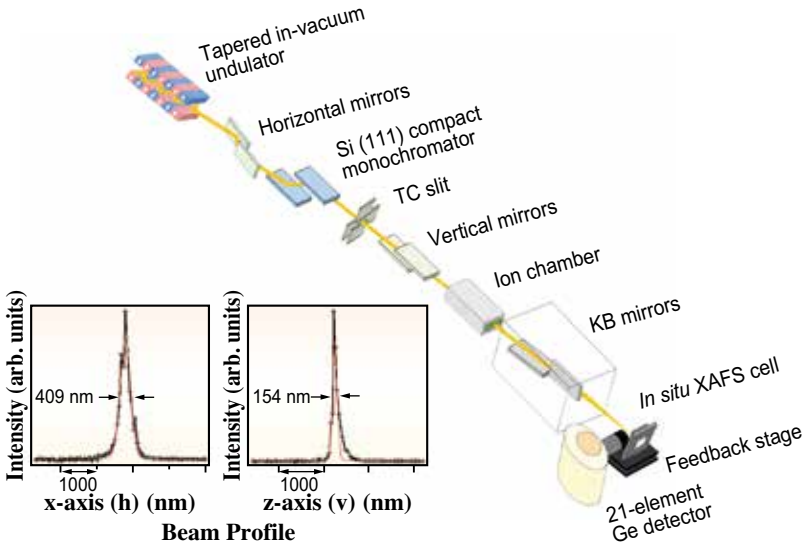

Fig. 1. Experimental setup of nano-XRF and nano-XAFS and the beam profile of the X-ray nanobeam focused by Kirkpatrick-Baez (KB) mirrors at beamline BL36XU.

processes at 423 and 573 K. Black dotted lines show the positions of Pt particles attached to CZ. In the case of Particle 1, in which Pt was located on the side of the CZ particle, the Ce valence state changed smoothly during both oxygen storage and release processes at 573 K (Figs. 2(c-1) and 2(e-1)). Unreacted parts inside the CZ particle were observed for the oxygen storage at 423 K, but were found to be unrelated to the position of Pt (Fig. 2(b-1)).

It should be noted that Particle 2, in which Pt was attached to an edge of the CZ particle, exhibited an isotropic gradient in the Ce oxidation state with respect to the center of the Pt particle for the oxygen release process at 423 K (Fig. 2(d-2)), indicating that the Pt catalyst played a crucial role in the oxygen release by H_2. These results clearly suggest that the initiation of the oxygen release locally proceeds from the attached Pt catalyst on CZ then oxygen diffusion spreads into the CZ bulk. The scanning nano-XAFS imaging evidenced the significance of the interface between the Pt catalyst and the CZ particle as a preferential oxygen release site. On the other hand, the color change in the CZ particle was found to be unrelated to the position of Pt for the oxygen storage at 423 K (Fig. 2(b-2)), suggesting that the oxygen storage occurred in domains of the CZ particle without the contribution of the Pt catalyst. After oxidation at 573 K, all the Ce species in Particle 2 had fully reacted (Fig. 2(c-2)).

In the case of Particle 3, oxygen storage similarly proceeded even though Pt was not attached on the CZ particle (Fig. 2(b-3)). Differences in the color changes in the CZ particles imply differences in the reactivity of each CZ particle derived from non-uniform domain structures in the CZ particles. In contrast, the oxygen release was too slow at 423 K and was not completed at 573 K (Fig. 2(d/e-3)), suggesting that the absence of Pt strongly affected the reaction rate of the oxygen release.

In conclusion, the nano-XAFS images obtained using hard X-ray nanobeams showed the modes of the changes in the Ce valence state for the oxygen storage/release processes. Practically, novel metal-nanoparticle-attached catalysts on a ceria-based support have been used for three-way conversion systems. Solid support particles intrinsically have structural heterogeneity, and nanoparticle catalysts attaching and spreading on the support surface should make up for the heterogeneous reactivity of each domain structure in the support. Nano-XAFS imaging is promising for providing new insights and a deeper understanding of heterogeneous catalysis and for developing new practical catalyst systems [2].

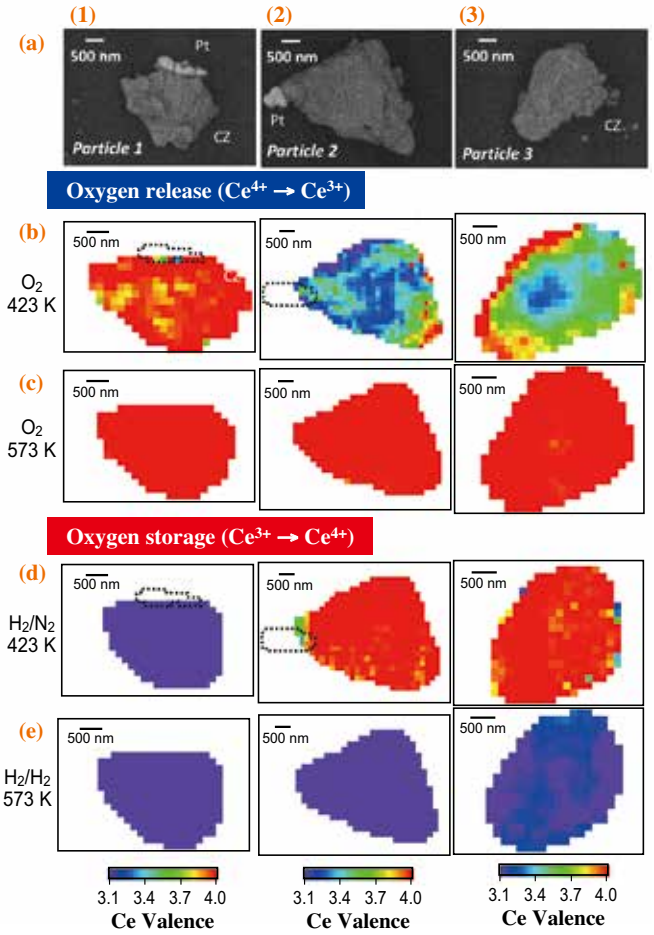

Fig. 2. **(a)** SEM images (BEI mode) and **(b-e)** 2D mappings of Ce valence states of Particles 1–3 after the oxygen storage and release processes at 423 and 573 K. Black dotted lines show the positions of Pt particles [2].

Hirosuke Matsui[a], Nozomu Ishiguro[b] and Mizuki Tada[a,b,*]

[a] Graduated School of Science & Research Center for Materials Science (RCMS) and Integrated Research Consortium on Chemical Sciences (IRCCS), Nagoya University
[b] RIKEN SPring-8 Center

*Email: mtada@chem.nagoya-u.ac.jp

References

[1] A. Suda *et al.*: J. Ceram. Soc. Jpn. **110** (2002) 126.
[2] *H. Matsui, N. Ishiguro, K. Enomoto, O. Sekizawa, T. Uruga, M. Tada: Angew. Chem. Int. Ed.* ***55*** *(2016) 12022.*
[3] N. Ishiguro *et al.*: Chem. Phys. Chem. **15** (2014) 1563.

Structural probe of novel fcc Ru nanoparticles with enhanced CO oxidation activity

Metallic ruthenium (Ru) adopts a hexagonal close-packed (hcp) structure at all temperatures, and novel face-centered cubic (fcc) Ru nanoparticles (NPs) have attracted much attention recently as a catalyst for CO oxidation because of their higher catalytic activity than conventional hcp-type Ru NPs when the diameter is larger than 3 nm [1]. CO oxidation catalysts are required for the purification of automobile exhaust gases and for the prevention of CO poisoning in electrolyte fuel-cell systems.

The atomic-scale structures of Ru NPs have been determined by high-energy X-ray diffraction (HEXRD) coupled with Rietveld analysis, pair distribution function (PDF), and reverse Monte Carlo (RMC) modeling methods. Here we demonstrated the three-dimensional (3D) atomic arrangements of Ru metal NPs, which deviates significantly from their corresponding bulk crystalline structures [2,3].

The surface structures of the Ru metal NPs are involved in the back-donation of electrons from the metal surface to the π antibonding orbital of CO. Hence, the CO interacts with a metal atom with a higher coordination number, where electrons are more delocalized. In this study, we present the correlation between the mean and atomic-scale structure and the catalytic activity of Ru NPs as a function of the crystal structure and particle size. The origin of the CO oxidation activity of Ru NPs is discussed on the basis of Rietveld analysis as well as the short to intermediate-range structures in terms of the coordination-number and bond-angle distributions.

HEXRD measurements were performed using a two-axis diffractometer installed at SPring-8 **BL04B2**. The incident X-ray beam energy was 61.46 keV, which corresponds to a wavelength of 0.02017 nm. The synthesized fcc- and hcp-types Ru NPs were loaded into a capillary column with 1.0 mm inner diameter and measured at room temperature. Fine powders of bulk 99.9% Ru and poly(*N*-vinyl-2-pyrrolidone) (PVP) were used as the reference materials. HEXRD intensity data were corrected for the background, polarization, and absorption and were then normalized by the structure factor and Fourier transformed using the analysis software provided in beamline BL04B2. HEXRD patterns for the fcc- and hcp-types Ru NPs were analyzed using the Rietveld refinement method with a pseudo-Voigt function. The RMC modelings for 3D structures of Ru NPs were guided by the experimental structure factor. The RMC modelings were carried out using the RMC_POT software set up for the case of nonperiodic boundary conditions.

From the Rietveld refinement analysis for the mean structure of Ru NPs with a long-range order, we investigated the relationship between the *B* factor, which appears in the Debye-Waller factor related to the r.m.s. amplitude of the atomic vibration, and the particle size (Fig. 1). The *B* factor can be regarded as an indication of the relative thermal vibrational motion, which is related to the static atomic displacement. Atoms with a small *B* factor belong to a part of the structure that is well ordered. In contrast, atoms with a large *B* factor generally belong to a part of the structure that is very flexible or is more reactive to the ambient environment. By comparing fcc-type Ru NPs with hcp-type Ru NPs of a similar particle size, we found that the *B* factor of the fcc-type Ru NPs is considerably larger than that of the hcp-type Ru NPs. As a result, we suggest that the higher catalytic activity of the fcc-type Ru NPs is due to the larger lattice distortion and *B* factor.

To understand the catalytic properties of the fcc- and hcp-types Ru NP catalysts, atomic-scale structure information was obtained from HEXRD data coupled with PDF analysis and RMC modeling methods. We observed broader peak profiles in all Ru NP PDFs than in the bulk Ru, which strongly indicates that the structures of the NPs are disordered. In addition, the PDF data imply that the positions of the coordination shells are distorted owing to the size and structure of the Ru NPs.

Figure 2 shows the behavior of the calculated order parameters S_{fcc} and S_{hcp}, of Ru NPs and the bulk, evaluated by the pair correlation function and

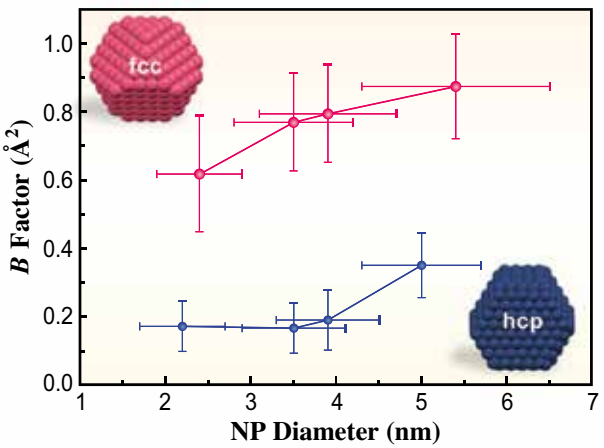

Fig. 1. Dependence of *B* factor on particle diameter.

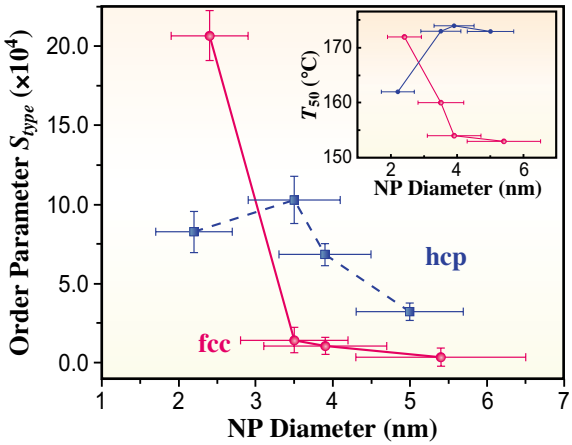

Fig. 2. NP-diameter dependence of the order parameters. The inset shows the temperature dependence for 50% conversion of CO to CO_2 (T_{50}) *vs*. particle size [1].

bond angle distribution obtained by RMC models as a function of the NP diameter. Upon comparing the fcc-type Ru NPs with the hcp-type Ru NPs, we observed that the structural parameter for the fcc-type NPs decreased with increasing NP diameter. Conversely, the order parameter for the hcp-type Ru NPs was larger than that for the fcc-type NPs for a diameter above 3 nm and above which confirmed that the catalytic activity (such as CO oxidation) was reduced as a result of the dense close-packing atomic arrangement of the larger hcp-type NPs.

We also evaluated the first-shell coordination number (CN) by counting the number of Ru atoms in a spherical shell with a radius between 0.23 and 0.32 nm around each central atom. Figure 3 shows 3D RMC models of the fcc-type Ru NPs with different CNs in highlighted colors. The 5.4 nm fcc-type Ru NP model shows a higher probability of the existence of step-edge (CN = 10) and sawtooth (CN = 11) sites as well as lower probability of containing close-packed (CN = 9) and square-planar (CN = 8) sites compared with the 5.0 nm hcp-type Ru NP model. According to the surface topologies observed through CN analysis, the newly discovered fcc-type Ru NPs are more reactive than the conventional hcp-type Ru NPs.

HEXRD coupled with the Rietveld refinement analysis, PDF analysis, and RMC modeling methods are appropriate techniques for investigating the atomic-scale structure of NPs that are much smaller than the X-ray spatial coherence length. In this study, we found that the relative thermal vibration acquired from the *B* factor of the fcc-type Ru NPs is considerably larger than that of the hcp Ru NPs. Here we demonstrated highly disordered NP structures on the basis of atomic PDF analysis and 3D NP models constructed by the RMC modeling method. In particular, the enhanced catalytic activity of the novel fcc-type Ru NPs is consistent with observed order parameters and coordination number analysis based on the RMC NP models. The advanced structural characterization technique that we have used here is expected to be a promising and helpful tool for characterizing nanostructure materials.

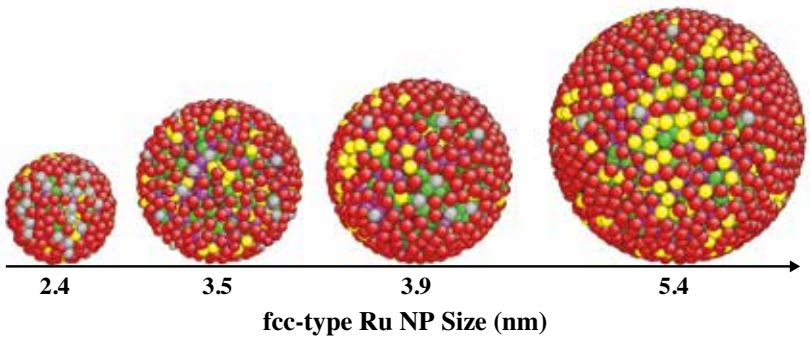

Fig. 3. RMC models of fcc-type Ru NPs with different coordination numbers in highlighted colors (gray: ≤ 4, red: 5 to 7, yellow: 8, green: 9, magenta: 10, brown: 11, and purple: ≥12).

Osami Sakata[a,b,*], Rosantha Kumara[a] and Chulho Song[a]

[a] Synchrotron X-ray Station at SPring-8, National Institute for Materials Science (NIMS)
[b] Department of Materials Science and Engineering, Tokyo Institute of Technology

*Email: SAKATA.Osami@nims.go.jp

References

[1] K. Kusada *et al.*: J. Am. Chem. Soc. **135** (2013) 5493.
[2] *C.H. Song, O. Sakata, L.S.R. Kumara, S. Kohara, A. Yang, K. Kusada, H. Kobayashi and H. Kitagawa: Sci. Rep.* ***6*** *(2016) 31400.*
[3] *L.S.R. Kumara, O. Sakata, S. Kohara, A. Yang, C.H. Song, K. Kusada, H. Kobayashi and H. Kitagawa: Phys. Chem. Chem. Phys.* ***18*** *(2016) 30622.*

Temperature measurement and chemical reaction observation in combustion gas by X-ray Compton scattering

Recent automobile technologies require elucidation of complex combustion phenomena to achieve cleaner exhaust gas and less carbon dioxide emission. The combustion occurs owing to complex interactions involving heat, mass, and momentum transfer. The local flow temperature is a key factor for elucidating complex phenomena and must be accurately measured. Nonintrusive temperature measurements offer important advantages in the elucidation of combusting flows since they do not affect the flow characteristics and change the temperature distribution. Holographic temperature measurements have been suggested as a mean of accurately determining the refractive index in flames in order to infer the temperature distribution [1]. However, these measurements are sensitive to mechanical noise; hence, it is not easy to obtain accurate temperature data using a combustion instrument.

High-energy X-ray Compton scattering can be used for the nonintrusive measurement of the temperature distribution in the combustion gas of a flame with high accuracy and robustness because it does not have the drawbacks of an interferometric instrument. In this study, we developed a method of temperature measurement and chemical reaction observation for combustion flames using X-ray Compton scattering.

The experiment was performed at SPring-8 **BL08W** [2,3]. A cylindrical Bunsen burner (inner diameter, d_{in} = 10 mm) was used to provide a laminar mixture of propane (6 wt%, 450 ml/min) and air (94 wt%, 8 l/min). The burner provided a laminar propane/air jet at the outlet. The air and combustible gases were pure synthetic gases.

Figure 1(a) shows a side view of the self-sustaining flame. The bright flame front, at which CH* and OH* radicals emit light [4], has a cone shape. Figure 1(b) shows a cross-sectional map of the temperature distribution along the cylindrical axis of the flame shown in Fig. 1(a). The ambient temperature of 298 K is almost constant in the inner flame region, which is shown as the blue triangular region in Fig. 1(b). Figure 1(b) shows that the temperature increases suddenly at the bright flame front shown in Fig. 1(a), and reaches 1500 K just outside the flame. The temperature distribution shown in Fig. 1(b) was compared with those obtained using conventional thermocouples. The results indicate that temperature measurement using Compton scattering enables more precise measurement than that using thermocouples. This is because it is a noncontact method and there is no effect of thermal inflow from the thermocouple wire on the measurement.

In addition, analysis of the spectra of Compton-scattered X-rays enables chemical reaction measurement. Figure 2 shows differences in Compton profiles $\Delta J_{x\text{mm}}$ (p) between x = 0 mm (where the gas is a mixture of air and the combustion gas at ambient temperature) and x mm (where the gas is undergoing the combustion reaction) at y = 5 mm. $\Delta J_{x\text{mm}}$ (p) for x = 4 mm, just inside the combustion reaction zone, is almost zero within the range of experimental error.

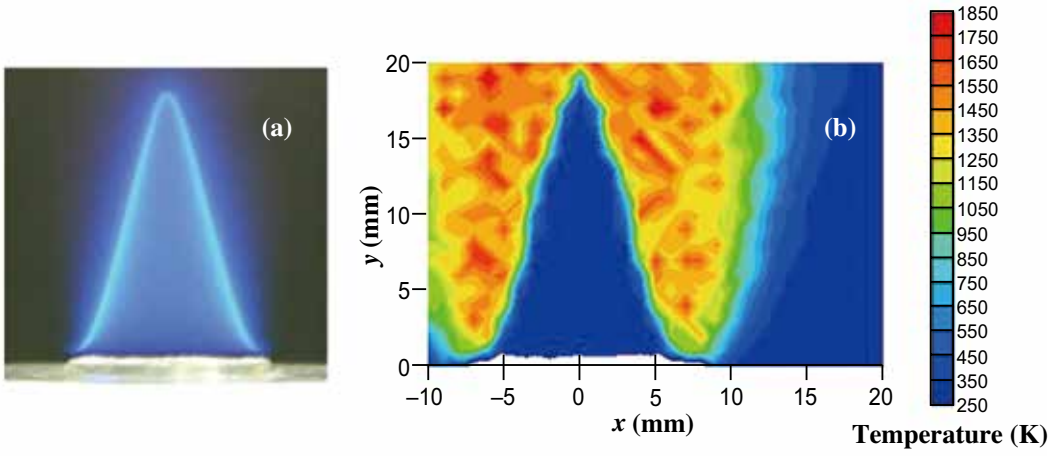

Fig. 1. **(a)** Photograph of self-sustaining flame. **(b)** Cross-sectional map along the cylindrical axis of the flame shown in (a). The flame center is at x = 0 mm.

This shows that the chemical reaction does not take place. This is consistent with the fact that the ambient temperature of 298 K remains almost constant just inside the combustion reaction zone, as shown in Fig. 1(b). It should be noted that $\Delta J_{xmm}(p)$ in the combustion reaction zone ($x = 4.5$ mm) is almost zero within the range of experimental error, although bright luminescence in the combustion reaction zone is observed, as shown in Fig. 1(a) and the temperature is 800 K, as shown in Fig. 1(b). This suggests that the main type of chemical bonding remains, but a combustion reaction, such as radical luminescence, starts at the combustion reaction zone. $\Delta J_{xmm}(p)$ just outside the combustion reaction zone ($x = 5$ mm) deviates from zero. This indicates that the main type of chemical bonding, or molecular species, has changed drastically. This means that the combustion reactions are complete just outside the combustion reaction zone and that a 1500 K high temperature region without luminescence extends into the outer region of the combustion reaction zone as a result of the flame gas flow.

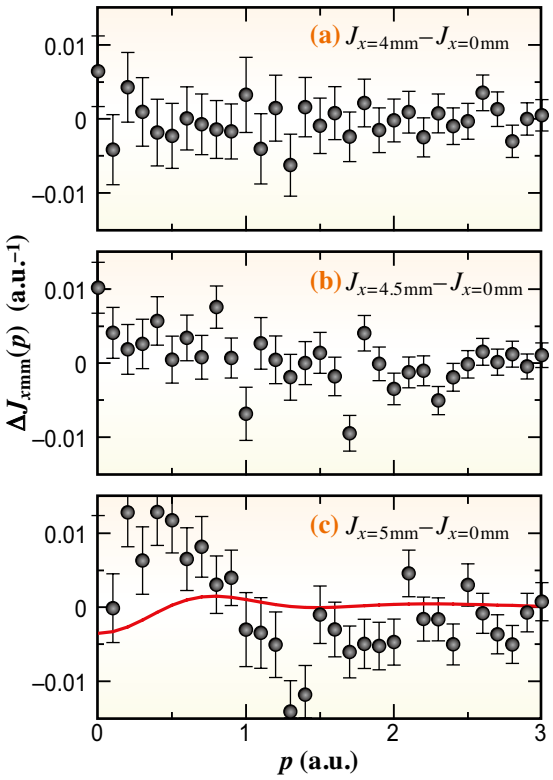

Fig. 2. Difference Compton profiles, $\Delta J_{xmm}(p)$, between a position at the center of the flame, $x = 0$ mm and **(a)** $x = 4$ mm (just inside the combustion reaction zone), **(b)** $x = 4.5$ mm (at the edge of the combustion reaction zone), and **(c)** $x = 5$ mm (just outside the combustion reaction zone) shown in Fig. 1(b). Here, $y = 5$ mm. The difference in the Compton profile calculated using CRYSTAL09 codes assuming the ideal chemical combustion reaction is shown by the solid line. p is the momentum.

The calculated $\Delta J_{xmm}(p)$ for $x = 5$ mm assuming the following ideal chemical reaction [1] and using CRYSTAL09 codes [5] is also shown in Fig. 2(c) by the solid line.

$$C_3H_8 + 7.8(O_2 + 3.76N_2) \rightarrow 3CO_2 + 4H_2O + 29.3N_2 + 2.8O_2$$

Although the dip structure for $|p| < 0.5$ a.u. seems to be reproduced by the calculation, positive values with $|p| < 1$ a.u. and negative values with $|p| > 1$ a.u. are not reproduced. Through the comparison of further Compton profiles calculated using CRYSTAL09 codes [5] for air (O_2+3.76N_2), CO_2, H_2O, and C_3H_8, and the Hartree-Fock calculation for atomic H [6], the deviation from the ideal chemical reaction can be explained by the presence of many atomic H with OH radical species [4].

This method can be used for noncontact measurement of the temperature distribution and chemical reactions in internal combustion engines because high-energy X-rays with high permeability are used in this analytical method. This measurement method is expected to help advance the development of innovative engine technology with improved efficiency.

Hiroshi Sakurai[a,*], Nobuyuki Kawahara[b] and Masayoshi Itou[c]

[a] Department of Electronics and Informatics, Gunma University
[b] Department of Mechanical Engineering, Okayama University
[c] Japan Synchrotron Radiation Research Institute (JASRI)

*Email: sakuraih@gunma-u.ac.jp

References

[1] S.M. Tieng *et al.*: Meas. Sci. Tehcnol. **3** (1992) 1179.
[2] Y. Sakurai: J. Synchrotron Rad. **5** (1998) 208.
[3] *H. Sakurai, N. Kawahara, M. Itou, E. Tomita, K. Suzuki and Y. Sakurai: J. Synchrotron Rad. **23** (2016) 617.*
[4] J.L. Beduneau *et al.*: Combust. Flame **156** (2009) 642.
[5] R. Dovesi *et al.*: Z. Kristallogr. **220** (2005) 571.
[6] F. Biggs *et al.*: At. Data Nucl. Data Tables **16** (1975) 201.

Quantum coherence and temperature dependence of the anomalous state of nanoconfined water in carbon nanotubes

There has been considerable interest in water confined in carbon nanotubes as a model for the flow of water in biological channels and, in its own right, as a filtration system due to the super-rapid (compared to Poiseuille) flow observed in tubes of the same diameter. Water is usually thought of as a collection of weakly interacting molecules, held together by hydrogen bonds. Just like a school of fish in an ocean can move independently, but yet responds to its group simultaneously as a whole, similarly for water in the smallest level (quantum), there is unity and cooperation between them (coherence), which allows them to respond together as a larger unit. Neutron Compton scattering measurements [1] in the last few years have shown that the proton momentum distribution in nanoconfined water, with water confined on the scale of 20 Å, differs greatly from that expected of a water molecule in bulk water. The proton delocalizes over distances of 0.2–0.3 Å, and the confining potential appears to be a double well, rather than the covalent bond of the water molecule.

It has been shown recently by X-ray Compton scattering that water confined in Nafion is in a new state, not describable by the usual picture, with the protons delocalized over distances on the order of 0.2–0.3 Å and the electron momentum distribution strongly perturbed from its value in bulk water [2]. Also in the simplest system for which this has been observed are single wall (SWNT) and double wall (DWNT) carbon nanotubes, where the momentum distribution of the proton is sensitive to the size of the confinement. The momentum distribution narrows in the case of SWNTs, and broadens in the DWNTs, with very different temperature dependencies in the two cases. A classical simulation of the low temperature structure of water confined in a SWNT, with inner diameter 14 Å is shown in Fig. 1. For this system, the momentum distribution of the protons is temperature independent up to 230 K, where the structure changes to one resembling bulk water, whereas for the DWNT, inner diameter 16 Å, the momentum distribution, and hence the confining potential, varies continuously with temperature.

The confining potential for the protons is provided by the valence electrons. Changes in that potential must therefore reflect changes in the distribution of the valence electrons. These can be observed in the changes in the momentum distribution of the electrons with X-ray Compton scattering. Measurement of the changes in the Compton profiles (CP) of water was

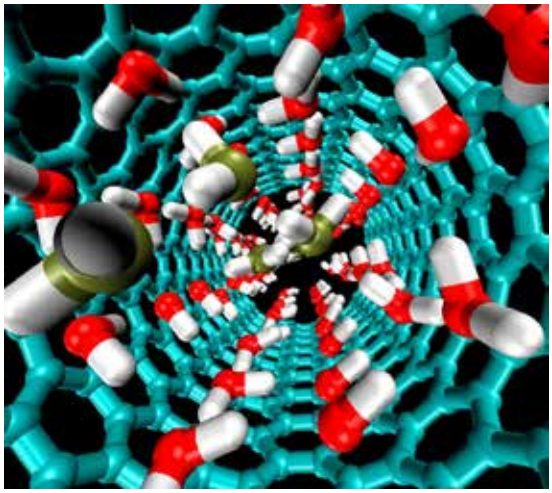

Fig. 1. MD (molecular-dynamics) simulated structure of water in 14 Å SWNT (cyan). The confined square ice sheet of water molecules (red and white) surrounds a chain of water molecules (green and white).

performed at the High Energy Inelastic Scattering beamline **BL08W**, SPring-8. The study for the first time was performed by confining water in both SWNTs (14 Å) and DWNTs (16 Å) and have shown that this temperature and size dependence is observable in the CP, demonstrating that the quantum ground state of the electron-proton system in nanoconfined water is a new state of water, qualitatively different from the bulk molecular state. The carbon nanotubes have been taken as a model system for the study of water flow through protein channels in cell membranes. This model is very useful as it resembles the confinement similar to the distance between the elements of our cells which is typically 20 Å. This state of water, and its properties, is the state that is relevant for the biological functioning of our cells [3].

We see from Fig. 2 for SWNT, that there is no change in the CP of the electrons between 10 K and 170 K, and a large change between 170 K and 300 K, consistent with the observations of the temperature variation of the proton momentum distribution. The results are compared with the fits with changes in the CP of bulk water due to substitution of D for H (Nygård *et al.* [4]) and increasing the O-H distance by 0.003 Å (Juurinen *et al.* [5]). The changes due to confinement are about 30 times those calculated by Juurinen *et al.* [5] In contrast with the SWNT case, Fig. 3 shows that the CP in the DWNT's vary continuously, consistent with the neutron Compton results. They are

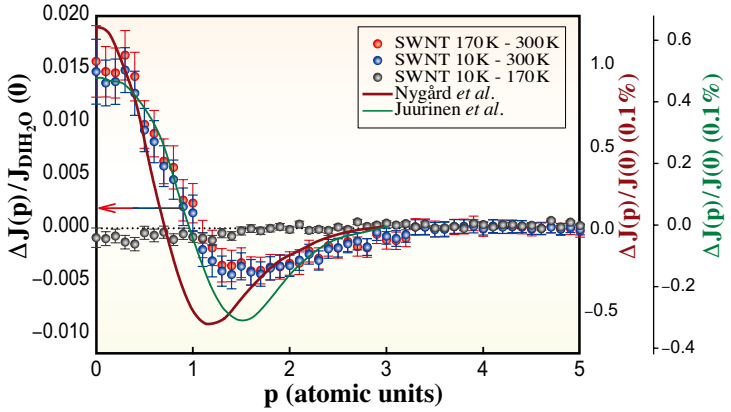

Fig. 2. Difference of X-ray Compton profiles for SWNT and temperatures shown in the inset. Amplitude given by axis on left. Solid curves are comparisons with calculations for D replacing H in bulk water [4] and varying O-H distance in alcohol water mixtures [5]. The amplitudes are represented by the axes on right (which are in parts per thousand).

larger by about a factor of 60 than the simulated results that assumed a small displacement of the protons from their position in the hydrogen bonded bulk liquid.

These results, together with the neutron Compton scattering results, demonstrate that nanoconfined water is not the weakly hydrogen bonded molecular network of bulk water, but is in a unique quantum state of the electrons and protons. Earlier work measuring the X-ray CP of water in Nafion at room temperature, [2] and an experiment on water confined in xerogel at room temperature, demonstrate that this state is still present at room temperatures. The flow of water through carbon nanotubes with diameters on the order of 20 Å is anomalous, being both much faster than continuum mechanics would predict, and much slower than classical simulations of molecular water would predict. It is the momentum carrying excitations of this state that determine the flow rate through the nanotubes. Since the elements of our cells are separated by a characteristic distance of 20 Å, it is the properties of this state, not that of bulk water, that determine the functioning of the cells of our bodies.

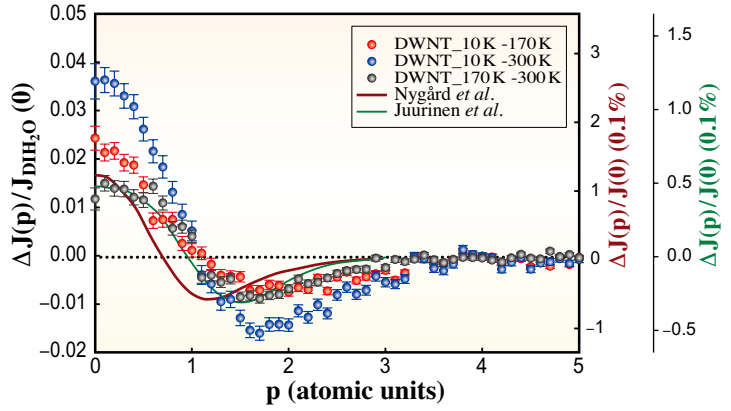

Fig. 3. Difference of X-ray Compton profiles for DWNT and temperatures shown in the inset. Amplitude given by axis on left. Comparison with calculations for D replacing H in bulk water [4] and varying O-H distance in alcohol water mixtures [5]. The amplitudes are represented by the axes on right (which are in parts per thousand).

Aniruddha Deb[a,*] and George F. Reiter[b]

[a] Department of Chemistry, University of Michigan, USA
[b] Physics Department, University of Houston, USA

*Email: debani@umich.edu

References

[1] G.F. Reiter *et al*: Phys. Rev. Lett. **97** (2006) 247801.
[2] G.F. Reiter *et al*.: Phys. Rev. Lett. **111** (2013) 036803.
[3] *G.F. Reiter, A. Deb, Y. Sakurai, M. Itou and A.I. Kolesnikov: J. Phys. Chem. Lett. 7 (2016) 4433.*
[4] K. Nygård *et al*.: J. Chem. Phys. **126** (2007) 154508.
[5] I. Juurinen *et al*.: Phys. Rev. Lett. **107** (2011)197401.

Ultrafast dynamics of a nucleobase analogue illuminated by an ultrashort intense X-ray pulse of SACLA

The advent of X-ray Free Electron Lasers (XFELs) has opened new avenues in research fields such as the dynamic imaging of matter. X-ray time-resolved study on the time scale of femtoseconds allows us to monitor, for the first time, atoms and electrons in action. X-ray single-shot imaging of non-crystallized nanometer-size objects, such as bio-macromolecules, has been transformed from a remote goal into a tangible reality. A fundamental issue connecting these two realms of XFEL-based research is radiation damage. The amount of energy deposited in a target by a single XFEL pulse is sufficiently high to cause its total destruction. A question to be answered from the viewpoint of structural imaging is whether the time scale of these changes is sufficiently slow for the collected data to capture structural information about the original object. Our present study addresses this question.

The experimental approach we are taking is the three-dimensional momentum correlation measurement of the atomic ions emitted via the Coulomb explosion of a molecule, called Coulomb Explosion Momentum Imaging (CEMI). We expect that highly charged ions will be created by an intense XFEL pulse in the femtosecond time scale [1] and that detailed information of the Coulomb explosion can be extracted from the CEMI data [2]. We have illuminated an iodine-containing nucleobase analogue (5-iodouracil) by an ultrashort (10 fs) high-intensity X-ray pulse of SACLA. The CEMI data were simulated on the basis of theoretical models to analyze the ultrafast radiation damage to I-containing molecules [3,4].

We conducted the experiments at experimental hutch 3 (EH3) at SACLA **BL3** [5]. The XFEL beam with a photon energy of 5.5 keV was focused by a Kirkpatrick-Baez (KB) mirror system onto a molecular beam of 5-iodouracil in an ultrahigh-vacuum reaction chamber. The focus size was ~1 μm (FWHM) and the resulting peak fluence was 26 μJ/μm^2. We detected ionic fragments using a recoil-ion momentum spectrometer and determined the three-dimensional momentum of each fragment ion. We evaluated the kinetic energy distributions, two-body momentum correlations and three-body momentum correlations of fragment ions. We found that the dynamics of charge build-up, charge redistribution and early-stage fragmentation leaves an imprint on the final momentum vectors of the fragment ions [3].

Representative results of two-body momentum correlations are shown in Fig. 1. We denote the distributions of cos(θ) between the momenta of various ejected ion pairs as SP_2(A; B), where the cosine of the angle θ between the momenta of the two ionic fragments A and B is given by $\cos(\theta) = \vec{P}_A \cdot \vec{P}_B / |\vec{P}_A||\vec{P}_B|$. The observed maxima in the $SP_2(I^{q+}; H^+)$, $SP_2(I^{q+}; O^+)$ and $SP_2(I^{q+}; N^+)$ distributions correspond to the geometric structure of 5-iodouracil, whereas the maxima in the $SP_2(I^{q+}; C^+)$ distribution do not correspond to the molecular structure. These differences result from the dissociation dynamics in 5-iodouracil after the illumination with the XFEL pulse.

We carried out numerical calculations at two different levels in order to understand how the XFEL-illuminated molecule breaks. In the first approach, we adopted a Coulomb explosion model with charge evolution (CCE-CE model), where only the Coulomb repulsions between the ions were taken into account [3,4]. We introduced two effects of charge dynamics into the classical Coulomb explosion model: the build-up of molecular charge with time owing to the multiple XFEL ionization and the charge redistribution that occurs among atoms. We evaluated the momentum correlations of fragment ions emitted from 5-iodouracil, as depicted by red lines in Fig. 1. We found good agreement with the experimental results when we chose specific time scales of charge build-up in the molecule (~10 fs) and of charge redistribution over the molecule (~2 fs).

As the second approach, we employed a semi-

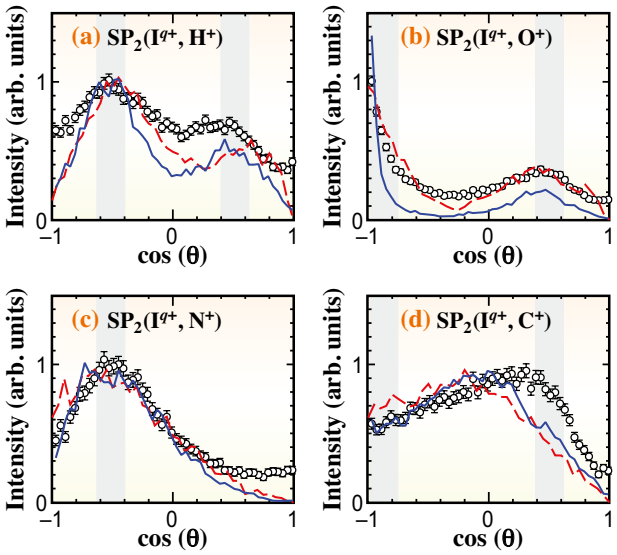

Fig. 1. Distribution of the normalized scalar product of momentum vectors, SP_2(A,B), as a function of $\cos(\theta) = \vec{P}_A \cdot \vec{P}_B / |\vec{P}_A||\vec{P}_B|$, displayed for fragment ion pairs **(a)** I^{q+}-H^+, **(b)** I^{q+}-O^+, **(c)** I^{q+}-N^+ and **(d)** I^{q+}-C^+. Gray shaded areas indicate the equilibrium angles between atoms in 5-iodouracil. The open circles, red dashed lines and blue lines are the experimental data, CCE-CE results and SCC-DFTB results, respectively. [4]

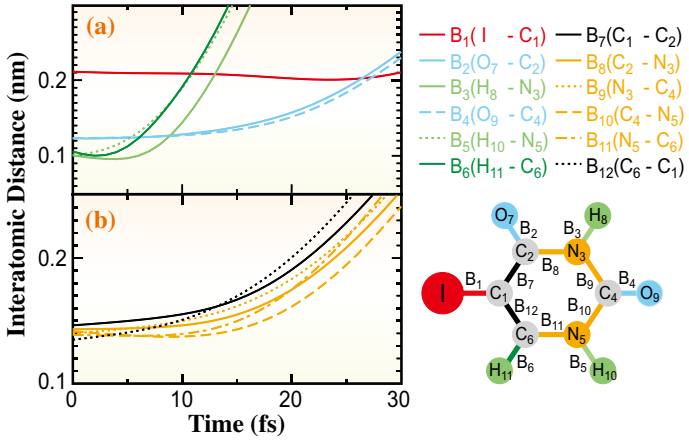

Fig. 2. Time evolution of interatomic distances in 5-iodouracil obtained by CCE-CE calculations. **(a)** Interatomic distance of I-C (red line), O-C (sky-blue lines), H-C (dark-green line), and H-N (light-green lines) pairs. **(b)** Interatomic distance of C-C (black lines) and C-N (orange lines) pairs. [4]

empirical method in which the forces on atoms were calculated by the self-consistent-charge density-functional-based tight-binding (SCC-DFTB) method [4]. Chemical bonds are explicitly taken into account in the SCC-DFTB method, unlike in the CCE-CE model. In the SCC-DFTB approach, bond dissociation processes are triggered by the excess vibrational energy injected into molecules during the Auger cascades as well as Coulomb repulsion. We introduced an electronic temperature T_e in order to reflect electronic excitation and charge redistribution, i.e., the contribution from various excited electronic states. The results of SCC-DFTB simulations are given by blue lines in Fig. 1. Good agreement with the experimental results was obtained by incorporating the effects of vibrational and electronic excitation on XFEL-induced multiple ionization into the SCC-DFTB approach. We clarified why two apparently contradictory approaches, namely, the CCE-CE model and the SCC-DFTB approach, function well by analyzing the SCC-DFTB results.

Based on the success of the numerical calculations, we deduced the temporal changes in interatomic distances as shown in Fig. 2. CCE-CE calculations revealed that the H-C and H-N distances increase by 50–100% from the initial lengths at t = 10 fs, whereas the changes in the C-O, C-N and C-C distances are less than several percent. The SCC-DFTB approach also reproduced the ultrafast ejection of H^+. The results of our simulations clearly indicate that the ultrashort escape time of hydrogen ions, which is comparable to the pulse width of the XFEL, makes their escape sensitive to the intramolecular charge dynamics and its time scale. In contrast, the I-C length of 5-iodouracil does not change in 30 fs, which is presumably due to the large iodine mass as well as the fact that the carbon atom adjacent to the I atom is surrounded by three heavy atoms (iodine and two carbons).

In summary, we investigated the radiation damage of the 5-iodouracil molecule illuminated by an X-ray pulse of SACLA and well reproduced the obtained experimental results of CEMI by using two different theoretical approaches. The consistency among the theoretical approaches and the experimental results deepened our understanding of the mechanism of XFEL-induced Coulomb explosion. The present results, obtained for a realistic biologically relevant molecule, give an important indication that, if sufficiently short XFEL pulses are used, the single-shot coherent diffraction imaging approach will enable the interrogation of target samples of single bio-macromolecules.

Kiyonobu Nagaya[a,b], Hirohiko Kono[c] and Kiyoshi Ueda[b,d,*]

[a] Department of Physics, Kyoto University
[b] RIKEN SPring-8 Center
[c] Department of Chemistry, Tohoku University
[d] Institute of Multidisciplinary Research for Advanced Materials, Tohoku University

*Email: ueda@tagen.tohoku.ac.jp

References

[1] H. Fukuzawa *et al.*: Phys. Rev. Lett. **110** (2013) 173005.
[2] K. Motomura *et al.*: J. Phys. Chem. Lett. **6** (2015) 2944.
[3] *K. Nagaya, K. Motomura, E. Kukk, H. Fukuzawa, S. Wada, T. Tachibana, Y. Ito, S. Mondal, T. Sakai, K. Matsunami, R. Koga, S. Ohmura, Y. Takahashi, M. Kanno, A. Rudenko, C. Nicolas, X.-J. Liu, Y. Zhang, J. Chen, M. Anand, Y. H. Jiang, D.-E. Kim, K. Tono, M. Yabashi, H. Kono, C. Miron, M. Yao and K. Ueda: Phys. Rev. X* ***6*** *(2016) 021035.*
[4] *K. Nagaya, K. Motomura, E. Kukk, Y. Takahashi, K. Yamazaki, S. Ohmura, H. Fukuzawa, S. Wada, S. Mondal, T. Tachibana, Y. Ito, R. Koga, T. Sakai, K. Matsunami, K. Nakamura, M. Kanno, A. Rudenko, C. Nicolas, X.-J. Liu, C. Miron, Y. Zhang, Y. Jiang, J. Chen, M. Anand, D.E. Kim, K. Tono, M. Yabashi, M. Yao, H. Kono and K. Ueda: Faraday Discuss.* ***194*** *(2016) 537.*
[5] K. Tono *et al.*: New J. Phys. **15** (2013) 083035.

Capturing photoexcited states of tungsten trioxide by pump-probe X-ray absorption fine structure (XAFS) in SACLA

The production of hydrogen (H_2) from water (H_2O) using sunlight is an ideal and ultimate process for producing an energy resource with neither extra energy consumption nor by-products. The conversion of H_2O to H_2 is a key technology for realizing a sustainable human society, and it is one of the most important subjects of modern science and technology. A photocatalyst plays a central role in hydrogen production from sunlight. Many photocatalysts have been developed for decades and new photocatalysts are still being developed. Tungsten trioxide (WO_3) has drawn much attention as a promising photocatalyst. A catalytic system combining WO_3 and TaON shows the potential to decompose H_2O into H_2 and O_2 using sunlight; such catalysts are called 'Z-scheme catalysts' [1].

The photocatalytic properties of WO_3 can be understood from its band structure. The band structure of WO_3 is shown in Fig. 1. When WO_3 is irradiated by light whose energy is greater than its band gap (about 2.6–2.8 eV), electrons in the valence band are excited to the conduction band. Photoelectrons emerge in the conduction band and photoholes emerge in the valence band. The photoelectrons promote reduction and the photoholes promote oxidation. The catalytic activity of WO_3 depends on the energy levels of the valence band and conduction band relative to the redox potential of H_2O and the lifetimes of photocarriers.

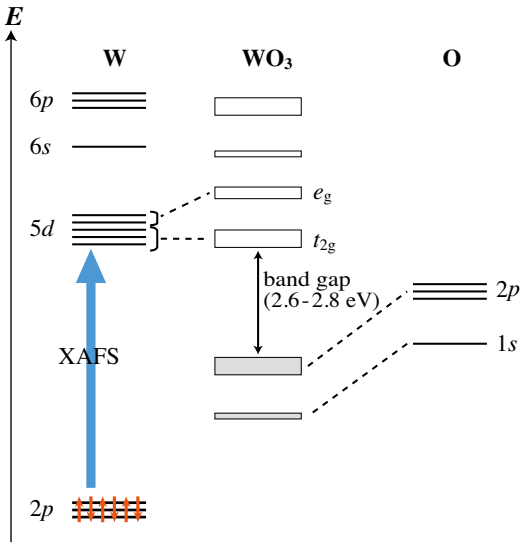

Fig. 1. Energy diagram of the band structure of WO_3.

The band structure and energy positions have been studied by density functional theory (DFT) [2] and the lifetimes of photocarriers have been observed by spectroscopic techniques using visible or infrared light as a probe [3].

Despite the development of photocatalytic materials and the fundamental studies of photocatalysts for many years, mechanisms of photocatalytic reactions are not well understood. It is difficult to determine where the photocarriers reside during a photocatalytic reaction, which is vital for understanding the reaction mechanism. The local structures and electronic states of photocatalysts in excited states can give crucial information related to the reaction mechanisms. In this study, we performed pump-probe XAFS experiments at SACLA to observe the changes in the local structure and electronic state of WO_3 to determine the photoexcited state of WO_3 [4]. XAFS gives element specific information (in this case, W). The W L_{III}-edge XAFS spectrum was measured. The W oxide produces a strong peak called a white line, which originates from the transition of inner electrons from 2*p* states to 5*d* states (see Fig. 1). The XAFS spectra were measured 500 fs to hundreds of picoseconds after a suspended WO_3 sample was irradiated by a 400 nm excitation laser to observe the creation and relaxation of the excited states of WO_3. The time resolution of our experimental setup was 500 fs. The W L_{III}-edge XAFS spectrum in the excited state gives the changes in WO_3 related to the generation of photoelectrons.

The W L_{III}-edge XAFS spectrum of WO_3 in the ground state and the difference spectra between the excited state and the ground state of WO_3 at several delay times are shown in Fig. 2. There were three energy values (denoted as A, B and C) where the X-ray absorption of the excited state changes considerably from the ground state. The increase in X-ray absorption at position A originates from a redshift of the absorption edge of W. This implies that W^{5+} species were created by photoabsorption. The increase in X-ray absorption at position A was observed 700 ps after the sample was irradiated by the excitation laser. The peak at position C was also seen shortly after the laser excitation. This was due to the initial redshift. However, the relaxation process of the peak was different from the process at position A. The peak intensity at position C reached its maximum around 200 ps after the laser excitation. Similar behavior was seen at position B. The increase at position B did not start until several picoseconds

after the laser excitation. The peak intensity changed gradually by 200 ps then recovered to its initial intensity. These results display that the photoexcited state of WO_3 decayed in multiple processes.

The overall changes of the photoexcited state in WO_3 are displayed in Fig. 3. We found that the excitation process of WO_3 consists of three processes. The first process was the formation of WO_3* due to photoabsorption, which should be in less than 500 fs. The second process is the change in the initial excited state WO_3* to another excited state (WO_3**). This process is considered to be a structural transformation around W. The third process is the gradual decay of WO_3** to the ground state. The kinetic constants of the second and third processes were estimated from the time evolution of the peak at position C.

The photoexcitation process was observed by pump-probe XAFS method at SACLA **BL3**. It was found that the relaxation of the excited WO_3 includes multiple steps. The structural change in WO_3 should occur after the formation of W^{5+}. The process of the structural change was not clarified in our previous experiments [5]. We are now attempting to determine the structural parameters of WO_3* and WO_3** by EXAFS analyses and theoretical calculations. The structural parameters of the photoexcited states can provide fundamental information on the local structures of WO_3 in the excited states and new insights into the mechanisms of the photocatalytic reaction of WO_3.

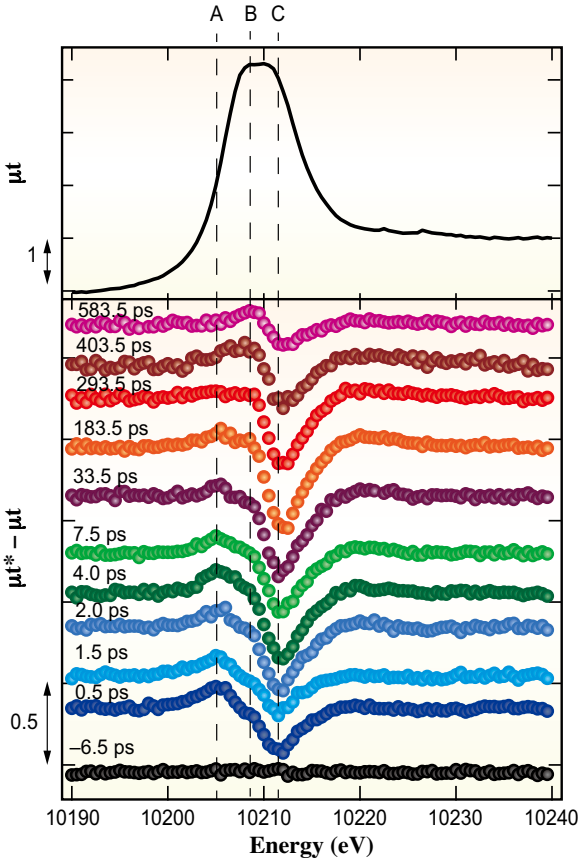

Fig. 2. W L_{III} XAFS difference spectra between the excited state (μt*) and the ground state (μt) at several delay times.

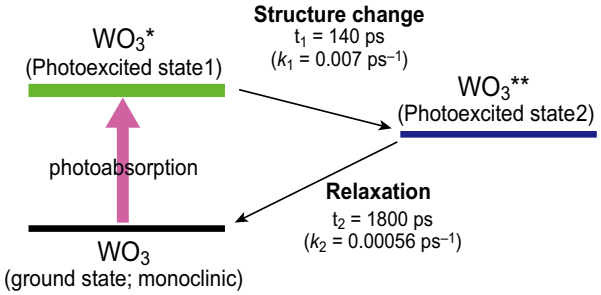

Fig. 3. Diagram of the photoexcitation process of WO_3.

Y. Uemura[a,*], T. Kido[b], T. Yokoyama[a] and K. Asakura[b]

[a] Institute for Molecular Science
[b] Institute for Catalysis Hokkaido University

*Email: y-uemura@ims.ac.jp

References

[1] R. Abe *et al.*: J. Am. Chem. Soc. **130** (2008) 7780; R. Abe *et al.*: Chem. Commun. (2005) 3829.
[2] Y. Ping *et al.*: Phys. Rev. B **87** (2013) 165203; F. Wang *et al.*: Chem. Cat. Chem. **4** (2012) 476; F. Wang *et al.*: J. Phys. Chem. C **116** (2012) 8901; G.A. de Wijs *et al.*: Phys. Rev. B **59** (1999) 16463.
[3] F. Amano *et al.*: J. Phys. Chem. C **117** (2013) 22584; F.M. Pesci *et al.*: J. Phys. Chem. Lett. **2** (2011) 1900; I. Bedja *et al.*: J. Phys. Chem. **97** (1993) 11064.
[4] *Y. Uemura, D. Kido, Y. Wakisaka, H. Uehara, T. Ohba, Y. Niwa, S. Nozawa, T. Sato, K. Ichiyanagi, R. Fukaya, S. Adachi, T. Katayama, T. Togashi, S. Owada, K. Ogawa, M. Yabashi, K. Hatada, S. Takakusagi, T. Yokoyama, B. Ohtani and K. Asakura: Angew. Chem. Int. Ed. **55** (2016) 1364.*
[5] Y. Uemura *et al.*: Chem. Lett. **43** (2014) 977.

Very low isotope ratio of iron in anthropogenic aerosols related to its contribution to the surface ocean: A speciation and isotopic study

Iron (Fe) is an essential nutrient for phytoplankton, but its concentration in surface seawater is very low, since Fe(III) is normally insoluble in seawater (approximately pH 8). Thus, phytoplankton growth in high-nutrient, low-chlorophyll (HNLC) regions is limited by the soluble Fe concentration [1]. The sources and budget of soluble Fe on the surface ocean should be clarified because phytoplankton plays an important role in the carbon cycle through photosynthesis, which can eventually affect climate change [2]. It has been suggested that aerosols deposited from the atmosphere may be the main source of Fe in HNCL regions in open oceans. However, the source of the aerosols that controls the amount of soluble Fe remains debatable. In modern systems, aerosols are generally classified into two origins, namely anthropogenic and natural [3]. The different formation processes cause varying solubility ranges of Fe in aerosols. The seawater-soluble fraction of anthropogenic Fe species is higher than that of Fe-containing dust, and anthropogenic aerosols can serve as soluble Fe sources on the surface ocean. However, the relative contribution of Fe in anthropogenic aerosols to the soluble Fe fraction in seawater in actual systems remains unclear. One of the tools to determine the contribution of Fe from different sources is the Fe stable isotope ratio, which is generally used to discuss the geochemical cycles of various elements on the Earth's surface. If the Fe stable isotope differs between anthropogenic and dust aerosols, the contribution of anthropogenic Fe in aerosols to the surface ocean can be estimated. In this study, the Fe isotope ratios of aerosols in seven size-fractionated samples were measured to identify the Fe isotope ratio of the anthropogenic component. The soluble fraction and chemical species of Fe in aerosols were determined through leaching experiments and X-ray absorption fine structure spectroscopy (XAFS), respectively. These results can be related to the source of Fe in aerosols and subsequent Fe-related chemical processes in the atmosphere during transport. The size dependence of the Fe stable isotope ratio and Fe species helped identify the anthropogenic Fe species and their isotope ratios, which are associated with the soluble fraction of Fe in the surface seawater.

With this background, we have measured Fe *K*-edge XAFS at SPring-8 **BL01B1** and **BL37XU** to determine

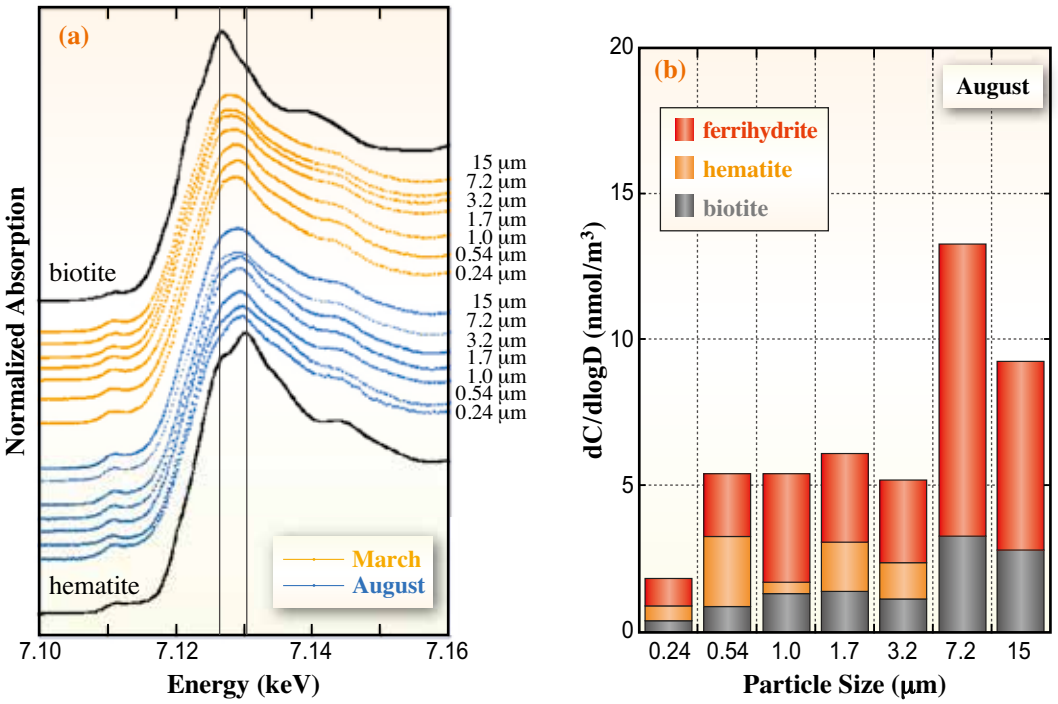

Fig. 1. **(a)** XANES spectra of aerosol samples with different particle sizes; **(b)** Iron concentration of each Fe species determined by XAFS analysis.

the average Fe species in bulk aerosol samples and the Fe speciation for single particles, respectively. The iron isotopes of Fe for different particle sizes were measured by a multi-collector ICPMS (Neptune) installed at the Department of Earth and Planetary Science, The University of Tokyo. The aerosol samples employed in this study were collected in March and August 2013 in an urban environment in Higashi-Hiroshima, Japan, and in a marine environment (northwestern Pacific).

The leaching experiments revealed that the iron in the fine particles in the urban sample was more soluble in simulated seawater (approximately 25%), compared with less than 10% for Fe in the coarse particles. XAFS analysis (Fig. 1) showed that the hematite fraction was larger in the fine particles than in the coarse particles, whereas biotite/chlorite (a natural mineral) was relatively more abundant in the coarse particles than in the fine particles as reported previously [4]. Although the ferrihydrite and hematite in the coarse particles of crustal origin, which may have undergone alteration during the long-range transport, dominate the Fe species for bulk aerosols [5], the main Fe species in the finer aerosols are most likely ferrihydrite and hematite produced by anthropogenic processes.

The μ-XANES results for some particles collected in Higashi-Hiroshima showed high intensities of Fe with (i) relatively strong signals of V and nickel (Ni) and (ii) a weaker signal of K. Particles could not be distinguished individually because of their finer size than that of the X-ray microbeam. However, the presence of V and/or Ni, which are often used as indicators of aerosols produced through fossil fuel combustion, suggests that the particles were emitted during combustion processes. Ferrihydrite and hematite were the main Fe chemical species of the particles, which again suggested that the oxidized species were emitted during the combustion processes.

The Fe isotope ratios ($\delta^{56/54}$Fe) of the coarse particles were close to the crustal value (0.04‰ to 0.30‰) (Fig. 2). By contrast, the Fe isotope ratios of the fine particles, ranging from –0.56‰ to –2.01‰, were lower than the crustal value. The $\delta^{56/54}$Fe values of the soluble fraction in the fine particles were very low (–1.87 to –3.91‰), suggesting that anthropogenic aerosols have a very low Fe isotope ratio. The very low Fe isotope ratio (δ^{56}Fe= –3.91‰) could be observed in this study because of the successful separation of anthropogenic components in aerosols collected in Higashi-Hiroshima. This value was the lowest among the reported $\delta^{56/54}$Fe values of materials collected on the Earth's surface environment because of the much larger isotopic fractionation through combustion. This large isotope fractionation can be explained by the kinetic isotope fractionation during the combustion of Fe species at high temperatures coupled with the refractory characteristics of Fe.

Marine aerosols around the northwestern Pacific were also analyzed. The Fe isotope ratio in the fine particles was also lower than that in the coarse particles. This finding indicates that anthropogenic aerosols contribute to marine aerosols. These results may be important to quantitatively estimate anthropogenic Fe components deposited on the surface ocean on the basis of the Fe isotopes of possible Fe components supplied to the surface ocean.

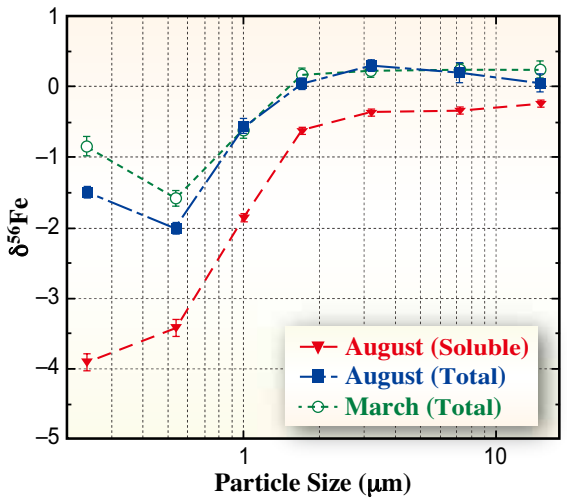

Fig. 2. Iron isotope ratios for aerosol samples given by $\delta^{56/54}Fe(‰)=\{(^{56}Fe/^{54}Fe)_{sample}/(^{56}Fe/^{54}Fe)_{IRMM\text{-}014}-1\}\times1000$ for total Fe and water-soluble components.

Minako Kurisu and Yoshio Takahashi*

Department of Earth and Planetary Science,
The University of Tokyo

*Email: ytakaha@eps.s.u-tokyo.ac.jp

References

[1] J.H. Martin and S.E. Fitzwater: Nature **331** (1988) 341.
[2] J.D. Jickells *et al.*: Science **308** (2005) 67.
[3] Y. Takahashi *et al.*: Atmos. Chem. Phys. **13** (2013) 7695.
[4] *M. Kurisu, Y. Takahashi, T. Iizuka and M. Uematsu: J. Geophys. Res. Atmos.* ***121*** *(2016) 11119.*
[5] Y. Takahashi *et al.*: Atmos. Chem. Phys. **11** (2011) 11237.

Chemical forms of silver nanoparticles and silver in antimicrobial fabrics in soil

The increased use of silver (Ag)- and silver nanoparticle (AgNP)-containing products has raised concerns about their effect on the environment. Owing to their bacteriocidal properties, Ag and increasingly AgNPs are being employed in a wide range of commercial products, but the fate and behavior of Ag released into the environment are poorly understood. It has been demonstrated that Ag in sock textiles can dissolve as ionic and colloidal forms under household washing condition [1]. As a result of various effluent pathways, one of the largest sinks of Ag generated in municipal areas may be wastewater treatment plants and landfill. The soil is also a potential sink for Ag in the environment. Synchrotron-based X-ray absorption fine structure (XAFS) spectroscopy is a technique that provides information on the oxidation state and coordination environment of metals in the solid phases of soil. Few studies are available on Ag speciation with regard to how AgNPs undergo phase transformations (e.g., sulfidation, complexation and adsorption) in the soil. Similarly, little is known about the solubility and speciation of Ag embedded in fabrics being disposed in landfill sites.

Transformation of AgNP in soil

Silver *K*-edge extended X-ray absorption fine structure (EXAFS) spectroscopy was performed at SPring-8 **BL01B1** [2]. Soil spiked with manufactured AgNPs was incubated under aerobic (slightly wet) and anaerobic (flooded) conditions for 30 days. Possible Ag species in the soil were determined by linear combination fitting (LCF) of the EXAFS spectra using known reference compounds and by a shell fit of Fourier transformed (FT) EXAFS spectra. The EXAFS spectrum of Ag in the aerobic soil was very similar to that of metallic Ag. The LCF indicated that metallic Ag was the primary species, accounting for 88% of the total Ag in the aerobic soil spiked with AgNP, indicating that the majority of AgNPs remained persistently in the aerobic soil. This is in agreement with the result of the shell fit of the FT-EXAFS spectrum, showing Ag–Ag coordination in the first shell (Fig. 1). In contrast, in the anaerobic soil, 83% of AgNPs were transformed into Ag_2S, accompanied by significant decreases in water- and acid-extractable Ag concentrations. The shell fit of the FT-EXAFS spectrum determined the Ag–S and Ag–Ag coordination in the first and second shells, respectively. Our study suggests that the transformation of AgNPs in soil depends on the redox condition, and an important consequence of the reaction of AgNPs with S is the reduced solubility and potential toxicity of Ag in the environment.

Ag species in textiles

To examine the situation in that Ag-containing fabrics are disposed of as landfill, we investigated how the solubility and speciation of Ag in sock textiles are changed in soil. The microscale distribution and speciation of Ag at the interface between socks and soil particles were investigated using micro-X-ray fluorescence (μ-XRF), and Ag speciation was determined by micro-X-ray absorption near edge structure (μ-XANES) spectroscopy at SPring-8 **BL37XU** [3]. Pieces of Ag-containing sock fabric were added to soil with different water contents. After 60 days, a portion of the soil including the sock fabric was freeze-dried and embedded with epoxy resin. A soil thin section of soil with 80 μm thickness was sliced

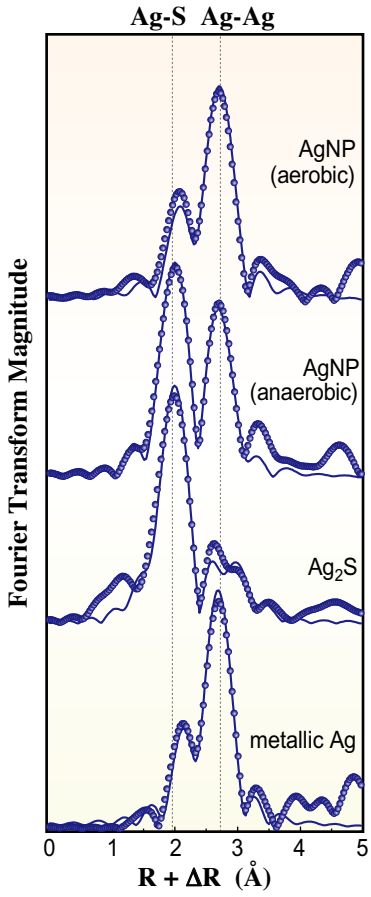

Fig. 1. Experimental (circles) and fitted (solid lines) data for Fourier transformed EXAFS spectra of Ag reference compounds and AgNPs added to aerobic and anaerobic soils. Vertical lines are included as a guide to the eye.

using a microtome (Leica, SP1600) and analyzed by μ-XRF and μ-XANES.

The result of μ-XRF showed that Ag is enriched in the fabric and can also be found in the soil matrix ~10 μm from the edge of the fabric, attesting to the possible dissolution of Ag from the fabric at the microscale. As points of interest (POIs), we selected Ag-accumulating spots on the μ-XRF maps and performed μ-XANES analysis followed by LCF using Ag reference spectra. A light-microscope image and μ-XRF element maps of the sock sample incubated under anaerobic conditions are shown in Fig. 2. The silver at the selected spots was mainly present as metallic Ag (51-89%) and Ag_2S (17-32%), depending on the location in the soil matrix (Fig. 2). At a 10 μm distance from the fabric (POIs #4 and #5), 25% and 32% of the Ag in the fabric were found to be Ag_2S, which was also found at POI #3, 20 μm away from the edge of the fabric. Part of the Ag at POIs #1 and #2, located ~20 μm from the edge of the fabric, was bound to soil clay minerals. XRD determined that the Ag in sock fabric was present in the form of metallic Ag and Ag_2S, suggesting that these Ag species in the sock fabric remained persistently without notable phase transformations in the soil but associated with the soil minerals to some extent. A long-term study on the transformation of Ag species in fabrics is essential to elucidate the environmental fate of Ag.

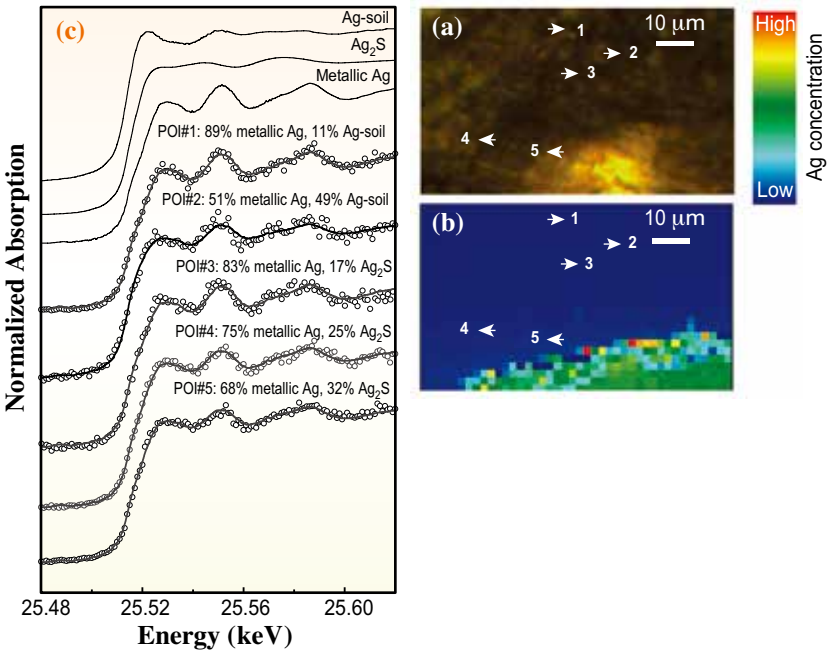

Fig. 2. Thin sections of soils with added Ag-embedded fabrics analyzed by a light microscope (panel **a**) and micro-XRF for Ag mapping (panel **b**), and normalized Ag *K*-edge XANES spectra of selected reference compounds. Also shown are points of interest (POIs) on the thin soil sections with their best component fit by LCF (solid lines). "Ag-soil" is a reference Ag sorbed with kaolinite. "Metallic Ag" is an Ag foil reference.

Satoshi Takeuchi† and Yohey Hashimoto*

Dept. of Bioapplications and Systems Engineering,
Tokyo University of Agriculture and Technology

*Email: yhashim@cc.tuat.ac.jp

† Present address: National Federation of Agricultural Cooperative Associations (ZEN-NOH)

References

[1] T.M. Benn, P. Westerhoff: Environ. Sci. Technol. **42** (2008) 4133.
[2] *Y. Hashimoto, S. Takeuchi, S. Mitsunobu, Y.S. Ok: J. Hazard. Mater.* ***322*** *(2017) 318.*
[3] *S. Takeuchi, Y. Hashimoto, N. Yamaguchi, K. Toyota: J. Hazard. Mater.* ***317*** *(2016) 602.*

Compressional sound velocity of hexagonal close-packed iron up to 163 GPa and 3000 K

Seismological data reveal important physical properties of Earth's core, such as density and elasticity. Earth's core is mainly composed of iron (Fe), and the stable crystal structure of Fe under the inner core conditions is the hexagonal close-packed (hcp) structure. The density of the inner core based on the Preliminary Reference Earth Model (PREM) [1], which was proposed by using seismological data, is about 2–5% less than that of hcp-Fe (a core density deficit), and it is accepted that the inner core consists of iron and light elements, such as silicon, sulfur, oxygen, hydrogen, and carbon.

To constrain the sound velocity of the inner core and the abundances of light elements, the sound velocities of Fe and Fe alloys have been measured at high pressures by inelastic X-ray scattering (IXS) and nuclear resonant inelastic X-ray scattering (NRIXS). However, due to experimental difficulties, sound velocity measurements with static compression above 2000 K have never been reported. Some previous studies of IXS using external heated DAC showed a small temperature effect on the velocity; however, the maximum temperature range was limited to around 1100 K and the temperature dependence is still not sufficiently clear to discuss the Earth's core.

It is necessary to determine the sound velocity of hcp-Fe at high temperatures in order to quantitatively clarify the difference in the sound velocity between Earth's inner core and hcp-Fe. An important point is that the constituents of the Earth's inner core should fill the gap of both the density and the sound velocity between hcp-Fe and those in seismological models, such as PREM, under the inner core conditions. Here, we report the compressional sound velocity (V_P) of hcp-Fe up to 163 GPa and 3000 K (Fig. 1) based on a combination of laser-heated DAC [2] and IXS measurements at SPring-8 **BL35XU** [3].

V_P for hcp-Fe as a function of density is shown in Fig. 2, together with data obtained at 300 K [4] and shock compression data [5]. These data were fitted by allowing the coefficients in the linear ρ-V_P relation to vary with the temperature, so that Birch's law is preserved at any fixed temperature. A good fit to the data is possible by assuming a first order and linear temperature dependence of the coefficients. The dependence was parameterized as

$$V_P(\rho, T) = M\rho + B + A(T - T_0)(\rho - \rho^*) \quad (1).$$

We choose T_0 to be 300 K; thus, M and B are the coefficients of Birch's law at room temperature, while A and ρ^* indicate the temperature dependence. Fitting our data combined with room temperature data [3] and shock compression data along the Hugoniot [4] gives $M = 1.160 \pm 0.025$, $B = -3.43 \pm 0.29$, $A = 7.2 \pm 3.6 \times 10^{-5}$, and $\rho^* = 14.2 \pm 1.5$.

To demonstrate the difference in density and V_P between hcp-Fe and Earth's inner core, we compare the ρ-V_P characteristics under the conditions of the inner core boundary (ICB). The recent arguments on the thermal state of the outer core based on melting experiments of iron-light element systems suggest that the temperature at the ICB is around 5500 K. V_P at 330 GPa and 5500 K can be calculated by using the density of hcp-Fe and the temperature dependence of Birch's law given in Eq. 1. The obtained V_P for hcp-Fe at 5500 K is shown as a function of density in Fig. 3(a) and compared with PREM in the inner core [1]. The density and compressional velocity of hcp-Fe under the ICB conditions (330 GPa and 5500 K) are calculated to be 13.42 g/cm^3 and 11.85 km/s, respectively. Thus, both the density and V_P for hcp-Fe are higher than those in PREM, which are 12.76 g/cm^3 and 11.03 km/s at the ICB, respectively. The Earth's inner core has a 4–5% smaller density and 7% smaller V_P than hcp-Fe. Thus, we can conclude that the light elements or the combination of the light elements and nickel in the inner core decreases both the density and compressional velocity of hcp-Fe simultaneously under the inner core conditions.

The sound velocity and density of Fe and Fe alloys have been experimentally measured in order to demonstrate the effect of light elements on the properties of iron. Figure 3(b) shows the ρ-V_P plots of

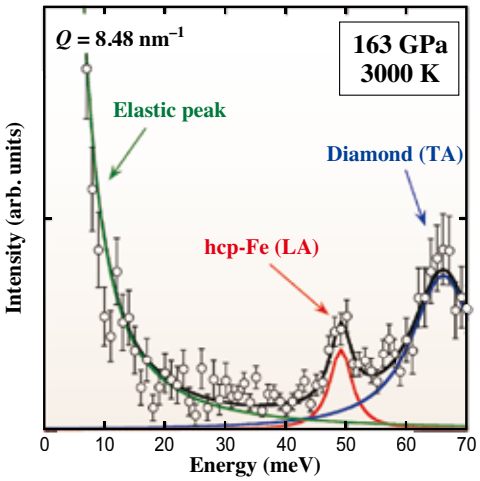

Fig. 1. IXS spectrum of hcp-Fe at 163 GPa and 3000 K. The peak at zero energy is from elastic scattering. Curves are individual contributions (green: elastic scattering, red: LA phonons of hcp-Fe, blue: TA phonons of diamond), with the experimental data fitted with Lorentzian functions.

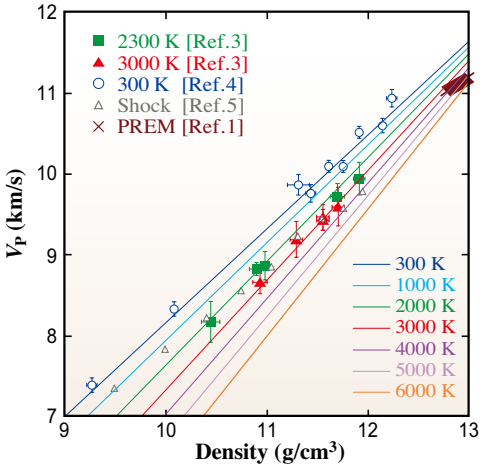

Fig. 2. Compressional velocity of hcp-Fe at several temperatures as a function of density along with high-temperature data [3] and room-temperature data [4] based on IXS and shock compression experiments [5]. Isothermal ρ-V_P fitting lines are expressed as $V_P = [1.160\rho - 3.43] + [7.2\times10^{-5}\times(T-300)\times(\rho-14.2)]$.

hcp-Fe, hcp-$Fe_{92}Ni_8$, dhcp-Fe, hcp-$Fe_{85}Si_{15}$, Fe_3S, FeO (B1/rhombohedral phase), Fe_3C, and Fe_7C_3. Each ρ-V_P plot of iron alloys and iron-light element compounds is shown from the center of the Earth (364 GPa) to the ICB (330 GPa). Star symbols indicate the ρ-V_P points at 330 GPa and 5500 K, obtained by extrapolating to the ICB conditions assuming that the temperature effect on these compounds is the same as that for hcp-Fe. In order to account for the composition of Earth's inner core, the triangles (Fe, Fe-Ni alloy, Fe-light element compounds) need to overlap with the star of PREM. Assuming the ideal mixing of hcp-Fe, hcp-Fe-Ni, and Fe-light element alloys, we obtain the average ρ-V_P for Fe alloy with light elements. As a result, we demonstrate that oxygen and carbon may not be major light elements in the inner core. On the other hand, silicon, sulfur, and hydrogen are potential candidates because they can decrease both the density and velocity. In particular, hydrogen is a good candidate because the mixing of hcp-Fe, hcp-$Fe_{92}Ni_8$, and dhcp-FeH can account for the ρ-V_P plot of PREM. Thus, there is a possibility that the inner core is a hidden hydrogen reservoir in the Earth. In addition, silicon and sulfur can also be major light elements if their temperature effects on V_P are larger than that of hcp-Fe.

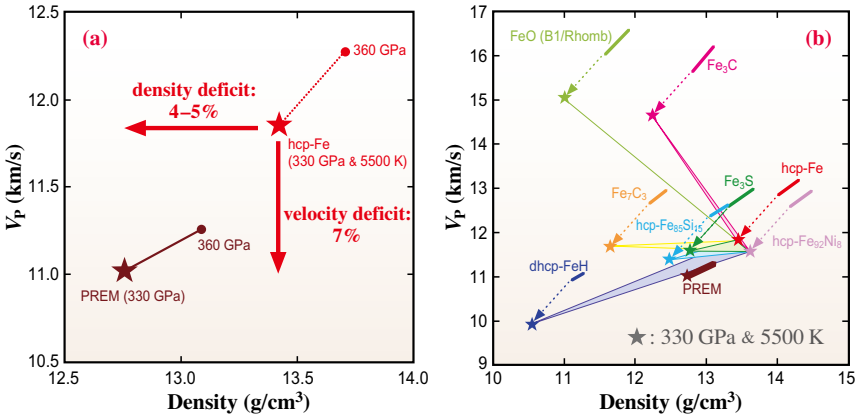

Fig. 3. ρ-V_P plot of hcp-Fe under inner core conditions. **(a)** Comparison of the ρ-V_P plot between hcp-Fe and PREM [1]. Stars indicate V_P and ρ for hcp-Fe and PREM at 330 GPa. The difference in the ρ-V_P plot between PREM and hcp-Fe at 5500 K shows a 4–5% core density deficit and a 7% core velocity deficit. **(b)** Comparison of the ρ-V_P plot between hcp-Fe and Fe-light element compounds. The values for hcp-Fe and the Fe-light element compounds (hcp-$Fe_{92}Ni_8$: purple, dhcp-FeH: blue, hcp-$Fe_{85}Si_{15}$: aqua, Fe_3S: green, FeO [B1/rhombohedral phase]: yellow-green, Fe_3C: pink, Fe_7C_3: orange) show distributions from the inner core boundary (ICB) to the center of the earth. The obtained ρ-V_P for hcp-Fe at 5500 K is indicated by red and star represents the expected ICB conditions. The other stars denote ρ-V_P for Fe-light element compounds under ICB conditions assuming the temperature effects of these compounds are the same as those of hcp-Fe (the dashed arrows are the temperature effects). Triangles connecting the three stars (Fe, Fe-Ni alloy, Fe-light element compounds) indicate the potential ρ-V_P region obtained by mixing the three components.

T. Sakamaki[a]*, E. Ohtani[a], H. Fukui[b,c] and A. Q. R. Baron[c]

[a] Department of Earth and Planetary Materials Science, Tohoku University
[b] Center for Novel Material Science under Multi-Extreme Conditions, University of Hyogo
[c] RIKEN SPring-8 Center

*Email: sakamaki@m.tohoku.ac.jp

References

[1] A.M. Dziewonski, D.L. Anderson: Phys. Earth Planet. Inter. **25** (1981) 297.
[2] H. Fukui *et al.*: Rev. Sci. Instrum. **84** (2013) 113902.
[3] *T. Sakamaki, E. Ohtani, H. Fukui, S. Kamada, S. Takahashi, T. Sakairi, A. Takahata, T. Sakai, S. Tsutsui, D. Ishikawa, R. Shiraishi, Y. Seto, T. Tsuchiya, A.Q.R. Baron: Science Adv. **2** (2016) e1500802.*
[4] E. Ohtani *et al.*: Geophys. Res. Lett. **40** (2013) 5089.
[5] J.M. Brown, R.G. McQueen: J. Geophys. Res. **91** (1986) 7485.

Experimental determination of the electrical resistivity of iron under Earth's core conditions

Earth continuously generates a dipole magnetic field in its convecting liquid outer core by a self-sustained dynamo action. Metallic iron (Fe) is the dominant component of the outer core, so its electrical and thermal conductivity control the dynamics and thermal evolution of Earth's core. Since free electrons are the primary carrier of both electric current and heat, the electron scattering mechanism in Fe under high pressures and temperatures holds the key to understanding the transport properties of planetary cores. Extensive efforts have been made to measure the electrical resistivity of Fe at high pressures since the earliest high-pressure mineral physics experiments, but its direct measurement under the conditions of Earth's core is still challenging. Recent density functional theory calculations predicted the core resistivity to be 20–50% of these conventional estimates [1,2]. Static high-pressure, low-temperature experiments also suggested a low core resistivity because the resistivity saturates at high temperatures [3]. These values suggest that Earth's core has been cooling rapidly, which implies a young inner core and high initial core and mantle temperatures. However, the saturation of resistivity and the resulting low electrical resistivity of Earth's core have not been verified by experiments under the relevant high-pressure, high-temperature conditions.

In this study [4], we measured the electrical resistivity (the reciprocal of electrical conductivity) of Fe at high temperatures (up to 4500 K) and pressures (megabars) corresponding to those of Earth's core in a laser-heated diamond anvil cell. We made use of advanced experimental techniques, including the shaping of the sample-and-electrode composites, to measure the electrical resistivity of Fe at ultrahigh pressures and temperatures (Fig. 1(a)). The Fe foil was shaped into a single member with four probes by using focused ion beam apparatus. This shaping technique enables us to prepare samples with uniform geometry corresponding to each anvil culet size. Concurrently with all high-pressure, high-temperature resistivity measurements, we performed synchrotron X-ray diffraction (XRD) measurements at SPring-8 **BL10XU** (Fig. 1(b)).

We carried out the electrical resistivity measurements at pressures between 75 and 212 GPa, in which only the ε phase was found (Fig. 2). From the high-pressure, low-temperature (up to 450 K) data, we obtained the slope of the temperature–resistivity relation in a wide pressure range (Fig. 2(a)). These measurements indicated that the resistivity increased linearly with increasing temperature. However, the present experiments, performed up to 4500 K in the range 80–157 GPa (Figs. 2(b)-(f)), demonstrate that the measured resistivity is clearly lower than the value predicted from the lower-temperature experiments shown in Fig. 2(a). The low resistivity of ε Fe observed in this study may be attributed to the well-known effect of resistivity saturation at high temperatures (in which the increase in resistivity is suppressed at high temperatures). The electrical resistivity of metal asymptotically approaches the Ioffe-Regel value (that is, saturation resistivity, ρ_{sat}) when the mean free path of free electrons becomes comparable to the interatomic distance. An empirical description of the resistivity saturation in a simple shunt resistor model can be applied to a variety of metals [5]. The present temperature-resistivity data at each pressure is well explained by the shunt resistor model with a reasonable value of ρ_{sat} (black lines in Figs. 2(b)–(f)). Thus, the present results up to 4500 K demonstrate the effect of resistivity saturation, which defines the upper bound for the resistivity and leads to the low electrical resistivity (high thermal conductivity) of Earth's core.

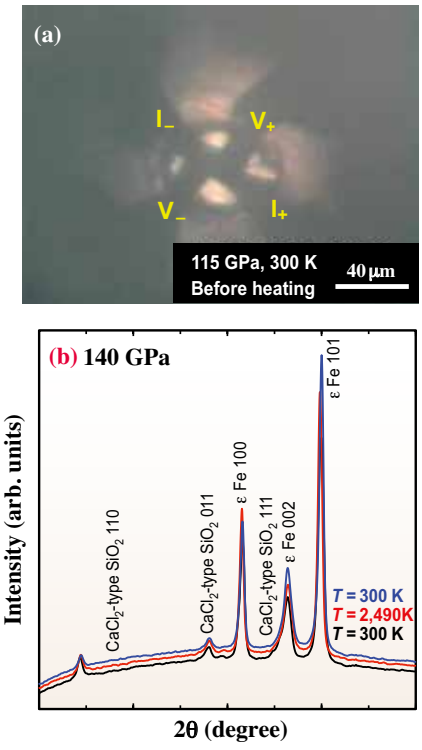

Fig. 1. **(a)** Photomicrographs of a sample chamber viewed through a diamond anvil cell at 115 GPa and 300 K. The four-probe method was used for electrical resistance measurements. **(b)** XRD patterns of ε Fe samples at 140 GPa.

The present data demonstrate the electrical resistivity of Fe to be 40.4 (+9.7/–6.5) μΩcm at 140 GPa and 3750 K (Fig. 2(e)), close to the core-mantle boundary conditions. This corresponds to the electronic thermal conductivity $\kappa_{el} = 226\,(+71/-31)$ W/m/K when the Wiedemann–Franz relation ($\kappa_{el} = L_0 T/\rho$, for the ideal Lorenz number $L_0 = 2.445 \times 10^{-8}$ WΩ/K^2) is applied. Since Earth's core contains some nickel and light elements in addition to Fe, we consider the effect of such impurity elements. The resistivity of solid $Fe_{67.5}Ni_{10}Si_{22.5}$, a possible outer core composition inferred from its density, is calculated to be 86.9 (+15.4/–21.6) μΩcm at 140 GPa and 3750 K, considering the saturation effect. When the 20% resistivity increase upon melting is taken into account, we obtain 104 (+18/–26) μΩcm, giving a thermal conductivity of 88 (+29/–13) W/m/K for liquid $Fe_{67.5}Ni_{10}Si_{22.5}$. As a consequence, the present study supports the high thermal conductivity of Earth's core, suggesting rapid core cooling and a young inner core less than 0.7 billion years old [1-3].

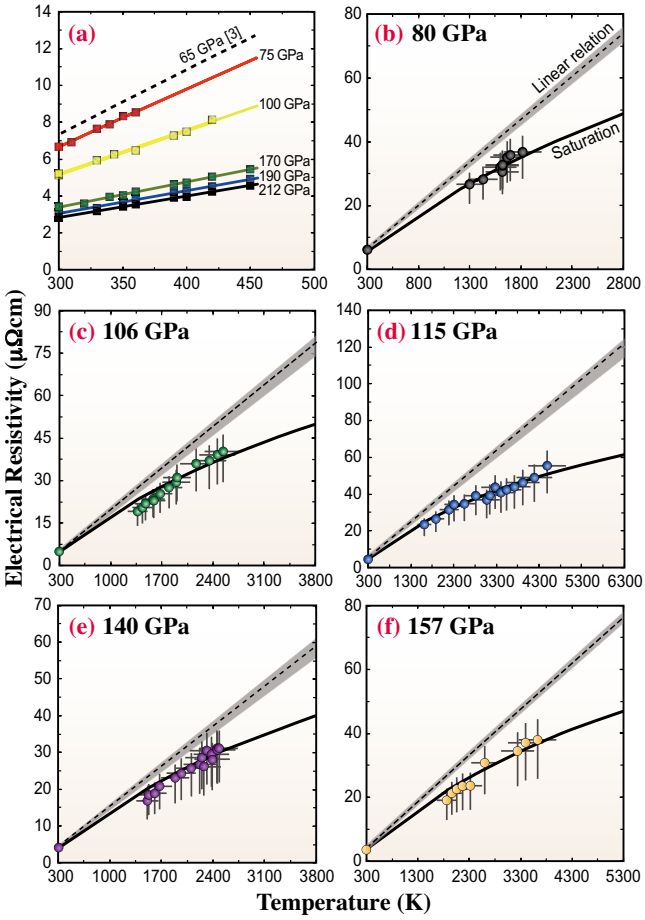

Fig. 2. Change in the resistivity of ε Fe with increasing temperature. **(a)** Temperature dependence of the resistivity up to 450 K at 65–212 GPa fitted by a linear function (colored lines). Similar results at 65 GPa from [3] are also shown. **(b)–(f)** Electrical resistivity measured at 80 GPa up to 1820 K (b), at 106 GPa up to 2540 K (c), at 115 GPa up to 4490 K (d), at 140 GPa up to 2490 K (e), and at 157 GPa up to 3630 K (f). The resistivity measured at high pressures and high temperatures in this study is lower than that predicted by the linear relation (dashed lines with grey uncertainty band) with parameters obtained from the high-pressure, low-temperature measurements in (a). Such a low resistivity can be accounted for by the effect of resistivity saturation at high temperature (solid curves).

Kenji Ohta

Department of Earth and Planetary Sciences,
Tokyo Institute of Technology

Email: k-ohta@geo.titech.ac.jp

References

[1] M. Pozzo *et al.*: Nature **485** (2012) 355.
[2] N. de Koker *et al.*: Proc. Natl. Acad. Sci. **109** (2012) 4070.
[3] H. Gomi *et al.*: Phys. Earth Planet. Inter. **224** (2013) 88.
[4] *K. Ohta, Y. Kuwayama, K. Hirose, K. Shimizu, Y. Ohishi: Nature* ***534*** *(2016) 95.*
[5] H. Wiesmann *et al.*: Phys. Rev. Lett. **38** (1977) 782.

Crystallographic preferred orientation of bridgmanite: implications for the mantle dynamics in the lower mantle

Rheology is one of the most important physical properties of rock and minerals and plays a major role in controlling the dynamic processes in the Earth's mantle. The Earth's mantle consists of an upper mantle (depth: >410 km), transition zone (depth: 410–660 km) and lower mantle (depth: 660–2900 km), which have been distinguished by seismological and mineralogical studies. The lower mantle occupies ~65 vol% of the Earth's mantle. It is important for understanding the Earth's mantle dynamics to know the rheology of its lower mantle.

Recently, the results of P-wave tomography [1] have suggested four types of geometry of subducted slabs under the deep mantle; I-stagnant slabs above the 660 km discontinuity; II-slabs penetrating the 660 km discontinuity; III-slabs trapped in the uppermost lower mantle; and IV-slabs descending far into the deep lower mantle. Seismic tomography can be used to examine the present status of subducted slabs but does not give any direct insight into the flow directions of the slabs. On the other hand, seismic anisotropy, which could be caused by the crystallographic preferred orientation (CPO) of the constituent minerals yielded by deformation of the mantle dynamics, provides information on the flow direction in the deep mantle. At the uppermost part of the lower mantle around subduction slabs (e.g., the Tonga-Kermadec slab), seismic observation demonstrated clear shear wave splitting [2,3]. Therefore, if the CPO of the Earth's lower mantle minerals was well known, the observed seismic anisotropy could give insight into mantle flow directions around slabs.

In pyrolitic mantle model, the minerals constituting the lower mantle are bridgmanite (77 vol%), which is (Mg,Fe)SiO_3 perovskite with space group *Pbnm*, ferropericlase (16 vol%) and CaSiO3-perovskite (7%). The contribution to the CPO of ferropericlase, which has nearly isotropic elasticity under the uppermost lower mantle conditions, is negligible. CaSiO3-perovskite cannot contribute to seismic anisotropy in the lower mantle because of its very limited amount, although the elasticity of CaSiO3-perovskite has large anisotropy. On the other hand, the seismic anisotropy is expected to be produced by the CPO of bridgmanite, which is an elastically anisotropic mineral and the most abundant mineral in the lower mantle. Thus, knowledge of the deformation-induced CPO of bridgmanite is the most important factor for understanding the mantle flow direction from the observed seismic anisotropy in the lower mantle.

The rheology of the lower mantle materials is unknown because of experimental limitations. The available maximum pressure and temperature for deformation experiments are still lower than the Earth's lower mantle conditions, although the experimental techniques at high pressures have significantly developed in the last decade (e.g., [4]). In this study, we further developed the experimental method for simple shear deformation experiments at high pressures to realize the deformation conditions (e.g., geometry and pressure) of the lower mantle using deformation-DIA-type high-pressure apparatus as a Kawai-type cell assembly (6–8 type). Shear deformation experiments on bridgmanite with a controlled strain rate under the uppermost lower mantle conditions (25 GPa and 1873 K) were performed for the first time using the developed techniques [5]. The starting materials were sintered $(Mg_{0.97}Fe_{0.03})SiO_3$ bridgmanite aggregates, which had an equigranular texture with a typical grain size of 15 μm and a random crystallographic orientation as shown in Fig. 1(a). Simple shear deformation of samples at a high pressure and high temperature was applied by 45°-cut alumina pistons and differential rams. The total strain and average strain rate of shear deformation under the uppermost lower mantle conditions were γ~0.8 and $\dot{\gamma}$~2×10^{-4}/s, respectively.

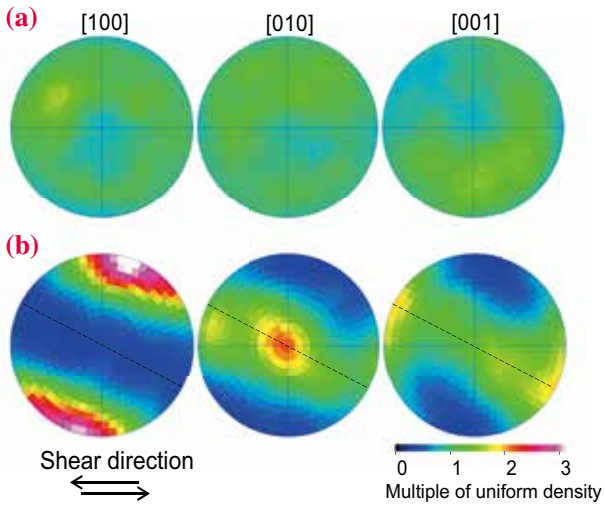

Fig. 1. Pole figures of bridgmanite showing the variation of the crystallographic orientation of the [100], [010] and [001] directions. The coordinate system is defined with respect to the deformation geometry of bridgmanite **(a)** before and **(b)** after shear deformation experiments. Black dashed lines represent the long axis of the strain ellipsoid of the deformed bridgmanite.

The crystallographic orientation of the bridgmanite before and after the shear deformation experiments was determined from the 2D monochromatic X-ray diffraction patterns collected at SPring-8 **BL04B1**.

Bridgmanite aggregates with shear deformation demonstrated a strong fabric (Fig. 1(b)), whereas the starting material had a random crystallographic orientation (Fig. 1(a)). In the sheared bridgmanite, the [001] direction is oriented parallel to the shear direction. The [100] and [010] directions are aligned perpendicular to the shear plane and normal to the shear direction on the shear plane, respectively. These results clearly indicate that the dominant slip system of bridgmanite is the [001](100) system under the conditions of 25 GPa and 1873 K, similar to the uppermost lower mantle conditions.

Figure 2 shows the shear wave anisotropy formed by the CPO of deformed bridgmanite in the present study, which was calculated on the basis of the elastic constant. Black dashes represent the polarization direction of the fastest shear wave in Fig. 2. For the shear wave anisotropy of deformed bridgmanite, in a horizontal flow, the velocity of horizontally polarized shear waves (V_{SH}) is ~1% higher than that of vertically polarized shear waves (V_{SV}), whereas V_{SV} is 0.03–1.10% higher than V_{SH} in a vertical flow. Figure 3 shows the observed shear wave splitting around the Tonga-Kermadec subduction slab, which is trapped at a depth of 1000 km in the uppermost lower mantle (type III according to P-wave tomography). Between the Tonga-Kermadec subduction zone and the Australian continental seismic station, shear wave splitting with $V_{SH} > V_{SV}$ is observed above the subduction zone in the uppermost lower mantle. This seismic anisotropy can be explained by horizontal flow with the CPO of deformed bridgmanite, whose direction is parallel to the subducted plate. In addition, opposite shear-wave anisotropy ($V_{SV} > V_{SH}$) was observed on the front arc side from the Tonga-Kermadec subduction zone to the western North America stations. To explain the seismic anisotropy, a vertical flow is needed with the CPO of deformed bridgmanite. It is thus concluded that both the observed shear-wave anisotropies around the Tonga-Kermadec subduction zone are well explained by the CPO of bridgmanite yielded by the penetration of subducted slabs down to 1000 km by vertical motion and by the stagnation at around 1000 km depth with a horizontal flow in the pyrolitic mantle as shown in Fig. 3. Therefore, the present results on CPO of the bridgmanite coupled with the observation of seismic anisotropy provide strong evidence for understanding the direction of the mantle flow, which can be predicted from seismic tomography.

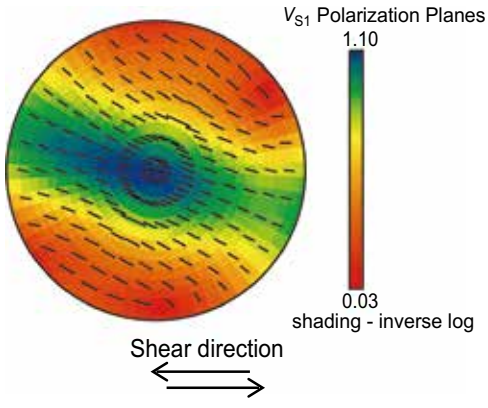

Fig. 2. Trace of the v_{S1} polarization plane of bridgmanite aggregates subjected to shear deformation under the uppermost lower mantle pressure and temperature in a horizontal flow.

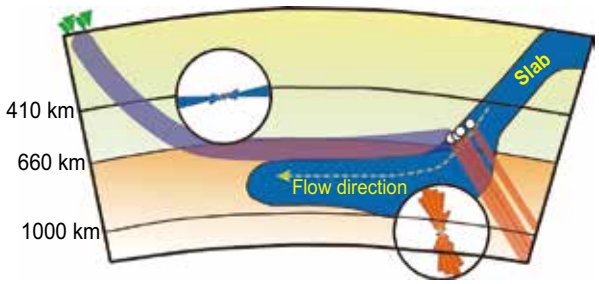

Fig. 3. Schematic cross section of subducted slab of the Tonga-Kermadec arc. Blue and orange lines respectively represent shear seismic ray paths nearly parallel and perpendicular to the section used for the observation of shear wave anisotropies. Blue and orange polar histograms show the polarization of the fast shear wave perpendicular to blue and orange seismic ray paths, respectively. Yellow dashed lines correspond to flow direction of the subducted slab.

Noriyoshi Tsujino[a,*], Yu Nishihara[b] and Daisuke Yamazaki[a]

[a] Institute for Planetary Materials, Okayama University
[b] Geodynamics Research Center, Ehime University

*Email: tsujino@okayama-u.ac.jp

References

[1] Y. Fukao & M. Obayashi: J. Geophys. Res. **118** (2013) 5920.
[2] J. Wooky *et al.*: Nature **415** (2002) 777.
[3] A. Nawacki *et al.*: Geochem. Geophys. Geosys. **16** (2015) 764.
[4] T. Kawazoe *et al.*: American Mineral. **96** (2011) 1665.
[5] *N. Tsujino, Y. Nishihara, D. Yamazaki, Y. Seto, Y. Higo, E. Takahashi: Nature **539** (2016) 81.*

Operando XAFS study of highly active Au-Ni bimetallic clusters for NO-CO reaction in simulated automobile exhaust

Exhaust-gas catalysts can promote the simultaneous purification of harmful automotive exhaust components, such as carbon monoxide (CO), unburned hydrocarbons (HCs), and nitrogen oxide (NO_x) from automotive engines. The catalytic converters are placed under the floor and/or beside the engine, and their devices are installed in exhaust pipes. These catalysts typically comprise (i) platinum group metals (PGMs), i.e., Pt, Pd, and Rh, (ii) oxide supports (Al_2O_3, CeO_2, ZrO_2, etc.) to disperse these precious metal particles at the nanometer scale, and (iii) catalytic promoters. In particular, the PGMs are essential components since they provide catalytically active sites that remove harmful emissions. Recently, owing to the growing need for global environmental protection, exhaust gas regulations have gradually become stricter worldwide. Corresponding to this trend, the demand for automotive catalysts has increased year after year, increasing in the consumption of PGMs. Therefore, the scarcity of PGM resources has inspired us to develop an alternative catalyst to PGMs. Achieving sufficient catalytic activity with a non-PGM catalyst has been considered to be difficult, especially for the NO reduction reaction.

In the process of our research and development, we discovered that a Au-Ni bimetallic cluster catalyst exhibited high NO purification activity matching that of PGMs in the NO-CO reaction under simulated automobile exhaust conditions. Bimetallic clusters have been identified as one possibility for non-PGM catalysts. Although several studies have been carried out on the use of Au-Ni bimetallic system in some applications, to the authors' knowledge, there have been few studies on its use for automobile exhaust purification reactions.

In this study, we attempted to clarify the catalytic mechanism of the high NO-CO activity of the Au-Ni bimetallic clusters utilizing the *operando* XAFS (X-ray Absorption Fine Structure) method [1]. *Operando* XAFS analysis can provide the chemical states and molecular structures of catalysts in their working states as well as their catalytic activity. This methodology has been well established along with intense synchrotron radiation sources. We have constructed a high-speed and high-sensitivity *operando* XAFS system for catalysis at the Toyota beamline **BL33XU**, SPring-8 [2]. The gas transfer unit is made up of three independent gas supply lines to simulate actual auto exhausts, whose compositions vary instantaneously with the engine operation. Its mass analyzer can analyze five gas species at intervals of 50 ms. The *operando* cell was specially designed for the transient XAFS method while minimizing the dead volume. This *operando* system can enable the real-time visualization of the catalytic working state.

In this work, we prepared Au, Ni, and Au-Ni metal nanoparticles via the liquid-phase reduction method. The loadings of Au and Ni in the Au-Ni cluster/SiO_2 were 1.92 wt% and 0.61 wt%, respectively. Rh/SiO_2 as a reference PGM-containing catalyst was also prepared by the conventional wet impregnation process. Figure 1 shows the NO purification conversion as a function of temperature for the NO-CO reaction over the catalysts studied herein. The conversion of NO on both the monometallic Au cluster/SiO_2 and the Ni cluster/SiO_2 was less than 10% up to 600°C. These results indicate that Au or Ni alone on a SiO_2 support has only negligible activity for the NO-CO reaction. In contrast, the Au-Ni cluster/SiO_2 shows significantly higher NO reduction activity over the entire temperature range than both monometallic cluster samples. Furthermore, NO conversion over the Au-Ni cluster/SiO_2 began at less than 300°C, which is comparable to the light-off temperature of the Rh/SiO_2 catalyst. It is assumed that the high NO purification activity over the Au-Ni cluster/SiO_2 is caused by the Au-promoted reduction of NiO to metallic Ni. This hypothesis can be probed by time-resolved *operando* XAFS, which can show the correlation between catalytic activity and the oxidation state of an active site via analysis of the X-ray Absorption Near Edge (XANES) region under actual reaction conditions. Figure 2 shows the energy shift (ΔE) of the Ni *K*-edge under the *operando* NO-CO conditions, along with serial time-resolved Ni *K*-edge XANES spectra of the Au-Ni cluster/SiO_2 and the Ni cluster/SiO_2. The ΔE values of the Ni *K*-edge for both samples at low temperatures were almost equivalent to that for

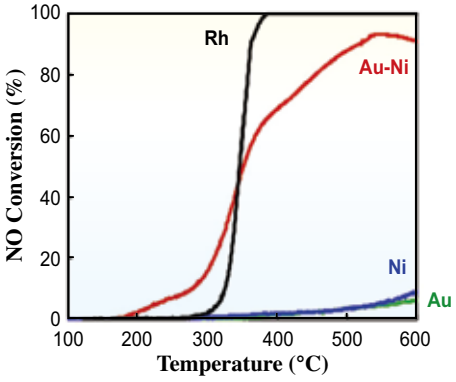

Fig. 1. NO conversion as a function of the reaction temperature under a NO-CO feed: 3000 ppm NO, 4000 ppm CO after pretreatment in 10% O_2 (N_2 bal.) at 350°C.

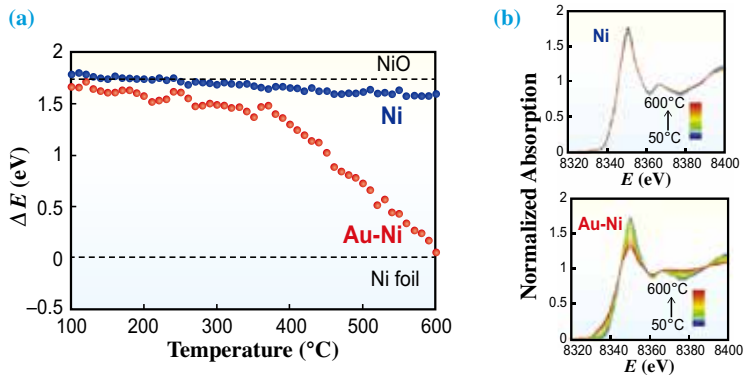

Fig. 2. **(a)** Energy difference (ΔE) calculated by subtracting the Ni *K*-edge absorption energy for Ni foil (base) from that for the Au-Ni cluster/SiO_2 (red) and the Ni cluster/SiO_2 (blue) under a NO-CO feed. **(b)** Normalized XANES spectra of the Ni *K*-edge during the NO-CO reaction.

NiO powder, indicating that the initial oxidation state was Ni^{2+}. The ΔE value of the Ni cluster/SiO_2 slightly decreased with increasing temperature. Moreover, it should be noted that the Au-Ni cluster/SiO_2 catalyst exhibited a more significant shift towards metallic Ni. These results suggest that Ni^{2+} is more easily reduced to a metallic Ni active site for NO reduction in the Au-Ni cluster/SiO_2 than the monometallic Ni cluster/SiO_2. To investigate the correlation between the structure of the supported Au-Ni clusters and the NO purification activity under a NO-CO feed, Au L_3-edge XAFS analysis was also performed on the Au-Ni cluster/SiO_2. As shown in Fig. 3, the XANES spectrum of the Au cluster/SiO_2 under NO-CO at 600°C hardly changed. On the other hand, the peak height of the white line at 11,929 eV for the Au-Ni cluster/SiO_2 significantly increased. As already reported, the increase in the Au white line intensity at 11,929 eV reflects the formation of the Au-Ni alloy species. It is clear that the increase in the Au white line intensity of the Au-Ni/SiO_2 is due to the formation of the Au-Ni alloy in the NO-CO reaction.

In conclusion, the Au-Ni cluster/SiO_2 exhibited the same level of NO purification activity as the Rh/SiO_2, whereas the Au cluster/SiO_2 and the Ni cluster/SiO_2 showed very low activity. *Operando* XAFS analysis revealed that the reduction of NiO in the Au-Ni cluster/SiO_2 was significantly promoted under the NO-CO reaction despite the initial separation of NiO and Au particles. It is suggested that the easy formation of Au-Ni alloy species shows a synergistic effect of the metallic Ni as a dissociative adsorption site for NO and the Au as an oxygen release site in the NO purification reaction.

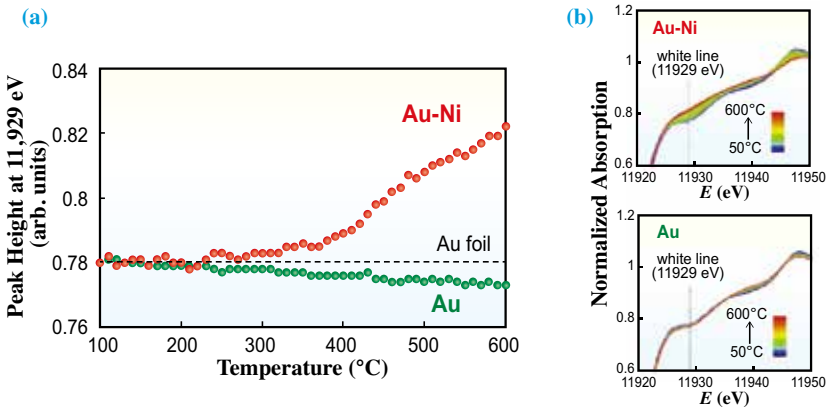

Fig. 3. **(a)** Peak height at 11,929 eV for the Au L_3-edge XANES spectrum under a NO-CO feed. **(b)** Normalized XANES spectra of the Au L_3-edge during the NO-CO reaction.

Yasutaka Nagai[a,*] and Shogo Shirakawa[b]

[a] TOYOTA Central R&D Labs., Inc.
[b] TOYOTA Motor Corporation

Email: e1062@mosk.tytlabs.co.jp

Reference

[1] *S. Shirakawa, M. Osaki, Y. Nagai, Y.F. Nishimura, K. Dohmae, S. Matsumoto, H. Hirata: Catalysis Today* ***281*** *(2017) 429.*
[2] Y. Nagai: SPring-8 Research Frontiers (2013) 110.

Strain-induced transformation process of SUS304 stainless steel revealed by *in situ* X-ray diffraction and high-resolution TEM observation

Metastable austenitic (γ) stainless steels such as SUS304 (Japanese industrial standard type 304 stainless steel) are commercially used as structural materials because of their excellent mechanical properties, including well-balanced corrosion resistance and ductility [1]. It is well known that SUS304 exhibits a strain-induced martensitic transformation, which is defined as a phase transformation from austenite to α'-martensite induced by plastic deformation. One of the important aspects of this transformation is that the enhancement of tensile strength and elongation to fracture results from the appearance of α'-martensite.

Some previous studies by *in situ* transmission electron microscopy (TEM) observations reported that no intermediate ε-martensite was present during the transformation processes and that α'-martensite formed from the twin structures on account of the fcc structure [2]. The appearance of intermediate ε-martensite strongly depends on the subtle balance between the stacking-fault energy and the surface energy. Recently Hatano *et al.* reported a substantial reduction of tensile ductility was found in hydrogen-charged SUS304, which should originate from the formation of ε-martensite of high density at room temperature [3]. In order to elucidate the nanoscale microstructures significantly affecting the transformation processes forming the α'-martensite from austenite in SUS304 at room temperature, we have performed X-ray diffraction experiments and high-resolution TEM observations. It is clearly demonstrated that ε-martensite with hexagonal symmetry appears as an intermediate structure during the plastic deformation of SUS304 stainless steel. In addition to stacking faults and dislocations, interfaces between the twin structures presumably play a key role in the formation of ε-martensite [4].

The materials employed in the present study were commercial SUS304 steel sheets with 0.4 mm thickness. Flat specimens, with 60 mm length and 12.5 mm width at the gauge section, were prepared along the rolling direction. X-ray diffraction experiments were performed using a PILATUS 100 K detector at SPring-8 **BL02B1** in the transmission geometry [5]. The experimental setup is shown in Fig. 1. The energy of an incident X-ray beam was 30.05 keV. The beam size was 3.0 × 0.5 mm^2. The distance between the specimen and the detector was 1100 mm and the detector was fixed at a diffraction angle where the typical diffraction peaks of the α'-martensite and γ-phases could be measured. In an *in situ* measurement under applied stress, the loading device was mounted on the diffractometer. Diffraction data were collected under stepwise stress application. The exposure time for each measurement was 60 min. High-resolution lattice images of microstructures associated with the γ-phase and ε-martensite were obtained using a JEM-2100F TEM apparatus at room temperature.

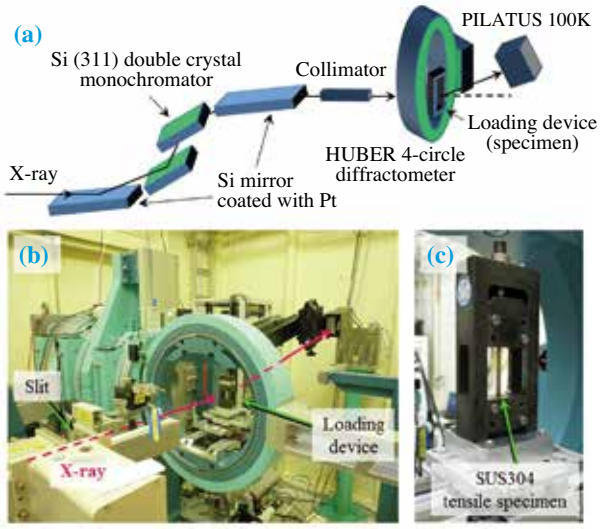

Fig. 1. Instruments for *in situ* measurement of X-ray diffraction data under stress. **(a)** Schematic illustration of experimental layout. Photographs of **(b)** 4-axis diffractometer at BL02B1 and **(c)** SUS304 tensile specimen mounted on a loading device.

Figure 2 shows the *in situ* X-ray diffraction patterns under the application of external stress. In the unstressed specimen, only the diffraction peaks for the γ-phase were observed. As a result of stress application, the diffraction peak for ε-martensite appeared and the intensity increased with increasing stress. However, the intensity was very weak compared with that of the γ-phase, indicating that the volume fraction of the ε-martensite was very small. The diffraction peak for α'-martensite also appeared and the intensity increased in the same manner as for ε-martensite. Our results revealed that ε-martensite was present in some of the specimens at room temperature.

Thus, to clarify the formation process of α'-martensite, we carried out a high-resolution TEM observation of the 20%-elongated specimen. Figure 3 shows a series of high-resolution TEM images obtained around the twin structures in respect of the formation of α'-martensite. As shown in Fig. 3(a), there were many twin structures in the specimen.

Figure 3(b) is a high-resolution TEM image of the square region in Fig. 3(a) showing the presence of ε-martensite in the γ-phase. In the region indicated by an arrow ε-martensite appeared at the interface of the twin structure generated by the strain of the fcc austenite phase. Figure 3(c) is a high-resolution TEM image obtained from the region indicated by the dotted square in Fig. 3(b). A stacking pattern characterizing the hexagonal close-packed structure was observed in the region indicated by "ε" in Fig. 3(c). These results imply that ε-martensite appeared at the nanoscale level near the interface of the twin structure in the strained fcc austenite phase.

We proposed the formation process of α'-martensite from the γ-phase induced by plastic deformation, which is schematically summarized in Fig. 3(d). As the first step, microtwin structures of approximately 10 nm widths are formed in the γ-phase by plastic deformation at about 10% elongation, as evident in Fig. 3(a). The formation of the microtwin structures increases the interface energy. Intermediate ε-martensite appears around the interface of the microtwin structures, as shown in Figs. 3(b) and 3(c). This implies that the formation of ε-martensite from the γ-phase accompanies the reduction of the total volume and reduces the increase in the interface energy. By applying further plastic deformation, the strain energy increases and ε-martensite transforms into α'-martensite.

In situ synchrotron diffraction measurements revealed the formation of a very small amount of ε-martensite as an intermediate phase during the strain-induced transformation from the γ-phase to the α'-phase. High-resolution TEM observations clearly demonstrated that the intermediate nanosized ε-martensite appeared near the twin boundaries in the strained γ-phase. ε-martensite grew at the twin boundaries in the γ-phase and served as the intermediate structure in the transformation process from the γ-phase to α'-martensite. The presence of ε-martensite in the plastic deformation of SUS304 stainless steel was thus demonstrated for the first time.

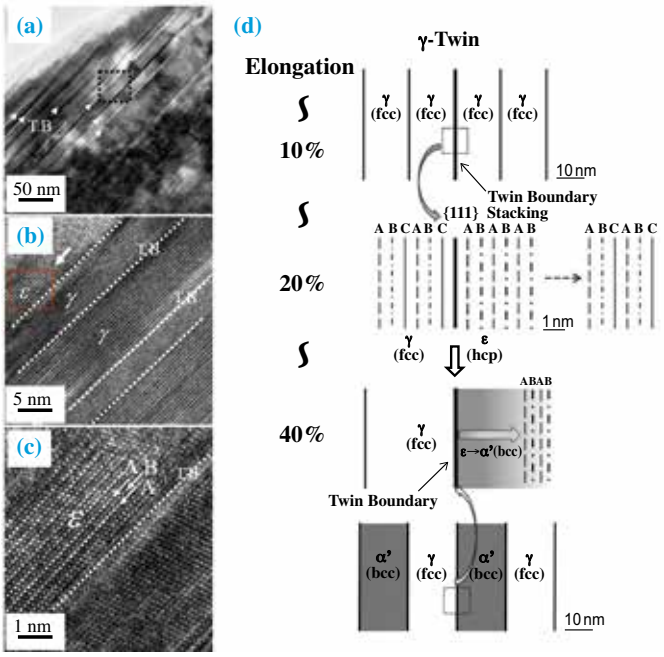

Fig. 3. Microstructures obtained in the 20%-elongated specimen. **(a)** Bright-field images showing twin structures in the fcc austenite phase. Arrows indicate twin boundaries (T.B). **(b)** High-resolution TEM image showing the twin structures, indicated by white dotted lines. **(c)** High-resolution TEM image obtained from the region enclosed by the dotted square in (b). The hexagonal structure is characterized as alternately stacked A and B layers, as indicated in (c). **(d)** Schematic illustrations of formation process of the strain-induced α'-martensite phase of tensile strained SUS304 at room temperature.

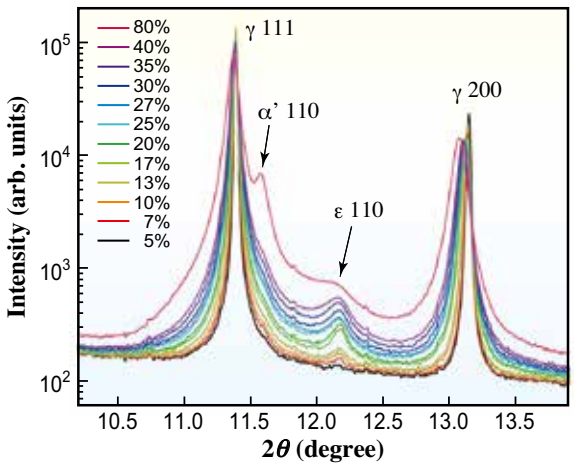

Fig. 2. Evolution of X-ray diffraction patterns in *in situ* measurement under stress. The percentages indicate the elongation applied to the specimen.

Yoshiki Kubota[a,*], Masaharu Hatano[b] and Shigeo Mori[c]

[a] Dept. of Physical Science, Osaka Prefecture University
[b] R&D Center, Nippon Steel & Sumikin Stainless Steel Corp.
[c] Dept. of Materials Science, Osaka Prefecture University

*Email: kubotay@p.s.osakafu-u.ac.jp

Reference

[1] Japan Stainless Steel Association: Stainless Steel Handbook. 3rd Edition. The Nikkan Kogyo Shimbun, Ltd., Tokyo (1995) 554.
[2] T. Katayama and H. Fujita: J. Jpn. Inst. Met. Mater. **52** (1988) 935.
[3] M. Hatano *et al.*: Acta Mater. **67** (2014) 342.
[4] *M. Hatano, Y. Kubota, T. Shobu and S. Mori: Phil. Mag. Lett. **96** (2016) 220.*
[5] M. Sano *et al.*: Adv. Mater. Res. **996** (2014) 33.

Anomalous lattice deformation in GaN/SiC(0001) measured by *in situ* synchrotron X-ray diffraction

Gallium nitride (GaN) is widely used for LEDs and high-frequency power devices and has the potential to drastically reduce power consumption beyond what has been achieved by conventional materials such as silicon (Si) or gallium arsenide (GaAs). Thus, the more widespread use of GaN-based devices is expected to help realize a future low-energy society. Despite these technological advances, many issues affecting the crystal growth of GaN still remain. For example, the lattice deformation of GaN in the initial growth stage has not been fully clarified. In the case of GaN/SiC(0001) heteroepitaxy, this property should be characterized at the growth temperature because of a large thermal mismatch between the film and the substrate, which would induce large state variations during cooling [1]. Reflection high-energy electron diffraction (RHEED) is commonly used for *in situ* monitoring in molecular beam epitaxy (MBE), and the surface morphology can be evaluated from changes in the RHEED pattern or intensity [2]. Furthermore, this technique can provide the lattice parameter along the in-plane direction, which is estimated from the spacing between streaks [3]. However, conventional *in situ* monitoring is insensitive to the lattice parameter along the surface normal direction, knowledge of which is necessary to estimate the lattice deformation more precisely. In this study, *in situ* synchrotron X-ray diffraction (*in situ* XRD) was conducted to measure the lattice parameters of GaN in both the in-plane and out-of-plane directions. The combined use of a high-brilliance synchrotron radiation source and a two-dimensional (2D) detector has enabled high-speed measurements with atomic-scale resolution. Using this method, we found anomalous lattice deformation during the initial growth of GaN, and a new deformation model that defies conventional theory was proposed.

Experiments were performed at SPring-8 **BL11XU** using a plasma-assisted MBE system that is directly coupled to an X-ray diffractometer [4]. In the MBE chamber, following the removal of native oxides from the Si-faced 6H-SiC(0001) substrate by high-temperature heating, GaN was directly grown on the substrates as shown in Fig. 1. X-rays with the energy of 20 keV were focused to a size of 0.1×0.1 mm^2 by a four-blade slit. The diffracted X-ray signals were detected by a 2D detector (PILATUS 100K) with an angular resolution of 0.014°.

Figure 2 shows typical obtained experimental data. The diffraction peak of GaN-101 was confirmed to emerge as the thickness of the GaN film reached 0.8 nm, corresponding to approximately two atomic layers. This means that our real-time measurement is quite effective for evaluating lattice deformation quantitatively at the atomic layer scale.

Figure 3 shows film-thickness dependences of the diffraction-peak positions along the out-of-plane (L) and in-plane (H) directions. These positions are related to the reciprocal of the lattice spacing of GaN in each direction. In the conventional strain relaxation of crystals, the lattice spacing in the L-direction changes in conjunction with that in the H-direction. That is, when a film with a larger lattice constant than the substrate is relaxed, the rate of decrease in the lattice spacing along the L-direction is almost identical to the rate of increase along the H-direction; this is known as conventional elastic theory. However, Fig. 3 shows that the variation in the H-direction is small compared with that in the L-direction. In order to understand this anomalous phenomenon, a new

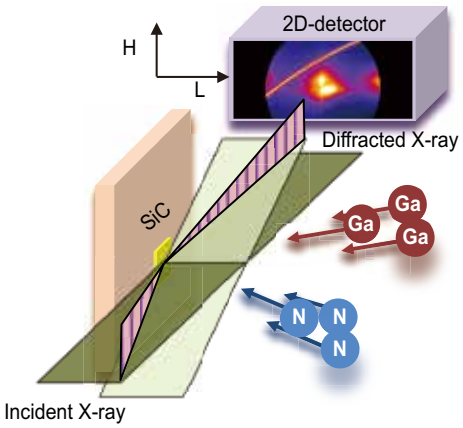

Fig. 1. Schematic of *in situ* XRD during the growth of GaN on a SiC substrate.

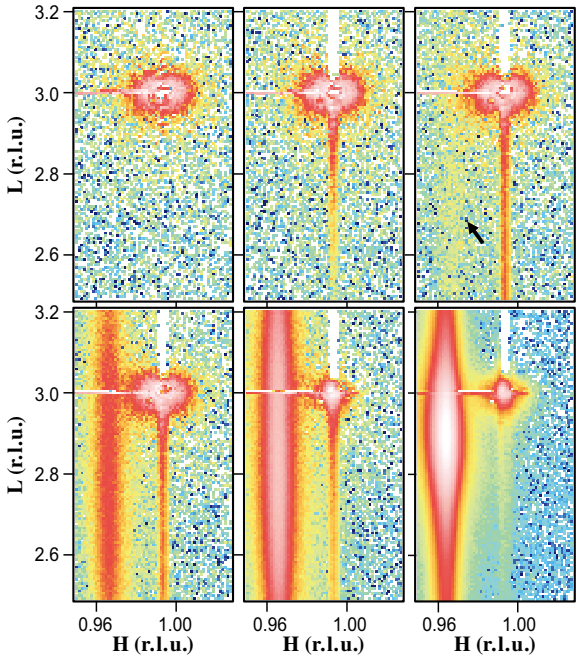

Fig. 2. Typical reciprocal space maps obtained by *in situ* XRD. The GaN thicknesses are 0 (before growth), 0.5, 0.8, 1.0, 2.1, and 10 nm. With increasing GaN film thickness, the diffraction peak of GaN becomes larger and its peak position is gradually shifted.

lattice-deformation model reflecting lattice expansion due to the incorporation of point defects (Ga anti-site defects) was considered, leading to a good fitting with the experimental data as shown by the calculation result in Fig. 3. This suggests that depending on the growth condition, many more point defects than are expected can be incorporated into the GaN film [5].

We have proposed the new lattice-deformation model of the GaN film on the basis of the results of real-time observation. Since this model is important for controlling the point-defect density in GaN, it is expected to optimize the growth conditions for GaN films with high quality and a low defect density in the future.

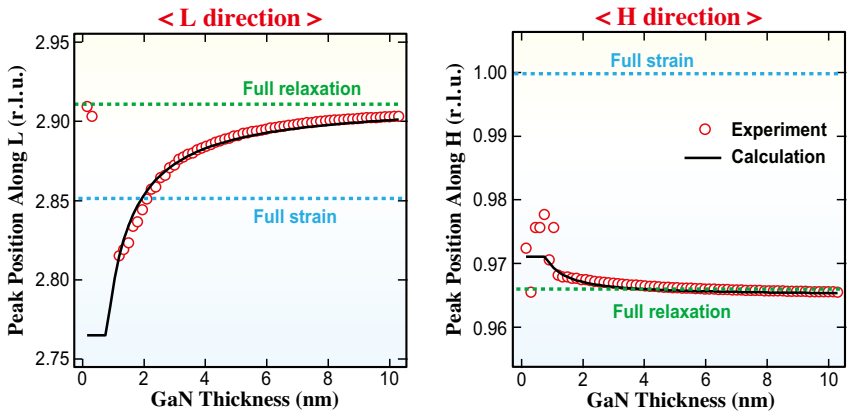

Fig. 3. Film-thickness dependences of the peak positions. It is clear that the lattice spacing along the L-direction shifted more than that along the H-direction, indicating a difference from conventional elastic theory. "r.l.u." indicates reciprocal lattice unit and a large (small) value corresponds to a small (large) lattice spacing of GaN.

Takuo Sasaki* and Masamitsu Takahashi

Synchrotron Radiation Research Center, QST

*Email: sasaki.takuo@qst.go.jp

Reference

[1] D.G. Zhao *et al.*: Appl. Phys. Lett. **83** (2003) 677.
[2] N. Grandjean & J. Massies: Appl. Phys. Lett. **71** (1997) 1816.
[3] G. Koblmüller *et al.*: Appl. Phys. Lett. **93** (2008) 243105.
[4] T. Sasaki *et al.*: Jpn. J. Appl. Phys. **55** (2016) 05FB05.
[5] *T. Sasaki, F. Ishikawa and M. Takahasi: Appl. Phys. Lett.* ***108*** *(2016) 012102.*

Real-time analysis of the crystallization dynamics of organolead halide perovskite

Organolead halide perovskite solar cells are expected to be highly efficient and inexpensive, and competition in the research and development of these solar cells is accelerating. A simple process for the fabrication of these solar cells would be of interest from an industrial perspective, such as the mixing of a lead halide and amine halide to produce perovskite crystals. High-performance solar cells with reduced cost are expected to be achieved with the use of perovskites. Intensive studies based on both solution processing and vacuum deposition have been carried out since 2013, and the power conversion efficiency reached more than 20% within a couple of years [1]. The study of the crystallization processes of the perovskites is important because their performance in solar cells is strongly affected by their crystal structure and morphology. In particular, the elucidation of the crystallization mechanism is of great importance. The author's group has been focusing on the real-time analysis of the formation process of organic thin films by X-ray diffraction using the SPring-8 large synchrotron radiation facility [2]. The use of synchrotron radiation is very useful for *in situ* analysis because high-speed X-ray diffraction measurement is possible using the high-intensity light source with a two-dimensional X-ray detector. We started the real-time analysis of the formation process of organolead halide perovskites in 2014. The solution-based reaction from source materials into the perovskite was investigated in order to elucidate the mechanism of crystallization.

In this study [3], SPring-8 **BL46XU** was used for the real-time observation of X-ray diffraction with a two-dimensional X-ray detector (PILATUS 300K). An organolead halide perovskite ($CH_3NH_3PbI_3$) was fabricated by the dropwise addition of a solution of CH_3NH_3I in 2-propanol onto a PbI_2 thin film, which was mounted on a measurement stage (Fig. 1). Ten-frame-per-second real-time X-ray diffraction measurements were conducted to analyze the reaction process.

The measurement result in Fig. 2 shows the reduction in the amount of PbI_2 raw material over time and the formation process of the perovskite crystal. Analysis of the rate of progression of this reaction revealed that the reaction progression did not follow the normal diffusion phenomenon but instead followed an anomalous diffusion process. This is thought to be because when CH_3NH_3I diffuses into the PbI_2 thin-film medium, the CH_3NH_3I diffuses by branching, reflecting the heterogeneity of the medium.

Next, the angles of the X-ray diffraction patterns were analyzed (Fig. 3). In the early stage of the reaction the formed crystals were oriented in two specific directions, but with the progress of time they changed to a random orientation. This finding suggests that the crystals changed continuously during the process of formation of the perovskite crystal.

This is not the only study to have observed and reported on the formation process of a perovskite crystal by using X-ray diffraction. However, in this study, we measured this process with a high

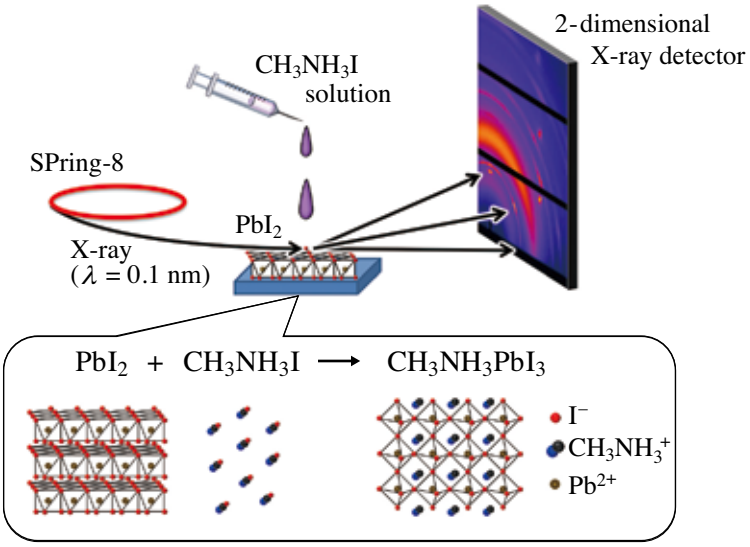

Fig. 1. Schematic illustrations of the measurement setup for real-time crystallization analysis.

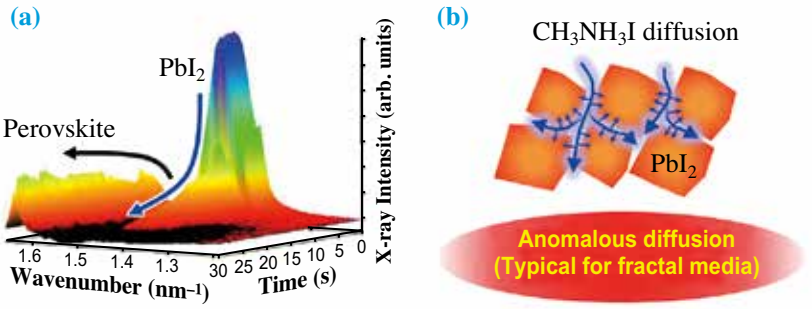

Fig. 2. **(a)** Changes in X-ray diffraction intensity over time and **(b)** schematic diagram of diffusion of CH_3NH_3I into PbI_2 thin-film medium.

measurement speed of 10 frames per second; a detailed analysis of the reaction rate and crystal orientation was performed, which resulted in the finding of novel phenomena such as the anomalous diffusion and continuous changes in the crystal orientation. These behaviors appearing during the crystallization process are considered to be the cause of the poor reproducibility of perovskite thin-film formation. Therefore, achieving the control over these novel phenomena is the key to the highly reproducible fabrication of highly efficient solar cells.

The X-ray diffraction method using synchrotron radiation has now been proven to be a valid method for analyzing the formation process of perovskite crystals. An increasing number of studies related to this topic have recently been reported [4,5]. It is important to conduct structural analysis and device development in a complementary manner in order to accelerate the research and development of organolead perovskite solar cells.

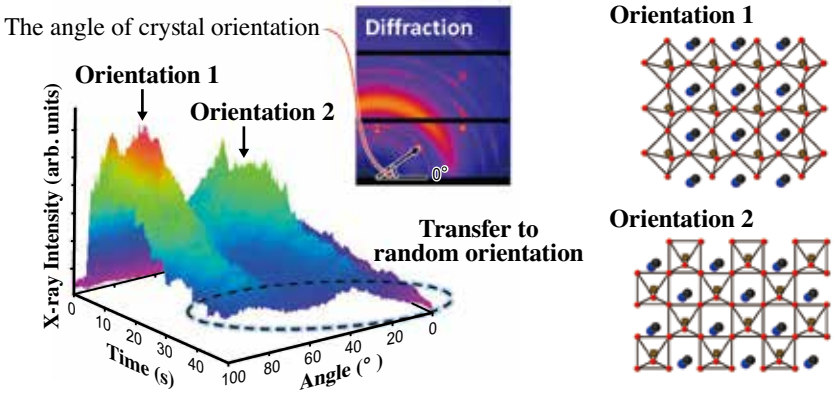

Fig. 3. Changes in the direction of the X-ray diffraction (reflecting the crystal direction) over time. In the early stage of the reaction, the crystals were oriented in two specific directions, but they later changed to a random orientation.

Tetsuhiko Miyadera

Research Center for Photovoltaics, National Institute of Advanced Industrial Science and Technology (AIST)

Email: tetsuhiko-miyadera@aist.go.jp

Reference

[1] National Renewable Energy Laboratory (NREL), http://www.nrel.gov/ncpv/images/efficiency_chart.jpg.
[2] K. Sasaki *et al.*: Appl. Phys. Express **6** (2013) 041601.
[3] *T. Miyadera, Y. Shibata, T. Koganezawa, T.N. Murakami, T. Sugita, N. Tanigaki and M. Chikamatsu: Nano Lett.* ***15*** *(2015) 5630.*
[4] S. Lilliu *et al.*: Cryst. Eng. Comm. **18** (2016) 5448.
[5] L.H. Rossander *et al.*: Cryst. Eng. Comm. **18** (2016) 5083.

Accelerators & Beamlines Frontiers

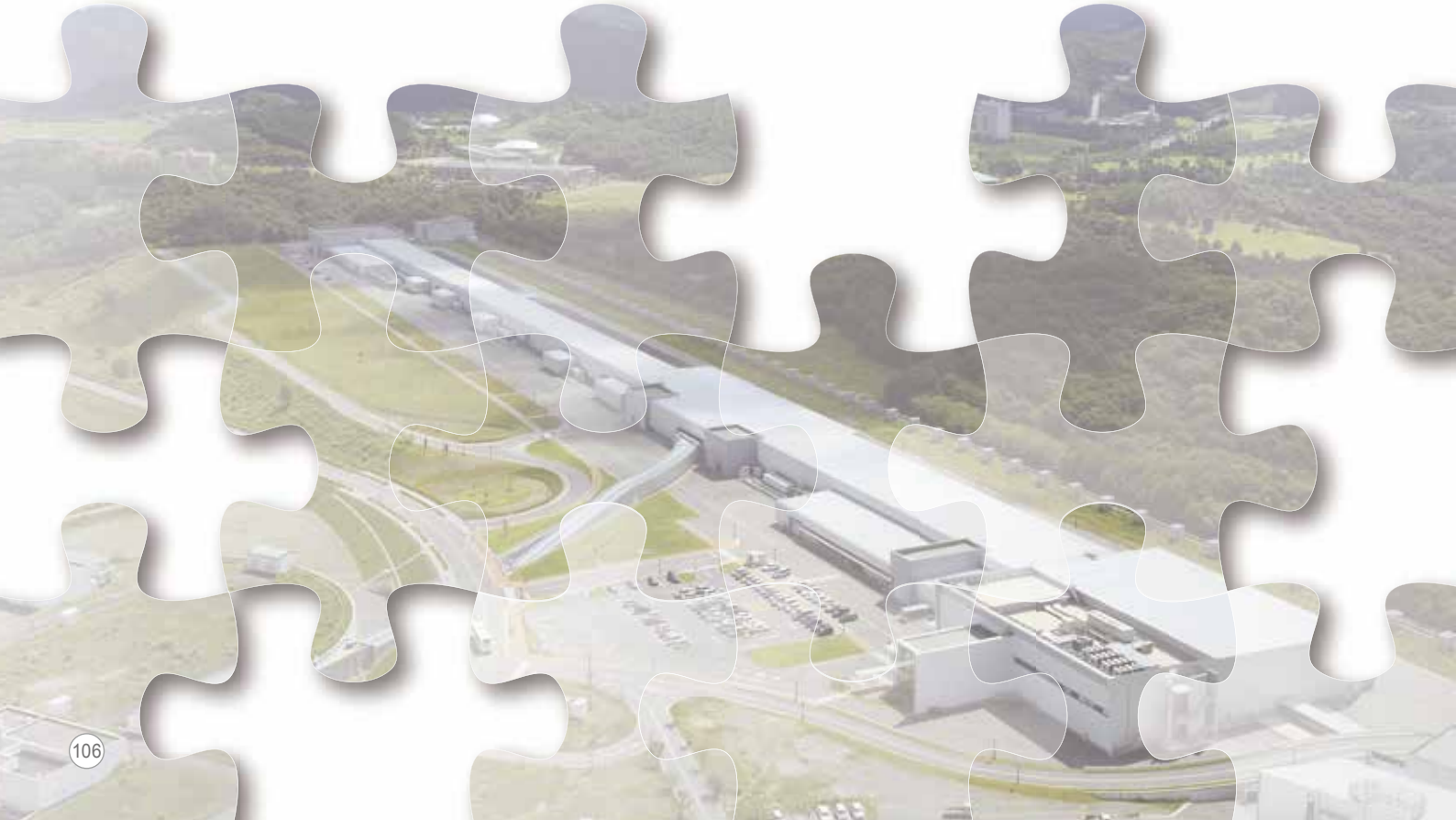

SPring-8 Beam Performance

Recent update of accelerator operations

Most of the recent machine developments have the aim of maintaining stable and reliable accelerator operation. These developments are essential to provide stable light source performances for user experiments without significant machine operation problems. Simultaneously it is important to pursue these developments as a preparation for the future major upgrade currently being discussed. Three of these developments are presented as follows.

1) One of the key components of accelerators for stable beam operation is the so-called bunch-by-bunch feedback (BBF) system. The beam position monitor detects the offset of a passing beam position from an ideal orbit and the downstream kicker kicks it back by a closed loop feedback system. Without it, the spatial position and angle of synchrotron radiation in downstream X-ray optics could fluctuate turn by turn, increasing the effective radiation beam size integrated over the measurement time. Thus, the BBF system is kept operational during user operations so that an undesired beam oscillation excited by any kind of perturbation is damped before it has a significant effect on user experiments.

Nevertheless, beam instabilities in the vertical direction were intermittently observed, especially in a specific operation mode called the A-mode. This mode is also referred to as the 203-bunch mode as 203 out of 2436 buckets in the storage ring are supposed to be filled with electron beams with equal separation between them. However, in 2016 we had to make the decision to operate the A-mode with a 406-bunch mode from June 19 to July 2 and from September 15 to 24 due to the vertical instability, during which 406 buckets instead of 203 were filled with beams. After a detailed investigation, the internal electric circuit of the BBF system was revised (see Fig. 1 for the new digital feedback processor involving the revised internal electric circuit), and since then the vertical instability appears to have been suppressed. Thus, the next A-mode user operation from November 29 to December 11 was operated with the 203-bunch mode without notable instabilities. As the beam instability is one of the most important issues for stable and reliable accelerator operation, we will continue paying attention to this issue.

Fig. 1. New digital feedback processor for the BBF system.

There have been two further developments of the BBF system. First, the system has been reassembled and its sophistication has been increased so that accelerator operators can easily change the internal system settings by using a new GUI on the accelerator control computer. When the user operation is switched from a certain mode to another, for example, the operator simply needs to implement a single-click operation to adjust the BBF settings. This new feature is beneficial not only for quick operation but also for reliable management of the accelerators. Second, it has become possible to measure betatron tunes while the accelerator is being operated without noticeable perturbation for users. It is well known from beam dynamics that the betatron tunes have to be kept away from some harmful values to avoid instabilities originating from resonances. With the new capability, we are now able to measure betatron tunes anytime and adjust them if necessary. These two aspects were implemented by introducing a new digital feedback processor developed at SPring-8.

2) Some of the insertion devices at the SPring-8 storage ring generate a betatron coupling of the transverse motion, and consequently the vertical beam size increases. To correct the coupling, we installed skew quadrupole magnets for 12 insertion devices that have particularly large effects on the coupling. A GUI has been developed so that the excited coupling is now automatically corrected. This function has been applied in user operations since December 2016.

3) In the beamline BL43LXU, three short-period undulators are installed in tandem in a magnet-free long straight section. Since the photon beam axes of these undulators must be aligned with each other, the required stability and reproducibility of the electron beam orbit are severer than for the other beamlines, being less than 1 μrad in the vertical direction and 2 μrad in the horizontal direction. We hence carried out fine tunings of the strengths of correctors to make a closed local bump for orbit control as perfectly as possible and developed a single-click GUI to perform a quick orbit correction for three undulators at the same time in both the horizontal and vertical directions. From April 2017, this GUI will be used to quickly recover the change in the orbit caused by beam refilling and by some perturbations during user operation.

T. Watanabe*, M. Takao and K. Soutome

Japan Synchrotron Radiation Research Institute (JASRI)

*Email: twatanabe@spring8.or.jp

SACLA Beam Performance

Since July 2016 [1], users have conducted experiments on BL1, which enables the simultaneous utilization of SXFEL and XFEL beamlines for different experiments. Despite a decrease in the total operation time for SACLA due to budgetary constraints, the total user time in FY2016 across user shifts at BL1 to BL3 is expected to exceed 4000 h, maintaining high laser availability with efficient multi-beamline operations. Through a high-power test for more than 1000 h, the first user experiment was implemented with a repetition rate of 60 Hz in autumn 2016, as shown in Fig. 1. A high XFEL repetition rate of 60 Hz will be fully available for user experiments in 2017.

In order to meet the increasing demand for XFEL utilization, pulse-by-pulse BL2/BL3 operation [2,3] has been offered since February 2016. However, the available peak power for the XFEL has been limited to around several GW due to degradation of the electron beam caused by strong CSR (coherent synchrotron radiation) through a dogleg composed of a bend and bend-back of 3 degrees. Since most experiments require a short pulse of less than 10 fs and a high laser pulse energy of several hundred μJ, enabling pulse-by-pulse BL2/BL3 operation with full laser performance is critical for further improving utilization efficiency. Therefore we investigated a new

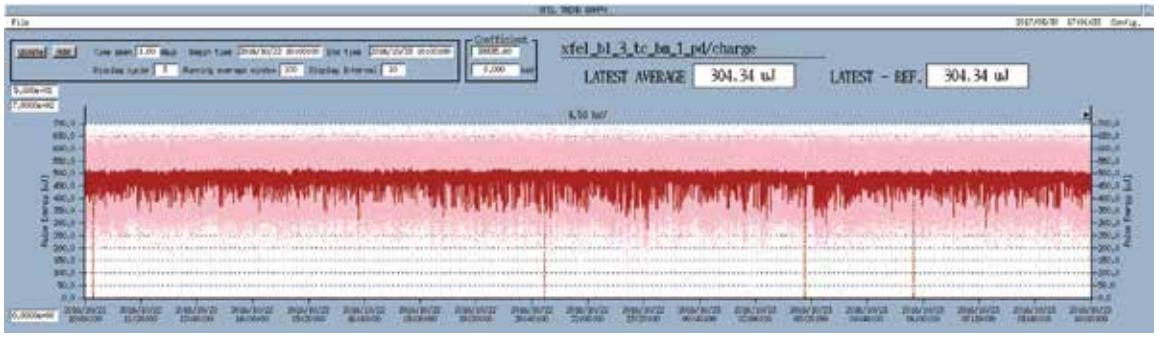

Fig. 1. Laser intensity trends for the first user experiment with a repetition rate of 60 Hz from October 22 to 23, 2016. The beamline is BL3 and the photon energy is 4.5 keV.

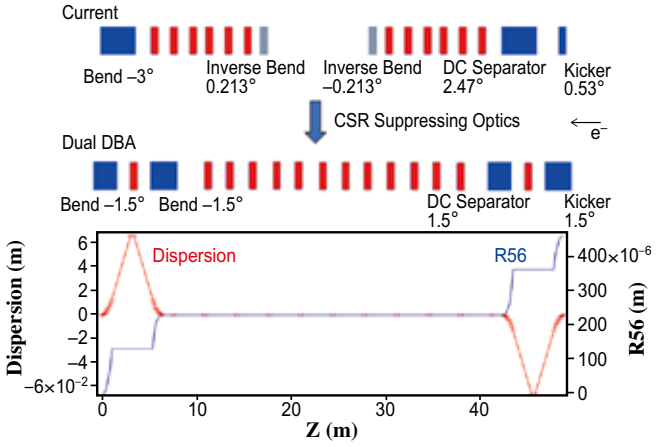

Fig. 2. Comparison of the previous dogleg configuration with the new dual DBA dogleg. The new design provides more symmetric optics for cancelling out perturbation effects caused by CSR compared with the current design. The lower figure shows the dispersion and R56 distributions over the new dogleg configuration.

beam-switching scheme to suppress the degradation caused by CSR and found that a dogleg based on a dual DBA (double bend achromat) with a matched phase advance of π (Fig. 2) could sufficiently reduce degradation [4]. The suppression mechanism is a result of the electron beam modulation occurring at the upstream DBA with a bend angle of +3 degrees being precisely canceled out at the downstream DBA with a bend angle of –3 degrees up to the second order of perturbation. This new scheme therefore allows us to generate XFEL with a high peak current of more than 10 kA, enabling both high laser peak power and high laser pulse energy. On the other hand, since this scheme requires a challenging 0.3 MW pulse power supply with extremely high stability (currently not commercially available), we have been working with Nichicon Corporation to develop a new power supply. Following the installation of the whole system (scheduled for winter 2016), the new beam switching system will be commissioned in February 2017.

During the summer shutdown of 2016, two C-band RF acceleration units were installed (Fig. 3) to increase the maximum electron beam energy for BL1 to 800 MeV. This energy upgrade widened the available photon energy range to 120 eV (sub-10-nm wavelength). Beam commissioning for the upgraded BL1 accelerator system started in autumn. By the end of November, a pulse energy of about 100 μJ had been obtained at a photon energy of 100 eV. The wider photon energy range will be fully available for user experiments at the BL1 beamline in 2017.

Fig. 3. BL1 to BL3 beamlines in the undulator hall taken from the experimental hall side (i.e., the downstream side) of BL1. The white circle indicates the newly installed C-band accelerator units in the BL1 accelerator.

Hitoshi Tanaka

RIKEN SPring-8 Center

Email: tanaka@spring8.or.jp

References

[1] T. Inagaki *et al.*: Proc. 13th Annual Meeting of the Particle Accelerator Society of Japan, Chiba, Japan (2016) p. 286.
[2] T. Hara *et al.*: Phys. Rev. Accel. Beams **19** (2016) 020703.
[3] T. Hara: SPring-8/SACLA Research Frontiers 2016 (2017) p. 110.
[4] T. Hara *et al.*: Proc. 13th Annual Meeting of the Particle Accelerator Society of Japan, Chiba, Japan, (2016) p. 282.

Pulse-by-pulse multi-beamline operation of SACLA

X-ray Free Electron Lasers (XFELs) have distinctive characteristics such as high peak intensity, short pulse duration and coherence. Since XFELs require a high-brightness electron beam for lasing, a linear accelerator is used as an electron beam driver. Therefore, the electron beam is generally provided to only one beamline at the same time. In order to improve the usability and efficiency of XFEL facilities and satisfy the increasing demand for user experiments, the distribution of the electron beam to multiple beamlines has become an important issue.

SPring-8 Angstrom Compact free-electron LAser (SACLA) has been open to user experiments since 2012 [1]. Currently two XFEL beamlines (**BL2** and **BL3**) and one EUV FEL beamline (**BL1**) are in operation. BL1 is driven by the SCSS+ accelerator and independently operated from XFEL beamlines. In 2015, a switchyard composed of a kicker magnet and a DC septum magnet was installed at the end of the linear accelerator of SACLA. The switchyard can distribute 60 Hz electron bunches from pulse to pulse in three directions corresponding to the two XFEL beamlines and an electron beam injection line to the SPring-8 storage ring [2]. Figure 1 is a schematic of the current SACLA facility.

Since the stability of the electron beam orbit inside undulators is critically important for XFELs to ensure interaction between electrons and photons, high stability and reproducibility are required for the switchyard, particularly for the kicker magnet. At the switchyard, the destination of the electron beam is determined by the kicker magnet, which deflects the beam by either 0° or ±0.5°. The deflected beam is further bent by the DC septum magnet (2.5°) as shown in Fig. 1. The deflection angle of the kicker magnet is made as small as possible to relax the stability requirement for the pulsed power supply. The pulsed power supply employs PWM (pulse width modulation) regulation using eight FETs connected in parallel and it generates bipolar trapezoidal current waveforms with arbitrary amplitudes to cover various beam energies. Figure 2 shows the pulse-to-pulse stability of the kicker magnetic fields measured by a gated Nuclear Magnetic Resonance (NMR) probe. The typical peak-to-peak stability is 1×10^{-5} except for a slow drift, which can be corrected by electron beam orbit feedback.

In the multi-beamline operation, several user experiments are performed in parallel. Consequently, the wavelengths of the XFEL may be different between

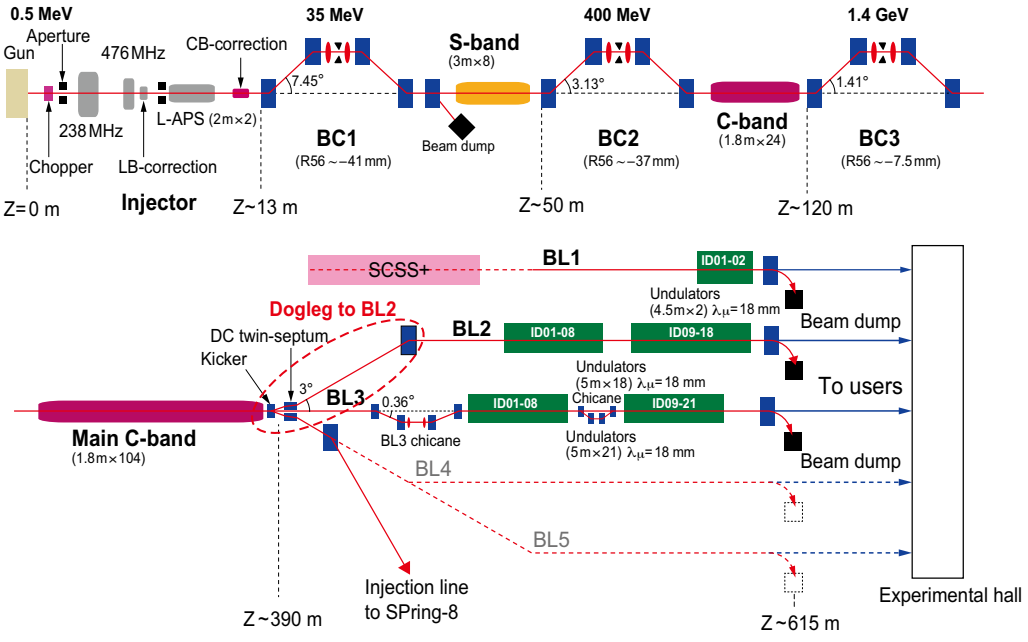

Fig. 1. Schematic of the current SACLA facility.

the experiments. In this case, it is necessary to change the electron beam energy of each beamline. At SACLA, the multi-energy operation of the linear accelerator has been successfully achieved, in which the beam energies of the electron bunches are controlled by changing the repetition rate of accelerator tubes [3].

The first multi-beamline operation of SACLA was demonstrated in January 2015. In the demonstration, 30 Hz electron bunches were alternately sent to the two beamlines, BL2 and BL3 [2]. Figure 3 shows the laser pulse energies measured at the two beamlines. Although stable lasing was successfully obtained at both beamlines, the peak current of the electron bunches was limited to 2 kA, as compared with 10–15 kA currently used for the nominal operation of BL3. The limitation of the peak current is due to CSR (coherent synchrotron radiation) at the dogleg in the electron beam transport line to BL2 (Fig. 1). When the electron bunch passes through a bending magnet, the beam energy is modulated inside the bunch owing to CSR. Then the emittance is degraded and the beam orbit becomes unstable for high-peak current bunches. Since SACLA BL2 has been operated with low peak currents to avoid the effects of CSR, the pulse energy has remained around 150 μJ, which is about a quarter of that of BL3 in the nominal operation.

To mitigate the effects of CSR, the electron beam optics of the BL2 dogleg transport line is planned to be rearranged in January 2017, in which symmetric optics based on a DBA (double bend achromatic) lattice is employed. In the new lattice, the deflection angles of all bending magnets are made the same (1.5°) to cancel out the effects of CSR between the bending magnets. Multi-beamline operation with the full laser performance of SACLA will be obtained after the lattice modification.

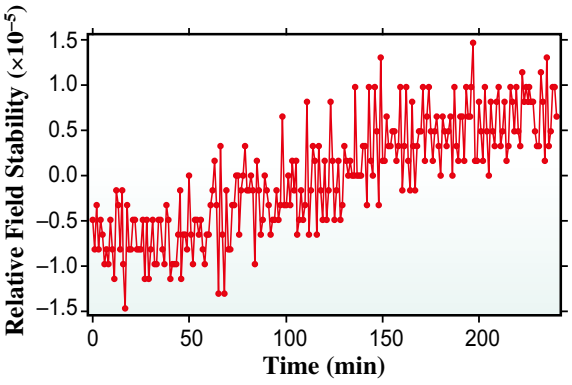

Fig. 2. Stability of the kicker magnetic fields.

The switchyard of SACLA is used not only for the multi-beamline operation of the XFEL but also for beam injection to the upgraded SPring-8 storage ring [4]. For the beam injection, the bunch length should also be controlled in addition to the beam energy from pulse to pulse, and the beam injection occurs at an arbitrary timing for top-up injection. To satisfy these requirements, the development of a new low level RF and timing system is under way. The beam injection test of the SPring-8 storage ring is scheduled for 2018.

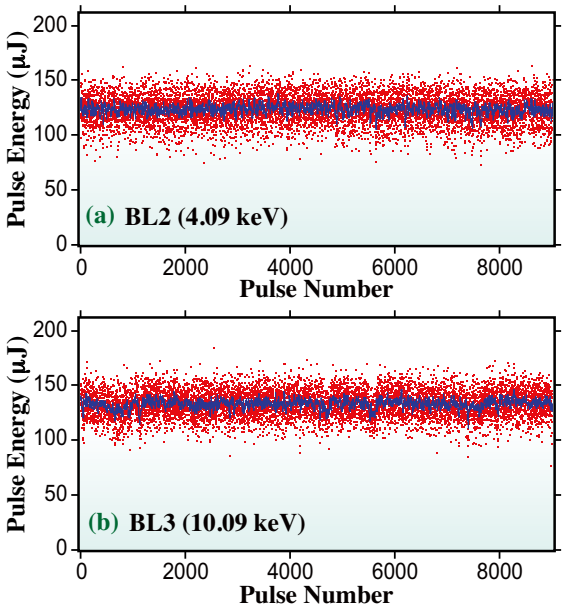

Fig. 3. XFEL pulse energies measured at **(a)** BL2 and **(b)** BL3 in multi-beamline operation. Red dots are single-shot data and blue lines are averaged values over 15 shots. The electron beam energies were 6.3 GeV and 7.8 GeV for BL2 and BL3, respectively.

Toru Hara

RIKEN SPring-8 Center

Email: toru@spring8.or.jp

References

[1] T. Ishikawa *et al.*: Nat. Photonics **6** (2012) 540.
[2] *T. Hara, K. Fukami, T. Inagaki, H. Kawaguchi, R. Kinjo, C. Kondo, Y. Otake, Y. Tajiri, H. Takebe, K. Togawa, T. Yoshino, H. Tanaka and T. Ishikawa: Phys. Rev. Accel. Beams* ***19*** *(2016) 020703.*
[3] T. Hara *et al.*: Phys. Rev. ST Accel. Beams **16** (2013) 080701.
[4] H. Tanaka: Synchrotron Rad. News **27** (2014) 23.

A beam branching method for timing and spectral characterization of hard X-ray free electron lasers

X-ray Free Electron Lasers (XFELs) generate ultra-brilliant, coherent, and femtosecond X-ray pulses. These unique properties allow one to directly probe the electronic and structural dynamics of matter with angstrom and femtosecond spatiotemporal resolution.

Photon diagnostics of XFEL pulses are critical for accurate data analysis, because most of the current XFEL sources show shot-to-shot variations in radiation properties owing to a self-amplified spontaneous emission (SASE) scheme. For example, stochastic fluctuations are observed in the pulse energy, temporal duration, spatial profile, wavefront, and spectrum.

Furthermore, diagnostics on arrival timings between XFEL and optical laser pulses are indispensable to improve the temporal resolution in ultrafast experiments, because the intrinsic temporal resolution, which is determined by the temporal duration of an X-ray or optical pulse, can be significantly deteriorated by a possible timing jitter between these pulses. At XFEL facilities, X-ray/optical cross-correlators have been developed for this purpose. In this scheme, one probes a transient change of optical reflectivity/transmittance accompanied with a rapid increase of free-carrier densities generated in semiconductor materials by intense X-ray irradiation. In the hard X-ray region at LCLS, this method has required XFELs with a large pulse energy on the order of millijoules due to the weak interaction between matter and hard X-rays [1].

At SACLA, Sato *et al.* have developed highly efficient arrival timing diagnostics using a spatial encoding technique [2]. The required pulse energy has been successfully reduced to 12 μJ at 12 keV by combining a one-dimensional focusing mirror and a GaAs target comprising high-Z materials that have high absorption coefficients of X-rays. Also, Inubushi *et al.* have developed a dispersive spectrometer with a high resolution of 14 meV [3]. However, these photon diagnostics cannot be used as shot-to-shot monitoring tools in user experiments owing to their photon-destructive nature.

To perform these photon-destructive diagnostics simultaneously with experiments, we proposed and developed a scheme using a transmission grating to split an X-ray beam into a main branch and several sub-branches [4]. This beam-splitting scheme enables advanced photon-destructive diagnostics to be performed under a quasi-noninvasive condition by using the main branch and sub-branches for experiments and diagnostics, respectively. Here, the +1st-order and –1st-order branches are utilized for measuring the spectrum and the arrival timing jitter, respectively.

The whole optical system is implemented at SACLA **BL3** (Fig. 1). As key optics devices in this scheme, we employ one-dimensional transmission gratings, which diffract a small fraction of the incoming X-ray beam into multiple branches. The +1st-order and –1st-order branches propagate in the vertical plane with the deflection angle given by $\theta_S = a\sin(\lambda/d)$, where λ is the wavelength and d is the period of the grating. The diffraction efficiency can be controlled in the range of 2.1 - 21.6% at 10 keV by tilting the grating along the vertical axis.

For the arrival timing monitor, the –1st-order X-ray beam is reflected by two (flat and elliptical) mirrors located ~8 m from the grating. After the reflection, the –1st-order X-ray beam is irradiated on a GaAs surface with a one-dimensional focused profile. The spatial modulation of the optical transmittance is recorded using a CCD detector with a spatial resolution of 1.1 μm/pixel, which corresponds to 2.6 fs/pixel from

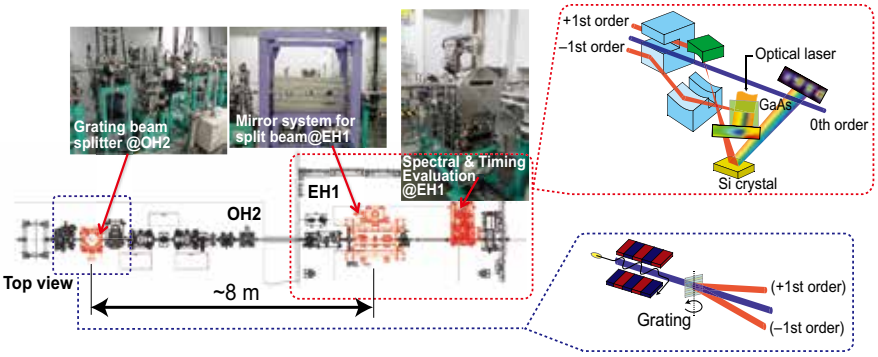

Fig. 1. Whole optical system installed at BL3 of SACLA: the grating beam splitter, the mirror system, and the spectral and timing evaluation chamber are the main components for quasi-noninvasive XFEL characterization in the spectral and timing domains.

the optical geometry. For the dispersive X-ray spectrometer, the elliptical mirror increases the divergence of the +1st-order branch to 2.5 mrad. A silicon analyzer crystal diffracts dispersed X-rays and an MPCCD detector records the spectrum. The spectral resolution and observable range can be tuned by switching the reflecting plane of the analyzer crystal.

To evaluate the performance of the system, we measured a correlation by performing an independent measurement using the main branch (0th-order branch). Figure 2(a) presents the correlation between the arrival timings of the –1st-order and 0th-order branches. We can observe excellent agreement between the two diagnostics. The temporal jitter is obtained from the graphic in Fig. 2(b), where the RMS width is 256 fs. The residual error after the linear fitting of the correlation can be defined as the overall accuracy, as shown in Fig. 2(c). The error graphic in Fig. 2(d) has an RMS width of 7.0 fs. This sub-10-fs accuracy should allow the temporal resolution to be improved down to the femtosecond regime, which is mainly governed by the temporal duration of the optical lasers. We also confirmed the applicability of this method to a wide photon energy range (5-15 keV) to cover the operation of SACLA with a pulse energy of less than 10 μJ.

Figure 3 shows the single-shot spectra of the +1st-order and 0th-order branches. Using a Si (660) reflecting plane, the spike features of SASE radiation were completely resolved (Fig. 3(a)). The spectral range of these two spectrometers was 6.4 eV, while we only show spectra in the overlapping area (~3 eV) between them in Fig. 3(a). We found reasonable agreement in both the energy dispersion (horizontal) and the spatial chirp (vertical) directions between the spectra. The average spike width was determined to be 470 meV. Note that we can easily switch the reflecting plane to a lower index, such as Si (220), in order to cover a wide photon energy range, as shown in Fig. 3(b).

In conclusion, we have developed a beam branching method to enable advanced photon diagnostics with small perturbation using a grating splitter. The 0th-order transmission branch, which retains over 90% of the original intensity at 10 keV, is provided for a diverse range of applications.

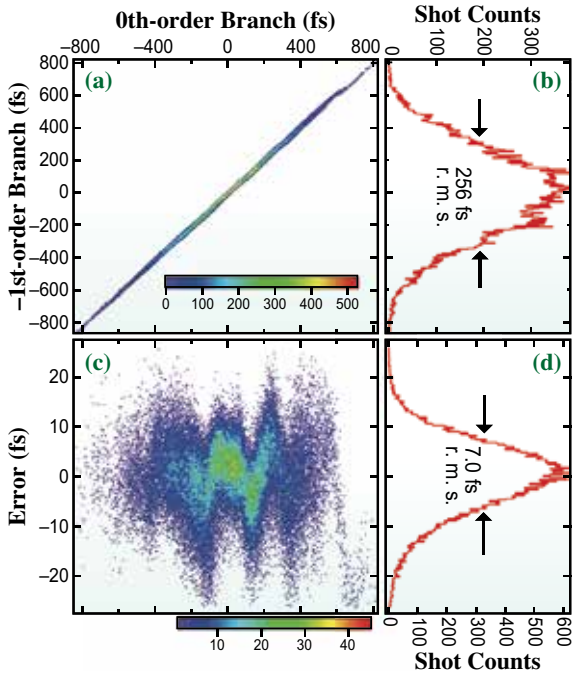

Fig. 2. **(a)** Scatter plot colored by density showing the correlation between the arrival timings of the two branches. **(b)** Graphic showing the temporal jitter. The bin width was 5 fs. **(c)** Residual errors after the linear fitting of the scatter plot. **(d)** Graphic corresponding to (c) with a bin width of 0.2 fs.

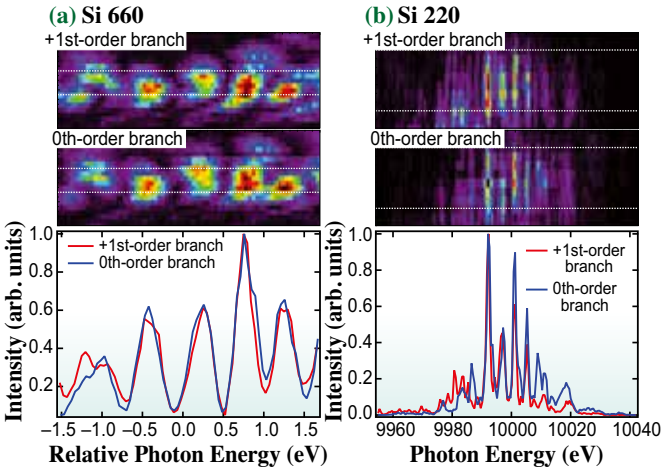

Fig. 3. **(a)** Single-shot spectra measured with Si (660) analyzer crystals using the +1st-order (red line) and 0th-order (blue line) branches. The center of the relative photon energy corresponds to 9999.75 eV. **(b)** Wide-range single-shot spectra measured with Si (220) analyzer crystal. The white dotted lines represent the area of the integration used to extract the spectra.

Tetsuo Katayama[a,b,*] and Makina Yabashi[b]

[a] Japan Synchrotron Radiation Research Institute (JASRI)
[b] RIKEN SPring-8 Center

*Email: tetsuo@spring8.or.jp

References

[1] M. Harmand *et al.*: Nat. Photonics **7** (2013) 215.
[2] T. Sato *et al.*: Appl. Phys. Exp. **8** (2015) 012702.
[3] Y. Inubushi *et al.*: Phys. Rev. Lett. **109** (2012) 144801.
[4] *T. Katayama, S. Owada, T. Togashi, K. Ogawa, P. Karvinen, I. Vartiainen, A. Eronen, C. David, T. Sato, K. Nakajima, Y. Joti, H. Yumoto, H. Ohashi and M. Yabashi: Struct. Dyn.* ***3*** *(2016) 034301.*

FACILITY STATUS

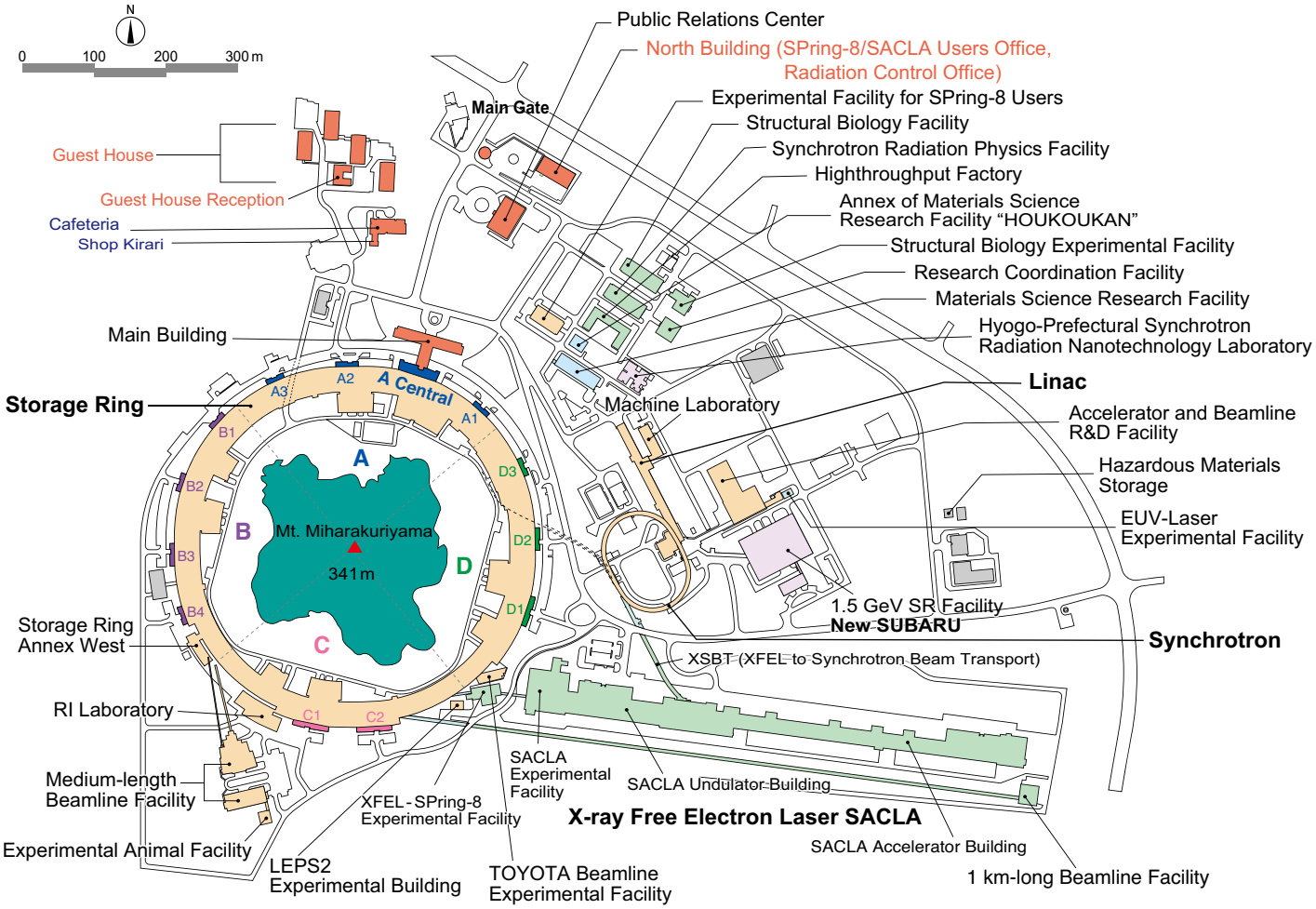

SPring-8

I. Introduction

SPring-8 was stably operated throughout FY2016 with the total operation time of the accelerator complex and the total user beam time of 4951.7 h and 4125.5 h, respectively, and a total downtime of 23.1 h. Because of the major renovation of an extra-high-tension power source from the end of December 2016 to the end of March 2017, SPring-8 had to complete all its operations by the middle of December 2016, making the machine schedule quite tight and, thus, challenging.

Regarding its research proposal system, the duration of the designation period of a priority field for the public beamlines "New Industrial Area Program" has been extended. Concerning the contract beamlines, there were five interim reviews conducted for WEBRAM (BL15XU, National Institute for Materials Science), Laser-Electron Photon II (BL31LEP, Research Center for Nuclear Physics, Osaka University). NSRRC BM (BL12B2), NSRRC ID (BL12XU), and RISING II (BL28XU, Kyoto University), and the continuation of their projects was authorized. Upon the expiration of their contract terms, reviews were also conducted for JAEA Actinide Science I (BL22XU), JAEA Actinide Science II (BL23SU), QST Quantum Dynamics I (BL11XU), QST Quantum Dynamics II (BL14B1), and Catalytic Reaction Dynamics for Fuel Cells (BL36XU, The University of Electro-Communications), and their proposals for the next term were approved.

At the time of writing this report, SPring-8 users numbered as many as 11,000, all of whom are respected members of the SPring-8 User Community (SPRUC). It is important for SPring-8 to jointly organize scientific events with SPRUC, such as the SPring-8 Symposium, to facilitate dialogue between users and the facility staff. In 2016, the SPring-8 Symposium was held at Kwansei Gakuin University. SPring-8 also accelerates communication between users and industry. The Joint Conference on Industrial Applications of SPring-8, held in Kobe on September 7-8, 2016, had 248 participants. As part of its continuous effort towards fostering human resources in synchrotron sciences, SPring-8 organized the 16th SPring-8 Summer School with 91 students of graduate schools nationwide, in cooperation with Hyogo University, Kwansei Gakuin University, the University of Tokyo, Okayama University, Osaka University, Japan Atomic Energy Agency, National Institutes for Quantum and Radiological Science and Technology, and RIKEN.

II. Machine Operation

The operation statistics for the last five fiscal years are shown in Fig. 1. In FY2016, the total operation time of the accelerator complex was 4951.7 h. The operation time of the storage ring was 4941.1 h, 84.0% of which (4125.5 h) was for SR experiments. This excellent figure of user time represents a storage ring availability of 99.4%, which ranks with the best record of 99.5% established over the previous two years. The downtime resulting from failure accounted for 0.56% (23.1 h) of the total user time. This is somewhat longer compared with that (16.8 h) in FY2015. This is because in FY2016, severe damage was incurred as a result of natural disasters such as an earthquake and power loss due to thunderstorms. The intensity of the light source, i.e., the stored current is kept extremely stable thanks to the top-up operation, in which the current is filled up at any time on demand. The dead band of the stored current in the top-up operation is routinely 0.03 mA (0.03%) and the current stays within 0.1% in 99.6% of the user time in FY2016, as well as in FY2015.

The variety of operation modes is one of the characteristics of SPring-8. The operation modes are grouped into the multibunch, several-bunch, and hybrid-filling modes. There has been no user operation in the multibunch mode since FY2011. The several-bunch mode consists of equally spaced bunches or bunch trains, i.e., 203 bunches, or 29 trains of 11 bunches, and the hybrid-filling mode is composed of a long bunch train and isolated single bunches, as shown in Table 1, where the share of each operation mode is also shown. An isolated bunch impurity is routinely maintained at less than 10^{-8} in the top-up operation by bunch cleaning in the booster. The bunch current is also kept constant within a 1% band by the top-up operation. In the

operation of the 203 bunches mode in the 2nd, 3rd, and 5th cycles of user time, beam instability occurred, so the equivalent filling mode of 406 bunches was applied. By the machine tuning, the instability was suppressed, and the 203 bunches mode in the 7th cycle was operated as before.

Table 2 summarizes the beam parameters of the storage ring.

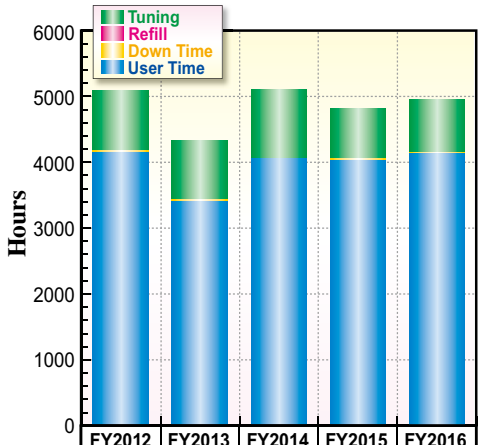

	FY2012	FY2013	FY2014	FY2015	FY2016
Accelerator Operation Time	5078.8	4330.0	5099.3	4817.9	4951.7
Storage Ring Operation Time	5063.1	4265.5	5080.7	4804.8	4941.1
Tuning & Study (Acc. & BL)	883.8	898.0	1019.3	767.2	803.1
Refill	5.2	3.5	5.1	5.3	3.4
Down Time	39.2	20.0	17.1	16.8	23.1
Mean Time Between Failures	107.7	213.0	163.2	202.8	229.2
Achieved User Time	4155.6	3408.5	4057.8	4033.9	4125.5
Planning User Time	4200.0	3432.0	4080.0	4056.0	4152.0
Availability (%)	98.9	99.3	99.5	99.5	99.4

Fig. 1. Operation statistics for most recent five fiscal years.

Table 1. Operation modes in FY2016

	Single bunch current (mA)	Share of operation time (%)
203 bunches		24.9
4 bunch-train × 84		8.1
11 bunch-train × 29		25.4
1/7-filling + 5 single bunches	3	9.2
2/29-filling + 26 single bunches	1.4	3.5
1/14-filling + 12 single bunches	1.6	8.7
4/58-filling + 53 single bunches	1	0.0
11/29-filling + 1 single bunch	5	20.2

Table 2. Beam parameters of the SPring-8 storage ring

Energy [GeV]	8
Number of buckets	2436
Tunes (ν_x / ν_y)	41.14 / 19.34
Current [mA]:	100
Bunch length (σ) [psec]	13
Horizontal emittance [nm·rad]	2.4 *
Vertical emittance [pm·rad]	4.8 *
Coupling [%]	0.2
RF Voltage [MV]	14.4 ** ~ 16
Momentum acceptance [%]	3.2 (~256 MeV)
Beam size (σ_x / σ_y)* [μm]	
Long ID section	333 / 7
ID section	316 / 5
BM1 section	94 / 12
BM2 section	100 / 12
Beam divergence (σ_x' / σ_y')* [μrad]	
Long ID section	8 / 0.7
ID section	9 / 1.0
BM1 section	58 / 0.5
BM2 section	68 / 0.5
Lifetime [h]:	
100 mA (multi-bunch)	~250
1 mA (single-bunch)	~30
Horizontal dispersion [m]:	
Long ID section	0.153
ID section	0.146
BM1 section	0.039
BM2 section	0.059
Fast orbit stability (0.1 – 200 Hz) [μm]:	
horizontal (rms)	~4
vertical (rms)	~1

* Assuming 0.2% coupling
** Power saving mode

III. Beamlines

The SPring-8 storage ring can accommodate up to 62 beamlines: 34 insertion devices, 4 long undulators, and 24 bending magnets. At present, 56 beamlines are in operation, covering a wide variety of research fields involving synchrotron radiation science and technology. The beamlines are classified into the following three types.

(1) Public Beamlines
(2) Contract Beamlines
(3) RIKEN Beamlines

There are now 26 public beamlines in full operation. The beamlines that are proposed and constructed by external organizations, such as

universities, research institutes, private companies and consortiums, are called contract beamlines and are exclusively used by the contractors for their own research purposes. At present, 19 contract beamlines are in operation. The contract beamlines include the NSRRC BM (BL12B2) and NSRRC ID (BL12XU) beamlines, which were constructed by the National Synchrotron Radiation Research Center of Taiwan. The beamlines constructed by RIKEN except for public beamlines are called RIKEN beamlines, and are mainly used for RIKEN's own research activities, with partial availability for public use. RIKEN is now operating 11 beamlines and is reconstructing one beamline.

To illustrate the beamline portfolio of SPring-8, a beamline map is shown in Fig. 2 together with the beamline classification. The research fields of beamlines are presented in Table 3.

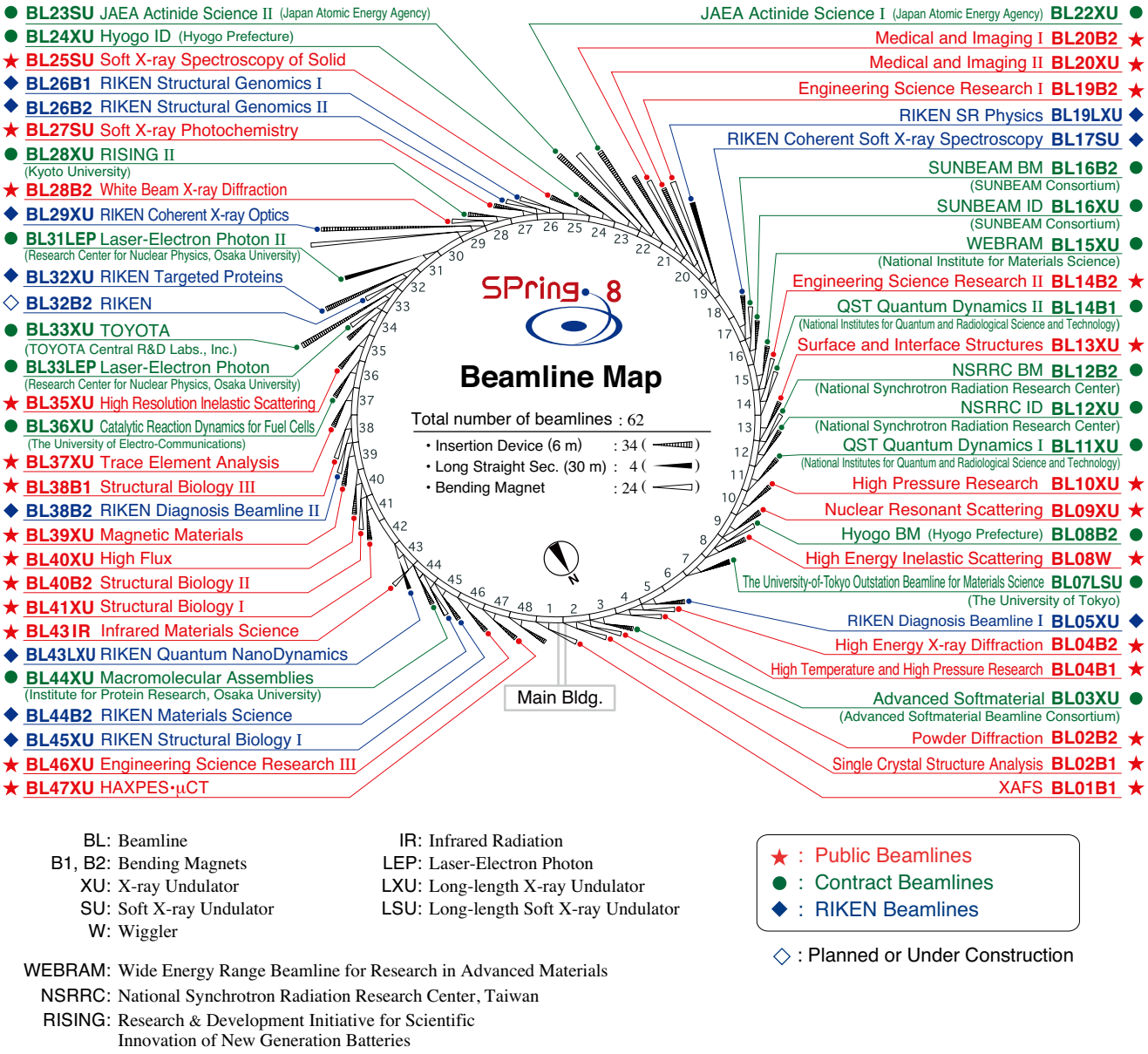

Fig. 2. Beamline map.

Table 3. List of beamlines

BL #	Beamline Name	(Public Use) or (First Beam)	Areas of Research and Available Techniques
★ Public Beamlines			
BL01B1	XAFS	(Oct. 1997)	XAFS in wide energy region (3.8 to 113 keV). XAFS of dilute systems and thin films. Quick XAFS with a time resolution of seconds to tens of seconds.
BL02B1	Single Crystal Structure Analysis	(Oct. 1997)	Charge density study and crystal structure analysis from accurate single crystal diffraction measurements. (X-ray energy range: 8 – 115 keV)
BL02B2	Powder Diffraction	(Sept. 1999)	Charge density study and phase identification of crystalline materials from accurate powder diffraction measurements. (X-ray energy range: 12.4 – 35 keV)
BL04B1	High Temperature and High Pressure Research	(Oct. 1997)	High temperature and high pressure research with the multi-anvil press by powder X-ray diffraction, radiography and ultrasonic measurement.
BL04B2	High Energy X-ray Diffraction	(Sept. 1999)	Pair distribution function analysis for glass, liquid, and amorphous materials. High-energy X-ray total scattering. Containerless levitation.
BL08W	High Energy Inelastic Scattering	(Oct. 1997)	Magnetic Compton scattering. High-resolution Compton scattering. High-energy Bragg scattering. High-energy fluorescent X-ray analysis.
BL09XU	Nuclear Resonant Scattering	(Oct. 1997)	Lattice dynamics using nuclear inelastic scattering. Mössbauer spectroscopy, especially for the surface/interface study and under the extreme conditions. Hard X-ray photoelectron spectroscopy (HAXPES). Depth analysis of HAXPES with high flux and energy resolution.
BL10XU	High Pressure Research	(Oct. 1997)	Structure analysis and phase transitions under ultra high pressure (DAC experiment). Earth and planetary science.
BL13XU	Surface and Interface Structures	(Sept. 2001)	Atomic-scale structural analysis of surfaces and interfaces of crystalline materials, ultra-thin films, and nanostructures. Surface X-ray diffraction (SXRD). Microbeam diffraction.
BL14B2	Engineering Science Research II	(Sept. 2007)	XAFS in wide energy region (3.8 to 72 keV). XAFS of dilute systems and thin films.
BL19B2	Engineering Science Research I	(Nov. 2001)	Residual stress measurement. Structural analysis of thin film, surface, interface. Powder diffraction. X-ray imaging, X-ray topography. Ultra-small angle X-ray scattering.
BL20XU	Medical and Imaging II	(Sept. 2001)	Microimaging. Hard X-ray microbeam/scanning microscopy, imaging microscopy, microtomography, phase-contrast microtomography X-ray diffraction tomography (XRD-CT), X-ray holography, coherent X-ray optics, and other experiments on X-ray optics and developments of optical elements. Refraction-enhanced imaging, phase-contrast CT. Ultra-small angle scattering.
BL20B2	Medical and Imaging I	(Sept. 1999)	Microimaging: microtomography, phase-contrast microtomography with grating interferometer for biological specimen and other kinds of specimen. Evaluation and development of various kinds of optical elements for novel imaging techniques. Large field X-ray topography.
BL25SU	Soft X-ray Spectroscopy of Solid	(Apr. 1998)	Study of electronic state of solids by soft X-ray photoemission spectroscopy (PES) including angle-resolved PES (ARPES). Atomic arrangement analysis of surfaces by photoelectron diffraction (PED) technique using two-dimensional photoemission analyzer. Magnetic state analysis by magnetic circular dichroism (MCD) of soft X-ray absorption and its element-specific magnetization curve measurements. Chemical and magnetic imaging by soft X-ray scanning microscopy and photoelectron emission microscopy (PEEM).
BL27SU	Soft X-ray Photochemistry	(May 1998)	Ambient atmospheric pressure soft X-ray photoabsorption spectroscopy. Chemical state analysis of light elements in dilute samples (NEXAFS). Elemental and chemical mapping using micro soft X-ray beam. Soft X-ray emission spectroscopy for solids.
BL28B2	White Beam X-ray Diffraction	(Sept. 1999)	White X-ray diffraction and topography. Time-resolved energy-dispersive XAFS (DXAFS) for studies of chemical and/or physical reaction process. Biomedical imaging and radiation biology studies. High energy X-ray microtomography.
BL35XU	High Resolution Inelastic Scattering	(Sept. 2001)	Materials dynamics on ~meV energy scales using inelastic X-ray scattering (IXS).
BL37XU	Trace Element Analysis	(Nov. 2002)	X-ray microbeam spectrochemical analysis. Ultra trace element analysis. High energy X-ray fluorescence analysis.
BL38B1	Structural Biology III	(Oct. 2000)	Structural biology. Macromolecular crystallography. Automatic data collection.
BL39XU	Magnetic Materials	(Oct. 1997)	X-ray magnetic circular dichroism (XMCD) spectroscopy and element-specific magnetometry under multiple-extreme conditions. XMCD/XAS using a 100 nm focussed X-ray beam. X-ray emission spectroscopy. Resonant X-ray magnetic scattering.
BL40XU	High Flux	(Apr. 2000)	Time-resolved diffraction and scattering experiments. Microbeam X-ray diffraction and scattering experiments. X-ray photon correlation spectroscopy. Fluorescence analysis. Quick XAFS. Submicrometer-scale single crystal structure analysis with high flux and zone plate focused X-ray beam. Single shot imaging with X-ray choppers. Laser pump-X-ray probe experiment.
BL40B2	Structural Biology II	(Sept. 1999)	Noncrystalline small and wide angle X-ray scattering.
BL41XU	Structural Biology I	(Oct. 1997)	Structural biology. Macromolecular crystallography. Microcrystallography. High resolution data collection.
BL43IR	Infrared Materials Science	(Apr. 2000)	Infrared microspectroscopy.
BL46XU	Engineering Science Research III	(Nov. 2000)	Structural characterization of thin films by X-ray diffraction and X-ray reflectivity measurement. Residual stress measurement. Time resolved X-ray diffraction measurement. Hard X-ray photoemission spectroscopy.
BL47XU	HAXPES·μCT	(Oct. 1997)	Hard X-ray photoelectron spectroscopy (HAXPES). Depth analysis of angle resolved HAXPES with wide acceptance lens. Projection type microtomography. Imaging type microtomography. Hard X-ray microbeam/scanning microscopy.

BL #	Beamline Name	(Public Use) or (First Beam)	Areas of Research and Available Techniques
	● Contract Beamlines		
BL03XU	**Advanced Softmaterial** (Advanced Softmaterial Beamline Consortium)	(Nov. 2009)	Structural characterization of softmaterials using small- and wide-angle X-ray scattering. Grazing-incidence small- and wide-angle X-ray scattering for thin films. X-ray diffraction and reflectivity measurements for softmaterials.
BL07LSU	**The University-of-Tokyo Outstation Beamline for Materials Science** (The University of Tokyo)	(Oct. 2009)	Time-resolved soft X-ray spectroscopy, nano-beam photoemission spectroscopy, ultra high-resolution soft X-ray emission spectroscopy, and any methods requiring the highly brilliant soft X-ray beam.
BL08B2	**Hyogo BM** (Hyogo Prefecture)	(Jun. 2005)	XAFS in a wide energy region. Small angle X-ray scattering for structural analyses of polymer and nanocomposite materials. X-ray topography. Imaging. Powder diffraction with a high angular-resolution.
BL11XU	**QST Quantum Dynamics I** (National Institutes for Quantum & Radiological Science & Technology)	(Oct. 1998)	Nuclear scattering. Surface and interface structure analysis with MBE. Inelastic X-ray scattering. XAFS.
BL12B2	**NSRRC BM** (National Synchrotron Rad. Res. Center)	(Oct. 2000)	X-ray absorption spectroscopy. Powder X-ray diffraction. High resolution X-ray scattering. Protein crystallography.
BL12XU	**NSRRC ID** (National Synchrotron Rad. Res. Center)	(Dec. 2001)	Non-resonant or resonant inelastic X-ray scattering. Hard X-ray photoemission spectroscopy.
BL14B1	**QST Quantum Dynamics II** (National Institutes for Quantum & Radiological Science & Technology)	(Dec. 1997)	Materials science under high-temperature and high-pressure. *In situ* study on catalysis using dispersive XAFS. X-ray diffraction for structure physics.
BL15XU	**WEBRAM** (National Institute for Materials Science)	(Jan. 2000)	Hard X-ray photoelectron spectroscopy. High-precision X-ray powder diffraction.
BL16B2	**SUNBEAM BM** (SUNBEAM Consortium)	(Oct. 1998)	Characterization of secondary battery related materials, semiconductors, fuel cells, catalysts, and several industrial materials using X-ray absorption fine structure measurements, X-ray diffraction (including X-ray reflectivity technique) and X-ray topography.
BL16XU	**SUNBEAM ID** (SUNBEAM Consortium)	(Oct. 1998)	Characterization of secondary battery related materials, semiconductors, fuel cells, catalysts, and structural materials using X-ray diffraction, X-ray microbeam based evaluation techniques (including X-ray magnetic circular dichroism), hard X-ray photoemission spectroscopy and fluorescence X-ray analysis.
BL22XU	**JAEA Actinide Science I** (Japan Atomic Energy Agency)	(May 2002)	Materials science under high-pressure. Resonant X-ray scattering. Speckle scattering. Residual stress/strain distribution analysis.
BL23SU	**JAEA Actinide Science II** (Japan Atomic Energy Agency)	(Feb. 1998)	Surface chemistry with supersonic molecular beam. Biophysical spectroscopy. Photoelectron spectroscopy. Magnetic circular dichroism.
BL24XU	**Hyogo ID** (Hyogo Prefecture)	(May. 1998)	Surface/interface analysis for industry by fluorescent X-ray analysis, strain measurements and grazing incidence X-ray diffraction. Microbeam formation studies for material and life sciences. Scanning and imaging microscope. Micro-tomography. Micro-XAFS. Microbeam small- and wide-angle X-ray scattering for local structure analysis. Bright field X-ray topography.
BL28XU	**RISING II** (Kyoto University)	(Apr. 2012)	Characterization of rechargeable battery reactions and battery related materials by resonance X-ray diffraction, X-ray absorption spectroscopy (XAS), X-ray diffraction spectroscopy (XDS), and hard X-ray photoemission spectroscopy (HAXPES).
BL31LEP	**Laser-Electron Photon II** (RCNP, Osaka University)	(Oct. 2013)	Production of high intensity GeV photon beam by laser-backward Compton scattering. Hadron physics via photonucleon and photonuclear reactions. Test and calibration of detectors with GeV gamma-ray and converted electrons/positrons.
BL33LEP	**Laser-Electron Photon** (RCNP, Osaka University)	(Jun. 1999)	Meson photoproduction from nucleon and nucleus. Photoexcitation of hyperons, nucleon resonances, and other exotic states. Photonuclear reactions. Beam diagnoses. Test and calibration of detectors with GeV photon beam.
BL33XU	**TOYOTA** (TOYOTA Central R&D Labs., Inc.)	(Apr. 2009)	Time-resolved XAFS. Characterization of industrial materials, such as catalysts, secondary batteries, fuel cells.
BL36XU	**Catalytic Reaction Dynamics for Fuel Cells** (The University of Electro-Communications)	(Jan.2013)	Real time analysis of catalytic reaction dynamics for fuel cells: time resolved XAFS and X-ray diffraction, 2D scanning microscopic XAFS, 3D computed tomography/laminography XAFS, ambient pressure hard X-ray photoelectron spectroscopy.
BL44XU	**Macromolecular Assemblies** (IPR, Osaka University)	(May 1999)	Crystal structure analysis of biological macromolecular assemblies (e.g., membrane protein complexes, protein complexes, protein-nucleic acid complexes, and viruses).
	◆ RIKEN Beamlines		
BL05XU	**RIKEN Diagnosis Beamline I**	(Mar. 2004)	Accelerator beam diagnostics. R&D of accelerator components. Nano-forensic science.
BL17SU	**RIKEN Coherent Soft X-ray Spectroscopy**	(Sept. 2003)	High resolution photoemission spectroscopy. Soft X-ray emission spectroscopy. Soft X-ray diffraction spectroscopy. Soft X-ray microspectroscopy.
BL19LXU	**RIKEN SR Physics**	(Oct. 2000)	SR science with highly brilliant X-ray beam.
BL26B1	**RIKEN Structural Genomics I**	(Apr. 2002)	Structural biology research based on single crystal X-ray diffraction.
BL26B2	**RIKEN Structural Genomics II**	(Apr. 2002)	Structural biology research based on single crystal X-ray diffraction.
BL29XU	**RIKEN Coherent X-ray Optics**	(Dec. 1998)	X-ray optics, especially coherent X-ray optics.
BL32XU	**RIKEN Targeted Proteins**	(Oct. 2009)	Protein microcrystallography.
BL38B2	**RIKEN Diagnosis Beamline II**	(Sept. 1999)	Accelerator beam diagnostics.
BL43LXU	**RIKEN Quantum NanoDynamics**	(Oct. 2011)	High resolution inelastic X-ray scattering for investigating atomic and electronic dynamics.
BL44B2	**RIKEN Materials Science**	(Feb. 1998)	Structural materials science research using powder X-ray diffraction.
BL45XU	**RIKEN Structural Biology I**	(Jul. 1997)	Time-resolved and static structures of non-crystalline biological materials using small-angle scattering and diffraction techniques.

IV. User Program and Statistics

SPring-8 calls for public use proposals twice a year, in principle. The submitted proposals are reviewed by the SPring-8 Proposal Review Committee (SPring-8 PRC). Since 1997, SPring-8 has accepted a variety of proposals. For the promotion of research on industrial applications at SPring-8, the Industrial Application Division was established in 2005. With consultation support for industrial users provided by the division's coordinators, currently, Industrial Application Proposals account for approximately 16%–20% of the total number of proposals conducted at the public beamlines. In addition, the Measurement Service was introduced in 2007B, wherein the personnel of the Industrial Application Division carries out XAFS measurements on behalf of users at BL14B2. SPring-8 also launched a Protein Crystallography Data Collection Service at BL38B1 and a Powder X-ray Diffraction Measurement Service at BL19B2 in 2009B, a Hard X-ray Photoemission Spectroscopy (HAXPES) Measurement Service and a Thin Film Analysis (GIXD/XRR) Measurement Service at BL46XU in 2012B, and a Small Angle Scattering (SAXS) Measurement Service at BL19B2 in 2014B.

In FY2016, JASRI extended the duration of the designation period of the priority field "New Industrial Area Program" for public beamlines, facilitating research and development in new industrial areas toward proposals newly using SPring-8, from the end of 2015B to the end of 2017B.

SPring-8 has consistently provided ~4,000 h of user beamtime per year. Since the start of its operation in 1997, SPring-8 has succeeded in providing a total beamtime of 74,925 h to users. The beamtime available to users, the number of experiments conducted, and the number of user visits at the public and contract beamlines are summarized in Fig. 3. Part of the proposals are for proprietary use, for which refereed reports are not required.

More details can be found at *http://www.spring8.or.jp/en/about_us/spring8data/*.

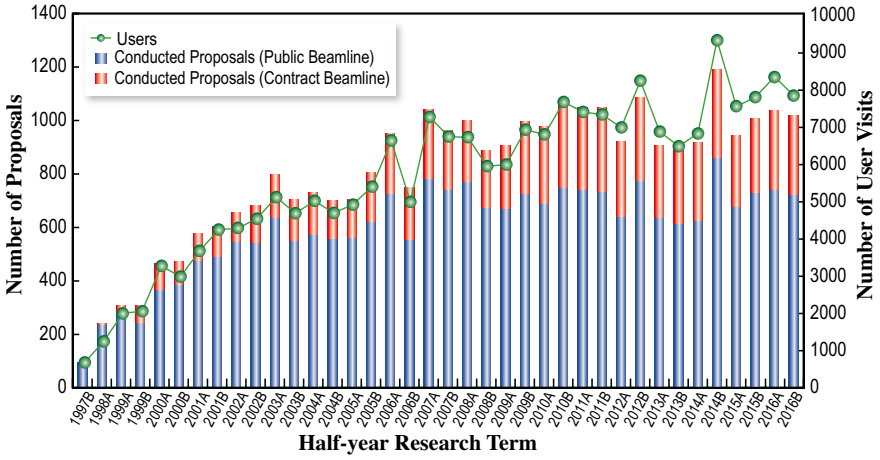

Fig. 3. Numbers of user visits and conducted experiments.

V. Research Outcome

As of March 2017, the total number of registered refereed papers from SPring-8 was 12,743. More details can be found at *https://user.spring8.or.jp/uisearch/publication2/* .

VI. Budget and Personnel

When SPring-8 started operation in 1997, it was jointly managed by RIKEN, JAERI (now JAEA), and JASRI. However, JAERI withdrew from the management of SPring-8 on September 30, 2005. SPring-8 is currently administered by RIKEN and JASRI collaboratively.

The total budget for the operation of SPring-8 in FY2016 was 9.6 billion yen. As of October 2016, RIKEN and JASRI had a total of 488 staff members.

VII. Research Complex

The facilities of SPring-8, SACLA, and NewSUBARU form the Center of Excellence (COE) at the SPring-8 campus where JASRI, public beamline users, the contractors of contract beamlines, RIKEN, and the University of Hyogo work in close cooperation, forming a research complex where each member has their own role in delivering high-quality results to the field of synchrotron radiation science and technology. The organizational charts of RIKEN and JASRI, which are at the center of this research complex, are shown in Fig. 4 and Fig. 5, respectively.

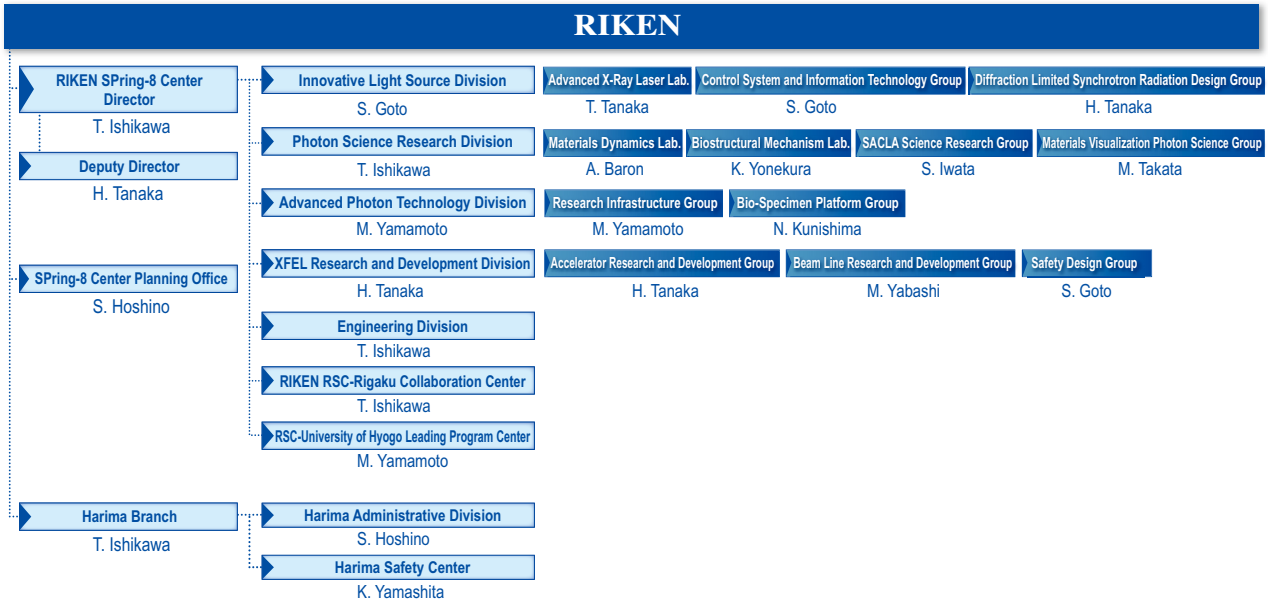

Fig. 4. RIKEN Harima Campus chart as of April 2017.

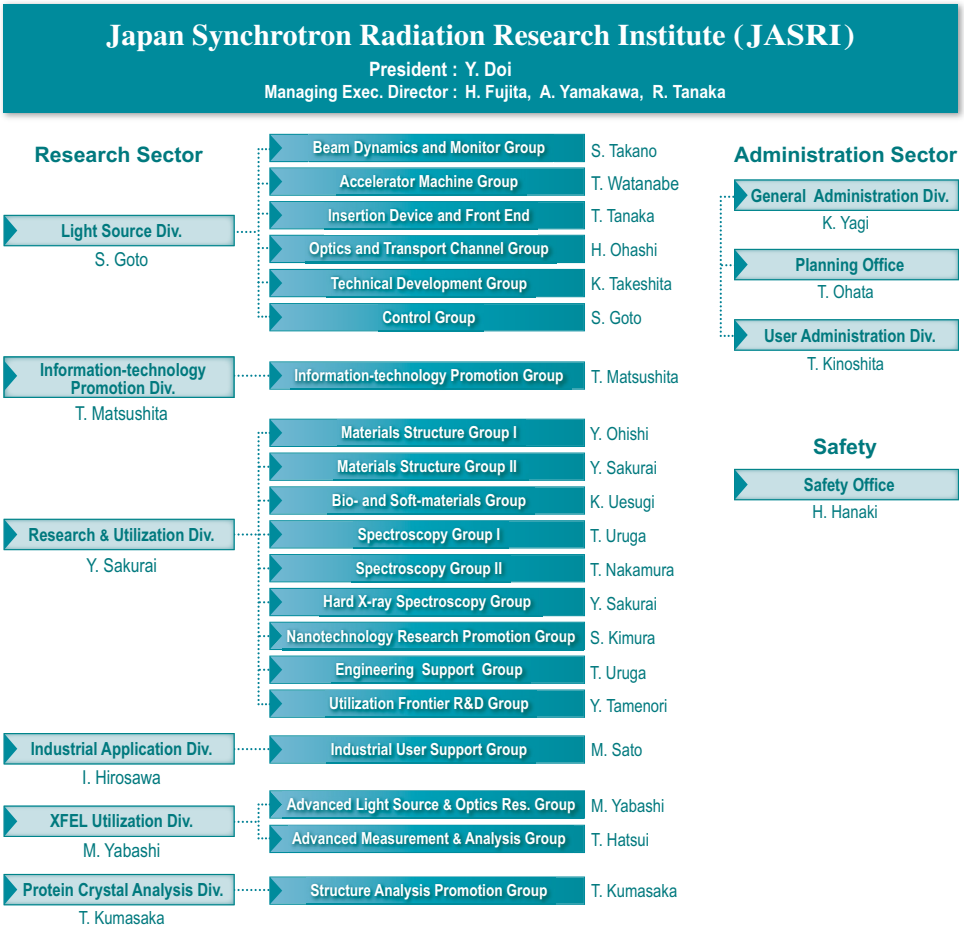

Fig. 5. JASRI chart as of April 2017.

VIII. Users Societies and Other Activities

SPring-8 Users Community (SPRUC)

The SPring-8 Users Community (SPRUC) is a user society that includes not only all users but also potential users who are interested in using SPring-8. In addition to these individuals, representative organizations comprising about 25 institutes (principal universities, national/international research institutes, industries, beamline consortiums) participate in SPRUC to discuss further promotion of the utilization of SPring-8 from strategic and perspective viewpoints.

As one of the key activities of SPRUC, the SPring-8 Symposium is held annually at the site of one of the representing organizations jointly with RIKEN and JASRI. SPring-8 Symposium 2016, with the theme "Environmental and Energy Issues Addressed by Synchrotron Radiation Research," was held at Kwansei Gakuin University on August 29 and 30, 2016, with 331 participants. SPRUC provides the Young Scientist Award to recognize notable achievements in the development of a new experimental technique or a new method for data analysis, or remarkable results in the studied field obtained by making use of the characteristic features of SPring-8. The award ceremony and award lecture were held at the SPring-8 Symposium. The SPRUC 2016 Young Scientist Award was conferred to two young scientists (Dr. Hideaki Kato, Stanford University, USA, and Dr. Yujiro Hayashi, TOYOTA Central R&D LABS., INC). SPring-8 Symposium 2017 is scheduled to be held on September 4 and 5 at Hiroshima University.

SPRUC has continued to promote the activities of "SPRUC multidisciplinary research groups" in order to develop the use of SPring-8 in the new areas that will be important to future science and technology. Four multidisciplinary research fields were designated in accordance with comprehensive advice from the advisors of the SPRUC research groups in 2014. Two multidisciplinary research groups for nanodevice science and application were launched in 2015, and they made innovative use of SPring-8 through organic collaboration with JASRI and RIKEN this year. The other two groups are now gearing up to start at a different timing from the preceding research groups. In addition, 3rd Term Research Groups actively organized each workshop in FY2016.

In order to discuss medium- and long-term plans for the future performance of detectors and measurement systems, a SPRUC working group on high-performance beamline technologies was launched on December 1, and their 1st meeting was held on December 23, 2016.

Young Scientist Award
Prof. J. Mizuki, Dr. H. Kato, Dr. Y. Hayashi, and Prof. A. Nakagawa

SPring-8 Symposium 2016

Other Activities

To unearth new users in unexplored fields of application, SPring-8 holds various serialized seminars named “Workshop on Advanced Techniques and Applications at SPring-8”. Here are some representatives.

- The new techniques of cultural heritage analysis
  June 4, 2016 • Nara University (Nara)
- Innovation from SPring-8 for the future
  June 7, 2016 • Campus Plaza Kyoto (Kyoto)
- Complementary utilization of Aichi-SR and SPring-8 in the industrial field
  (Co-hosted by Aichi Synchrotron Radiation Center)
  October 25, 2016 • WINK AICHI (Nagoya)
- Present status of advanced measurement techniques at SPring-8 public beamlines
  February 2–3, 2017 • Akihabara UDX (Tokyo)
- Meeting on the next generation advanced device (Co-hosted by Industrial Users Society of SPring-8)
  March 21, 2017 • AP Shinagawa (Tokyo)
- Seminars on complementary utilization of X-ray and neutron: Observation of the internal structure with quantum beams (Co-hosted by Comprehensive Research Organization for Science and Society: CROSS)
  February 17, 2017 • Kenkyusha English Center Building (Tokyo)

SPring-8 Summer School

SACLA

I. Introduction

SACLA is the world's second X-ray Free Electron Laser (XFEL), following the Linac Coherent Light Source (LCLS) in the US. Currently, these are the only two XFELs in operation. SACLA delivers the shortest wavelength XFEL. SACLA achieved its first lasing on June 7, 2011, within three months of electron beam commissioning, and launched user operations in 2012A. Since then, we have operated SACLA in five years with reasonable stability and reliability.

II. Machine Operation & Beamlines

Our fifth year of operations proceeded without any significant issues. Operation statistics are summarized in Table 1. The ratio of downtime to user time was kept below 4%, a reasonably low rate for linac-based light sources.

Table 1. Operation Statistics for FY2016

	Time (h)
Total operation time	5861
User time	4026
Facility tuning time	710
Study time	1749
Downtime	130

In 2012, two beamlines, BL3 for XFEL and BL1 for broadband spontaneous light, were open for users, while all experiments were conducted with BL3. As the newest beamline, construction of BL2 was completed during the summer shutdown of 2014, and first laser amplification was achieved on October 21. An upgraded beamline for soft X-ray FEL, BL1, which combines the prototype accelerator of SACLA (SCSS), started operation in 2016. For more details, please refer to SACLA Beam Performance in this volume.

III. User Program and Statistics

SACLA calls for public user proposals twice per year. Proposals fall into two categories: General Proposals for general research with no specific research theme, while Priority Strategy Proposals are on strategic themes that are designated by the national policy. Currently there are two strategic themes: Hierarchical Structure Dynamics of Biomolecules and Pico/Femto Second Dynamic Imaging. Table 2 shows the research themes for each group.

In FY2016, JASRI introduced the proprietary research of General Proposals and the Proprietary Time-Designated Proposals. The project leaders of these proprietary proposals are not required to publish their research results, but required to pay each beamtime fee. In addition, to apply for the proprietary research the project leaders should be affiliated with a corporate enterprise located and registered in Japan.

Table 2. Research themes for each group

1. Hierarchical Structure Dynamics of Biomolecules	1-1 Structural Analysis of Drug-targeted Membrane Protein Nanocrystals
	1-2 Imaging of Whole Cell and Its Components in the Living State
	1-3 Single Molecule Structural Analysis of Supramolecular Complex
	1-4 Dynamics Research Combining Single Molecule X-ray Diffraction Experiments and Supercomputer Analysis
	1-5 Dynamic Structural Analysis Using Pump-Probe Techniques
2. Pico/Femto Second Dynamic Imaging	2-1 Gas-Phase/Liquid-Phase/Solid-Phase Reaction Dynamics
	2-2 Ultrafast Interface Reaction Processes
	2-3 Charge Generation/Charge Transfer Dynamics
	2-4 Ultrafast Processes under Extreme Conditions
	2-5 Dynamic X-ray Spectroscopy

Table 3, Figs. 1 and 2 provide statistics on proposals, users, and beamtime.

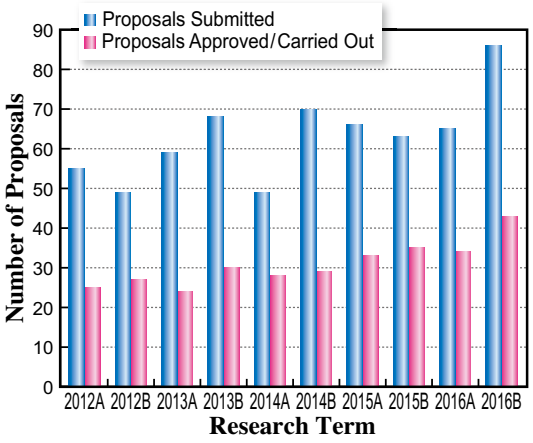

Fig. 1

Table 3. Number of proposals submitted, proposals approved/carried out, cumulative users, and beamtime available by research term

Half-year Research Term	Proposals Submitted	Proposals Approved / Carried Out	(Priority Strategy Proposals)	(General Proposals)	Cumulative Users	Beamtime Carried Out (Shifts)
2012A	55	25	(12)	(13)	297	126
2012B	49	27	(19)	(8)	461	154
2013A	59	24	(15)	(9)	268	117
2013B	68	30	(19)	(11)	410	139
2014A	49	28	(20)	(8)	400	147
2014B	70	29	(17)	(12)	430	140
2015A	66	33	(23)	(10)	527	144
2015B	63	35	(23)	(12)	552	152
2016A	65	34	(21)	(12)	538	158
2016B	86	43	(21)	(20)	650	197

One shift = 12 hours at SACLA beamlines

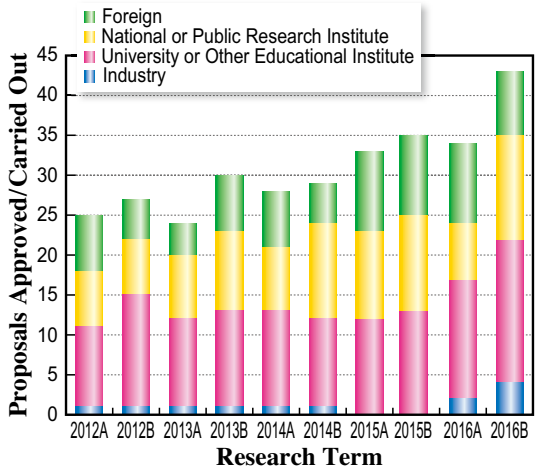

Fig. 2

IV. Research Outcome

As of March 2017, the total number of registered refereed papers from SACLA was 316 many of which were published in high-impact journals. More details can be found at *https://user.spring8.or.jp/uisearch/publication2/*.

NewSUBARU

The NewSUBARU synchrotron light facility is operated by the Laboratory of Advanced Science and Technology for Industry (LASTI), University of Hyogo. This facility consists of an electron storage ring and nine beamlines. Electron injection is supplied from a 1 GeV linac of the SPring-8 facility. The conceptual layout of the NewSUBARU facility is illustrated in the figure. Nine beamlines are operated and in our lab, and these beamlines are focused on the research and development (R&D) of extreme ultraviolet lithography, the LIGA (German acronym for Lithographite, Galvanoformung and Abformung) process, chemical analysis, and novel light source study.

1) BL01 gamma-ray beamline is used in nuclear physics research and for the generation of high-energy positrons used in nondestructive material inspections.

2) BL02 and BL11 are the nano-micro manufacturing beamlines using large area X-ray lithography of micron order and in high aspect ratio patterning using LIGA processing technology.

3) BL03, BL09 and BL10 are the beamlines for the R&D of EUV lithography of next generation semiconductor devices. EUV resist evaluation technology and EUV mask inspection technologies are developed.

4) BL05, BL06, BL07 and BL09 are the material analysis beamlines used in the soft X-ray spectroscopy technologies such as X-ray absorption fine structure, X-ray photoelectron spectroscopy, and X-ray emission spectroscopy.

All NewSUBARU beamlines are open both for industrial usage and fundamental science research. Promotions of both the use and technical assistance for industrial users are supported by MEXT's "Project for Creation of Research Platforms and Sharing of Advanced Research Infrastructure."

Takeo Watanabe
Director of LASTI, University of Hyogo

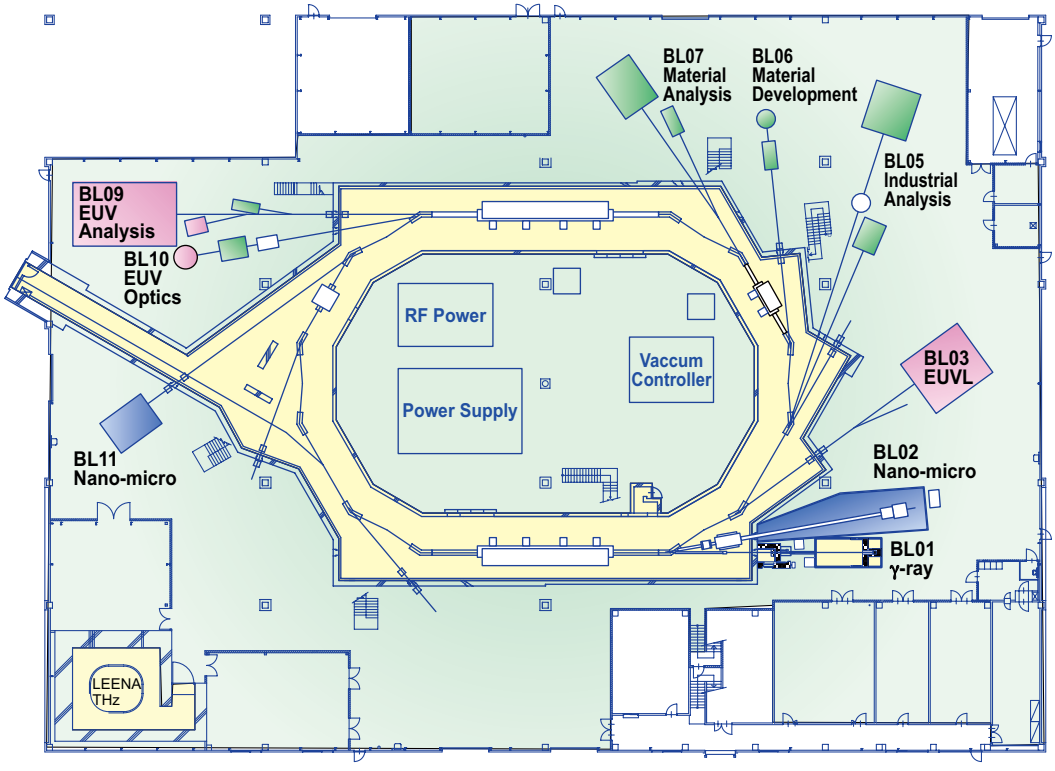

Study of the fluorinated self-assembled monolayer by photoemission and NEXAFS spectroscopies

The study of surface modification using the fluorinated self-assembled monolayer (F-SAM) has attracted significant interest for a wide range of applications because its surface covered by F-SAM has good properties of anti-adherence, lubrication, and water resistance [1]. In the field of nanoimprint lithography, which is a promising method of fabricating various nanostructures at low cost and with a high throughput by pressing a mold, F-SAM has been used as an antisticking layer of nanoimprint molds to avoid resist adhesion [2]. Since the antisticking layer of a nanoimprint mold repeatedly comes into direct contact with the resist in the process of nanoimprint lithography, it is critical to obtain information on the surface of the F-SAMs, the interface between the F-SAMs and the Si substrate, and the molecular orientation in F-SAMs. Therefore, we have measured the photoemission spectra to clarify the electronic structures, such as the chemical compositions and components, on the surface of F-SAMs. In addition, the near-edge X-ray absorption fine structure (NEXAFS) spectra of F-SAMs with different thicknesses were measured to investigate the molecular orientation.

Four kinds of F-SAMs denoted as FAS-3, FAS-9, FAS-13, and FAS-17 were prepared from the fluorinated silane coupling agent $CF_3(CF_2)_n(CH_2)_2Si(OCH_3)_3$ with n=0, 3, 5, and 7, respectively [3]. The number after FAS means the number of F atoms. With increasing number of F atoms, the length of the C-C chain arising from the $(CF_2)_n$ part increases. The schematic diagrams of the four kinds of F-SAMs with different chain lengths are shown in Fig. 1. All photoemission and NEXAFS spectra were measured at BL07B end station of the NewSUBARU synchrotron radiation facility, University of Hyogo.

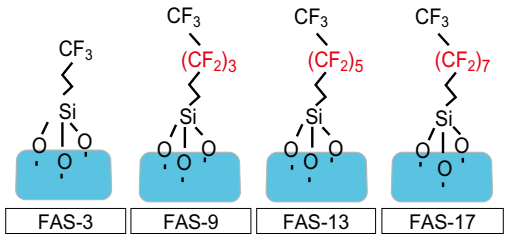

Fig. 1. Four kinds of F-SAMs with different chain lengths.

In Fig. 2, the photoemission spectra (dots) of the C 1*s* core-level region in four kinds of F-SAMs with different chain lengths are plotted. In the photoemission spectra of the C 1*s* core level, three peaks at 292, 286, and 284.5 eV were observed in FAS-3 although four peaks at 293, 291, 286, and 284.5 eV were observed in FAS-9, FAS-13, and FAS-17. With increasing chain length, the intensity of the peak at 291 eV increased while the intensities of the peaks at 293 and 286 eV did not change. On the basis of the chemical compositions of the four kinds of F-SAMs with different chain lengths, the four peaks at 293, 291, 286, and 284.5 eV in FAS-9, FAS-13, and FAS-17 were assigned to the CF_3, CF_2, CH_2, and C-C components, respectively. In FAS-3, the peak at 292 eV was assigned to the CF_3 component, since there is no C-C chain arising from the $(CF_2)_n$ part, as shown in Fig. 1. To clarify further details of the chemical environments, the curve fitting analysis for the photoemission spectra of the C 1*s* core level was performed by a least-square method. The best-fit curves (lines) of the four kinds of F-SAMs with

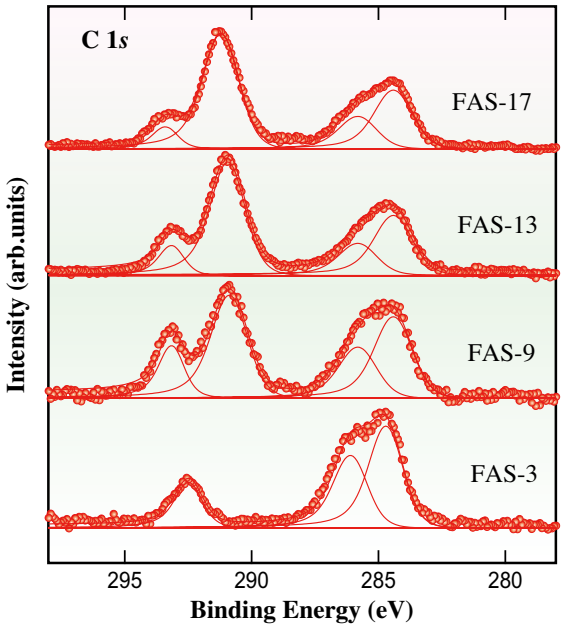

Fig. 2. Photoemission spectra (dots) of the C 1*s* core-level region in four kinds of F-SAMs with different chain lengths. The fitted results (lines) are also plotted for each photoemission spectrum.

different chain lengths are also shown. Figure 3 shows the NEXAFS spectra of the four kinds of F-SAMs with different chain lengths. Several peaks were observed at the photon energies of 285, 289, 290, 292, 295, and 299 eV. With increasing chain length, the intensities of the peaks at 292 and 299 eV increased while that of the peak at 289 eV decreased. On the other hand, the intensities of the peaks at 285, 290, and 295 eV were almost unchanged with increasing chain length. This indicates that the peaks at 292 and 299 eV are derived from the $(CF_2)_n$ part of F-SAMs. In addition, the peaks at 292, 295, and 299 eV in this study were assigned to the σ*(C-F), σ*(C-C), and σ*(C-F) transitions from the C 1*s* core level, respectively [4]. The peak at 289 eV was also assigned to the σ*(C-H) transition arising from the $(CH_2)_2$ part of the F-SAMs. When the incidence angle θ increased from 0 to 75°, the intensities of the peaks at 292 and 299 eV assigned to the σ*(C-F) transitions decreased while that of the peak at 295 eV assigned to the σ*(C-C) transition increased. Since the direction of the electric field in synchrotron radiation is parallel to the surface in the case of θ = 0°, the incidence angle dependence indicates that the σ*(C-F) and σ*(C-C) orbitals in F-SAMs are parallel and perpendicular to the surface, respectively. Therefore, it is considered that the C-C chain in the $(CF_2)_n$ part of F-SAMs is perpendicular to the surface.

In summary, the electronic structures of four kinds of F-SAMs with different chain lengths were investigated by photoemission and NEXAFS spectroscopies. Not only the chemical compositions and components but also the molecular orientation in the F-SAMs were clarified in this study. These results would be useful in the fields of application, such as nanoimprint lithography.

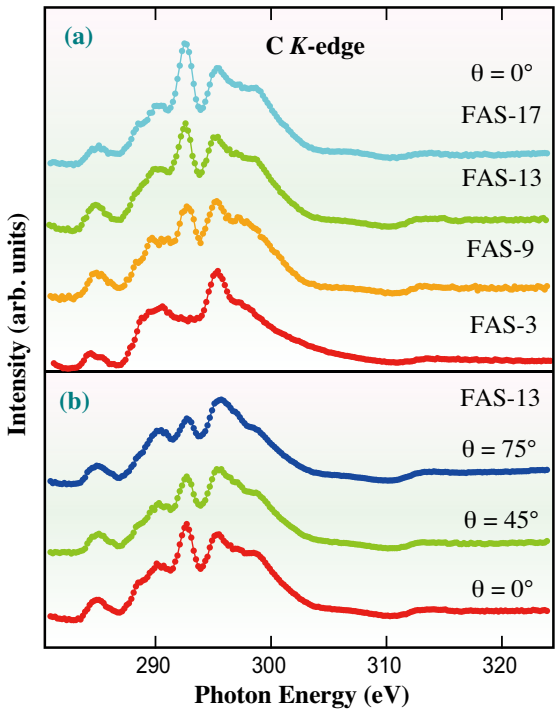

Fig. 3. **(a)** C *K*-edge NEXAFS spectra of four kinds of F-SAMs with different chain lengths. **(b)** C *K*-edge NEXAFS spectra in FAS-13 as a function of the incidence angle of the synchrotron radiation to the surface normal.

Yuichi Haruyama

Laboratory of Advanced Science and Technology for Industry, University of Hyogo

Email: haruyama@lasti.u-hyogo.ac.jp

References

[1] S.R. Wasserman *et al.*: Langmuir **5** (1989) 1074.
[2] S. Matsui *et al.*: J. Vac. Sci. Technol. B **19** (2001) 2801.
[3] Y. Nakai *et al.*: J. Photopolym. Sci. Tec. **23** (2010) 55.
[4] *Y. Haruyama, Y. Nakai and S. Matsui: Appl. Phys. A* ***121*** *(2015) 437.*

Editor
Naoto Yagi
Japan Synchrotron Radiation Research Institute (JASRI)

Editing, Design & Layout
Marcia M. Obuti-Daté
Japan Synchrotron Radiation Research Institute (JASRI)

Printing
Hokuoh Printing Co.

JASRI
Information & Outreach Section
Users Administration Division

1-1-1 Kouto, Sayo-cho, Sayo-gun
Hyogo 679-5198 • JAPAN
Tel. +81-(0)791-58-2785 Fax. +81-(0)791-58-1869

Email: frontiers@spring8.or.jp
http://www.spring8.or.jp/

August 2017

SPring-8 SACLA

http://www.spring8.or.jp

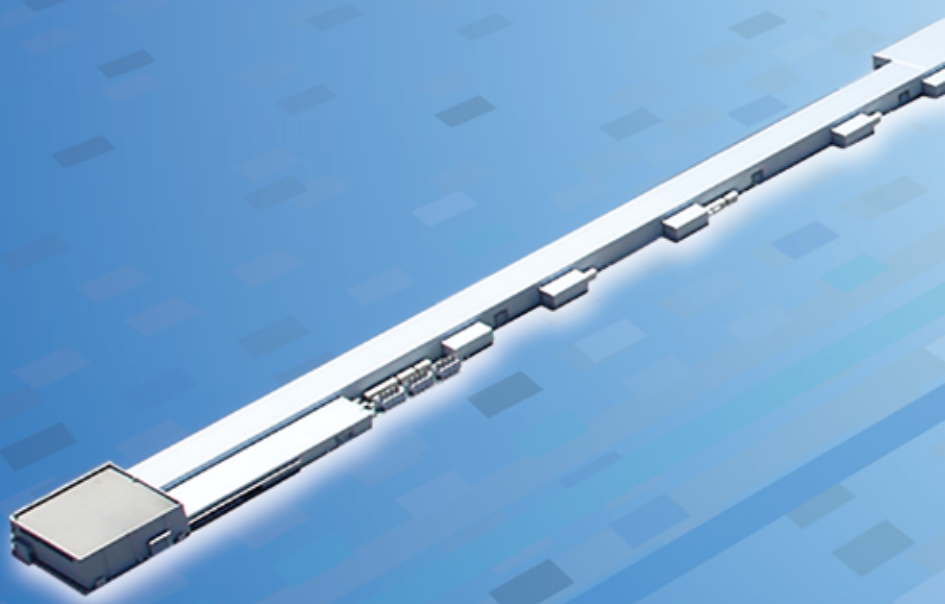

Japan Synchrotron Radiation Research Institute (JASRI)
1-1-1 Kouto, Sayo-cho, Sayo-gun, Hyogo 679-5198, Japan